

Initiation and Propagation of Localized Corrosion of Mild Steel in Marginally Sour
Environments

A dissertation presented to
the faculty of
the Russ College of Engineering and Technology of Ohio University

In partial fulfillment
of the requirements for the degree
Doctor of Philosophy

Wei Zhang

December 2020

©2020 Wei Zhang. All Rights Reserved.

This dissertation titled
Initiation and Propagation of Localized Corrosion of Mild Steel in Marginally Sour
Environments

by

WEI ZHANG

has been approved for
the Department of Chemical and Biomolecular Engineering
and the Russ College of Engineering and Technology by

Marc Singer

Associate Professor of Chemical Engineering

Mei Wei

Dean, Russ College of Engineering and Technology

Abstract

ZHANG, WEI, Ph.D., December 2020, Chemical Engineering

Pit Initiation and Propagation of Localized Corrosion of Mild Steel in Marginally Sour Environments

Director of Dissertation: Marc Singer

A systematic investigation of pitting failure of mild steel in marginally sour environments was performed with the objective of understanding and predicting the occurrence of localized corrosion. While localized corrosion can happen due to a variety of reasons, recent work has shown that mild steel was particularly susceptible to pitting in environments containing traces of H₂S (ppm level in the gas phase, which equates to ppb level of dissolved O₂ in the liquid phase) of H₂S. Relevant research works related to localized corrosion of mild steel exposed to O₂, CO₂ and H₂S containing aqueous environments were carefully reviewed and a critical comparison was performed, identifying experimental methodologies, common mechanisms and gaps in understanding. A comprehensive parametric study was conducted to identify the operating parameters controlling the occurrence of localized corrosion in marginally sour environments. As a result, pitting was found to occur under the following conditions: 0 mbar < p_{H₂S} < 0.15 mbar, p_{CO₂} > 0 bar, temperature < 60°C, bulk pH < 6, on X65 mild steel (not on pure iron), in NaCl concentrations of 0, 1, and 10 wt.%, with 3 ppb_(w) < [O₂]_{aq} < 40 ppb_(w). Surface analysis (FIB-TEM-SAED-PED) identified a typically 200 nm thick, porous, detached, and partially oxidized amorphous mackinawite layer precipitated within a Fe₃C network.

The role of O_2 was further investigated to explain the unexpected presence of oxides in the corrosion product layer. Initially, FeS was thought to have been oxidized during the post processing analysis. However, *in situ* Raman microscopy later showed that oxygen ingress during the experiment was the origin of iron oxide formation. In addition, when $[O_2]_{aq} < 3 \text{ ppb}_{(w)}$, neither corrosion product precipitation nor pitting was observed on the steel surface in any conditions tested, while the uniform corrosion rate remained low.

In this case, the protectiveness was due to the presence of a very thin FeS chemisorbed layer. In the presence of oxygen ($[O_2]_{aq} > 3 \text{ ppb}_{(w)}$ at 1 bar total pressure), this FeS chemisorbed layer partially oxidized, leading to the formation of iron oxides. The volume change caused by the phase change (FeS chemisorption layer to iron oxides) exposed the underlying steel surface to the corrosive environment. These exposed local spots corroded due to the presence of CO_2 , which can typically lead to corrosion rates as high as $3 \sim 4 \text{ mm/y}$, initiating pitting.

A phase equilibrium diagram was developed for the Fe/ H_2S / H_2O / O_2 system based on the minimization of Gibbs free energy. The diagram includes redox reactions involved in the transformation of several FeS polymorphs in aqueous solution driven by various concentrations of dissolved oxygen over a range of pH values. Pathways for the transformation of mackinawite into greigite, magnetite or hematite were identified depending on the concentration of dissolved oxygen. This study shows that the chemisorbed FeS layer can be partially oxidized in the presence of oxygen, leading to pit initiation in marginally sour environments.

The phase equilibrium diagram of the $\text{H}_2\text{S}/\text{H}_2\text{O}/\text{O}_2$ system indicated that in aqueous solution, H_2S could also be catalytically oxidized into SO_4^{2-} at $p\text{H}_2\text{S} = 4 \times 10^{-4}$ bar, releasing H^+ as a coproduct of this reaction. This was verified by monitoring the pH during the corrosion process. Water chemistry analysis revealed that a small portion of H_2S could have been oxidized into H_2SO_4 in the electrolyte, with Fe^{2+} and Ni^{2+} serving as the catalysts. At the active corrosion sites, the higher $[\text{Fe}^{2+}]$ may have further enhanced this process, leading to lower local pH and lower saturation degree of FeS to prevent regeneration of the product layer inside the pit. This mechanism, together with the galvanic coupling effect between the actively corroding pit (anode) and the mackinawite covered cathode, is thought to govern the pit propagation.

To summarize, the investigations reported herein have fully revealed the mechanism of localized corrosion of mild steel in marginally sour environments. In industrial processes, once the crude oil leaves the deep underground anoxic environments, it is not uncommon to measure oxygen content as high as 20 ppb_w (6×10^{-7} mol/L), which may not be low enough to prevent pitting in marginally sour environments.

Dedication

to

My Father, Zengnian Zhang and

My Husband, Yang Liu

Acknowledgments

I would like to express my sincere gratitude to my advisor, Dr. Marc Singer, for his unconditional support of my academic and personal life in the last six years. I would also like to express my gratitude to the director of the Institute of Corrosion and Multiphase Technology (ICMT), Dr. Srdjan Nestic, for admitting me and providing many opportunities to me. The director of the Corrosion Center Joint Industry Projects (CC-JIP), Dr. Bruce Brown, also helped me tremendously by supporting my experimental works and my research ideas. I would also like to thank Research Professor, Dr. David Young for his guidance on materials characterization techniques, crystal structure, and tutoring on English writing skills. Without these four scholars' help, the completion of my dissertation would have been a near impossible task.

Furthermore, I would like to acknowledge the CC-JIP sponsor companies for their funding and professional feedback. The research topic of this dissertation came from their experience and observation of industry practice.

I would also like to thank the staff of ICMT, Cody Shafer, Alexis Barxias and Rebecca Gill for their support whenever I needed it, especially Cody, for his collaboration with me in developing the *in-situ* Raman cell. I would like to thank Dr. Fernando Farelas Valencia for the SEM training and troubleshooting, Dr. Gheorghe Bota, Dr. Peng Jin and Dr. Xi Wang for FIB-TEM guidance, and Dr. Fei Lu for Raman microscopy guidance. My sincere gratitude also goes to Stephen Smith and Sytze Huizinga for their guidance in developing the thermodynamic verification of my experimental observations.

Last but not least, I would like to thank all my friends, classmates and colleagues in ICMT for their companionship all through these years.

Table of Contents

9

Abstract.....	3
Dedication.....	6
Acknowledgments.....	7
List of Tables	12
List of Figures	13
Chapter 1: Introduction.....	18
Chapter 2: Literature Review.....	21
2.1 Water Chemistry of Corrosive Aqueous Solutions Containing CO ₂ , H ₂ S and O ₂	21
2.1.1 Water Chemistry of CO ₂ - H ₂ O System.....	21
2.1.2 Water Chemistry of H ₂ S-H ₂ O System	22
2.1.3 Comparison Between H ₂ CO ₃ and H ₂ S Containing Aqueous Systems	23
2.1.4 Water Chemistry of O ₂ – H ₂ O System.....	24
2.1.5 Reaction Between H ₂ S and O ₂ in Aqueous Solution.....	25
2.1.6 Methods for Water Chemistry Analysis	26
2.2 Fundamentals of Aqueous H ₂ S/CO ₂ Corrosion of Mild Steel.....	30
2.2.1 Thermodynamics and Kinetics of CO ₂ Corrosion.....	30
2.2.2 Thermodynamics and Kinetics of H ₂ S Corrosion.....	32
2.2.3 Dominant Mechanisms in CO ₂ / H ₂ S Systems	36
2.2.4 Thermodynamics and Kinetics of O ₂ Corrosion.....	37
2.2.5 Oxidation and Transformation of Corrosion Products in Marginally Sour Environments in the Presence of Oxygen.....	38
2.3 Localized Corrosion in Marginally Sour Environments.....	47
2.3.1 Definition and Measurement of Localized Corrosion	47
2.3.2 Reports of Localized Corrosion in Marginally Sour Environments	48
2.3.3 Pitting Mechanism: The Three Fundamental Steps of Localized Corrosion	52
Chapter 3: Objectives, Hypotheses and Scope of Work.....	70
3.1 Motivation.....	70
3.2 Objectives	70
3.3 Hypotheses.....	71
3.4 Scope of Work	71

Task #1: Repeatability Study	72
Task #2: Parametric Study	73
Task #3: Characterization of Corrosion Product Layer	75
Task #4: Investigation on Water Chemistry near the Surface or Inside the Pits ..	75
Task #5: Development and Validation of Pitting Mechanism.....	75
Chapter 4: A Parametric Study Based on Formation of Protective Layers	76
4.1 Introduction.....	76
4.2 Experimental Setup and Procedure.....	83
4.2.1 Experimental Materials.....	83
4.2.2 Experimental Equipment	84
4.2.3 Experimental Matrix	85
4.2.4 Experimental Procedure.....	86
4.2.5 Evaluation of Pitting Ratio.....	88
4.2.6 Experimental Safety.....	90
4.3 Results and Discussion	90
4.3.1 Effect of H ₂ S Partial Pressure on Pitting	91
4.3.2 Effect of pCO ₂ on Pitting.....	103
4.3.3 Effect of pH on Pitting.....	115
4.3.4 Effect of Temperature on Pitting	129
4.3.5 Effect of Salt Concentration on Pitting.....	134
4.3.6 Effect of Microstructure on Pitting.....	140
4.3.7 Effect of Time on Pitting	148
4.4 Conclusions.....	152
Chapter 5: Pit Initiation Based on the Oxidation of the Chemisorbed Iron Sulfide Layers	156
5.1 Introduction and Research Goals	156
5.2 Experimental Procedure.....	162
5.3 Investigation of the Origin of O ₂ Ingress and the Formation of Oxides.....	165
5.4 Effect of Various Oxygen Concentrations	175
5.5 Proposed Mechanism of Pit Initiation in Marginally Sour Environments.....	186
5.6 Summary.....	187
Chapter 6: Pit Propagation Based on Acidification by Catalytic Oxidation of Dissolved Hydrogen Sulfide	189

6.1 Introduction.....	189
6.2 Contribution of the O ₂ Reduction to the Overall Cathodic Reaction.....	194
6.3 Thermodynamics of the oxidation of dissolved H ₂ S at low temperatures.....	195
6.4 Thermodynamics of the oxidation of mackinawite corrosion product layer	206
6.5 Kinetics of the Oxidation of Dissolved H ₂ S at Low Temperatures	210
6.5.1 Background and Previous Results	210
6.5.2 Experimental Procedure.....	213
6.5.3 Results and Discussion	214
6.6 Pit Propagation Mechanism: Solution Acidification near Steel Surface by Catalytic Oxidation of H ₂ S _(aq)	217
6.7 Summary	220
Chapter 7: Application of <i>in situ</i> Raman Microscopy on the Study of Corrosion Product Formation in Marginally Sour Environments	222
7.1 Introduction.....	222
7.2 Experimental Setup and Procedures	227
7.2.1 Experimental Equipment	227
7.2.2 Experimental Procedure.....	231
7.3 Results and Discussion	231
7.3.1 Seal test of the IRFC	231
7.3.2 Calibration with Minerals of Known Structures	233
7.3.3 Detection of Sulfate Species with <i>in situ</i> Raman.....	236
7.3.4 Possible Oxidation Products of Mackinawite	238
7.3.5 <i>In situ</i> Test Result on Precipitated Mackinawite Layer	252
7.3.6 <i>In situ</i> Test Result on Chemisorbed S _{ads} (Fe) Layer	253
7.4 Summary	258
Chapter 8: Conclusions and Future Work.....	260
8.1 Conclusions.....	260
8.2 Future Work	262
References.....	264

List of Tables

	Page
Table 1 Current methods for detection of sulfur containing anions [34].....	28
Table 2 Solubility of elemental sulfur (orthorhombic S ₈) at 25°C in organic solvents [41]	29
Table 3 Various iron sulfide formation reactions and saturation expressions for S _{FeS}	57
Table 4 Iron sulfides typically encountered in H ₂ S corrosion systems	58
Table 5 Key concepts of “grey zone” theory systems	62
Table 6 Effect of H ₂ S concentration	73
Table 7 Test matrix of the parametric study (P _{total} = 1 bar, [O ₂] _{aq} ≈ 20 ppb _(w) , stir bar rotation speed = 300 rpm).....	74
Table 8 FeCO ₃ layer and FeS layer growth mechanisms*	80
Table 9 Chemical composition (wt. %) of API 5L X65 [142].....	83
Table 10 Sulfide analysis - possible match with Fe _{0.91} S.....	125
Table 11 Ionic strength of solutions of various NaCl weight percentage.....	136
Table 12 A Summary of FIB-TEM analysis of the product layer of the selected conditions related to the occurrence of localized corrosion. Iron oxides was found together with sulfides in the layer. (30 °C, p _{H₂S} = 0.04 mbar, [NaCl] = 1 wt. %, 7 days)	154
Table 13 Test matrix of the effect of various oxygen ingress concentrations	165
Table 14 Possible explanations for the presence of oxides.....	166
Table 15 Oxygen concentration in the experimental setup.....	172
Table 16 Reported Raman peak positions for mackinawite and other relevant iron sulfur- containing phases	241

List of Figures

	Page
Figure 1 Lewis structure and polarity of H ₂ O, H ₂ S and H ₂ CO ₃ molecules	24
Figure 2 Schematic representation of a double layer on an electrode (Bockris /Devanathan/Müller, BDM) model.	31
Figure 3 Potential-pH diagram for sulfur adsorbed on Fe (25°C, m _s = 10 ⁻⁴ mol kg ⁻¹). ..	33
Figure 4 pH-Eh diagram showing the mackinawite-greigite boundary at 25 °C, 1 bar total pressure, $\sum\{\text{Fe}\}_T = 10^{-3}$, and $\sum\{\text{S(-II)}\} = 10^{-3}$ and 10 ⁻⁶ mol/kg.	40
Figure 5 Stability diagram of mackinawite and greigite.....	41
Figure 6 Pourbaix diagram for H ₂ S-H ₂ O-Fe system with (left) Mackinawite / Greigite; (right) Mackinawite / Greigite / Pyrrhotite / Pyrite (T = 25°C, pH ₂ S = 0.1 bar, [Fe ²⁺] = 10 ppm, [Fe ³⁺] = 10 ⁻⁶ mol/L, pH ₂ = pO ₂ = 1 bar).	42
Figure 7 The crystal structure of both mackinawite and greigite and their phase transition mechanism.	43
Figure 8 Diffraction patterns obtained from oxidation of mackinawite (pH 3.6, 95°C, H ₂ S gas flow). 1). After 1 h of exposure; 2). After 172 h of exposure; 3). Ingress of O ₂ due to halt in H ₂ S-gas flow for 24 h; 4). Ingress of O ₂ for 96 h; 5). Ingress of O ₂ for 240 h.....	44
Figure 9 Pitting attack risk prediction based on partial pressure ratio and temperature..	49
Figure 10 Pitting attack reported at various conditions indicated in a risk prediction plot based on partial pressure ratio and temperature.....	52
Figure 11 Using the concept of scaling tendency to describe pit initiation in CO ₂ environments by undermining effect	64
Figure 12 Schematic representation of the three steps of localized corrosion.....	77
Figure 13 Microstructure of X65 (0.05 wt. % C) consisting of large ferrite grains with cementite precipitates.....	84
Figure 14 Experimental setup for the two-liter glass cell using a stable solution chemistry system for small-scale experiments	85
Figure 15 Optical profilometry measurement.....	88
Figure 16 Pit depth and general corrosion	90
Figure 17 Saturation degree of the bulk solution of both FeS _{mackinawite} (navy line and above) and FeCO ₃ (orange line and above) for different pH ₂ S values.	92
Figure 18 LPR (a) and weight loss (b) corrosion rates for different pH ₂ S values.	93
Figure 19 SEM cross-section images of specimens at different H ₂ S partial pressure after 7 days exposure.....	95

Figure 20	Surface profilometry analysis of specimens recovered for each experimental condition after 7 days exposure after corrosion product layer removed.....	97
Figure 21	TEM images of the cross section of the specimen for the baseline experiment cut out by FIB	99
Figure 22	TEM-EDS mapping results of the specimen of baseline condition experiment	100
Figure 23	TEM-EDS line scan results of the specimen in baseline condition.....	102
Figure 24	Saturation degree of bulk solution for both $\text{FeS}_{\text{mackinawite}}$ (blue line and above) and FeCO_3 (orange line and above) for varied pCO_2	104
Figure 25	LPR and weight loss corrosion rates for varied pCO_2	105
Figure 26	SEM cross-section images of specimens at different CO_2 partial pressure after 7 days exposure.....	107
Figure 27	Surface profilometry analysis of specimens recovered for each experimental condition after 7 days exposure after corrosion product layer removed.....	109
Figure 28	TEM images of the cross section cut out by FIB from the specimen of $\text{H}_2\text{S}/\text{N}_2$ experiments	111
Figure 29	TEM-EDS mapping results of the specimen of the $\text{H}_2\text{S}/\text{N}_2$ experiment.....	112
Figure 30	TEM-EDS line scan results of the specimen of $\text{H}_2\text{S}/\text{N}_2$ experiment.....	114
Figure 31	Saturation degree of both $\text{FeS}_{\text{mackinawite}}$ (blue line and above) and FeCO_3 (orange line and above) under various pH in the bulk solution.....	116
Figure 32	LPR and weight loss corrosion rates under various pH in the bulk solution .	117
Figure 33	SEM cross-section images at different pH after 7 days exposure	118
Figure 34	Surface profilometry analysis at different pH after 7 days exposure after corrosion product layer was removed.....	119
Figure 35	TEM images of the cross section cut out by FIB from the specimen of pH 6 experiments	121
Figure 36	TEM-EDS mapping results of the specimen of pH 6 experiment.....	122
Figure 37	TEM-EDS line scan results of the specimen pH 6 experiment.....	123
Figure 38	TEM-SAED results near the inner layer of the specimen of pH 6 experiment	124
Figure 39	Pattern analysis of the specimen of pH 6 experiment	125
Figure 40	Orientation/phase map by PED near the inner layer of the specimen of pH 6 sample	126
Figure 41	TEM-SAED results near the outer layer of the specimen of pH 6 experiment	127

Figure 42 Orientation/Phase Map by PED near the outer layer of the specimen of pH 6 experiment.....	128
Figure 43 Saturation degree of both $\text{FeS}_{\text{mackinawite}}$ (blue line and above) and FeCO_3 (orange line and above) at various temperatures in bulk solution	130
Figure 44 LPR and weight loss corrosion rates at various temperatures.....	131
Figure 45 SEM cross-section images of specimens at different temperatures after 7 days exposure	132
Figure 46 Surface profilometry scanning images of different temperatures after 7 days exposure after corrosion product layer removed	133
Figure 47 Saturation degree of both $\text{FeS}_{\text{mackinawite}}$ (blue line and above) and FeCO_3 (orange line and above) of various salt concentrations in bulk solution.....	135
Figure 48 LPR and weight loss corrosion rates of various salt concentrations	137
Figure 49 SEM cross-section images of specimens at different salt concentrations after 7 days exposure.....	138
Figure 50 Surface profilometry scanning images of specimens at different salt concentrations after 7 days exposure after corrosion product layer removed	139
Figure 51 Saturation degree in the bulk solution of systems featuring different working electrode materials	140
Figure 52 LPR and weight loss corrosion rates of different working electrode materials	142
Figure 53 The cross-section images by SEM backscattering and EDS mapping for the iron (blue), sulfur (yellow), carbon (red) and oxygen (green) element	143
Figure 54 Surface profilometry scanning images of specimens of X65 and pure iron specimens after 7 days exposure after corrosion product layer removed	144
Figure 55 TEM images of the corroded pure iron specimen cross section cut out by FIB	146
Figure 56 TEM-EDS mapping results of pure iron sample	147
Figure 57 TEM-EDS line scan results of pure iron sample	148
Figure 58 SEM images at different exposure time	150
Figure 59 Surface profilometry of steel surface after the layer was removed by Clarke solution at different exposure time	151
Figure 60 Factors that can lead to localized corrosion of mild steel in $\text{H}_2\text{S}/\text{CO}_2$ environments.....	158
Figure 61 Stable solution chemistry system for small scale lab test: (a) with hanging specimens and stir bar in a glass cell; (b) with fixed specimen holders and rotating impeller in a glass cell.....	163
Figure 62 Flow chart of experimental procedure.....	164

Figure 63 No oxidation observed on freshly polished X65 specimen	167
Figure 64 Oxidation of mackinawite with time measured with a Raman microscope (laser excitation line 532 nm, power 25W	169
Figure 65 Measuring dissolved oxygen concentration by placing oxygen meter at the end of the gas outlet of the experimental setup	171
Figure 66 Typical oxygen monitor results of a 7-day experiment in the type b setup as shown in Figure 61 (b).....	171
Figure 67 In situ Raman spectroscopy analysis: direct proof of oxidation of mackinawite into magnetite in the aqueous solution on a corroding surface.....	174
Figure 68 Linear polarization resistance (a) and weight loss (b) corrosion rate.....	176
Figure 69 FIB-TEM analysis of the corroded specimen with dissolved oxygen concentration less than 3 ppb _(w)	178
Figure 70 TEM-EDS analysis of the corroded specimen with dissolved oxygen concentration less than 3 ppb _(w)	179
Figure 71 Fe-S-H ₂ O Pourbaix diagram at 298.15 K considering chemisorbed layers, excluding the pyrite phase	181
Figure 72 Surface profilometry image after layer removal. (the specimens were corroded at 30°C, pH 5.01 ± 0.01, 0.97 bar CO ₂ , 0.04 mbar H ₂ S, 300 rpm stir bar, 7 days)	183
Figure 73 The change of total amount of [Fe ²⁺]/[Fe ³⁺] with time	184
Figure 74 pH changes with time	186
Figure 75 Proposed mechanism of pit initiation in marginally sour environments.....	187
Figure 76 Evans diagram in marginally sour environment with O ₂	195
Figure 77 Pourbaix diagram of the H ₂ S - H ₂ O system [298.15K, 1 atm, pH ₂ S = 0.01 bar (1 v.%)]	198
Figure 78 Pourbaix diagram of H ₂ S -H ₂ O system [298.15K, 1 atm, pH ₂ S = 0.04 mbar (40 ppm _v)]	199
Figure 79 Phase equilibrium diagram of the H ₂ S-O ₂ -H ₂ O system [298.15K, 1 atm, pH ₂ S = 0.01 bar (1 v.%)].....	202
Figure 80 Phase equilibrium diagram of H ₂ S-O ₂ -H ₂ O system [298.15K, 1 atm, pH ₂ S = 0.04 mbar (40 ppm _v)].....	204
Figure 81 Using phase equilibrium diagram of H ₂ S-O ₂ -H ₂ O system to predict formation of elemental sulfur (298.15K, 1 atm).....	205
Figure 82 Phase equilibrium diagram of the mackinawite-O ₂ -H ₂ O system [298.15 K, 1 atm, pH ₂ S = 0.01 bar (1 v.%)]	208
Figure 83 Phase equilibrium diagram of Mackinawite-O ₂ -H ₂ O system [298.15K, 1 atm, pH ₂ S = 0.04 mbar (40 ppm _v)]	209

Figure 84	Water chemistry analysis by UV/Vis & pH monitoring (30 °C, initial pH=5.01, pCO ₂ = 0.97 bar, pH ₂ S = 40 mbar, [O ₂] _{aq} = 7 ppb _(w)).	215
Figure 85	Toluene extraction after 7-day experiment for Raman analysis detection of elemental sulfur	217
Figure 86	Proposed pit propagation mechanism	219
Figure 87	2D design sketch of the 3D printed in situ Raman flow cell (IRFC) reactor	228
Figure 88	In situ Raman flow cell (IRFC) reactor 3D sketch	229
Figure 89	P&ID of the designed in situ Raman flow loop	230
Figure 90	Pictures of the in situ Raman flow cell & flow loop	230
Figure 91	Using methylene blue as oxygen indicator to test cell tightness	232
Figure 92	Sealing capacity of the IRFC	233
Figure 93	Calibration of IRFC with calcite mineral standard sample (×10 objective)	235
Figure 94	Calibration of IRFC with pyrite	236
Figure 95	Raman spectra of standard Na ₂ SO ₄ solution of various concentrations showing the characteristic peak of Na ₂ SO ₄ detectable above 0.01 mol/L	238
Figure 96	SEM analysis of the thick mackinawite layers	242
Figure 97	XRD analysis of the layer showing both mackinawite and pyrrhotite	243
Figure 98	Ex situ Raman spectra of the 3 μm thick mackinawite / pyrrhotite corrosion product layer and comparison with RRUFF data	244
Figure 99	TEM images of the cross section cut out by FIB from the specimen of pH 6 experiments	246
Figure 100	XPS results—the elemental composition of the corrosion product layers	247
Figure 101	XPS spectra of pure iron and X65 specimens exposed to the pH 6 condition (X65, 30°C, 0.04 mbar H ₂ S and 0.97 bar CO ₂ , pH 6.01 ± 0.01, 1wt.% NaCl, 300 rpm, 7 days)	248
Figure 102	Ex situ Raman spectra of the thin mackinawite corrosion product layer and comparison with RRUFF data	250
Figure 103	Surface condition of the corroding X65 steel specimens under naked eye and microscopy after 1, 3- and 7-days exposure	255
Figure 104	In situ and ex situ Raman spectra of the corroding surface after 1, 3, 7 days of exposure	257

Chapter 1: Introduction

Metals and their alloys have been widely used since the industrialization of society. However, metals such as iron are prone to return to their pre-extraction oxidation states, akin to their original condition as oxides, sulfides, etc., in the ore minerals from which they were produced. During their service lives, metallic structures come into contact with various environments. This contact brings destructive results to metals or alloys, which results in a diminution of asset integrity, economic losses, and even increased risk to human lives. For example, crude oil vapor explosions due to pipeline leakage, postulated to be linked to corrosion, killed 62 people in Qingdao, China, on November 22, 2013 [1]. A similar disaster occurred in Guadalajara, Mexico, on April 22, 1992 that resulted in 252 fatalities [2]. Therefore, metal structures and components, fabricated from appropriately selected materials, need to be protected against degradation, especially so when they are exposed to physically and chemically aggressive environments.

Each industrial sector has its own set of environmental challenges associated with materials degradation *via* specific corrosion mechanisms. This dissertation is focused on localized corrosion of mild steel in weak acidic H₂S/CO₂ environments containing traces of O₂, pertaining to the use of production tubulars, pipelines, tanks, and related infrastructure for the exploration, production, and transportation of natural gas and petroleum products. Research efforts in this area have significantly expanded since De Waard and Milliams published their first paper on modelling of CO₂ corrosion in 1975 [3]. Very thorough electrochemical models have been developed for both CO₂ and

CO₂/H₂S environments, based on a wealth of experimental data. Yet, many gaps still exist on the understanding of the mechanisms as most of the conducted research has focused on uniform corrosion of mild steel. Comparatively, localized corrosion, which is more often the cause of premature equipment failure, remains poorly understood.

There are typically three steps in the development of localized corrosion of metals or steels. The first step involves the formation of a protective layer. In the presence of CO₂, this layer usually takes the form of a product of corrosion precipitated on the steel surface. This layer can decrease the corrosion rates by acting as a mass transfer barrier and affecting the rates of electrochemical reactions [4, 5]. The formation of this layer is controlled by the water chemistry and more specifically by the saturation degree of the metal carbonate (FeCO₃ in this case) precipitate [6]. The second step involves the initiation of a pit due to damage of this protective layer. The reasons for the damage are numerous, from mechanical stresses to steel composition or challenges in local electrolyte chemistry. Once the pit is initiated, it can either propagate or get annihilated depending on if the local corrosive environment can be sustained. This scenario can vary depending on environment characteristics. In the presence of O₂, the protective layer can take the form of a thin passive oxide film [7]. In the presence of H₂S, the protective layer can take many forms as several polymorphs of FeS exist, making this topic not well understood. At moderate to high H₂S content, the presence of different types of FeS in the corrosion product layers is known to lead to surface heterogeneity that have been hypothesized to lead to galvanic coupling and initiate localized corrosion. In the presence of small concentration of H₂S, severe pitting has also been observed experimentally

although no mechanistic explanation has been proposed. As an example, it remains unclear whether or not the saturation degree of the FeS (mackinawite) can be applied in a similar way as in sweet environments. Yet, many other conditions involving H₂S are relatively benign in term of corrosion severity and will not yield any localized corrosion at all. In summary, localized corrosion in sour (CO₂/H₂S) environments is very complex and can take many forms, none of them adequately understood. Many research efforts are currently being undertaken to address this topic, this dissertation representing one of them.

This work focuses on localized corrosion of mild steel in marginally/slightly sour environments in order to advance the mechanistic understanding of its initiation and propagation. The mechanisms of localized corrosion in CO₂, H₂S and O₂ containing aqueous environments are reviewed in Chapter 2. The objectives and hypotheses of this research work are presented in Chapter 3. A systematic parametric study on the effects of operating parameters on the occurrence of pitting in marginally sour environments is presented in Chapter 4. Based on the layer characterization results, the effect of oxygen ingress on both the steel surface and water chemistry is further investigated in Chapter 5 and in Chapter 6, respectively. A qualitative mechanistic model is proposed in Chapter 8.

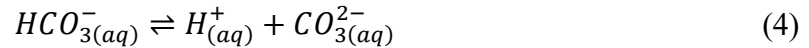
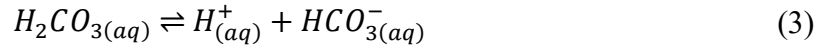
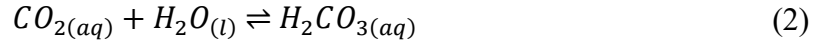
Chapter 2: Literature Review

This chapter introduces the current state of knowledge related to the reactions between mild steel, carbon dioxide (CO₂), hydrogen sulfide (H₂S), oxygen (O₂) and water (H₂O). It then presents the fundamental definition and basic mechanisms of localized corrosion.

2.1 Water Chemistry of Corrosive Aqueous Solutions Containing CO₂, H₂S and O₂

2.1.1 Water Chemistry of CO₂ - H₂O System

The presence of carbon dioxide and co-produced aqueous fluid with oil and gas is the main reason for the high risk of corrosion of pipeline materials. Carbon dioxide dissolves in water (reaction (1)) to a mole fraction value of 5.41×10^{-4} at 30°C, considering 1 bar CO₂ partial pressure [8]. For comparison, O₂ is less soluble and will dissolve to a mole fraction value of 2.12×10^{-5} at 30°C, 1 bar O₂ partial pressure [9]. Only a small portion (less than 1% [10], depending on the conditions) of the CO₂ hydrates to form carbonic acid (H₂CO₃, reaction (2)), which is a weak acid [11]. A portion of this carbonic acid dissociates into hydrogen ions (H⁺) and bicarbonate ions (HCO₃⁻, reaction (3)), then even fewer bicarbonate ions dissociate into hydrogen ions and carbonate ions (CO₃²⁻, reaction (4)) at pH values typically encountered in production conditions [12, 13]. Consequently, the presence of CO₂ is severely detrimental to steel structures as it constitutes a source of hydrogen ions (H⁺), decreasing the pH and increasing the corrosivity of the aqueous solution. Fortunately, there is a long trackable research history and many review papers detailing the equilibrium constants and modeling of CO₂/H₂O systems [14, 15].



2.1.2 Water Chemistry of H₂S-H₂O System

Hydrogen sulfide (H₂S) is often, but not always, present in oil and gas produced fluids and contributes to the corrosivity of the aqueous phase. H₂S dissolves in water to directly form a weak acid, aqueous hydrogen sulfide (reaction (5)). The solubility of H₂S (g) at 30°C is 1.66×10^{-3} (mole fraction), considering 1 bar H₂S partial pressure [16]. The solubility of H₂S in water decreases as temperature increases [17]. It also decreases as the salt concentration increases in solution, which is the so-called “salting out” effect [18]. Two steps of dissociation also happen to produce H⁺, HS⁻, and S²⁻ (reaction (6), (7)), although the second step is also reactant favored at pHs typically encountered in production conditions (3.5 < pH < 8). The concentrations of these species are governed by solution pH as well as the equilibrium constants for the aforementioned dissociation reactions. Therefore, for a near neutral pH solution, S²⁻ content is negligible [17]. Again, the detailed dissociation reactions and associated constants can be found in references [14].



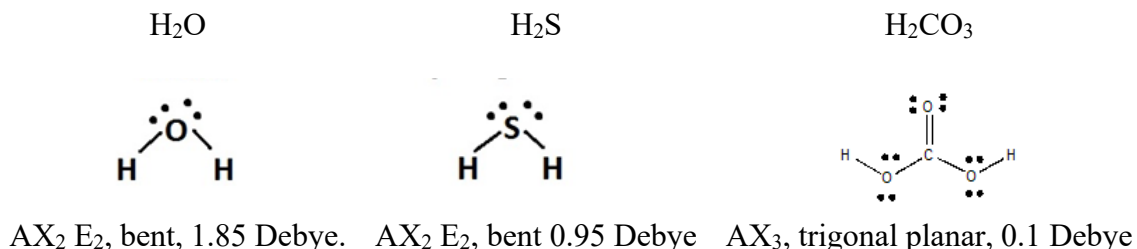
2.1.3 Comparison Between H₂CO₃ and H₂S Containing Aqueous Systems

Like H₂CO₃, dissolved H₂S is also a weak acid. They share common characteristics, in terms of their solubility in water (as dissolved CO₂ and H₂S), the trend of solubility changes with temperature and salinity, and the two steps of acid dissociation. Therefore, they can be readily compared with each other [18]. However, they do feature some very different characteristics. For example, HS⁻ and S²⁻ can be oxidized into polysulfide (S_x²⁻), elemental sulfur (S₈), thiosulfate (S₂O₃²⁻), sulfite (SO₃²⁻) or sulfate (SO₄²⁻) due to the multi-valent character of sulfur; this can further complicate the water chemistry of H₂S [17, 19]. According to the valence shell electron pair repulsion (VSEPR) theory (Figure 1) [20, 21], HS⁻ has a larger polarity and enhanced reactivity compared with HCO₃⁻, because, like OH⁻, HS⁻ also has lone pairs of electrons [22]. Additionally, HS⁻ has a smaller size than HCO₃⁻, but the most important point is that it can be adsorbed chemically onto metallic/alloy surfaces and undergo direct reaction, or chemisorption [23]. This process is much faster than precipitation, where metal cations are combined with CO₃²⁻ or S²⁻.

In comparison, the kinetics of OH⁻ adsorption on metals are much lower than for HS⁻, especially in the absence of O₂. As explained earlier, both OH⁻ and HS⁻ are adsorbed on the steel surface. It is known that a chemisorbed layer of FeS [S_{ads}(Fe)] can be formed quickly. The formation of FeO is more complicated [24]. Two adjacent adsorbed OH [OH_{ads}(Fe)] form one FeO and H₂O. Due to the high stability of H₂O, it is difficult for this reaction to happen without the presence of O₂. This will be further discussed in section 2.2.2.

Figure 1

Lewis structure and polarity of H₂O, H₂S and H₂CO₃ molecules

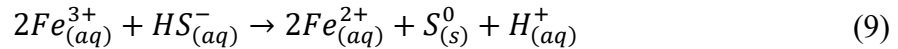
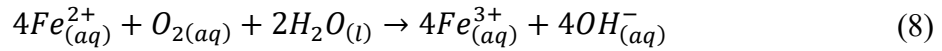


2.1.4 Water Chemistry of O₂ – H₂O System

O_{2(g)} is typically not present in reservoir conditions. However, as fluids are produced, O_{2(g)} ingress into the pipeline network (due to injection of fluids or chemicals, maintenance, pump leakage, etc.) is not uncommon. The solubility of O_{2(g)} in water or aqueous solution under 1 bar partial pressure of oxygen is one to two orders of magnitude lower than CO_{2(g)} and H₂S_(g); only about ten molecules of oxygen are dissolved per million molecules of water [8]. The diffusivity of O₂ in water is only about 0.00001 of its diffusivity in the air at 20°C [25]. However, agitation can help the mass transfer of O₂ within the water. Consequently, reactions involving O₂ cannot be ignored in an open system with continuous ingress of even a trace amount of O₂ [19]. However, oxygen is, as its name indicates, a strong oxidizer. It can oxidize sulfide species in solution. It can also be reduced at the metal surface and affect the rate of overall electrochemical reactions. In addition to changes in water chemistry, the presence of oxygen can also lead to the precipitation of metal oxides.

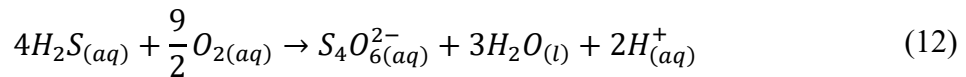
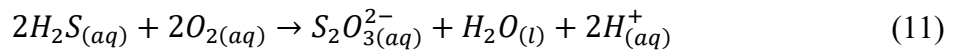
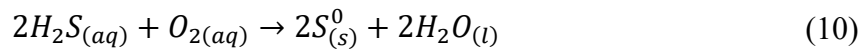
2.1.5 Reaction Between H_2S and O_2 in Aqueous Solution

In the gas phase, the reaction between H_2S and O_2 below $120^\circ C$ is negligible [26]. In aqueous solution, oxidation of HS^- by dissolved O_2 is kinetically slow. If there is Fe^{3+} or Mn^{3+}/Mn^{4+} in solution, these metal ions with higher valency can readily oxidize HS^- [27]. This process can be made into a catalytic cycle starting with Fe^{2+} oxidation by O_2 [19]. This process is shown in the following reactions (reaction (8), (9)):



As an example, compared with other typical O_2 scavengers (such as Na_2SO_3 , SO_2 , and N_2H_4), the rate of O_2 removal by HS^- oxidation without a catalyst is low [28]. The reaction rate is increased in the presence of catalysts (Fe^{2+} , Mn^{2+} , Cu^{2+} , Ni^{2+} , and Co^{2+}), especially at higher pH [28]. The most effective catalysts are Co^{2+} and Ni^{2+} [28]. This phenomenon is commonly observed as water samples from sour corrosion suddenly exposed to open air increase in turbidity due to the formation of elemental sulfur.

Oxidation of H_2S in the aqueous phase in the presence of O_2 can release H^+ , which leads to an acidification of the solution [29]. The proposed explanation is listed in reactions (10–(12)).



A precise water chemistry analysis is crucial to understand what happens after metals or alloys are exposed to such an aqueous environment. Introducing O_2 in a H_2S/CO_2 aqueous system is expected to affect significantly the water speciation, at least proportionally to the concentration of oxygen.

Over a range of temperatures (25, 40, 60, 80 °C), at a total pressure of 1 bar with $H_2S + O_2$ in a volumetric ratio of 5:1, a mmol level of SO_3^{2-} was found at 25 °C, $S_2O_3^{2-}$ and SO_4^{2-} were found at 25~80 °C [30]. Visibly detectable amounts of elemental sulfur were found in experiments at 40, 60, and 80 °C, but not at 25 °C. In other research at $24^\circ C \pm 2^\circ C$ and initial pH 3.9, 100 ppb (mass) SO_4^{2-} was detected in 35 g/L NaCl with 0.1 MPa H_2S and 500 ppb_(w) O_2 contamination [31]. It has been pointed out that the oxidation of H_2S will acidify the solution [31], which makes it more corrosive.

2.1.6 Methods for Water Chemistry Analysis

Experimentally, establishing suitable methods for water chemistry analysis is important in corrosion research. The simplest tools to characterize water speciation of corroding systems, in terms of ease of use and accessibility are pH electrodes and Fe^{2+} concentration measurement instruments, the latter typically using UV-vis spectrophotometry in conjunction with chelating agents. Many other analytical tools (such as NMR, HPLC) obviously exist but when it comes to sulfide (S^{2-}), sulfur (S_8), polythionate (S_n^{2-}), sulfite (SO_3^{2-}), thiosulfate ($S_2O_3^{2-}$) and sulfate species (SO_4^{2-}). It is difficult to find a suitable (and economical) method to facilitate their separation and identification [32]. One intrinsic reason is that some of these species are not particularly stable, being easily oxidized from one to another by air; dilution can even impact

speciation. Ion chromatography (IC) is a powerful and versatile method in water chemistry analysis, but its screening capacity depends on the type of column used and fluid to be characterized. For example, separating sulfide from common inorganic anions (chloride, nitrite, and nitrate) is difficult; sulfite and sulfate have similar retention times [33]. According to an IC instrument manufacturer [34], ion chromatography with suppressed conductivity can discriminate between and identify $S_2O_3^{2-}$ and SO_3^{2-} [31]. Ion-pair chromatography (IPC) can identify S_x^{2-} (**Table 1**). With IPC, sulfide and sulfite are quantitatively converted into stable thiocyanate and sulfate [33]. These conversions stabilize these anions and permit their complete separation from common anions [33]. In addition, H_2S can damage certain types of chromatographic columns, so it should be purged from solutions prior to analysis [31]. Specifically, $S_2O_3^{2-}$ can be titrated by I_3^- , however, S^{2-} can be oxidized at the same time if there is any in the system. Spectrophotometrically, vibrational modes associated with S-S or S-O bonding are weak in infrared spectra.

Another simple but effective analytical technique is the use of a barium chloride ($BaCl_2$) reagent to detect SO_4^{2-} by UV/Vis. The feasibility of this method in a complicated sulfur compounds system depends on the solubility of different barium sulfur compounds. The solubility of barium sulfide (BaS) is 6.97 g/100mL at 20 °C [35]. The solubility of barium sulfate ($BaSO_4$) in water is 0.2448 mg/100mL at 20 °C [36]. That is why the detectable limit of this method is 2 ppm. The solubility of barium sulfite ($BaSO_3$) is 11 mg/L [37]. Information on the solubility of barium thiosulfate (BaS_2O_3) is scarce and the only literature data found also reports 0.21 mg/100mL at 18 °C [38]. In

practice, precipitation of white crystals of BaSO_4 or BaS_2O_3 is clearly visible in solution above the solubility limit. Therefore, assuming BaS_2O_3 is not present in solution, BaSO_4 is the only detectable white precipitation in this test. Consequently, this method presents a relatively simple measurement method for SO_4^{2-} , with the only drawback being the lack of specificity between SO_4^{2-} and $\text{S}_2\text{O}_3^{2-}$.

Table 1

Current methods for detection of sulfur containing anions [34]

Detection methods	Sulfur containing anions
Iodometry	Sulfide
Direct current polarography	Sulfide
Differential pulse polarography	Sulfide
Spectrophotometry after derivatization with Methyl Blue	Sulfide
Spectrophotometry after derivatization with Ellman's reagent	Sulfite
<i>Ion chromatography with suppressed conductivity</i>	<i>Sulfite, Sulfate, Thiosulfate</i>
Ion chromatography with Electrochemical Detection	Sulfide
<i>Ion-pair chromatography</i>	<i>Polythionate</i>

CS_2 extraction can be used to identify S_8 [39]. However, CS_2 is highly toxic [40] and flammable. It is difficult to find other alternatives for good sulfur solvents [41] (see

Table 2). Toluene is much less toxic than benzene [42], which might be a promising substitute [43]. Trace amounts of S₈ in toluene could be detected by infrared spectroscopy or by a combustion method, as is commonly applied in fuel quality measurements [39]. Turbidity measurements by a nephelometer could be an indirect method to show the presence of sulfur in the aqueous solution, although formed S₈ may adhere to steel and other surfaces.

Table 2

Solubility of elemental sulfur (orthorhombic S₈) at 25°C in organic solvents [41]

(data in mass %) (Copyright © 1965 WILEY-VCH Verlag GmbH & Co. KGaA,

Weinheim)

Ethanol	Acetone	Diethyl ether	Dimethyl formamide	n-Hexane
0.066	0.079	0.181	0.191	0.40
Carbon tetrachloride	Nitrobenzene	Chloroform	Cyclohexane	Aniline
0.832	0.856	1.164	1.185	1.259
Xylene	Toluene	Benzene	Chlorobenzene	Carbon disulfide
2.051	2.070	2.093	2.370	34.8

2.2 Fundamentals of Aqueous H₂S/CO₂ Corrosion of Mild Steel

2.2.1 Thermodynamics and Kinetics of CO₂ Corrosion

When mild steel is put in contact with an aqueous solution containing dissolved CO₂, H₂O molecules adsorb on the steel surface to form a solvent layer that is oriented depending on the charge of the surface. An electrical double layer forms between the adsorbed water molecule layer and a second ordered layer of water molecules [44]. If present in solutions, solvated ions can also take part in the formation of these layers. The planes formed by the adsorbed water molecules are referred to as the inner and outer Helmholtz planes, as illustrated in Figure 2. This electrical double layer is analogous to a charged capacitor.

H⁺ released by dissociation of H₂CO₃ and HCO₃⁻ participates in the reduction reaction at the steel surface (equation (3) and (4)). H₂O can be reduced and gain an electron to form H₂ and OH⁻ (reaction (14)) [45]. Metal atoms in the steel are oxidized and lose electrons to become cations dissolved into the solution (reaction (15)). CO₂ hydration is the slowest step in this entire corrosion process. Therefore, CO₂ corrosion is mainly chemical reaction controlled, although it can also be charge transfer or mass transfer controlled depending on the conditions. Detailed information on CO₂ corrosion can be found elsewhere [14].

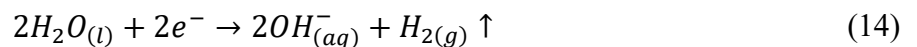
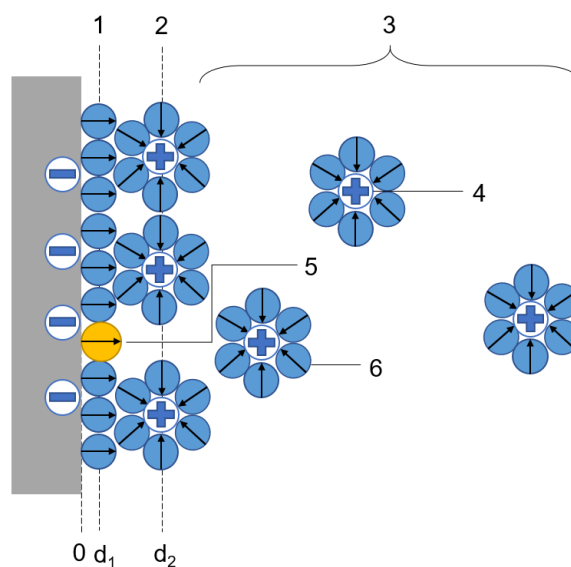


Figure 2

Schematic representation of a double layer on an electrode (Bockris /Devanathan/Müller, BDM) model.

1. Inner Helmholtz plane, (IHP), 2. Outer Helmholtz plane (OHP), 3. Diffuse layer, 4. Solvated ions (cations) 5. Specifically, adsorbed ions (redox ion, which contributes to the pseudocapacitance), 6. Molecules of the electrolyte solvent.



Below 120 °C, dissolved cations, for example, Fe^{2+} , can combine with CO_3^{2-} in the solution to form metal carbonate (typically FeCO_3) precipitates (reaction (16)) when the product of their concentrations exceeds the solubility limit [46]. Above 120 °C, both iron carbonate and magnetite (Fe_3O_4) will form [47]. The ratio of the product of concentrations to the solubility equilibrium coefficient is called the saturation degree [6]. At equilibrium, the saturation degree is 1 (unity). In certain conditions, the formation of these corrosion product layers can protect the steel from rapid corrosion by “shielding”

the active surface from electrochemical processes. The limited permeability of the layer also serves as a mass transfer barrier to electroactive species, thus changing the local water chemistry near the surface and inside the pore structure of the layer [48]. Although FeCO_3 is usually porous, sometimes it can be protective in terms of corrosion mitigation [49].



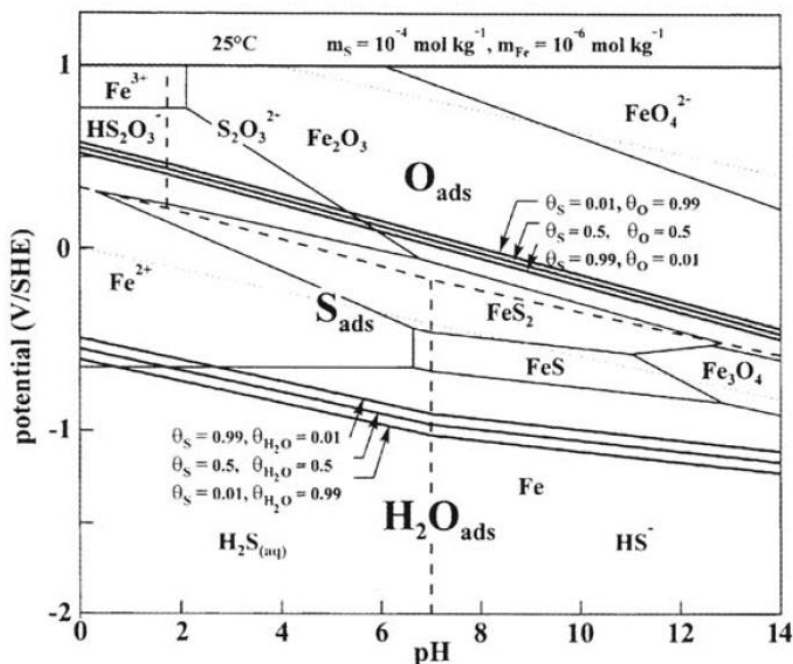
2.2.2 Thermodynamics and Kinetics of H_2S Corrosion

As mentioned in the previous section, H_2O can adsorb directly on the steel surface forming the inner Helmholtz plane. Similar to H_2O , $\text{H}_2\text{S}_{(aq)}$ could also adsorb as part of this inner layer when mild steel is exposed to sour environments (the yellow molecule stands for H_2S while the rest blue ones are H_2O in Figure 2). This means that $\text{H}_2\text{S}_{(aq)}$ changes the structure of the electric double layer [19]. When mild steels are exposed to sour environments, the chemisorption of $\text{H}_2\text{O}_{(l)}$ and $\text{H}_2\text{S}_{(aq)}$ on the steel surface leads to the formation of $\text{OH}_{\text{ads}}(\text{Fe})$, $\text{O}_{\text{ads}}(\text{Fe})$ and $\text{S}_{\text{ads}}(\text{Fe})$ [50]. Two adjacent $\text{OH}_{\text{ads}}(\text{Fe})$ moieties combine to form FeO and H_2O [50]. However, if $\text{S}_{\text{ads}}(\text{Fe})$ partially substitutes for $\text{OH}_{\text{ads}}(\text{Fe})$, this makes the formation of FeO more difficult. Also, $\text{S}_{\text{ads}}(\text{Fe})$ is more stable than $\text{O}_{\text{ads}}(\text{Fe})$. According to thermodynamic calculations of chemisorption processes in the $\text{Fe-H}_2\text{S-H}_2\text{O}$ system (**Figure 3**) based on Marcus's published data [50], $\text{S}_{\text{ads}}(\text{Fe})$ on an iron surface is very stable; this is also the case on Ni. In practical terms, this means it can exist even when sulfides are not expected to be stable according to the bulk solution conditions [24].

Figure 3

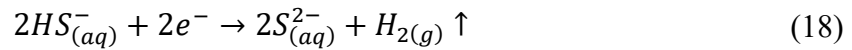
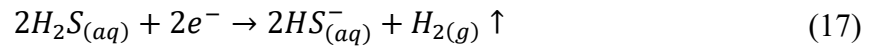
Potential-pH diagram for sulfur adsorbed on Fe (25 °C, $m_s = 10^{-4} \text{ mol kg}^{-1}$).

Reprinted with permission from [50]. Copyright 2002 Taylor and Francis Group LLC (Books) US.

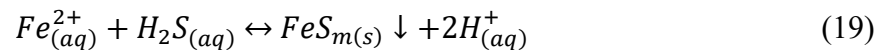


Consequently, it has been postulated that when $\text{H}_2\text{S}_{(\text{aq})}$ enters in contact with an iron surface, it rapidly adsorbs and forms a thin layer of chemisorbed iron sulfide [23]. This has been termed as a solid-state reaction or direct reaction [51], the accuracy of this description being questioned in the literature [52]. This chemisorbed layer is so thin that it is difficult to observe even under TEM. However, the proof of its existence is in the substantial decrease in general corrosion rate observed experimentally when H_2S is injected into a sweet (CO_2 containing) corrosive environment. This characteristic of H_2S

corrosion is unique as it indicates that there is seldom a bare steel surface condition in sour corrosion. The chemisorbed layer of FeS primarily affects the kinetics of charge transfer (i.e., of electrochemical reactions) as it is too thin to act as an effective mass transfer barrier. As an example, addition of 0.04 mbar of $H_2S_{(g)}$ into 1 bar CO_2 , for a pH 5.0 electrolyte, at 30°C brings the corrosion rate from 2-4 mm/y down to 0.2 mm/y [53] in a matter of minutes [54]. $H_2S_{(aq)}$ can react with the steel surface directly within a very short time. Oxidative dissolution of Fe at an anodic area still occurs (reaction (15)), as well as the reduction of H_2O (reaction (14)), $H_2S_{(aq)}$ (reaction (17)) and HS^- (reaction (18)) at cathodic sites.



As mentioned earlier, there are several pathways for the formation of FeS on the steel surface. The very thin chemisorbed FeS layer forms almost instantaneously on the steel surface [23]. However, precipitation of iron sulfides (FeS, reaction (19)) from the bulk solution can also happen. It can be expressed as follows.



FeS precipitates when the saturation degree becomes larger than unity [52]. Mackinawite is believed to be the first type of FeS that forms [55]. Within short time spans, or at low concentrations of $H_2S_{(g)}$, the resultant layer is typically a nanocrystalline mackinawite structure, which is often mischaracterized as amorphous by X-ray diffraction (XRD) [19]; this was before high-resolution microscopy techniques could prove its actual long-range structure [56, 57]. Mackinawite is not thermodynamically

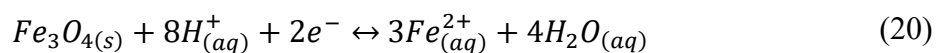
stable and can be readily oxidized into greigite (Fe_3S_4), then pyrite (FeS_2). With higher H_2S concentration, pyrrhotite can form together with mackinawite [58]. Pyrite mainly forms under high temperature and high-pressure conditions [59].

As mentioned earlier, the existence of various FeS polymorphs and related phases makes H_2S corrosion a complicated matter. Iron sulfides are a family of inorganic compounds, including mackinawite (FeS), greigite (Fe_3S_4), pyrite (FeS_2), pyrrhotite (Fe_{1-x}S , $x = 0$ to 0.2), etc. Their crystal structures govern their various physicochemical properties (e.g., solubility, conductivity, reactivity with certain chemicals under the same condition). Their morphological characteristics (including porosity and tortuosity) are also different from each other [19]. They tend to transform from one to another under certain conditions. Different morphologies and structures of the formed corrosion product layers will play a crucial role in the determination of the corrosion rates.

The fact that steel surfaces in sour environments are always covered with certain types of iron sulfides, and that the typical corrosion rates are much lower than what is observed in CO_2 corrosion, means that H_2S has been categorized by some researchers to act as a *de-facto* corrosion inhibitor [19]. It has even been argued that H_2S shares similarities with certain types of corrosion inhibitors in terms of chemical structure [19]. However, the extreme reactivity of H_2S and the complicated chemistry within the sulfide system proves that H_2S is more detrimental than mitigating as regards the corrosion of steel.

Recent research on high temperature (> 120 °C) H_2S corrosion revealed a multilayer structure on the steel surface, made of an inner layer of Fe_3O_4 and an outer

layer of iron sulfide [60]. The author mentioned that Fe_3O_4 had greater effect on the corrosion process than mackinawite. The proposed layer formation mechanism was as follows: 1) the Fe_3O_4 was formed by the electrochemical reaction between Fe^{2+} and water (reaction (20)); 2) The outer part of the Fe_3O_4 was converted into iron sulfide by reaction with H_2S ; 3) depending on different partial pressure of H_2S , mackinawite, troilite, pyrrhotite, and pyrite were detected at the outer layer. According to thermodynamic calculation, this trend of preferred formation of Fe_3O_4 at high temperature would reverse at 25 °C [60].



2.2.3 Dominant Mechanisms in CO_2 / H_2S Systems

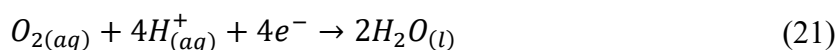
Petroleum engineers describe oil and gas containing carbon dioxide (CO_2) as being sweet [61], whereas if they contain hydrogen sulfide (H_2S), they are termed sour [62]. Often, however, both CO_2 and H_2S are present in the same environment. Since CO_2 and H_2S corrosion features striking differences, determining the specific conditions that govern which corrosion reaction will dominate has been a long-standing challenge and efforts have been made to categorize these environments. Until now, a commonly accepted practice relied on the ratio of partial pressure of CO_2 to partial pressure of H_2S to determine the transition between H_2S and CO_2 dominated corrosion systems. However, use of this ratio proved to be problematic since the corrosion product could be different for high H_2S content *versus* low H_2S content [63]. When the term “which reaction regime dominates” is used, general corrosion rate and chances of localized corrosion occurrence have to be considered, both of which are decided by the existence and protectiveness of

the corrosion product layer. However, conditions can be such that a CO₂/H₂S environment yields several corrosion product layers, seemingly coexisting as components of the layer: iron carbonate, iron sulfides and even iron oxides or hydroxides [53].

Operating parameters such as partial pressures of CO₂ and H₂S, temperature and pH are used to calculate the saturation degree of FeCO₃ and FeS and to thermodynamically predict layer constituents [64]. The presence of FeCO₃ has been observed experimentally underneath FeS in certain conditions. This was explained by the high Fe²⁺ concentration and the depletion of H₂S near the metal surface [65]. Recent research also found Fe₃O₄ [59] underneath FeS at temperatures of around 80°C and above.

2.2.4 Thermodynamics and Kinetics of O₂ Corrosion

Oxygen is an oxidizer in terms of corrosion of steel [23]. Steel in anoxic water (and in the absence of any acidic species) corrodes very slowly because, in terms of electrochemical reactions, the cathodic reaction with H₂O is very slow. However, if oxygen is present, it can be readily reduced according to the following reaction (21).



In O₂ containing solutions, the layer growth begins after adsorption of O₂ on the steel surface [66]. A three-dimensional iron oxide layer is formed, but its thickness is limited to no more than several nanometers [66].

When an anodic potential is applied, a passive layer is formed on the iron surface. This passive layer is up to 5 nm [7]. It has been found that this layer is very protective. However, if there is any defect in this layer, which is prominent enough to develop into layer breakdown, the possibility of occurrence of localized corrosion will be very high;

especially if the layer is originally very protective. Techniques such as Auger electron spectroscopy (AES) [67], electron spectroscopy for chemical analysis (ESCA) [68], and scanning tunneling microscopy (STM) [69] have been used to observe the composition of thin passive oxide films on metals and alloys [7]. To avoid the possible change to chemical composition of a passive layer in a drying process, *in situ* characterization has been tried; such as by XPS [68], AES [70] and Mössbauer spectroscopy [71]. Using a transfer device for Auger analysis, Bockris, et al., [70] concluded that the passive film on iron is mainly composed of $\text{Fe}(\text{OH})_2$ as well as other oxides and hydroxides in a multilayer configuration [68, 72]. The size and structure of the related sub-layers change with the electrode potential as well as other factors, such as the composition of the metal substrate and the electrolyte [73].

The addition of alloying elements such as nickel, chromium and molybdenum to steel have impact on the structure and composition of the oxide film and, thereby, the protectiveness of the corrosion product layer [66]. For example, the passivation of Fe-based alloys is due to the formation of metal-oxides based on alloying elements (Cr_2O_3 for stainless steel).

2.2.5 Oxidation and Transformation of Corrosion Products in Marginally Sour Environments in the Presence of Oxygen

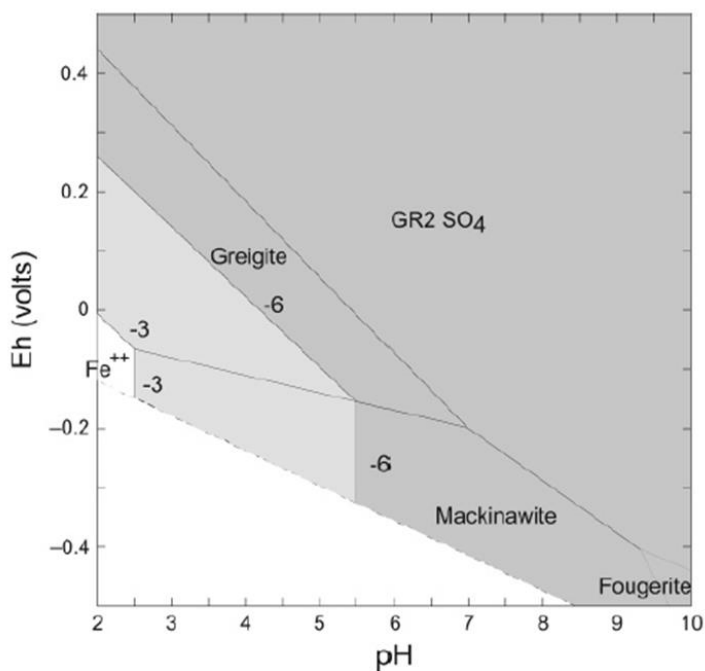
There has been some research related to oxidation of mackinawite and its possible transformation to greigite (Fe_3S_4) [19, 39], all the way to magnetite (Fe_3O_4) and/or hematite (Fe_2O_3) [74, 75]. However, there is no commonly accepted mechanism of mackinawite transformation yet.

Rickard [19] and his coworkers reviewed the homogeneous formation of mackinawite in fresh water and marine environments without the existence of metal, and its transformation to greigite. The thermodynamic plot of this information is shown in Figure 4. They found that mackinawite could react with water directly above 70°C, without O₂ or S²⁻ [19]. They also stated that greigite cannot form without high H⁺ concentration [19], which shows agreement in the fact that naturally formed greigite was found in freshwater rather than marine environments because the former usually has a lower pH value. However, whether this transformation can occur in the solid phase reaction or via the dissolution/precipitation is not definitively known.

Figure 4

pH-Eh diagram showing the mackinawite-greigite boundary at 25 °C, 1 bar total pressure, $\sum\{Fe\}_T = 10^{-3}$, and $\sum\{S(-II)\} = 10^{-3}$ and 10^{-6} mol/kg.

(Reprinted with permission from [19]. Copyright 2007 American Chemical Society.)



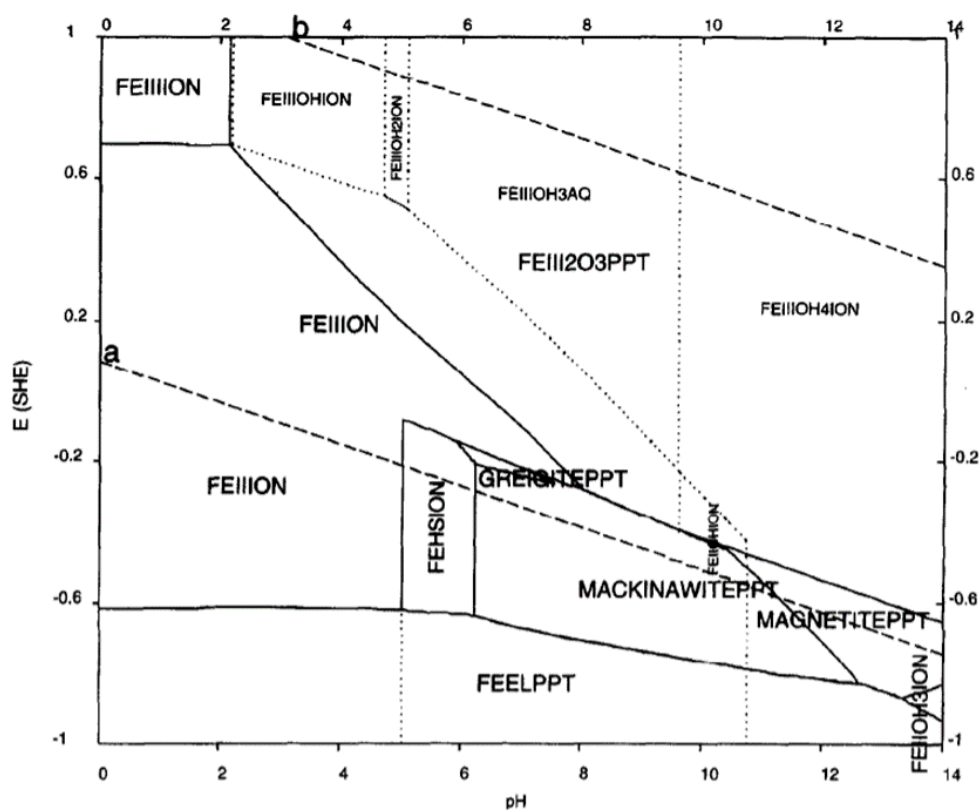
Anderko and Shuler also created Pourbaix diagrams (Figure 5) of mackinawite and greigite [76] for the purpose of corrosion modeling. They postulated that greigite could only be generated from mackinawite in the presence of oxygen. Therefore, the transformation from mackinawite to greigite can happen spontaneously in terms of thermodynamics.

Figure 5

Stability diagram of mackinawite and greigite.

(4×10^{-3} mol/kg H_2S in simulated oil field brine). Reprinted with permission from [76].

Copyright 1997 Elsevier.)

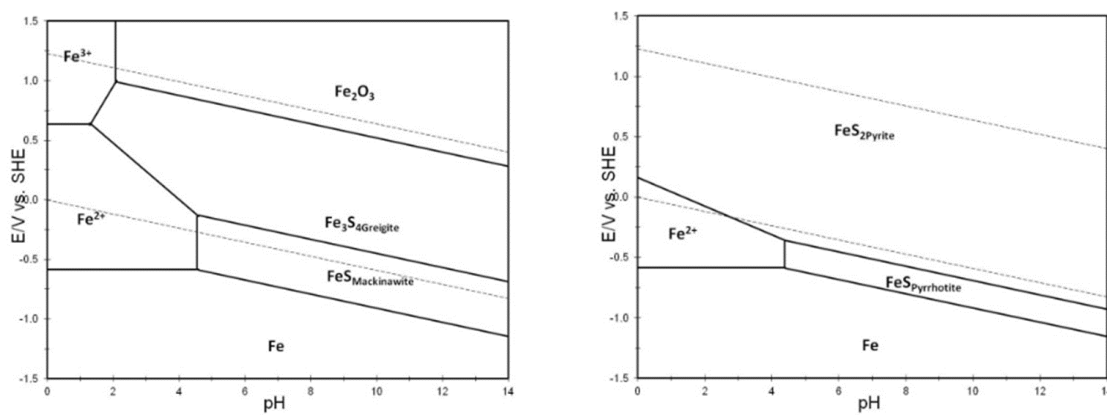


Ning's thermodynamic calculation in anoxic aqueous solution also proved that transformation from mackinawite to greigite, then to pyrite is thermodynamically possible as long as the electrochemical potential is high enough [77] (Figure 6).

Figure 6

Pourbaix diagram for H_2S-H_2O-Fe system with (left) Mackinawite / Greigite; (right) Mackinawite / Greigite / Pyrrhotite / Pyrite ($T = 25^\circ C$, $pH_2S = 0.1$ bar, $[Fe^{2+}] = 10$ ppm, $[Fe^{3+}] = 10^{-6}$ mol/L, $pH_2 = pO_2 = 1$ bar).

(Reprinted with permission from [77]. Copyright 2014 NACE.)

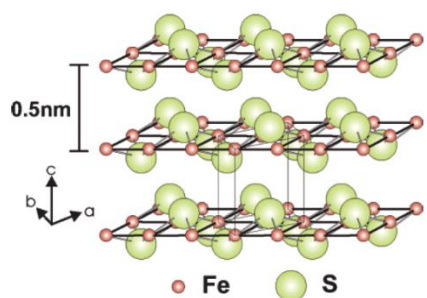


Mackinawite has a tetragonal layer structure (Figure 7 a). The mackinawite unit cell has $a = b = 3.6735$ Å and $c = 5.0329$ Å [78]. Greigite is the cubic thiospinel of iron, $Fe^{II}(Fe^{II}Fe^{III})S_4$, because molecular orbital [79] calculations suggest that the Fe in the octahedral B-sites is a mixture of Fe(III) and Fe(II); it could even be non-stoichiometric, mirroring its isomorphous oxide magnetite. (Greigite is the sulfur analogue of magnetite. It has a similar inverse spinel structure (Figure 7 b).) The cell parameter of greigite is $a = 9.876$ Å. Each cell consists of eight Fe_3S_4 units. The phase transition mechanism between mackinawite and greigite is shown in (Figure 7 c), which has been reprinted from Rickard's [80] and Lennie's [78] research. A rearrangement of Fe atoms in a cubic array of S atoms makes the transformation of mackinawite to greigite. The rearrangement

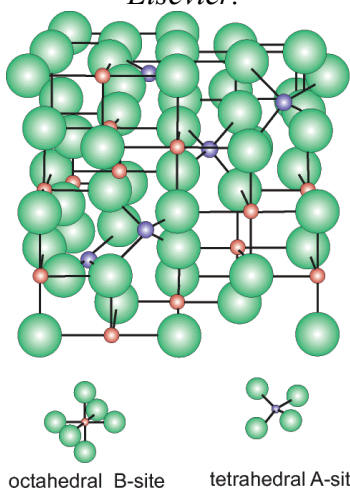
happens due to the oxidation of two-thirds of Fe(II) to Fe(III), because the Fe(III) acquires an octahedral coordination. This transformation leads a volume reduction of 12% in the cubic S array [78].

Figure 7

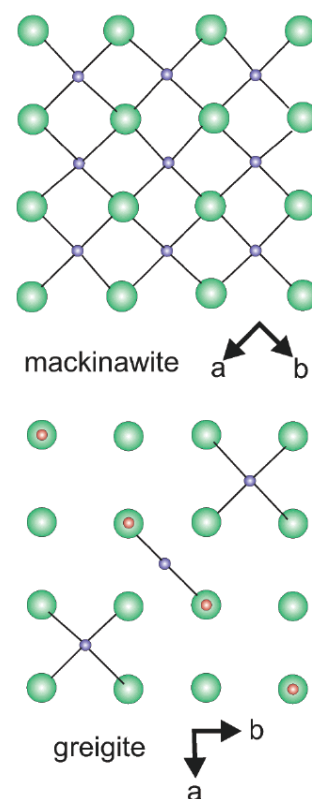
The crystal structure of both mackinawite and greigite and their phase transition mechanism.



(a) *Mackinawite structure. Reprinted with permission from [78]. Copyright 2005 Elsevier.*



(b) *Greigite is an inverse spinel, $A(AB)_2S_4$ where Fe(II) atoms occur in tetrahedral A-sites and mixed Fe(III) and Fe(II) occur in the octahedral B-sites. Reprinted with permission from [78]. Copyright 2005 Elsevier.*



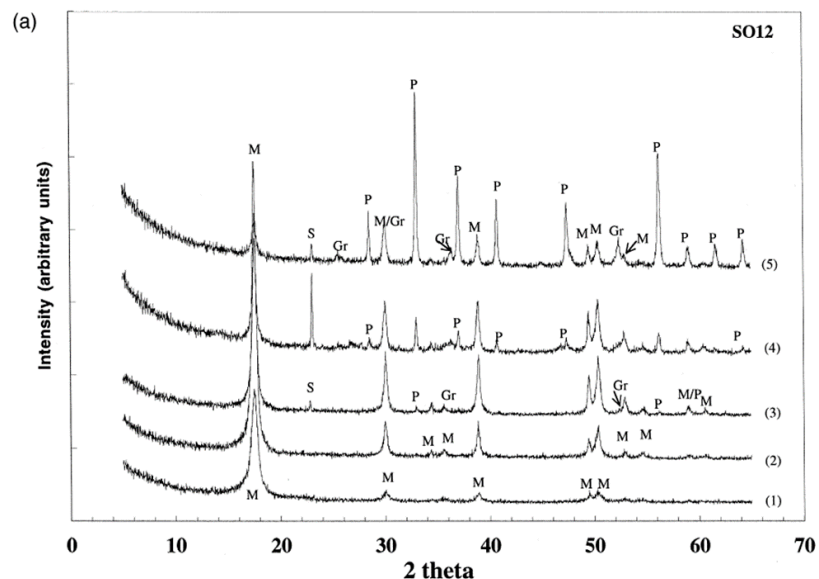
(c) *Homology of the mackinawite and greigite structures. Projections of both structures onto (001) emphasize the similarity in the close-packed cubic arrays of S-atoms in both minerals. Reprinted with permission from [80]. Copyright 2005 Elsevier.*

Benning and her coworkers [39] found that mackinawite was oxidized to greigite, then to pyrite at 70 - 95°C, at ca. pH 3.7 (**Figure 8**). The authors mentioned that a solid-state phase transformation was involved: Fe^{2+} on the surface layer of mackinawite was partially oxidized into Fe^{3+} , supported by two pieces of research on powdered mackinawite sample oxidation [81, 82]. The transformation was much slower under high pH condition, which agrees with Rickard's observation on greigite generation. Greigite is magnetic, so in their research [83] a magnet was used as the supporting evidence of existence of greigite. However, it should be noted that magnetite is also magnetic.

Figure 8

Diffraction patterns obtained from oxidation of mackinawite (pH 3.6, 95 °C, H₂S gas flow). 1). After 1 h of exposure; 2). After 172 h of exposure; 3). Ingress of O₂ due to halt in H₂S-gas flow for 24 h; 4). Ingress of O₂ for 96 h; 5). Ingress of O₂ for 240 h.

(Reprinted with permission from [39]. Copyright 2005 Elsevier.)



Most of these basic research studies were done by geochemists on synthesized mackinawite powder with high purity. XRD, XPS, TEM, STM, etc. can be applied to analyze these specimens, despite the fact that mackinawite tends to form with a nanocrystalline structure, which makes it seem “amorphous” under XRD [19]. Corrosion product layers formed in a sour environment, the major content of which is mackinawite, can be very difficult to characterize due to their extremely thin morphology. The Raman microscope could be a promising tool for this kind of application. In recent decades, researchers used *in situ* Raman to observe oxidation of mackinawite.

Bourdoiseau and colleagues are pioneers in the use of Raman microscopy to analyze corrosion product layers containing aged mackinawite and iron oxides [75]. They also used DFT calculations to further validate the experimental results from their Raman spectra [84].

Genchev and Erbe [74] characterized corrosion product layers formed in CH₃CO₂H and H₂S environments. They polarized their working electrode in order to get a thick enough layer (about 2 μm [85]) to collect prominent peaks under a Raman microscope, because the feedback signal will attenuate when it goes through a glass lens for *in situ* Raman measurements. Generally, as shown in reaction (22), the Fe(II) in the mackinawite corrosion product can first be oxidized into Fe(III), and then form oxyhydroxides or oxides depending on water content within the mackinawite layers.



However, another pathway has been proposed that does not involve greigite as the intermediate phase in the oxidation process of mackinawite, or it relates to a different

understanding of the valence state of greigite [86]. If Fe^{2+} in mackinawite can be oxidized into Fe^{3+} , Fe^{3+} could oxidize S^{2-} into S^0 or even SO_4^{2-} directly. Then, the next stage of oxidation product being $\text{Fe}^{\text{II}}\text{Fe}_2^{\text{III}}\text{S}_4^{\text{II}}$ (greigite) or $\text{Fe}^{\text{II}}\text{S}_2^{\text{I}}$ (pyrite) will be more difficult to explain. Another explanation could be that it is not Fe^{2+} but S^{2-} being oxidized in mackinawite, causing the formation of $\text{Fe}_3^{\text{II}}\text{S}_3^{\text{II}}\text{S}^0$, which is another understanding of the valence states of greigite [86]. Actually, the valence state of greigite might not be fully understood yet. X-ray study of powdered greigite shows that greigite has a spinel structure. Therefore, the stoichiometric formula of Fe_3S_4 was developed primarily by analogy to magnetite. The choice of oxidation states [a mixture of Fe(II) and Fe(III) with S(II)] was based on the evidence available from Mössbauer spectroscopy results [87]. The further detail of this discussion is beyond the topic of this work, future research works might combine both experimental observation and the molecular orbit calculation [88], as well as bandgap theory [89] to reveal the answer.

The sheer number of sulfur compounds that can exist in aqueous environments is a major source of complexity in sour corrosion phenomena. Sulfur, sulfide, sulfite, sulfate, thiosulfate and polysulfide can be generated and transform from one to another under different conditions. From the perspective of corrosion studies, sulfur containing compounds of higher oxidation states cause dissolution of metal through electrochemical reactions once moisture or liquid water is present. If other chemicals with high oxidizing potency exist in the H_2S system, such as O_2 or Fe^{3+} , higher valent sulfur compounds will come to be present that lead to other possible reactions, which will accelerate the corrosion of metal.

Although H_2CO_3 will not participate in these sulfur reactions/cycles directly, its buffering effect can greatly affect the water chemistry and the corrosion rate. It might even affect local pH changes. Formation of FeCO_3 when saturation is reached must be considered in terms of its protectiveness and mass transfer barrier effect.

The most detrimental effect that the sulfur cycle can bring to the metal is localized corrosion and stress cracking. Although there has been some research conducted on this topic, it still needs systematic study before the mechanisms involved are elucidated.

2.3 Localized Corrosion in Marginally Sour Environments

2.3.1 Definition and Measurement of Localized Corrosion

Corrosion is a destructive result of chemical reactions between a metal or metal alloy and its environment. Usually, a uniform removal of metal is called “uniform corrosion” [90]. When the loss of metal is not uniform at the steel surface, pits or grooves are produced due to preferential, localized, metal loss. That is termed “localized corrosion” [91].

Localized corrosion has various modes, one of which is pitting attack [91]. Pitting results in perforation and potential loss of pressure resistivity; while perforation leads to leakage from metal containers, a loss of pressure resistivity could lead to the explosion of a pressurized container. Therefore, research on the localized corrosion of mild steel in environments encountered in petroleum and natural gas production is industrially important.

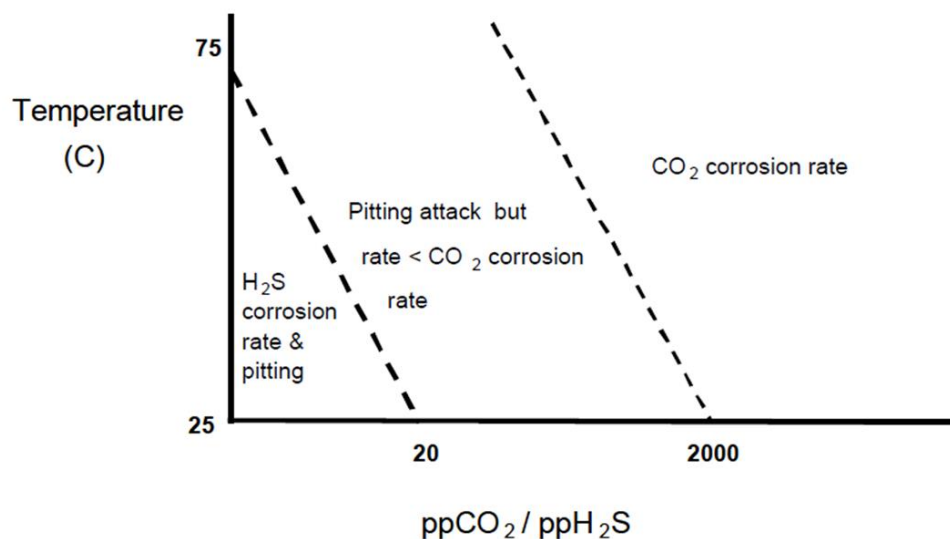
2.3.2 Reports of Localized Corrosion in Marginally Sour Environments

As mentioned earlier, both CO₂ and H₂S are often present in production conditions. The corrosion mechanisms of CO₂ and H₂S dominated environments are significantly different. Determining which mode will control the overall process in a CO₂/H₂S system can be challenging. The ratio of partial pressure CO₂ to partial pressure H₂S is still commonly used to determine the transition, although this approach has clear limitations [63]. Moreover, H₂S corrosion often shows pitting failure, which is extremely difficult to anticipate and complicates the encountered corrosion scenarios. Based on field experience, Kapusta [92] proposed a method to link occurrence of localized corrosion to temperature and pH₂S/pCO₂ ratio as shown in Figure 9. In this plot the partial pressure ratio pH₂S/pCO₂ was chosen as the controlling parameter determining the occurrence of localized corrosion. This ratio has been used to characterize which acid gas, be it CO₂ or H₂S, dominates the corrosion process. For example, the presence of 0.04 mbar of H₂S in a sweet system at 0.97 bar CO₂ leads to a stark reduction in the corrosion rate compared to a pure CO₂ case [93]. In this situation, the presence of H₂S dominates the corrosion process and the system is labeled sour. However, predicting accurately the transition between sour and sweet environments has been an elusive task, and seemingly dependent on a more complex interaction between parameters. Interestingly enough, Figure 9 fails to predict correctly the experimental conditions described above. This serves as an indication that oversimplified considerations and predictions solely based on particular field experience cannot be used as effective tools in this problematic system.

Figure 9

Pitting attack risk prediction based on partial pressure ratio and temperature

(Reprinted with permission from [92]. Copyright 2002 NACE.)



Later, researchers [93, 94, 95] in the Institute for Corrosion and Multiphase Technology (ICMT) reported localized corrosion in CO₂ environments with low concentrations of H₂S. They could identify certain sets of experimental conditions that favored the occurrence of localized corrosion.

Brown [65] found pitting on specimens with a thick layer of corrosion products in large-scale flow loop corrosion tests at 60 °C, pCO₂ of 7.7 bar, and pH₂S of 0.01 bar, at pH 4 and pH 5. Pits were also found at 40 °C, pCO₂ of 2.8 bar, pH₂S of 0.004 bar, and pH 5. FeS was identified as the main component of an outer layer while the inner layer, close to the steel surface, was FeCO₃. This was explained by limitations in the diffusion of HS⁻ through the Fe₃C network associated with the original microstructure of the steel.

The author built a statistical model covering a wide range of experimental conditions, which predicted the likelihood of localized corrosion. However, this model did not provide any mechanistic explanation for the initiation of pitting.

Yan [94] also reported localized corrosion at much lower concentrations of H₂S. The author found a threshold value of pH₂S for resisting pitting attack in H₂S and CO₂ environments in a large-scale flow loop system. This threshold value was shown to be between 30 ppm - 60 ppm (0.25 mbar to 0.5 mbar) under the studied experimental conditions (40 °C, pCO₂ = 8 bar, 1 wt. % NaCl, and pH 4.4 to pH 4.9). Yan hypothesized that a discontinuous and non-uniform FeS layer formed on the steel specimen due to local depletion of sulfide species close to the metal surface, leading to pit initiation.

Yaakob [95] reported that for top-of-the-line corrosion (TLC), a partially formed or damaged FeS layer was present at pH₂S of $1.5 - 3 \times 10^{-5}$ bar (1 bar CO₂). As pH₂S increased ($8 - 15 \times 10^{-5}$ bar), only uniform corrosion was observed. However, localized corrosion at 3×10^{-5} bar H₂S could not be sustained with time. The pits initiated in the first seven days of testing ceased to grow. Metal loss due to uniform corrosion eventually caught up with the pits, which seem to have disappeared after 28 days of experimental duration. Yaakob explained that the pits would not propagate further because a FeS layer was forming inside the pits. Yet, many questions remained unanswered about the actual process.

Navabzadeh-Esmaeely [93] reported similar findings near room temperature for very low pH₂S in glass cell experiments. Partial pressures of H₂S up to 9×10^{-5} bar in

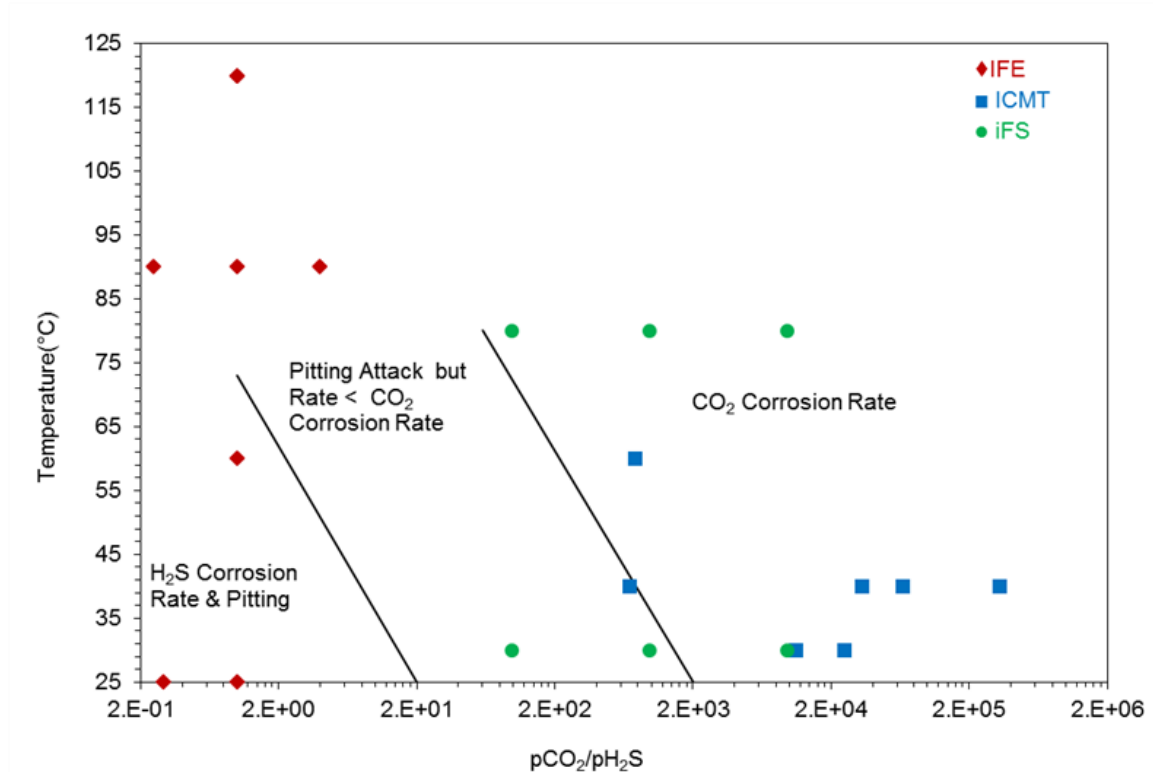
combination with 1 bar CO₂ initiated localized corrosion at 30 °C, while the general corrosion rate decreased.

Kvarekvål [96] also reported localized corrosion when pH₂S was very high, which is thought to be governed by very different mechanisms than those encountered in slightly sour environments. Figure 10 presents a summary of all the experimental conditions described above plotted together with the methodology initially proposed by Kapusta [92]. The graph shows that pitting corrosion can occur even in the range of conditions supposedly “safe”. This highlights the inadequacy of the current approach and the need for mechanistic investigation of localized corrosion in slightly sour environments.

Figure 10

Pitting attack reported at various conditions indicated in a risk prediction plot based on partial pressure ratio and temperature.

(The three data resources are the Institute for Energy (IFE) in Norway, the Institute of Corrosion and Multiphase Technology (ICMT) in USA, and the Institute of Functional Surfaces (iFS) in the UK. Reprinted with permission from [92]. Copyright 2002 NACE.)



2.3.3 Pitting Mechanism: The Three Fundamental Steps of Localized Corrosion

The occurrence of localized corrosion is typically described as a three-step process:

- (1) Protective Layer Formation: Localized corrosion happens due to the presence of an imperfect layer on the metal surface. This layer could be made of organic macromolecules (e.g., coatings), surfactant-type compounds (e.g., inhibitors), or

inorganic components (e.g., oxide-type passive layers, corrosion products, scales).

Only inorganic layers on mild steel surfaces will be addressed in this study.

- (2) Pit Initiation (Generation): When the layer or film displays certain defects, such as holidays in the coating, local desorption of inhibitor, or damage to the passive or corrosion product layers, the bare metal surface becomes exposed to the corrosive environment. The small area of the bare metal surface will be corroded preferentially, thus initiating localized attack.
- (3) Pit Annihilation or Propagation: After the initiation step, the locations on the steel surface that are corroding preferentially grow and propagate as long as no protective layer is generated on top of these “active spots”. Otherwise, if a new layer is regenerated, the “active spots” will not actively corrode anymore and the pits will be “annihilated”.

2.3.3.1 Protective Layer Formation. The characteristics of the protective layer govern whether or not localized corrosion happens and how it happens. Therefore, layer growth kinetics, morphology, and phase identity constitute the first step of this localized corrosion study.

Many materials that could suffer from pitting corrosion are known to spontaneously generate passive layers. According to Uhlig [97], there are two definitions of passivity:

“1. A metal is passive if it substantially resists corrosion in a given environment resulting from marked anodic polarization.... include most of the transition metals and their alloys, e.g. Cr, Ni, Co, W, Mo, Ti, the stainless steels, etc.;

2. A metal is passive if it substantially resists corrosion in a given environment despite a marked thermodynamic tendency to react.... include most examples under definition 1 plus many of the non-transition metals and their alloys, e.g. Zn, Cu, Sn, Pb, Mg, brasses, cupro-nickels, etc.”

Both definitions refer to the important role of a layer or a film. The difference is that this layer can bring a substantial rise to the open circuit potential in definition 1, while the corrosion product layer simply acts as a surface diffusion barrier in definition 2. Today, definition 1 is widely known as the definition of passivation, while definition 2 is not. As will be shown later in the preliminary results, localized corrosion in slightly sour environments exactly fit definition 2, which is pitting attack without passivation. The properties of the layer are the key in understanding this type of localized corrosion.

Layers formed on the surface of mild steel in slightly sour environments can contain several types of corrosion products:

- FeCO_3 : Most crude oils and natural gases contain CO_2 . Consequently, iron carbonate is commonly found as a corrosion product on the steel surface.
- FeS : Many produced petroleum fluids additionally contain H_2S , which can react with iron ions and form an iron sulfide (Fe_xS_y) corrosion product layer.
- Fe_3C : Cementite is a component of the steel microstructure, which does not readily corrode and remains as a residue on the steel surface after the ferrite (α -Fe) phase with which it is associated is dissolved. Corrosion products such as FeCO_3 and FeS will precipitate into the Fe_3C network, thus making it an important constituent part of the protective layers.

- Fe_3O_4 : According to thermodynamic calculations, Fe_3O_4 could be formed in sweet and slightly sour environments. Han reported that Fe_3O_4 was detected at $T = 80^\circ C$, pH ranges from 7.1 ~ 8.1, pCO_2 0.53 bar, NaCl 1 wt.%, in quiescent conditions [98].

The properties of these different corrosion products and how they are formed are briefly introduced in the following paragraphs.

(1) CO_2 Corrosion and $FeCO_3$ Layers. In CO_2 corrosion, precipitation happens when the product of the concentrations of Fe^{2+} and CO_3^{2-} in aqueous solution exceeds the solubility limit of $FeCO_3$. The degree of saturation (S_{FeCO_3}) is calculated by equation (23).

$$S_{FeCO_3} = \frac{[Fe^{2+}][CO_3^{2-}]}{K_{sp FeCO_3}} \quad (23)$$

where $K_{sp FeCO_3}$ represents the solubility of iron carbonate in $(mol/L)^2$, which is calculable for a broad range of conditions using equation (24) [4].

$$\log K_{sp FeCO_3} = -59.3498 - 0.041377T - \frac{2.1963}{T} + 24.5724 \log T + 2.518I^{0.5} - 0.657I \quad (24)$$

where T refers to temperature in Kelvin, I refers to ionic strength in mol/L.

When S_{FeCO_3} is greater than unity, iron carbonate precipitates although the kinetics of precipitation are strongly temperature dependent. Precipitated layers could be discontinuous/loose (unprotective) or continuous/compact/adherent (protective). Whether this layer is protective depends on the scaling tendency (ST) [99], as expressed in equation (25). The layer confers protectiveness when the ST is greater than unity.

$$ST = \frac{PR}{CR} \quad (25)$$

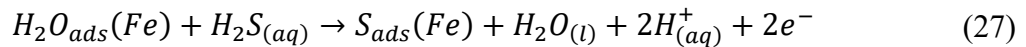
Where PR stands for Precipitation Rate in mol/(m³ · s), which is expressed in equation (26).

$$PR_{FeCO_3(s)} = e^{28.2 - \frac{64851.4}{RT}} \frac{S}{V} K_{sp FeCO_3} (S_{FeCO_3} - 1) \quad (26)$$

Where S/V is the surface to volume ratio of the iron carbonate in 1/m, which can be calculated based on porosity of the layers.

Porosity is an important parameter that affects the diffusivity of all the species from bulk solution to the steel surface. Porosity changes with time, due to both corrosion and precipitation processes [4].

(2) H₂S Corrosion and FeS Layers. According to Marcus, et al. [100], a very thin adsorbed iron sulfide layer rapidly forms on iron or steel in the presence of dissolved H₂S, as was proposed by Smith and Wright [101] and shown in reaction (27).



This very thin adsorbed ferrous sulfide layer constitutes the initial step of layer formation and is often labelled the “inner layer” in H₂S corrosion mechanisms. Another precipitated outer layer is known to form when concentrations of Fe²⁺ and S²⁻ ions in aqueous solution exceed the solubility limit of FeS. Different equilibrium reactions and expressions have been reported for determining saturation with respect to iron sulfide (S_{FeS}), as listed in Table 3.

Table 3

Various iron sulfide formation reactions and saturation expressions for S_{FeS}

(Reprinted with permission from [5]. Copyright 2014 OhioLINK.)

Iron sulfide (mackinawite) precipitation reactions	Expressions of saturation of FeS
$Fe_{(aq)}^{2+} + H_2S_{(aq)} \xrightleftharpoons{K_{sp, FeS(H_2S)}} FeS_{(s)} + 2H_{(aq)}^+ \quad (28)$	$S_{FeS} = \frac{[Fe^{2+}][H_2S]}{K_{sp, FeS(H_2S)}[H^+]^2} \quad (29)$
$Fe_{(aq)}^{2+} + HS_{(aq)}^- \xrightleftharpoons{K_{sp, FeS(HS^-)}} FeS_{(s)} + H_{(aq)}^+ \quad (30)$	$S_{FeS} = \frac{[Fe^{2+}][HS^-]}{K_{sp, FeS(HS^-)}[H^+]} \quad (31)$
$Fe_{(aq)}^{2+} + S_{(aq)}^{2-} \xrightleftharpoons{K_{sp, FeS(S^{2-})}} FeS_{(s)} \quad (19)$	$S_{FeS} = \frac{[Fe^{2+}][S^{2-}]}{K_{sp, FeS(S^{2-})}} \quad (32)$

The most frequently used solubility constant for mackinawite is $K_{sp(H_2S)}$ of reaction (35), as discussed by Benning [39]. This constant can be calculated by equation (33).

$$\log K_{sp, FeS(H_2S)} = \frac{2848.779}{T} - 6.347 \quad (33)$$

Precipitation rate can be calculated by Zheng's expression [5], as shown in equation (34).

$$PR_{FeS_{(s)}} = e^{48 - \frac{40000}{RT}} \frac{S}{V} K_{sp, FeS} (S_{FeS} - 1) \quad (34)$$

Where PR stands for precipitation rate in $\text{mol}/\text{m}^3 \cdot \text{s}$; S/V is the surface to volume ratio in $1/\text{m}$.

Depending on thermodynamic stability and kinetic pathways, different morphologies and polymorphs, as well as related phases, of iron sulfides will be generated under different conditions, as listed in Table 4 [5]. Most often, mackinawite is

expected in short duration experiments (exposure time less than a few days) at room temperature.

Table 4

Iron sulfides typically encountered in H₂S corrosion systems

(Reprinted with permission from [5]. Copyright 2014 OhioLINK.)

Name	Formula	Structure
amorphous	FeS	non-crystalline, nano-sized particles of mackinawite
mackinawite	FeS	tetragonal, 2D layer structure consisting of stacked FeS sheets
cubic FeS	FeS	cubic zinc blende (sphalerite) type lattice
troilite	FeS	hexagonal
pyrrhotite	Fe _{1-x} S	monoclinic, hexagonal or orthorhombic
greigite	Fe ₃ S ₄	cubic
pyrite	FeS ₂	cubic

(3) Fe₃C Network. Steel microstructure has a strong effect on the morphology of a corrosion product layer. For mild steel such as API X65, cementite (Fe₃C) affects its corrosion behavior by increasing the cathodic surface area, as well as by serving as a diffusion barrier. Cementite, also known as iron carbide, is generated during steel processing when austenite is cooled. It is electrically conductive. By weight, Fe₃C is 6.67% carbon and 93.3% iron. It has an orthorhombic crystal structure [102] and is hard

and brittle. The location, structure and amount of Fe_3C depend on carbon content, metallurgical composition, and heat treatment history. After X65 is corroded, residual Fe_3C is generally retained as a three-dimensional network on the steel surface. Therefore, in CO_2 corrosion, researchers [103, 104, 105] attribute the increase of corrosion rate with time to galvanic coupling between the anodic ferrite and the cathodic Fe_3C . Crolet [106] reported that this galvanic coupling could lead to mesa-type attack or localized corrosion. Brown [65] also found that the simultaneous precipitation of FeS and FeCO_3 within the Fe_3C networks can be an important factor related to pitting.

(4) Fe_3O_4 Layers. Fe_3O_4 has been found in CO_2 corrosion products at bulk pH 8 and 80 °C [98]. This Fe_3O_4 layer was reported to act as a pseudo-passive film. Typical pHs found in oil and gas applications are often lower than 7 but it is possible to get higher local surface pH when corrosion products (such as FeCO_3) precipitate on the steel surface [98].

There is no report on the passive behavior of mild steel in sour environments. As mentioned in the section on section 2.2.3, the first approach of localized corrosion in sour environments is to decide which part of the constituent is the key protector to bring down the general corrosion rate on the steel surface. Then, based on the structure and properties of the protective layer, breakdown reasons need to be investigated.

2.3.3.2 Pit Initiation. Pit initiation can be due to many factors, some being specific to the corroding material (microstructure, composition) and some being related to the electrolyte chemistry and flow characteristics. The most commonly accepted pit initiation mechanisms in systems containing $\text{CO}_2/\text{H}_2\text{S}/\text{O}_2$ are listed below.

Usually, localized corrosion is initiated due to factors such as:

- Transpassivation;
- Microstructural inhomogeneities;
- Coating/inhibitor defects;
- Fluid flow and cavitation;
- Stress or strain between the substrate metal and the layer;
- Chemically induced phenomena.

For passive metals, localized corrosion could be induced by either a change of potential or breakdown of the passive layer. Transpassivation is a phenomenon in which a passivated metal undergoes rapid dissolution (increase in corrosion rate) if the metal's electrode potential becomes too positive. The passive layer can be readily attacked by complexing species such as Cl^- . Because X65 is not a passive metal in the conditions of interest, transpassivation will not be included in this discussion. Theories related to layer breakdown could be helpful to understand non-passive metals; this is discussed below. Coating/inhibitor holidays will not be discussed here, as these parameters exceed the scope of this study.

(1) *Microstructural Inhomogeneities.* The chemical composition of the steel itself can also lead to pit initiation. Crolet [106] predicted that galvanic coupling between the Fe_3C and ferrite phases could generate localized corrosion at the interface between grains of ferrite and pearlite, although it is not clear how this process could extend to the macroscopic level considering the homogenous distribution of pearlite in the steel microstructure.

In addition, as mentioned above, it is quite common for FeCO_3 to precipitate within the Fe_3C network left over by the corrosion process rather than on the steel surface itself. In this condition, the presence of conductive Fe_3C residues could also affect the protectiveness of the FeCO_3 layer [107].

As stated in a previous context, co-existence of polymorphs of iron sulfides also falls into this category of layer inhomogeneity. Due to the different conductivity of each phase, galvanic corrosion could occur [108]. For example, pyrite could be formed as part of the corrosion product layer at high temperature and lead to localized corrosion [59, 109].

The occurrence of pitting on austenitic stainless steel is attributed to the presence of MnS inclusions in the microstructure [110, 111]. Although a passive oxide layer exists on the steel surface, pits can initiate at the boundary of the circumferential area of MnS inclusions as they are thought to dissolve preferentially. An extension of this postulate might not be applicable to carbon steel, especially in CO_2 environments, since it is difficult to expect that any pitting due to inclusions can be sustained. However, the presence of inclusions may have a more significant effect in sour environments, when considering the properties of the chemisorbed FeS layer.

Passive films or corrosion product layers contain defects and imperfections, such as Schottky defects (a type of point defect encountered in crystal lattices of ceramics); these cation vacancy-anion vacancy pairs can diffuse through the crystal lattices. If these vacancies move to the layer/solution interface, the layer becomes thinner. If they move to the metal/layer interface, the layer may detach, and pits will potentially develop,

depending on the diffusion rates of anions and cations in the layer. Cation diffusion can be enhanced by anion vacancy occupation by other anions from the solution, e.g., Cl⁻. [112] However, Schottky defects exist all the time, whether or not localized corrosion occurs so it is doubtful they play any central role in the occurrence of pitting. Another challenge facing this mechanism is that it failed to explain the short time required to initiate a pit (less than 1 s or 1 ms) in some cases [113] [114], since the concentration development of multiple vacancies is a rather slow process.

(2) Chemically Induced Phenomena. For CO₂ only conditions, a “grey zone” theory [6] was proposed to explain both initiation and propagation of localized corrosion. Table 5 shows the three main concepts of grey zone theory: high uniform corrosion when no layer is present ($S_{\text{FeCO}_3} < 1$), low uniform corrosion when the layer is protective ($S_{\text{FeCO}_3} \gg 1$), and localized corrosion when only a partially protective layer forms ($S_{\text{FeCO}_3} \approx 1$).

Table 5

Key concepts of “grey zone” theory systems

(Reprinted with permission from [6]. Copyright 2003 OhioLINK.)

$S_{\text{FeCO}_3} < 1$ No layer	$S_{\text{FeCO}_3} \approx 1$ Partially protective layer	$S_{\text{FeCO}_3} \gg 1$ Fully protective layer
High uniform corrosion No localized corrosion	Low/High uniform corrosion Localized corrosion	Low uniform corrosion No localized corrosion

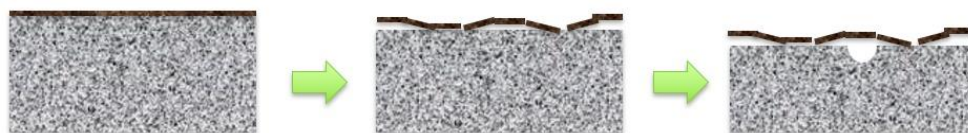
Based on Sun’s “Grey Zone” theory Han [98] and Li [115] proposed a mechanistic model for localized corrosion in CO₂ environments supported by extensive

experimental work. The authors noticed a large increase in potential whenever FeCO_3 would precipitate. They also identified the presence of Fe_3O_4 at the interface between the steel and the FeCO_3 layer in certain conditions. The low uniform corrosion was then attributed to the presence of this pseudo-passive Fe_3O_4 . However, if for any reason (flow effect, change in solution chemistry) the bare steel was to be exposed directly to the electrolyte, strong galvanic coupling could be experienced, leading to localized corrosion. The authors used a purely statistical approach to simulate the seemingly random process of local film/layer failure (*i.e.*, local depassivation).

Another useful concept is scaling tendency (ST), proposed by van Hunnik [99], as shown in equation (25) above. It is the ratio between precipitation and corrosion rate. This links competition between the ever-receding substrate, due to corrosion, and the growth of the precipitated layer; described as “undermining”. This competition is closely related to initiation of localized corrosion because the precipitated layers tend to break down due to receding of the substrate, exposing bare metal “active sites” to localized attacks (**Figure 11**).

Figure 11

Using the concept of scaling tendency to describe pit initiation in CO₂ environments by undermining effect



Apart from the changes brought to precipitation of the corrosion product layers, dissolution of the layer is also another way of chemically induced initiation of localized corrosion. It has been proposed that complexes such as FeSO_4^+ could be formed from the oxide film and SO_4^{2-} adsorbed thereon [116]. This process leads to thinning (dissolution) of the passive film brought by SO_4^{2-} . Chromium oxides are not easily dissolved to form such complexes, therefore Cr containing alloys could be resistant to pitting [117].

Chemical reactions, such as redox reactions, occurring on the protective layer could also lead to initiation of localized corrosion.

(3) Stress or Strain Induced Localized Corrosion. Generally speaking, strain due to thermal expansion is not applicable in aqueous systems below 100 °C. However, intrinsic stress generated by FeS layer growth was postulated by Sun to play a key role in spallation processes [4]. This has also been an area of ongoing research in ICMT, related to black powder formation as well as corrosion. The film-breaking mechanism in passive metal pitting theories uses the concept of internal stresses inside the passive film as the origin of breakdown. The authors hypothesized that a sudden change of potential could lead to water chemistry changes [118] or electrostriction [119, 120] and generate internal

stresses in the film. This mechanism is more suitable to the fast pit nucleation observed experimentally. In this case, the role of “aggressive anions” such as Cl^- is to diffuse inside the crack and prevent re-passivation [73].

(4) Fluid Flow and Cavitation-Induced Localized Corrosion. Shear stress associated with fluid flow might play a role in tearing apart the corrosion product at the pipe wall to initiate localized corrosion. Li [121] utilized a sensor flushed to the internal surface of a thin channel flow cell to directly measure the wall shear stress. These measurements were in good agreement with empirical correlations and computational fluid dynamics (CFD) simulations. However, the wall shear stresses typically encountered in oil and gas operations proved to be several orders of magnitude lower than the stress necessary to “peel off” corrosion product layers, or even inhibitor films.

(5) Pit Initiation Mechanism Related to Localized Corrosion in Sour Environments. The corrosion product layer formed in sour corrosion can be comprised of iron sulfides (FeS), iron carbonate (FeCO_3), iron carbide (Fe_3C), and iron oxides ($\text{Fe}_3\text{O}_4/\text{Fe}_2\text{O}_3$). However, FeS is often the dominant component. Many polymorphs of iron sulfides exist, such as mackinawite, pyrite, pyrrhotite, or greigite, depending on environmental conditions such as temperature and exposure time. Different formation/transformation mechanisms have been proposed [77]. The most common sour corrosion product is mackinawite. It features a bilayer structure [23] with the inner layer being formed by chemisorption, and the outer layer being formed by the precipitation. The thickness of the chemisorbed layer is of the order of several molecular lengths, while the outer layer could be as thick as several microns. The so-called “fast kinetics” [122] or

“solid-state reaction” [123] of inner mackinawite formation is used to characterize the greyish thin layer that rapidly covers the steel surface immediately after exposure to the electrolyte. However, it is unclear whether the inner layer or the outer layer plays the protective role in localized corrosion. Therefore, it is difficult to propose a breakdown mechanism because these mechanisms are proposed based on the structure and properties of the protective layers. Yet, several research studies linked the occurrence of localized corrosion in sour environments to the presence of certain types of iron sulfide such as pyrite [59,108,109] and pyrrhotite [124]. Layer heterogeneity and the resultant galvanic coupling was postulated to explain the initiation of localized corrosion. However, it is unclear whether any of the localized corrosion mechanisms presented earlier can be adapted directly to the initiation of pitting in H₂S environments.

2.3.3.3 Pit Annihilation or Propagation.

(1) Pit propagation Mechanism Related to Localized Corrosion in Aerated Environments. According to passivation theories, the pit nucleation stage is followed by several substages such as the early and later stages of pit growth, stable pit growth, and re-passivation stages. Several mechanisms have been proposed to explain each of these stages by correlating controlling parameters such as potential drops across the pit or various layers, pitting current density, geometry of the pit, local pH, and ion concentration in the pit. The core idea is an explanation of how aggressive ions could prevent re-passivation. In general, the presence of “aggressive” ions inside pits is identified as the main factor preventing re-passivation. Other factors such as the potential across the layer and local water chemistry would also interact and lead to either re-

passivation or stable pit growth. Sand's equation derived by one-dimensional transient salt diffusion was used to depict how the pitting current density changes with time, electrode geometry, and types of anions (their concentration and diffusion coefficient) [125]. The potential hydrolysis of corrosion product could lead to drastic pH drop within the pit. This type of modeling can be used to represent how aggressive anions can prevent re-passivation [125].

(2) Pit Propagation Mechanism Related to Localized Corrosion in Sweet

Environments. Whether or not pits created by local damages on a precipitated FeCO_3 layer can propagate depends on the ability of the environment to re-generate the corrosion product layer. Therefore, it is dependent on the local water chemistry (FeCO_3 saturation degree) inside the pit.

For pits to propagate, the surface of the pit needs to remain bare or at least not as well covered than the surrounding "protected" area. This way, it ensures that the pit penetration rate is always larger than the corrosion rate underneath the layer. If a pit and the layer protected area of the electrode surrounding it can develop a galvanic couple, the corrosion rate inside the pits will be higher than the bare steel corrosion rate. This situation can be difficult to maintain since both the pH and saturation degree inside the pit usually tend to increase as corrosion proceeds, due to the consumption of H^+ and oxidative dissolution of the metal or alloy. However, if there are other reactions inside the pit producing H^+ , or, if a galvanic couple can develop between the bare steel inside the pit and the surrounding area, it can act as the driving force of pit propagation.

Experimentally, Han designed an artificial pit set up to measure the galvanic coupling

current [48, 98] between bare steel and a FeCO_3 covered surface. He could verify that galvanic coupling can be the driving force for CO_2 localized corrosion as long as the local water chemistry inside the pit does not favor re-precipitation of FeCO_3 . Li [115] built a two-point electrochemical model for CO_2 localized corrosion to predict galvanic current and pit propagation/annihilation. In his model, pits were randomly initiated and their fate depended mostly on the extent of galvanic current and on grey zone criteria (i.e. FeCO_3 saturation degree in the bulk and inside the pit).

(3) Pit Propagation Mechanism Related to Localized Corrosion in Sour Environments. As it pertains to localized corrosion of mild steel in marginally sour environments, the galvanic coupling between discontinuous and/or heterogeneous corrosion product layers and the bare steel surface is thought to be the main driver [94] for pit propagation. The differences of conductivities between various corrosion products, most of which are polymorphs of FeS or related phases [126], are also thought to play a major role. Finally, changes in water chemistry due to iron sulfide transformation reactions happening within the pores of precipitated layers were also hypothesized to affect the dynamics of pit propagation/annihilation [127]. However, all these approaches remain tentative, highlighting the inherent complexity and the lack of clear understanding of H_2S corrosion mechanisms related to:

- The extent of how surface water chemistry deviates from the bulk is not completely known.
- The understanding of the kinetics of FeS formation is limited.

- The conditions leading to the transformation of FeS polymorphs and related phases are poorly understood.

Consequently, it is essential to first understand what makes a layer protective in order to establish how pits initiate on mild steel in marginally sour environments. In addition, the identification of sustainable defects or weak points on these otherwise protective layers is also paramount.

Chapter 3: Objectives, Hypotheses and Scope of Work

3.1 Motivation

According to the above literature review, several fundamental gaps in understanding could be identified related to corrosion of mild steel in marginally sour environments:

- (1) Local conditions at the steel surface are difficult to evaluate but are important to determine as they dictate whether or not a layer can form.
- (2) The characteristics of the formed layers (composition, structure, protectiveness), and whether they are the product of precipitation or chemisorption, are poorly understood.
- (3) The processes related to the formation of defects in the layer, eventually leading to pit initiation, have been insufficiently characterized.
- (4) Finally, no criterion for pit propagation/annihilation has ever been proposed for marginally sour environments.

3.2 Objectives

The main objective of this PhD project is to develop a mechanistic understanding for the initiation and propagation of localized corrosion of mild steel in marginally sour environments. To meet this objective, it is necessary to achieve specific goals as follows:

- (1) Ensure repeatability of previous work (i.e. occurrence of pitting corrosion in marginally sour environments);
- (2) Investigate the effects of influential parameters: partial pressure of H₂S and CO₂, temperature, pH, salt concentration, steel microstructure, O₂ concentration;

- (3) Correlate the corrosion product layer structure and properties to pit initiation, investigating the nature of defects or detachments that could lead to protection breakdown;
- (4) Correlate local water chemistry and galvanic coupling effects to pit propagation;
- (5) Propose a qualitative mechanistic pitting mechanism.

3.3 Hypotheses

In a marginally sour environment, localized corrosion is initiated and sustained when a partially protective corrosion product layer is formed.

The following hypotheses are used to guide this study:

- a) The Fe_3C network left by corrosion processes on the steel surface serves as a diffusion barrier for Fe^{2+} . Consequently, surface water chemistry deviates from that of the bulk. FeS precipitates when surface saturation is reached.
- b) Localized corrosion is initiated when a partially protective FeS layer is formed. Defects are due to gaps in surface coverage.
- c) Galvanic coupling exists between pits and their surrounding area covered by FeS layers. The magnitude of galvanic coupling current decides pit penetration rate.
- d) The pits annihilate if a protective corrosion product layer is generated inside the pit.

3.4 Scope of Work

According to the goals and hypotheses stated above, the following experimental tasks were proposed and completed during this PhD project:

Task #1. Repeatability of previous work;

Task #2. Parametric study of the occurrence of localized corrosion in slightly sour environments;

Task #3. Characterization of corrosion product layers;

Task #4. Investigation of the water chemistry near the surface or inside the pits;

Task #5. Development and experimental validation of pitting mechanism and verify it by experiments.

Each task is described in detail in this section.

Task #1: Repeatability Study

The first step was to ensure the reproducibility of previous work (**Table 6**).

Repeatability is especially critical to localized corrosion because pits are thought to be difficult to recreate since their initiation mechanism is poorly understood. The aim of this first test matrix was to repeat Navabzadeh's experimental results [93], in which this particular type of localized corrosion was first reported.

Table 6*Effect of H₂S concentration*

Temperature/°C	30		
pH	5		
Total Pressure/bar	1		
pCO ₂ /bar	0.97		
pH ₂ S/mbar	0	0.04	0.09
WE Material	X65		
NaCl/(wt.%)	1		
Time Duration/days	7		
Agitation/rpm	300		

Task #2: Parametric Study

The test matrix below (**Table 7**) was aimed at developing an experimental database for the initiation of localized corrosion by investigating the effects of the following parameters: pH₂S, pCO₂, pH, temperature, salt concentration and microstructure of the steel. The choice of numerical values selected for each of these parameters is based on what is typically experienced in field applications and on previous laboratory experimental work.

Task #3: Characterization of Corrosion Product Layer

XRD, XPS, FIB-TEM and *in situ* Raman microscopy were applied to identify the phases, structure, and morphology of the corrosion product layers formed on mild steel in marginally sour environments. The objective was to correlate the corrosion product layer structure and properties to the pit initiation, especially defects or detachments that could lead to protection breakdown. The characteristics of the layers formed under different conditions, favoring (or not) pitting, were compared. In addition, the characteristics of the layers formed inside the pit or outside the pit were determined. This approach provides useful information about the mechanism of layer breakdown and pit initiation.

Task #4: Investigation on Water Chemistry near the Surface or Inside the Pits

In this task, the effect of oxygen is discussed in terms of: reduction of O₂ at the steel surface; oxidation of the corrosion product layer (conversion routes from mackinawite to hematite); oxidation of H₂S in aqueous solution at low temperature to evaluate the effect of these side reactions on pit initiation and propagation.

Task #5: Development and Validation of Pitting Mechanism

Based on all the investigations, a mechanistic model of localized corrosion in marginally sour environments was proposed.

Chapter 4: A Parametric Study Based on Formation of Protective Layers

4.1 Introduction

As mentioned earlier, localized corrosion is a common failure mode found in oil and gas pipelines containing CO₂, H₂S, and brine [128]. More specifically, issues with pitting corrosion in marginally sour environments have also been reported by the industry [129]. Researchers in the Institute for Corrosion and Multiphase Technology (ICMT) at Ohio University have previously reproduced localized corrosion in CO₂ environments with low concentrations of H₂S [93, 94, 95, 130,131].

The term “marginally sour” is used to characterized environments with large CO₂ contents and only traces of H₂S [93, 94, 131]. This type of environment is susceptible to localized corrosion because it has been found that the presence of a trace amount of H₂S in a CO₂ dominated environment will lower the general corrosion rate by forming thin iron sulfide layers [122, 132], but at the same time increase the chances of localized attack [131]. Although these studies identified certain experimental conditions that lead to the occurrence of localized corrosion, a comprehensive window of operating conditions was not properly defined, nor was the mechanism of this type of localized corrosion fully clarified.

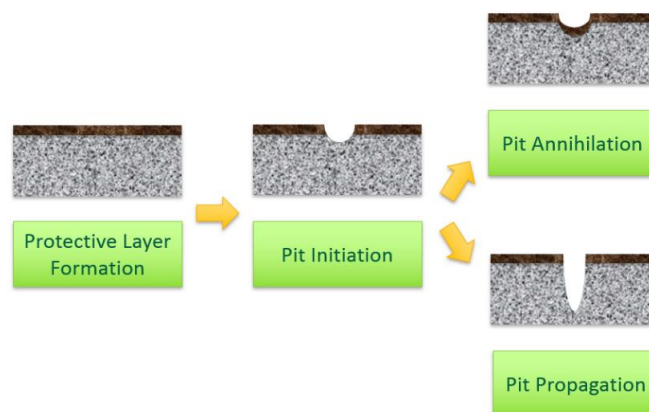
When investigating localized/pitting corrosion of steel, it is tempting to refer to the well-established theory of localized corrosion of stainless steel in an atmospheric environment (iron-oxygen-brine system), involving the disruption of the passive layer and pit acidification [133,134]. Passive layers are complicated structures on a nanometer

scale [73], composed of oxides and hydroxides. However, these mechanisms cannot be applied to localized corrosion of mild steel in marginally sour environments containing both H_2S and CO_2 because the formation, structure and properties of the protective layer are completely different. Therefore, any mechanistic study of this phenomenon should begin with a systematic evaluation of the controlling operating factors and of layer characterization.

As depicted in Figure 12, the localized corrosion mechanism is typically described as a three-step phenomenon: (i) protective layer formation; (ii) pit initiation (nucleation); (iii) pit propagation or annihilation. The characteristics of the protective layers are thought to govern whether or not localized corrosion will occur and to determine what mechanisms are involved. Therefore, layer growth mechanisms, kinetics, morphology, and phase identity constitute a major focus of the present localized corrosion study.

Figure 12

Schematic representation of the three steps of localized corrosion



Layers formed on the surface of mild steel in marginally sour environments might contain iron carbonate (FeCO_3), iron sulfide (Fe_xS_y), iron carbide (Fe_3C) and possibly iron oxides (Fe_xO_y). Knowledge on FeCO_3 and Fe_xS_y corrosion product layer growth mechanisms has been accumulating over several decades of systematic research on CO_2 and H_2S corrosion. The key points are summarized in Table 8. For FeCO_3 , it is understood that the layer is formed by precipitation [135], as shown by reaction (16). The driving force for precipitation is the degree of saturation of FeCO_3 in aqueous solution [6]. FeCO_3 precipitates when saturation degree is greater than unity, as shown by reaction (19). The layer growth rate is related to the activation energy and the aforementioned degree of saturation, as shown by reaction (25). This corrosion product layer can be “undermined” by corrosion of the underlying steel, if the ratio of precipitation to corrosion rates is near or less than unity, in line with equation (21). This “undermining effect” was proposed as an initiation mechanism for localized corrosion in sweet (CO_2 only) environments [6].

Corrosion products in sour environments contain at least one polymorph of iron sulfide, such as mackinawite (FeS), pyrite (FeS_2), pyrrhotite ($\text{Fe}_{(1-x)}\text{S}$, $x = 0 \sim 0.2$), or greigite (Fe_3S_4), depending on environmental conditions such as temperature and pH_2S , as well as exposure time, although there are different mechanisms proposed for their formation / transformation [19]. It is thought that mackinawite is always the initial FeS corrosion product [55] and that it is then converted into other forms of iron sulfide. Sun [136] proposed a mechanism of iron sulfide layer formation at the steel surface by direct reaction between H_2S and the iron in the steel, forming a thin layer that spalls and

reforms, to produce a thicker outer layer of iron sulfide. Zheng et al. further developed the “two layers” theory of iron sulfide formation and proposed that the inner layer forms by chemisorption [137], as previously postulated by others [24,138] (reaction (27)), while the outer layer forms by precipitation [137] (reaction (19)). The chemisorbed layer is also considered to be very thin; of the order of nanometers. The outer precipitated layer of FeS can be found on top of the chemisorbed layer, its formation being driven by the saturation degree of Fe^{2+} and S^{2-} in the aqueous solution near the steel surface (Equation (31)) [137]. The precipitated layer thickness is usually measured on a micron scale, and its growth rate can be defined via precipitation kinetics [137, 139] (Equation (34)). The exact role of different iron sulfides in corrosion protection and localized corrosion initiation/propagation is poorly understood. One type of localized corrosion in sour environments was found to be related to pyrite [59, 108, 109] and pyrrhotite [124], which usually appears in H_2S dominant environments. In actuality, most of the research found in the open literature was done in H_2S dominant environments, often without CO_2 . In addition, research on structure and morphology of the corrosion product layers related to localized corrosion in marginally sour environments is scarce.

Table 8*FeCO₃ layer and FeS layer growth mechanisms**

	In CO ₂ Corrosion (by precipitation)	In H ₂ S Corrosion (by precipitation)	In H ₂ S Corrosion (by chemisorption)
Layer Formation	$Fe_{(aq)}^{2+} + CO_{3(aq)}^{2-} \rightarrow FeCO_{3(s)} \downarrow$ (16)	$Fe_{(aq)}^{2+} + HS_{(aq)}^{-} \leftrightarrow FeS_{m(s)} \downarrow + H_{(aq)}^{+}$ (19)	$H_2O_{ads}(Fe) + H_2S_{(aq)} \rightarrow S_{ads}(Fe) + H_2O_{(l)} + 2H_{(aq)}^{+} + 2e^{-}$ (27)
When does the layer form?	$S_{FeCO_3} = \frac{[Fe^{2+}][CO_3^{2-}]}{k_{sp,FeCO_3}} > 1$ (23)	$S_{FeS} = \frac{[Fe^{2+}][HS^{-}]}{k_{sp,FeS}[H^{+}]} > 1$ (31)	When H ₂ S chemisorbs on the steel surface
How fast does the layer form?	$PR_{FeCO_3(s)} = e^{28.2 - \frac{64851.4}{RT}} \frac{S}{V} k_{sp,FeCO_3} (S_{FeCO_3} - 1)$ (26)	$PR_{FeS(s)} = e^{48 - \frac{40000}{RT}} \frac{S}{V} k_{sp,FeS} (S_{FeS} - 1)$ (34)	Almost instantaneous when H ₂ S present
Is this layer protective?	Can act as a diffusion barrier depending on scaling tendency $Scaling \ Tendency = \frac{Precipitation \ Rate}{Corrosion \ Rate}$ (25)	Can act as a diffusion barrier depending on scaling tendency	Yes - decreases the rate of electrochemical reactions

* Where S_{FeCO_3} stands for saturation degree of $FeCO_3$; S_{FeS} stands for saturation degree of FeS (mackinawite); $k_{sp,FeCO_3}$ stands for equilibrium constant of $FeCO_3$; $k_{sp,FeS}$ stands equilibrium constant of FeS (mackinawite); $PR_{FeCO_3(S)}$ stands for the precipitation rate of $FeCO_3$; $PR_{FeS(S)}$ stands for the precipitation rate of FeS (mackinawite); $\frac{S}{V}$ stands for surface volume ratio.

Another constituent of the corrosion product layer is often iron carbide (also called cementite), Fe_3C , which is a component of the steel microstructure. Since it does not readily corrode, it remains as a residue on the steel surface after the ferrite (α -Fe) phase is dissolved, the same being true in marginally sour environments. Corrosion products such as $FeCO_3$ and iron sulfide can precipitate within the exposed Fe_3C network, thus making it an important constituent of the protective surface layers in sour corrosion.

Iron oxides might be found together with $FeCO_3$ and/or Fe_xS_y due to higher surface pH [140], reactions with oxygen [74], or from water at elevated temperature [59, 109].

In CO_2 corrosion, the protective layer is $FeCO_3$, often present within the Fe_3C network. The loss of integrity of this layer has been linked to the occurrence of localized corrosion. Since the $FeCO_3$ layer is formed by precipitation, it is driven by the saturation degree of $FeCO_3$ in the solution. Therefore, the possibility of pitting can be predicted by the saturation degree of $FeCO_3$ (the grey zone theory [6], **Table 5**), as well as the rate of layer growth compared with the corrosion rate (scaling tendency [49], **Figure 11**). Iron

oxides have been found underneath the FeCO_3 layer and were linked to an increase of potential and development of localized corrosion [98].

Based on these findings in CO_2 corrosion, a similar hypothesis can be proposed for localized corrosion of mild steel in marginally sour environments. Since adding H_2S into a CO_2 environment leads to lower uniform corrosion rates, the formation of a FeS layer could be speculated to be more protective than the formation of an FeCO_3 layer. Therefore, saturation degree and scaling tendency of FeS can be used to predict if a protective layer of FeS is precipitated on a steel surface. Therefore, the central hypothesis of this research is as follows, “in a marginally sour environment, localized corrosion is initiated and sustained when a partially protective corrosion product layer is formed”.

In this chapter, a comprehensive parametric study was performed using a small-scale laboratory setup with the aim of changing the saturation degree of FeS and FeCO_3 by changing these conditions and filtering out the most influential factors of pitting in marginally sour environments. The parameters of interest were partial pressure of H_2S , bulk pH, temperature, the partial pressure of CO_2 , salt concentration, metal substrate microstructure and carbon content, and oxygen ingress. This series of experiments defined a window of operating conditions leading to the occurrence of pitting, and enabled the characterization of the corrosion product layer structure, and the identification of the mechanisms related to the initiation of pitting in marginally sour environments.

4.2 Experimental Setup and Procedure

4.2.1 Experimental Materials

API 5L X-65 mild steel [141] was chosen as the baseline steel type for this research due to its wide application for oil and gas pipelines. The composition of the steel is shown in Table 9 [142]. Its microstructure consists of large ferrite grains with small precipitates of cementite. Pearlite colonies are difficult to identify due to the low carbon content, as shown in Figure 13 [143]. The cylindrical working electrode was machined from the parent steel material and had a diameter of 1.20 cm and an exposed surface area of 5.4 cm². The steel specimens were obtained from a large piece of pipe provided by a major oil and gas company. The composition and microstructure are believed to be representative of materials used in production and transportation of hydrocarbon products.

Table 9

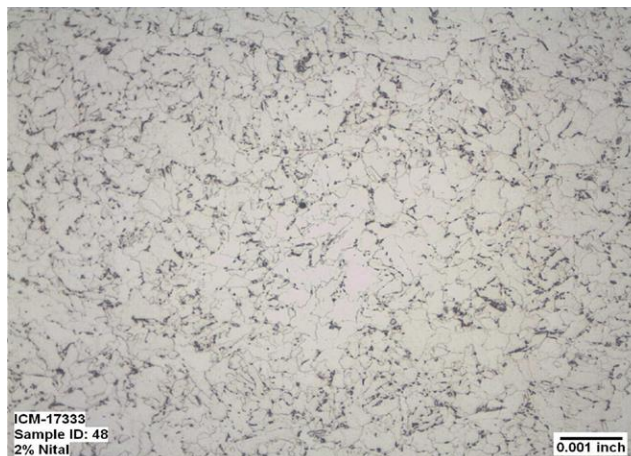
Chemical composition (wt. %) of API 5L X65 [142]

Fe%	Mn%	Ni%	Cr%	Cu%	Si%	Mo%	C%
97.3237	1.5052	0.2909	0.2519	0.1731	0.1668	0.0921	0.0454
V%	Nb%	Al%	Ti%	As%	N%	S%	Others%
0.0420	0.0338	0.0282	0.0120	0.0075	0.0067	<0.001	0.0136

Figure 13

Microstructure of X65 (0.05 wt. % C) consisting of large ferrite grains with cementite precipitates

(Reprinted with permission from [143]. Copyright 2014 OhioLINK.)

**4.2.2 Experimental Equipment**

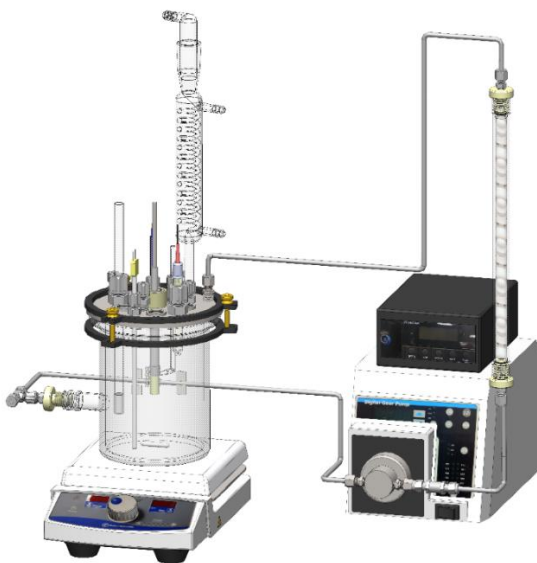
Experiments were conducted at atmospheric pressure in a 2-liter glass cell (Figure 14 [144]) with a 1 wt. % NaCl in deionized water solution. Gas (a mixture of hydrogen sulfide, H₂S and carbon dioxide, CO₂) was sparged through the cell continuously at a flow rate of around 100 ml/min. A three-electrode electrochemical setup was used and consisted of: a static cylindrical electrode as the working electrode (WE), a platinum wire as a counter electrode (CE) and a saturated silver-silver chloride (Ag|AgCl) reference electrode (RE) connected to the cell externally via a salt bridge with a Luggin capillary. A 2" magnetic stir bar at the bottom of the glass cell was used for mixing the solution. The concentration of H₂S was adjusted with the help of a gas rotameter and measured when exiting the cell by a gas sampling pump with H₂S colorimetric detector tubes. A

carbon scrubber was used to treat the gas coming out of the glass cell to remove the H_2S . Automatic adjustment of pH over time was achieved by using the measured pH value to control a pump moving a part of the solution through an ion exchange resin column.

Figure 14

Experimental setup for the two-liter glass cell using a stable solution chemistry system for small-scale experiments

(Image courtesy of Cody Shafer, ICMT).



4.2.3 Experimental Matrix

The test matrix (**Table 7**) was designed to develop an experimental database to screen the most influential factors of pitting in marginally sour environments. The following parameters were investigated: pH_2S , pCO_2 , pH, temperature, salt concentration, material microstructure and carbon content, and O_2 ingress. The core idea of these

designed experiments involving various factors is to use the changes of saturation degree to predict the structure and properties of corrosion product layers, then correlate the layer protectiveness with the initiation of pitting.

4.2.4 Experimental Procedure

The aqueous solution was initially sparged with CO₂ gas for at least three hours to purge dissolved oxygen. After the solution was deoxygenated, H₂S was added by sparging for about half an hour to saturate the solution. H₂S gas concentration was adjusted by sparging different ratios of CO₂ and H₂S, from 20 ppm_(v) to 150 ppm_(v) H₂S in CO₂, corresponding to a H₂S partial pressure $p_{H_2S} = 0.1$ mbar and 96.5 mbar respectively, at 30°C. The pH value was adjusted by adding a deoxygenated hydrochloric acid or sodium carbonate aqueous solution. Prior to immersion, the mild steel specimen surfaces were polished with 80, 400 and 600 grit sandpaper, rinsed with isopropyl alcohol, and dried with an air blower.

Polarization resistance (R_p) measurements were conducted by polarizing the working electrode from -5 mV to +5 mV vs. the open circuit potential. The scan rate was 0.125 mV/s. Solution resistance was measured independently using electrochemical impedance spectroscopy (EIS). The measured R_p was corrected by subtracting the measured solution resistance then. The linear polarization resistance (LPR) constant $B = 23$ mV/decade was determined by previous longer-term weight loss measurements in literature [5]. EIS measurements were carried out by applying an oscillating potential ± 5 mV around the open circuit potential of the working electrode, using the frequency range 5 kHz to 0.01 Hz.

Ferrous ion concentration in the water samples taken from the solution was measured by a spectrophotometer (Hach[®] DR900 Multiparameter Portable Colorimeter) using a 1,10 phenanthroline method and a multipoint standard adsorption curve at 510 nm. Deionized water was used as the control for the spectrophotometer. Multiple repeats of ferrous ion concentration measurements were done for each sample in order to establish the accuracy and repeatability of results.

Scanning electron microscopy (SEM, JEOL JSM-6390) and energy dispersive X-ray spectroscopy (EDS) were used to analyze the corrosion product layer structure and elemental composition.

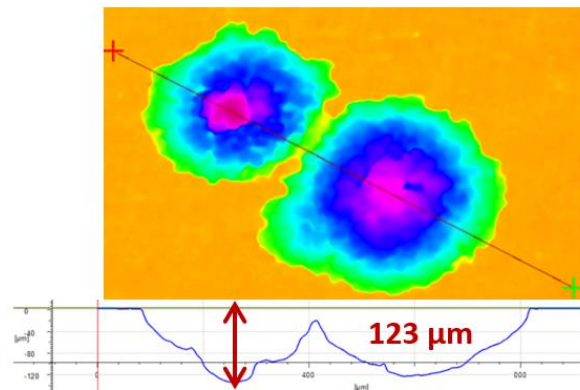
Specimens from selected conditions were analyzed by transmission electron microscopy (TEM). Sections were cut from the scale with a FEI Nova Nanolab 200 FEG-SEM/FIB for Focused Ion Beam (FIB) processing and imaged with a FEI Tecnai F30 ST TEM. Both SEM and TEM were combined with EDS to analyze the chemical composition of the surface layers. The identity of crystalline components of the layers was revealed by selected area electron diffraction (SAED). The selected points in the corrosion product layer were further probed by precession electron diffraction (PED) to further determine the crystal structures of specimen surface.

Pit penetration rate and pitting density were measured by a high-resolution optical profilometer, by scanning the steel surface after the corrosion product layer was removed by Clarke solution treatment [145]. Surface profilometry scanning on corroded specimen surface was performed on the Alicona InfiniteFocus profilometer microscope. Figure 15 shows an example of optical profilometry measurements that were used to identify the

maximum pit depth. The measured three-dimensional nature of the pit is illustrated here by using a color scale, where the maximum depth is shown in the line profile below.

Figure 15

Optical profilometry measurement



4.2.5 Evaluation of Pitting Ratio

Based on the ASTM standard on examination and evaluation on pitting corrosion [145], a rule has been developed to help decide whether localized corrosion occurred or not in the present experiments [146]. As demonstrated in Figure 16 after exposure to the corrosive environment, steel specimens suffered from both general metal loss and localized attack. General corrosion rate could be calculated from total mass loss (here weight-loss corrosion rate was used, denoted as CR_{WL} hereafter, equation (35), assuming that the contribution of pitting is negligible. The rate of localized attack could be evaluated by profilometry using the maximum pit depth (Equation (36)). The ratio of pit penetration rate (denoted as PPR hereafter) divided by general corrosion rate (here CR_{WL})

is defined as pitting ratio (denoted as PR hereafter) and is used as the criteria for determining the occurrence of localized corrosion [equation (37)].

The rule is as follows:

- A. when this ratio is smaller than 3, the corrosion is judged to be uniform;
- B. when this ratio is larger than 5, it is judged that localized corrosion occurred;
- C. when this ratio is between 3 - 5, the situation is unclear, it is possible that localized corrosion initiated but could not be sustained.

This criterion was only applied to pits that are deeper than 10 μm in order to distinguish them from general surface roughening.

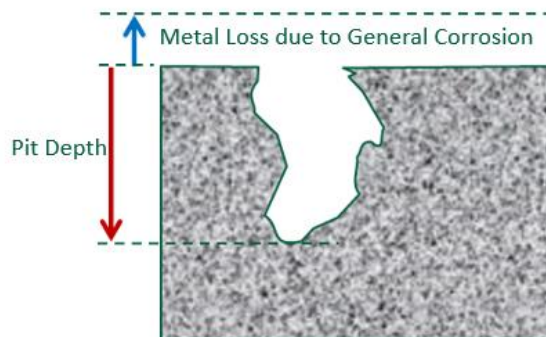
$$\text{Weight Loss Corrosion Rate} \left(\frac{\text{mm}}{\text{y}} \right) = \frac{\text{Measured Weight Loss}}{\text{Time}} \quad (35)$$

$$\text{Penetration Rate} \left(\frac{\text{mm}}{\text{y}} \right) = \frac{\text{Measured Pit Depth}}{\text{Time}} \quad (36)$$

$$\text{Pitting Ratio} = \frac{\text{Penetration Rate}/(\text{mm}/\text{y})}{\text{Weight Loss Corrosion Rate}/(\text{mm}/\text{y})} \quad (37)$$

Figure 16

Pit depth and general corrosion



4.2.6 Experimental Safety

For this work, it is required to carry out all experiments following the ICMT protocol for working with H₂S gas. All staff and students are trained before using the specially equipped H₂S room at the ICMT. People working in the room are equipped with a self-contained breathing apparatus (SCBA). There is always a buddy outside the room watching activities and he/she is equally equipped. The H₂S in the outlet gas is scrubbed through a series of scrubbers that prevents its release to the atmosphere.

4.3 Results and Discussion

The core idea of the designed experiments is to use changes of saturation degree to predict the morphologies and properties of corrosion product layers, then correlate the layer protectiveness with the initiation of pitting.

The electrochemical measurements have shown that the corrosion rates in all the experiments presented below were stable over the course of the 7-day experiments.

Furthermore, the time-averaged LPR measurements agreed well with the weight loss measurements; only the latter was used to report general corrosion rates in the text below.

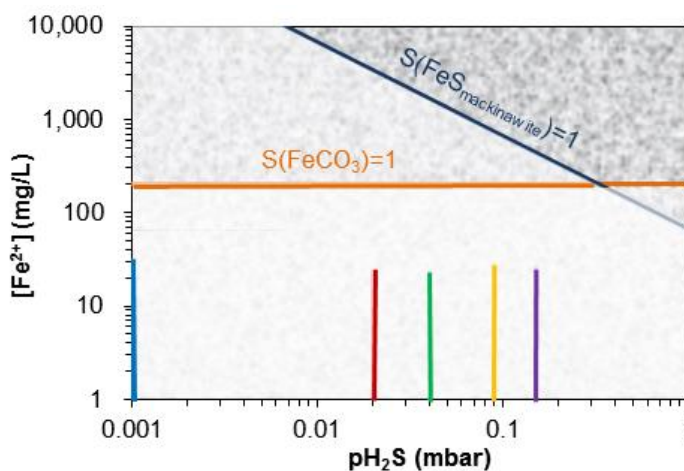
4.3.1 Effect of H₂S Partial Pressure on Pitting

Experimental results obtained with 0, 20, 40, 90, & 150 ppm of H₂S in 1 bar CO₂ and at 30 °C were compared to identify the lower and upper limits of H₂S for localized corrosion occurrence. Figure 17 shows the bulk saturation degree calculated for both FeS (mackinawite in this work), S(FeS), and FeCO₃, S(FeCO₃) under these conditions. The navy line is the saturation line for FeS and shows the conditions required, in terms of [Fe²⁺], to reach saturation S(FeS) = 1 at a given H₂S partial pressure. The orange line is the calculated saturation limit for FeCO₃ -- S(FeCO₃). The corresponding corrosion product layer (FeS and/or FeCO₃) is expected to form by precipitation at any point in this chart above the saturation lines. During each experiment at a specific H₂S partial pressure, the measured bulk ferrous ion concentration started at zero at the beginning of the experiment, and then increased and reached a stable value, usually after 4 days of exposure, as indicated by the colored vertical lines in Figure 17. In all five experiments, the bulk ferrous ion concentration did not reach the saturation value for either S(FeS) or S(FeCO₃). Therefore, no precipitated layer would be expected in any of these experiments based on bulk water chemistry conditions.

Figure 17

Saturation degree of the bulk solution of both $\text{FeS}_{\text{mackinawite}}$ (navy line and above) and FeCO_3 (orange line and above) for different pH_2S values.

(X65 carbon steel, 30 °C, pH 5, $\text{pCO}_2 = 0.97$ bar, $\text{pH}_2\text{S} = 0/0.02/0.04/0.09/0.15$ mbar, 1 wt.% NaCl, 300 rpm stir bar, 7 days exposure, $[\text{O}_2]_{\text{aq}} \approx 20$ ppb_(w).)



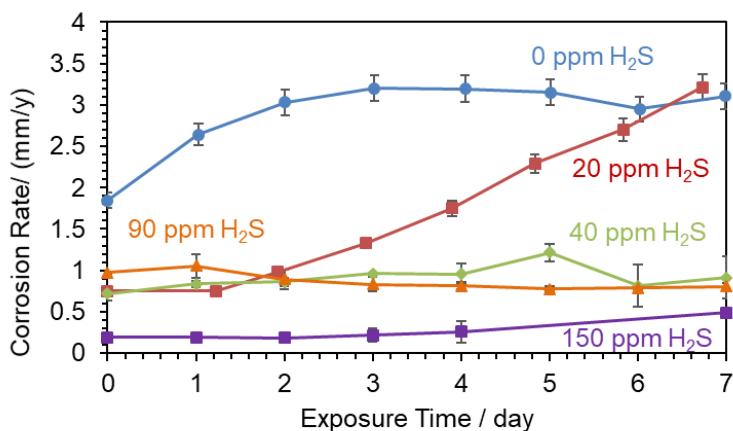
General corrosion rates are represented by the measured LPR and weight loss for different pH_2S values as depicted in Figure 18. Higher partial pressures of H_2S typically lead to lower steady state general corrosion rates. The reason for the decrease in corrosion rate has been attributed in the literature to the formation of a thin FeS layer on the steel surface, although the bulk conditions were unfavorable for the precipitation of corrosion products. This trend indicates that the FeS layer (not FeCO_3 , Fe_3C or Fe_2O_3 if they also existed in the layer) offers protection against corrosion in marginally sour environments. This observation fulfills one aspect of the “grey zone” theory, which

requires the formation of a protective layer. For the hypothesis to be verified, the occurrence of pitting should be linked to breakdown of this FeS layer.

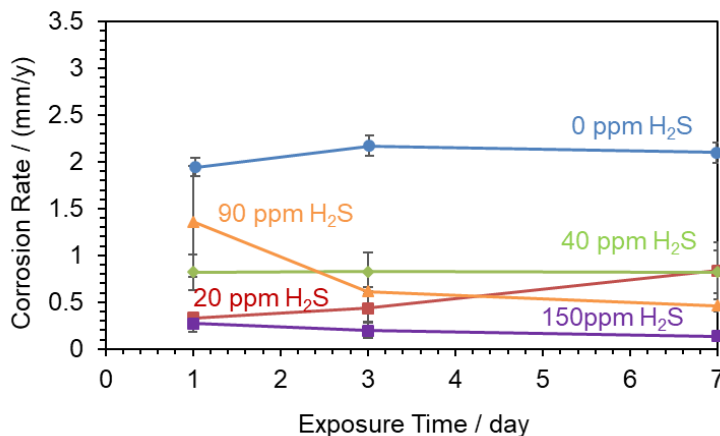
Figure 18

LPR (a) and weight loss (b) corrosion rates for different pH_2S values.

(X65 carbon steel, 30 °C, pH 5, $pCO_2 = 0.97$ bar, $pH_2S = 0/0.02/0.04/0.09/0.15$ mbar, 1 wt.% NaCl, 300 rpm stir bar, 7 days exposure, $[O_2]_{aq} \approx 20$ ppb_(w).)



(a) LPR corrosion rate



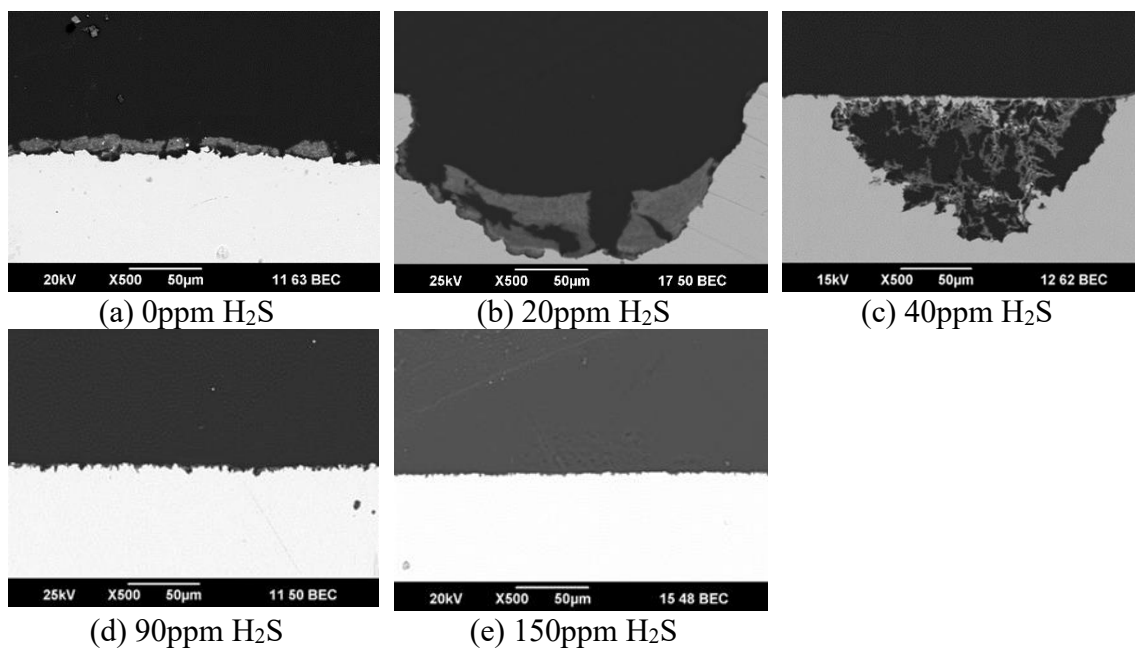
(b) Weight loss corrosion rate

In the absence of H_2S , SEM images in Figure 19 reveal that a relatively thick layer was formed while no visible layer was found for the other cases with H_2S (this observation is limited by the resolution of the SEM). More importantly, it indicates that extensive pitting occurred with 20 and 40 ppm H_2S but not in the other conditions. This is consistent with the findings of Navabzadeh [93]. The cross-section images also show the morphology of those pits, which seem to be mainly hemispherical and filled with FeS embedded in a Fe_3C network. A thin layer (most likely FeS) was left behind at the top of the pit. However, the resolution of these SEM images is insufficient to determine whether the thin layer exists on the remaining steel surface around the pits. It is thought that a very thin iron sulfide corrosion product layer (not visible in the SEM images) existed because sulfur was detected by EDS there, which is also true for similar experiments conducted previously [93]. XRD failed to show a pattern or peaks to support this speculation because the layer was too thin to be properly resolved [93].

Figure 19

SEM cross-section images of specimens at different H₂S partial pressure after 7 days exposure

(X65 carbon steel, 30 °C, pH 5, pCO₂=0.97 bar, pH₂S = 0/0.02/0.04/ 0.09/0.15 mbar, 1wt. % NaCl, 300 rpm stir bar, 7 days exposure, [O₂]_{aq} ≈ 20 ppb_(w))



Surface profilometry images of the corroded specimens, after corrosion product layer removal by Clarke solution, are displayed in Figure 20. High pitting density was observed at 20 ppm and 40 ppm H₂S. Lower pitting density was observed at 90 ppm H₂S. No pitting was found at 0 and 150 ppm H₂S. It seems therefore that there is a threshold of H₂S content for this type of pitting, indicating that the corrosion product layer became more stable as iron sulfide content increased, and was fully formed at 150 ppm H₂S since no pitting was observed. If this layer formed by precipitation, it can be speculated that the surface saturation degree of FeS must have been greater than unity, even though the bulk

value was not. It is also possible that the layer also underwent a continuous and partial process of dissolution, given that the bulk was under saturated with respect to FeS.

Figure 20 shows the pitting analysis and compares it to the general corrosion rates determined by weight loss. The error margins for the general corrosion rate listed in the captions of **Figure 20** were calculated as follows: each experiment was repeated, so the reported (general) corrosion rate is the average values for the two specimens. The error margins denote the minimum and maximum measured values. The pit penetration rate reported there was based on the deepest pit found on the two specimens from repeated experiments. The margin of error reported for the pit penetration rate is calculated based on the vertical resolution of the optical measurements.

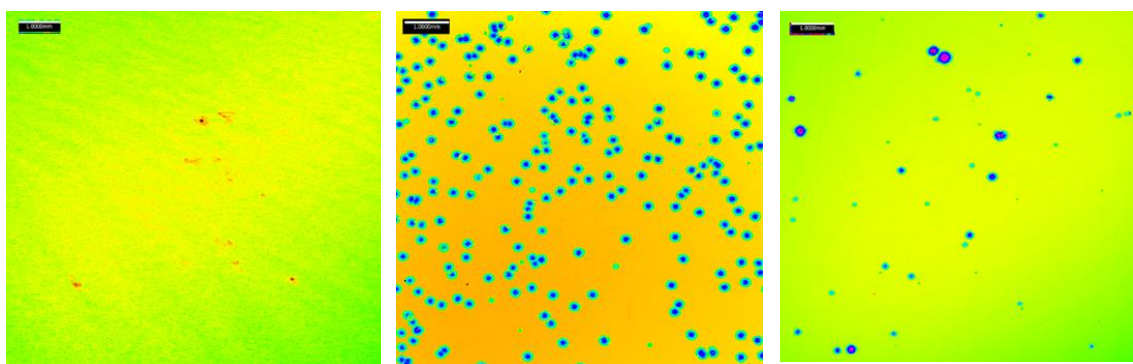
The CO₂ only (0 ppm H₂S) experiment yielded the highest general corrosion rate, *ca.* 2 - 2.5 mm/y. Adding 20 ppm of H₂S led to a considerable reduction in the general corrosion rate to less than 1.0 mm/y, although severe pitting would be expected to affect the calculations. In general, the higher the H₂S content in the gas phase was, the lower the general corrosion rates became.

According to the criterion for pitting defined by Brown [146], the specimens exposed to 20, 40 and 90 ppm_(v) H₂S clearly experienced pitting. The pitting density for the 90 ppm_(v) H₂S was much lower than what was observed for 20 and 40 ppm_(v), however, according to the ASTM standard [145], this pitting density was actually very high when compared to the threshold listed in the standard. Generally, the pitting density seemed directly related to H₂S concentration.

Figure 20

Surface profilometry analysis of specimens recovered for each experimental condition after 7 days exposure after corrosion product layer removed

(X65 carbon steel, 30 °C, pH5, pCO₂ = 0.97 bar, pH₂S = 0/0.02/0.04/0.09/0.15 mbar, 1 wt.% NaCl, 300 rpm stir bar, [O₂]_{aq} ≈ 20 ppb_(w))

(a) 0 ppm H₂S

$$\text{CR}_{\text{WL}} = 2.10 \pm 0.10 \text{ mm/y}$$

$$\text{Pit density} = 0 \text{ cm}^{-2}$$

The red spots are higher,
not lower than surface.

(b) 20 ppm H₂S

$$\text{CR}_{\text{WL}} = 0.84 \pm 0.31 \text{ mm/y}$$

$$\text{PPR} = 5.37 \pm 0.11 \text{ mm/y}$$

$$\text{PR} \approx 6$$

$$\text{Pit density} = 127 \text{ cm}^{-2}$$

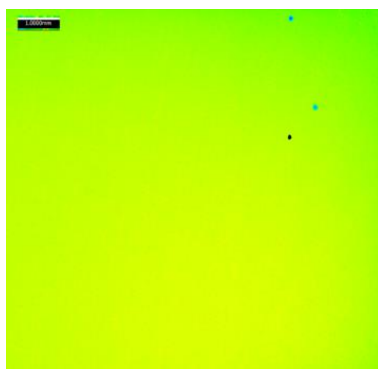
(c) 40 ppm H₂S

$$\text{CR}_{\text{WL}} = 0.82 \pm 0.22 \text{ mm/y}$$

$$\text{PPR} = 7.30 \pm 0.10 \text{ mm/y}$$

$$\text{PR} \approx 9$$

$$\text{Pit density} = 25.4 \text{ cm}^{-2}$$

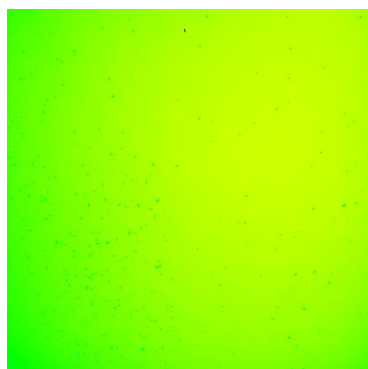
(d) 90 ppm H₂S

$$\text{CR}_{\text{WL}} = 0.46 \pm 0.07 \text{ mm/y}$$

$$\text{PPR} = 3.16 \pm 0.34 \text{ mm/y}$$

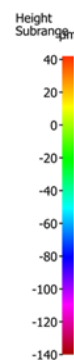
$$\text{PR} \approx 7$$

$$\text{Pit density} = 1.24 \text{ cm}^{-2}$$

(e) 150 ppm H₂S

$$\text{CR}_{\text{WL}} = 0.14 \pm 0.05 \text{ mm/y}$$

$$\text{Pit density} = 0 \text{ cm}^{-2}$$

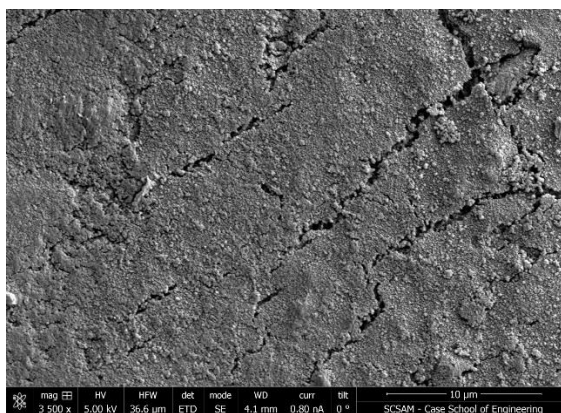


The 40 ppm H₂S specimen, where the most severe pitting happened in this series, was chosen for FIB-TEM analysis to reveal the detailed structure of the corrosion product layer formed. As shown in Figure 21, a very thin and porous layer of about 100 - 200 nm thickness was found on the steel surface. This layer was much thinner compared with the precipitated FeCO₃ layer typically observed in sweet corrosion (micron level), but still very thick compared with the passive layer on stainless steel (up to 5 nm). Most parts of the layers were detached from the substrate. Consequently, layer detachment alone cannot be used as an explanation for pit initiation.

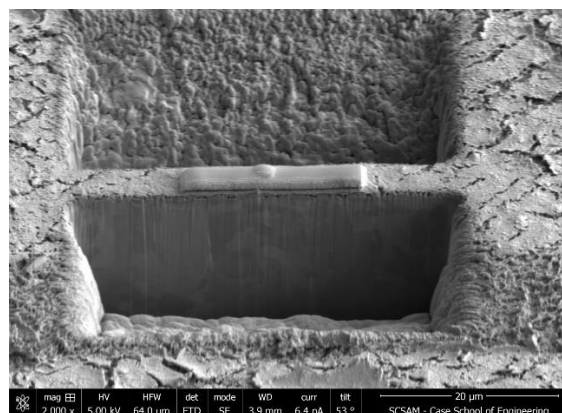
Figure 21

TEM images of the cross section of the specimen for the baseline experiment cut out by FIB

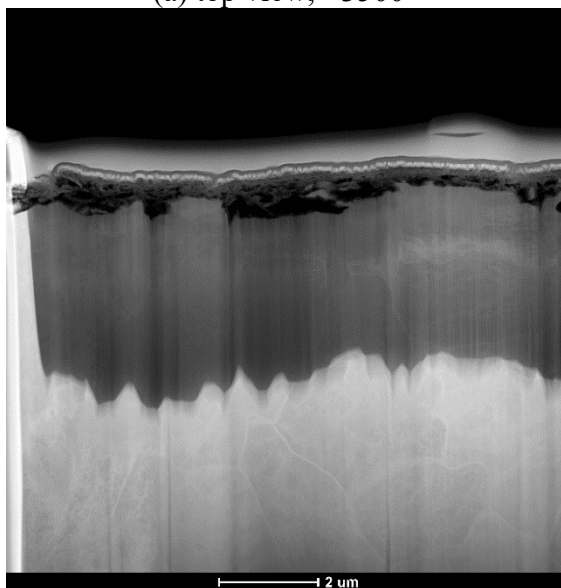
(30 °C, $p\text{CO}_2 = 0.97 \text{ bar}$, $p\text{H}_2\text{S} = 0.04 \text{ mbar}$, $\text{pH } 5$, X65, 1 wt.% NaCl, 300 rpm, 7 days, $[\text{O}_2]_{\text{aq}} \approx 20 \text{ ppb}_{(\text{w})}$)



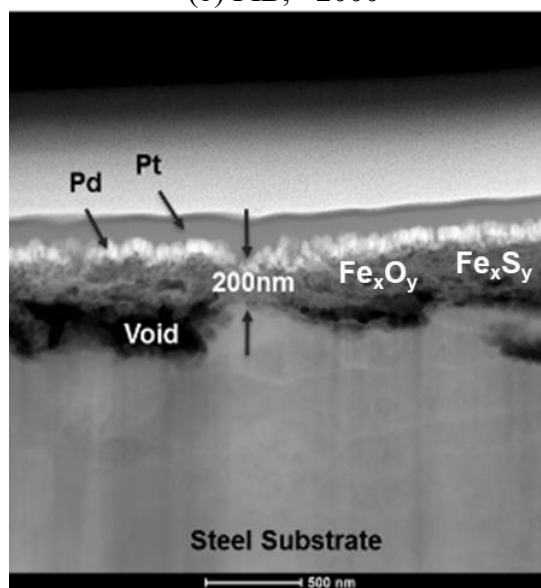
(a) top view, ×3500



(b) FIB, ×2000



(c) TEM, ×8500



(d) TEM, ×34000

TEM-EDS mapping results of the corrosion product layer on the 40 ppm H₂S specimen is shown in Figure 22. In this 100 - 200 nm porous layer, iron, nickel, sulfur, and oxygen were concentrated, indicating the formation of sulfides and oxides.

Figure 22

TEM-EDS mapping results of the specimen of baseline condition experiment

(30 °C, p_{H₂S} = 0.04 mbar, p_{CO₂} = 0.97 bar, X65 carbon steel, pH 5, 1wt.% NaCl,

300rpm, 7 days, [O₂]_{aq} ≈ 20 ppb_(w))

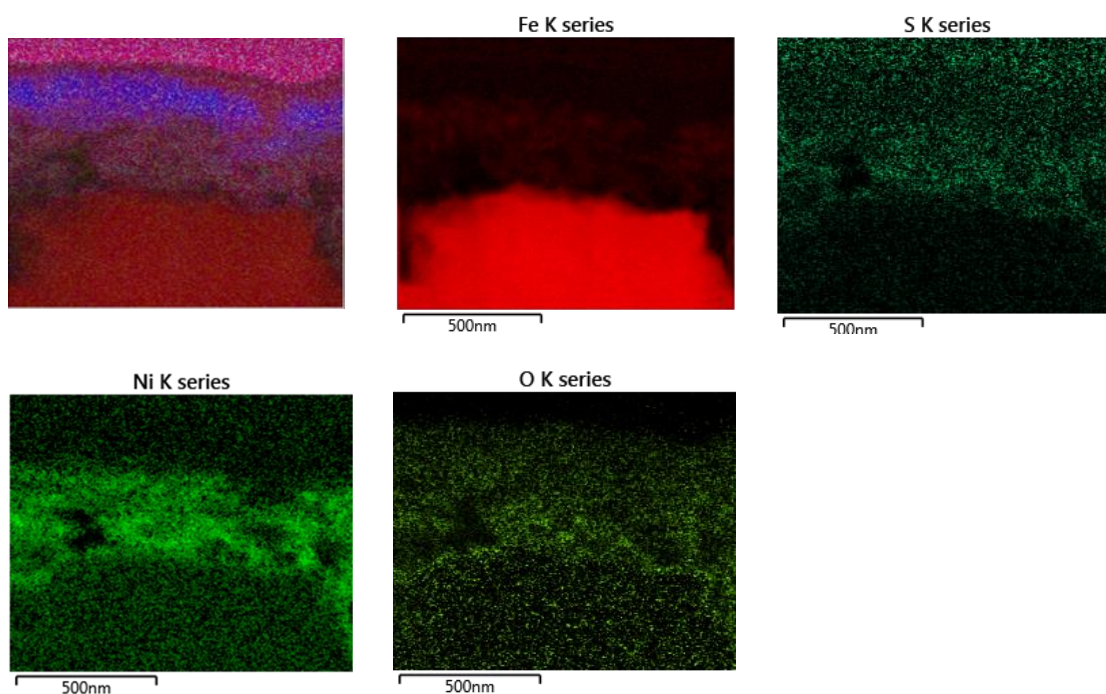


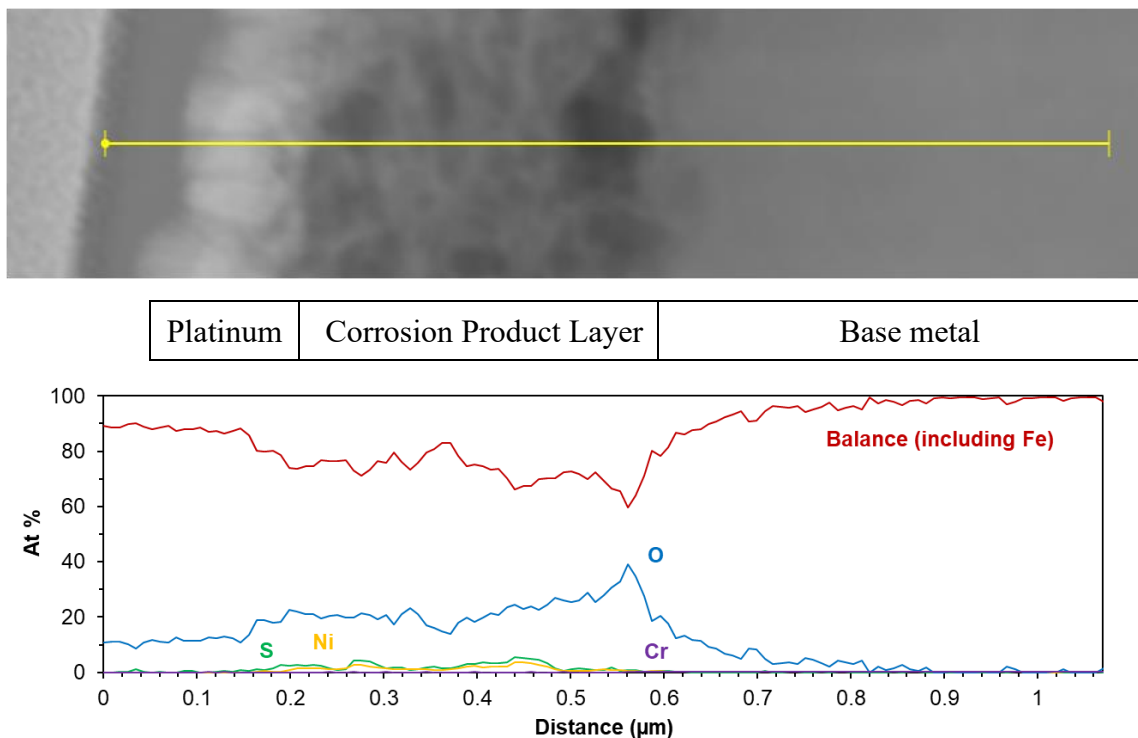
Figure 23 shows the EDS line scan result of the corrosion product layer on the 40 ppm H₂S specimen. From the left side to the right side of the image, the very top layer was platinum coated for FIB cutting. Underneath was one layer of palladium, which was plated after the steel specimen was drawn out from the glass cell to prevent oxidation.

Below these two plated layers, above the steel substrate, were corrosion product layers containing sulfur and oxygen. This result clearly shows that apart from sulfides or potentially elemental sulfur, oxides are an important part of the layer; especially the inner part of the layer near the steel surface. When and how these oxides were formed remained uncertain. Although further investigation was needed, SEAD cannot provide phase identification information of the layers, only the diffraction pattern of the steel substrate was obtained. A meaningful diffraction pattern of the layer is very difficult to obtain because the layer is actually nanocrystalline with not enough lattice repeat units for X-ray diffraction [19]. Such layers can be considered as being “X-ray amorphous”.

Figure 23

TEM-EDS line scan results of the specimen in baseline condition

(30 °C, $p_{H_2S} = 0.04$ mbar, $p_{CO_2} = 0.97$ bar, X65 carbon steel, pH 5, 1 wt.% NaCl, 300 rpm, 7 days, $[O_2]_{aq} \approx 20$ ppb_(w))



To summarize, the experimental results obtained at different H_2S partial pressures revealed that a thin FeS layer was responsible for a significant decrease in corrosion rate, as compared to the CO_2 only conditions. The general corrosion rates decreased with the increase of H_2S partial pressure. Localized corrosion happened when $0 < p_{H_2S} < 150$ ppm_(v). The pit initiation could have been related to the breakdown of the FeS layer formed under these conditions. The integrity of this protective layer seemed to be related to the partial pressure of H_2S , as no pitting was observed at $p_{H_2S} = 150$ ppm_(v). However,

no clear correlation could be associated with the saturation degree of FeS in the bulk solution.

4.3.2 Effect of $p\text{CO}_2$ on Pitting

The effect of $p\text{CO}_2$ on pitting in marginally sour environments was determined by running a series of experiments from 0 to 0.97 bar of CO_2 and at a fixed $\text{pH}_2\text{S} = 0.04$ mbar (40 ppm_(v)) with N_2 mixed as balance gas for a total pressure of 1 bar (atmospheric pressure). Figure 24 shows the saturation degree for both FeS and FeCO_3 . In all of these experiments, the measured bulk ferrous ion concentration was always far lower than the concentration required to reach the saturation value of 1 for either $\text{S}(\text{FeS})$ or $\text{S}(\text{FeCO}_3)$. Consequently, no precipitation was expected in these experiments based on bulk water chemistry conditions.

Figure 24

Saturation degree of bulk solution for both $FeS_{mackinawite}$ (blue line and above) and $FeCO_3$ (orange line and above) for varied pCO_2

(X65 carbon steel, 30 °C, pH 5, $pCO_2 = 0/0.53/0.82/0.97$ bar, $pH_2S=0.04$ mbar, total pressure is 1 bar, the balance is N_2 , 1 wt.% NaCl, 300 rpm stir bar, $[O_2]_{aq} \approx 20$ ppb_(w))

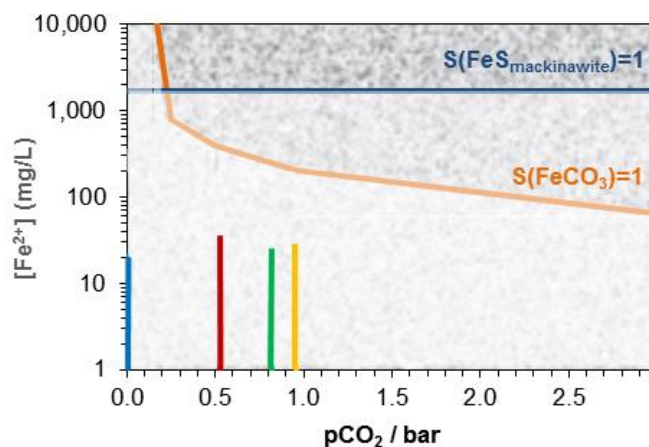
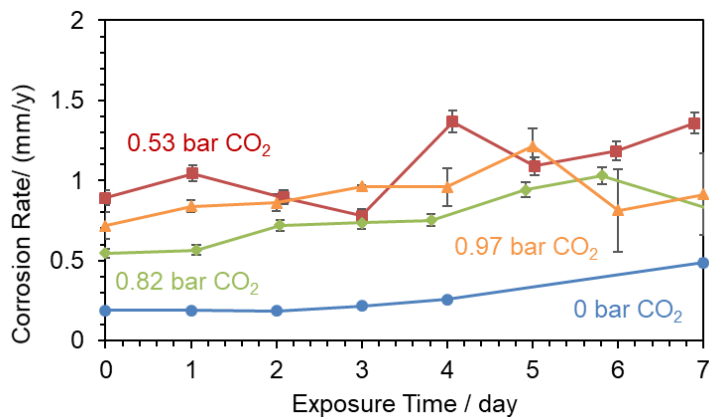


Figure 25 shows that any increase of CO_2 partial pressure generally leads to an increase of the general corrosion rates. The $pCO_2 = 0.53$ bar results were slightly higher than expected in this trend, although this experiment displayed higher pitting density (as shown in the next section); this could affect the average mass loss and consequently the general corrosion rate.

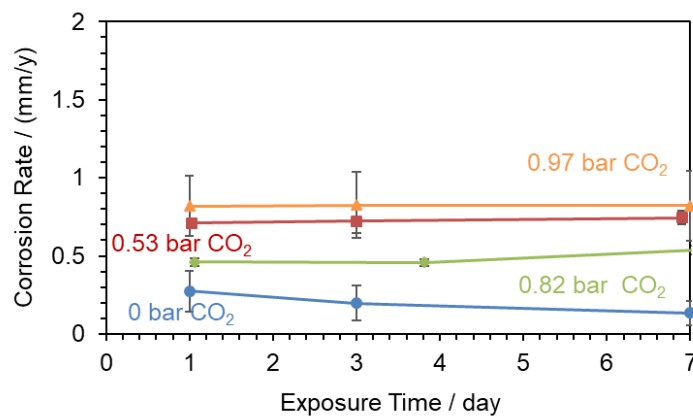
Figure 25

LPR and weight loss corrosion rates for varied $p\text{CO}_2$

(X65 carbon steel, 30 °C, pH 5, $p\text{CO}_2 = 0/0.53/0.82/0.97$ bar, $p\text{H}_2\text{S} = 0.04$ mbar, total pressure is 1 bar, the balance is N_2 , 1 wt.% NaCl, 300 rpm stir bar, $[\text{O}_2]_{\text{aq}} \approx 20$ ppb_(w))



(a) LPR corrosion rate



(b) Weight loss corrosion rate

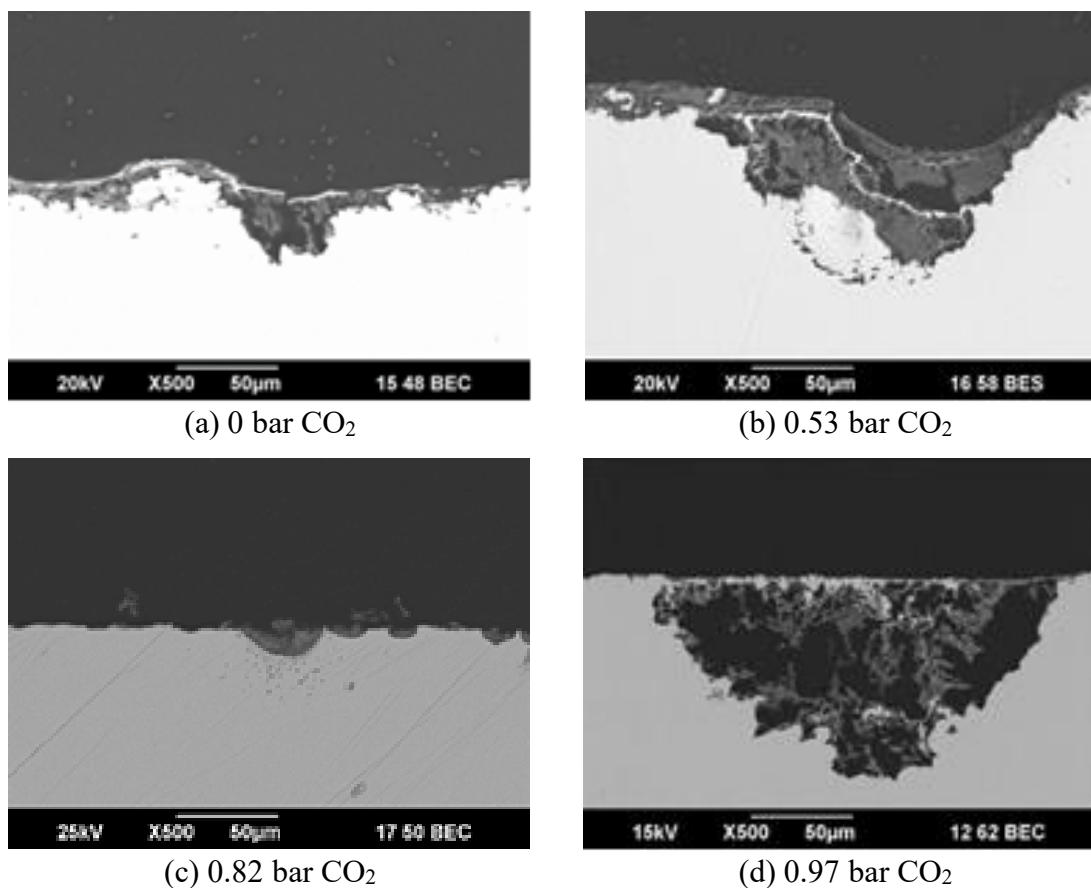
Figure 26 shows SEM cross-section images of specimens from experiments conducted at different $p\text{CO}_2$ values, where no distinct corrosion product layer can be seen on the surface of the steel. Although pitting initiation seems to be observed in the experiment conducted at $p\text{CO}_2 = 0$ bar, the pit depth is too low (10 - 15 μm deep pits) to

be truly characterized as pitting. In addition, specimens were retrieved after one, three- and seven-days exposure. The pit depths found on these samples were almost the same, and on the scale of surface roughness. Therefore, it can be deduced that at $p\text{CO}_2 = 0$ bar localized initiation may have happened, but no further propagation occurred. Similar results were previously reported by Fang, et al., in an H_2S only corrosion study [147]. This suggests that, in the experimental conditions selected for this study, pitting may initiate in the presence of H_2S , but does not propagate without CO_2 . For the specimens obtained at $p\text{CO}_2=0.53$ bar and $p\text{CO}_2 = 0.97$ bar, large pits were easily captured in the cross-sectional analysis. No pits were captured in the cross sections of the specimen from the $p\text{CO}_2 = 0.82$ bar CO_2 experiments, although there could have been some, according to the surface profilometry results in Figure 27 where pits are seen. The process of cross-sectioning a steel specimen does not always ensure that specific localized corrosion features will be captured, especially if the pitting density is low, since the specimen is cut at a random location.

Figure 26

SEM cross-section images of specimens at different CO₂ partial pressure after 7 days exposure

(X65 carbon steel, 30°C, pH5, pCO₂ = 0/0.53/0.82/0.97 bar, pH₂S = 0.04mbar, total pressure is 1 bar, the balance is N₂, 1 wt.% NaCl, 300 rpm, 7 days, [O₂]_{aq} ≈ 20 ppb_w)



The profilometry images (Figure 27) show that pitting occurred in all the cases that contained CO₂. A similar pitting density, independent of pCO₂, was observed for the different conditions. This finding supports the hypothesis that pitting in marginally sour environments is related to pH₂S and probably a very thin FeS layer. However, the

propagation rate of the pits seems to be related to $p\text{CO}_2$, or to a larger extent to the overall corrosivity of the fluid, for the range of conditions used. This is demonstrated by the fact that pit penetration rates for $p\text{CO}_2 = 0.53$ bar and $p\text{CO}_2 = 0.82$ bar were smaller than in the 0.97 bar $p\text{CO}_2$ experiment.

Figure 27

Surface profilometry analysis of specimens recovered for each experimental condition after 7 days exposure after corrosion product layer removed

(X65 carbon steel, 30°C, pH5, $p\text{CO}_2=0/0.53/0.82/0.97$ bar, $p\text{H}_2\text{S}=0.04\text{mbar}$, total pressure is 1 bar, the balance is N_2 , 1 wt.% NaCl, 300 rpm stir bar, $[\text{O}_2]_{\text{aq}} \approx 20 \text{ ppb}_{(\text{w})}$)

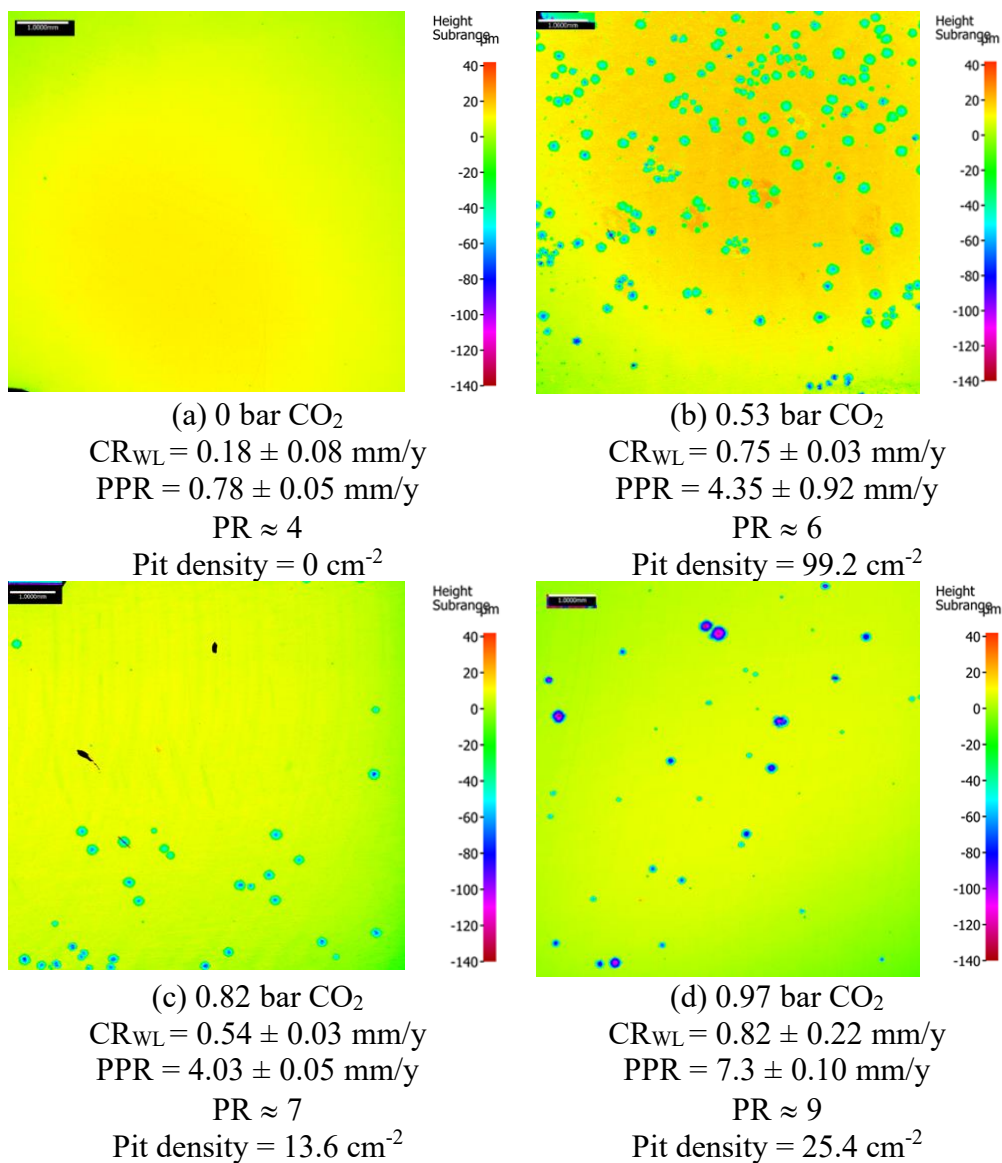
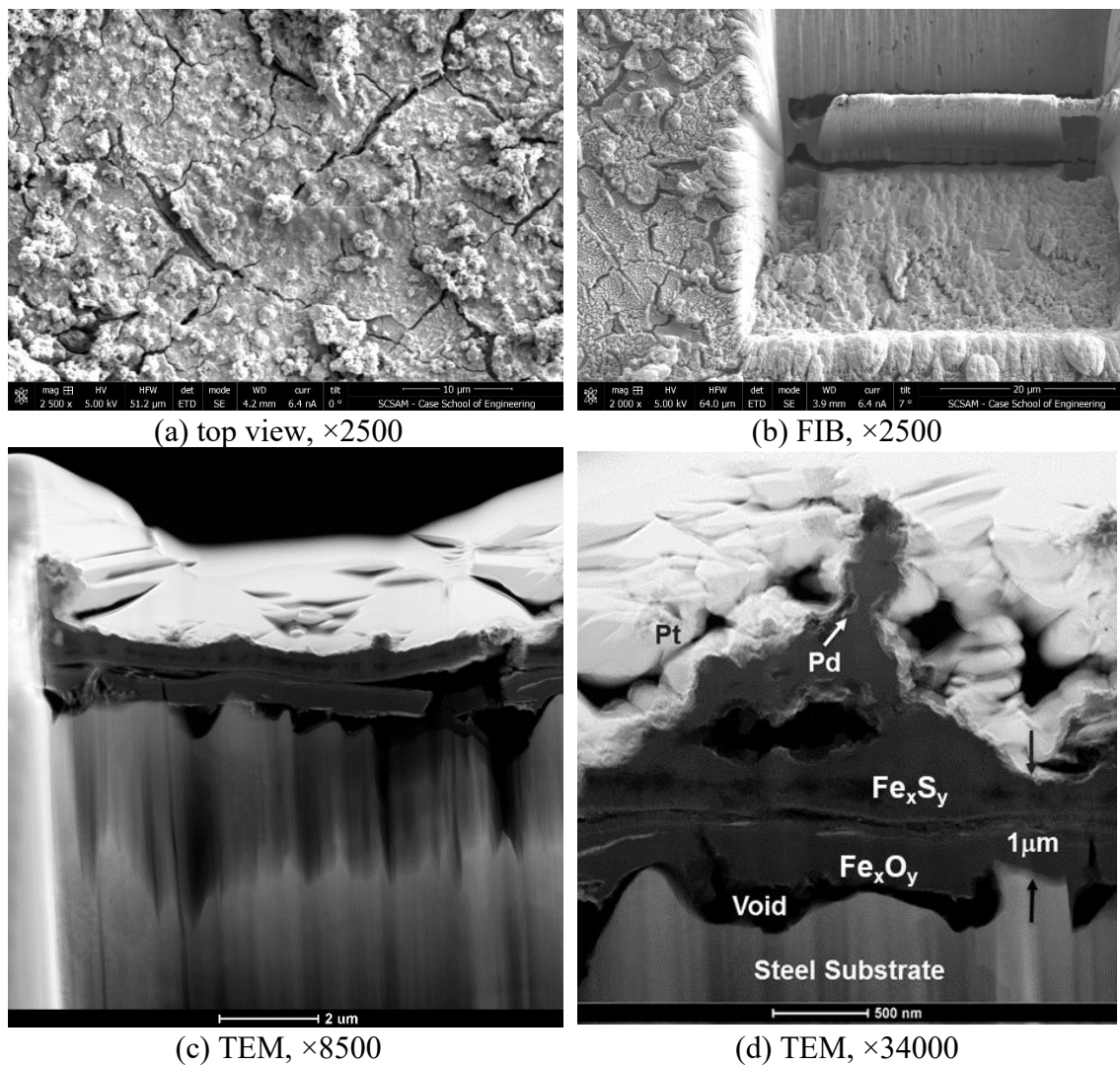


Figure 28, the TEM image for the $p\text{CO}_2 = 0$ bar experiment, reveals that, in H_2S only condition, a two-layer structure was formed. The total thickness of the two layers was about 500 nm. The layer seemed continuous and relatively dense. This layer offered some protection because: 1) the general corrosion rate was low (0.18 ± 0.08 mm/y); 2) no localized corrosion happened under this condition. Such a thick layer (compared with oxide layers or passive layers) was unexpected because the bulk solution was unsaturated with respect to mackinawite according to measurements of $[\text{Fe}^{2+}]$ and pH used for calculation of saturation degrees. Assuming that the layers were formed by precipitation, this indicated that the surface water chemistry was different from the bulk solution. Previous research findings in CO_2 only environments indicated that the surface pH value could be one to two units higher than that in the bulk solution [48, 108].

Figure 28

TEM images of the cross section cut out by FIB from the specimen of H_2S/N_2 experiments (30 °C, $pN_2 = 0.97$ bar, $pH_2S = 0.04$ mbar, X65, pH 5, 1 wt.% NaCl, 300 rpm, 7 days, $[O_2]_{aq} \approx 20$ ppb_(w))

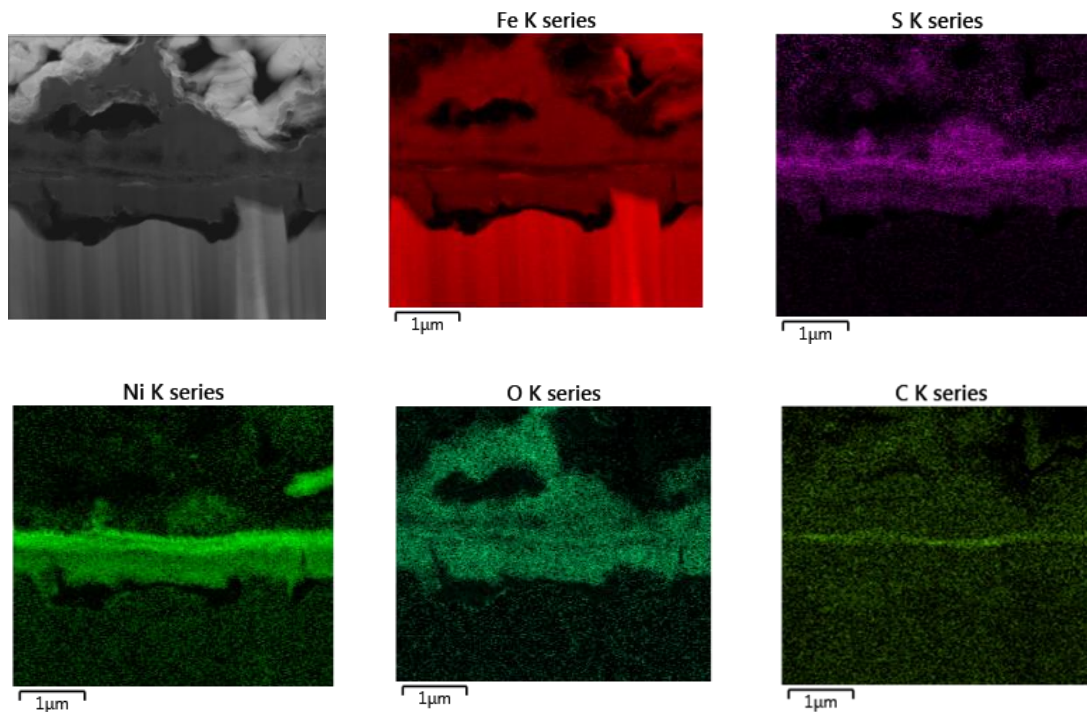


TEM-EDS mapping results (Figure 29) show that Fe, O, S, Ni elements were concentrated in the corrosion product layers. This indicates that sulfides and oxides were part of the composition of the corrosion product layers.

Figure 29

TEM-EDS mapping results of the specimen of the H_2S/N_2 experiment

($p_{H_2S} = 0.04$ mbar and $p_{N_2} = 0.97$ bar, X65 carbon steel, $30^\circ C$, pH 5, 1 wt.% NaCl, 300 rpm, 7 days, $[O_2]_{aq} \approx 20$ ppb_(w))



The TEM-EDS line scan results of the $p_{CO_2} = 0$ bar specimen are shown in Figure 30. From the left side to the right side of the image, the very top layer corresponds to the platinum coating for FIB cutting. Underneath that layer was another coating of palladium, which was sputtered after the steel specimen was withdrawn from the glass cell to prevent oxidation. Below these two plated layers, above the steel substrate, were two layers containing sulfur and oxygen, indicating the possible existence of iron sulfide, as well as iron oxide or hydroxide. The outer layer was richer in elemental sulfur, while

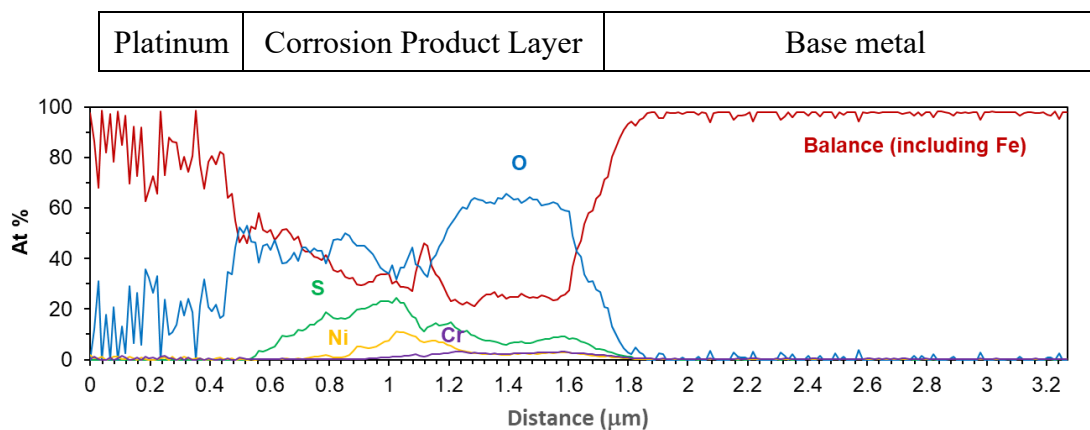
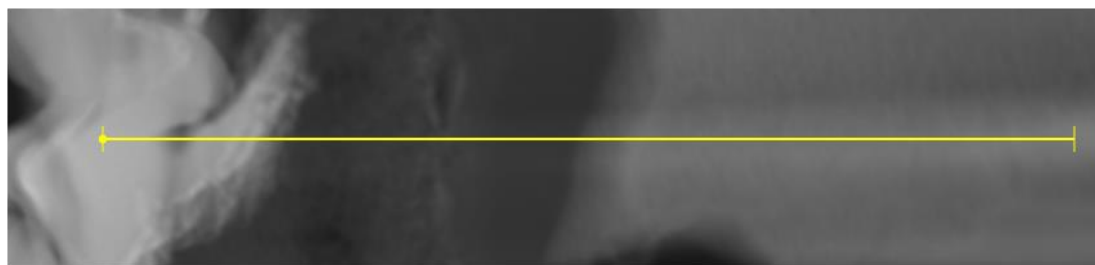
the inner layer was richer in elemental oxygen. The presence of oxygen is somehow unexpected. Nitrogen as a sparge gas was used to deaerate the aqueous solution for over two hours every time before the start of experiments, then N_2 and H_2S were bubbled in solution together for half an hour before the specimens were loaded. Consequently, it is not expected to retain significant dissolved O_2 in the environment (aqueous concentration of oxygen in solution was measured at around 20 $ppb_{(w)}$). Several explanations can be put forward to account for the presence of oxygen in the layer. The most logical one is that the layer could have been oxidized during post- retrieval, during sample handling, storage and/or analysis. These scenarios are revisited in depth in Chapter 5.

According to Table 9, manganese, nickel, and chromium are the most abundant alloying elements in the X65 steel specimen used in this study. However, only nickel was enriched in the two layers structure, especially in the upper layer. This enrichment of nickel could be due to the possible compound nickel sulfide (NiS) as it is found to be insoluble even in strong acid solutions. [19, 148, 149].

Figure 30

TEM-EDS line scan results of the specimen of H_2S/N_2 experiment

(30 °C, $p_{H_2S} = 0.04$ mbar, $p_{N_2} = 0.97$ bar, X65 carbon steel, pH5, 1 wt.% NaCl, 300 rpm, 7 days, $[O_2]_{aq} \approx 20$ ppb_(w))



It is clear from the experimental results that the presence of CO_2 is absolutely necessary for pitting initiation. Without CO_2 , the FeS layer appears fairly protective while the added acidity due to the presence of H_2CO_3 appears to be related to layer damage and loss of protectiveness. At this point, it is hypothesized that the presence of any weak acid (in addition to $H_2S_{(aq)}$) is enough to increase the local surface H^+ concentration, by dissociation, leading to local dissolution of the layer, preferential corrosion and pitting initiation. In addition, galvanic corrosion could also be involved since the pitting

penetration rate seems to be higher than the corrosion rate typically experienced in CO₂-only environments at the same pH value.

4.3.3 Effect of pH on Pitting

The effect of pH on pitting in marginally sour environments was evaluated at pH 4.0, 5.0 and 6.0 in the bulk solution. The vertical lines shown in Figure 31 represent the range of concentration of ferrous ions observed during each experiment. The saturation values for both FeS and FeCO₃ are dependent on solution pH value. Fewer ferrous ions were required to reach saturation at higher pH 6. Figure 31 shows that both FeS and FeCO₃ were far from saturation in the experiments at pH 4 and pH 5. At pH 6, S(FeCO₃) exceeded the saturation value of 1, while S(FeS) was very close to saturation, all based on bulk solution conditions. This indicates that supersaturation with respect to both types of corrosion products was likely at the steel surface. Consequently, a protective corrosion product layer, composed of possibly both FeS and FeCO₃, could have been expected in the pH 6 case.

Figure 31

Saturation degree of both $FeS_{mackinawite}$ (blue line and above) and $FeCO_3$ (orange line and above) under various pH in the bulk solution

(X65 carbon steel, 30 °C, pH 4/5/6, $pCO_2 = 0.97$ bar, $pH_2S = 0.04$ mbar, 1 wt.% NaCl, 300 rpm, 7 days, $[O_2]_{aq} \approx 20$ ppb_(w))

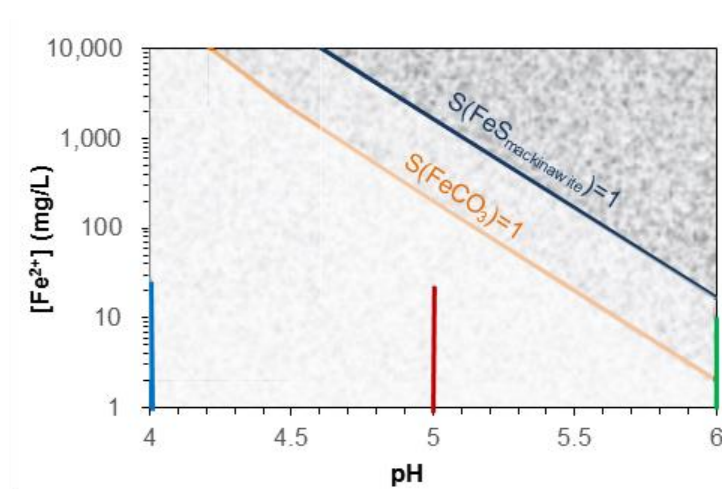


Figure 32 shows the trend of the changes of general corrosion rates with pH: increased H^+ concentration leads to higher corrosion rates. Since pH is the logarithmic value of $[H^+]$, this change is drastic. This agrees with the saturation degree calculation results in Figure 31. The scaling tendency (equation (25)) also increased with increasing pH, which would indicate a more protective FeS layer at higher pH, with no pit initiation. Compared with weight loss corrosion rates, the LPR corrosion rates are relatively higher. This is because when calculating the corrosion current density from LPR measurements, surface area of the working electrode should be divided. The existence of mackinawite and carbide on the steel surface increased the surface area, but this increase was not

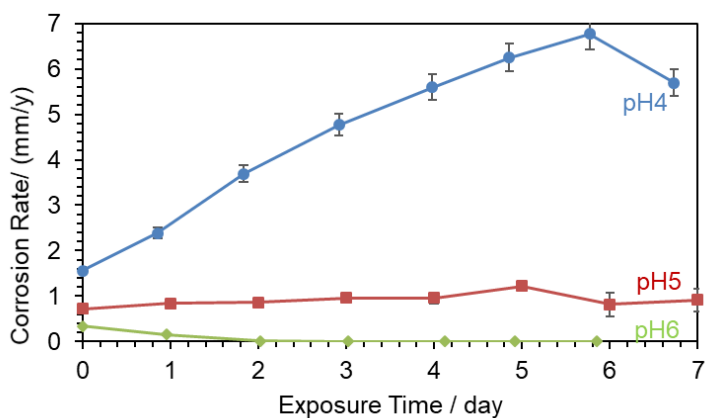
included in the calculation. Therefore, the corrosion rates calculated from LPR measurement are larger than the actual values.

Figure 32

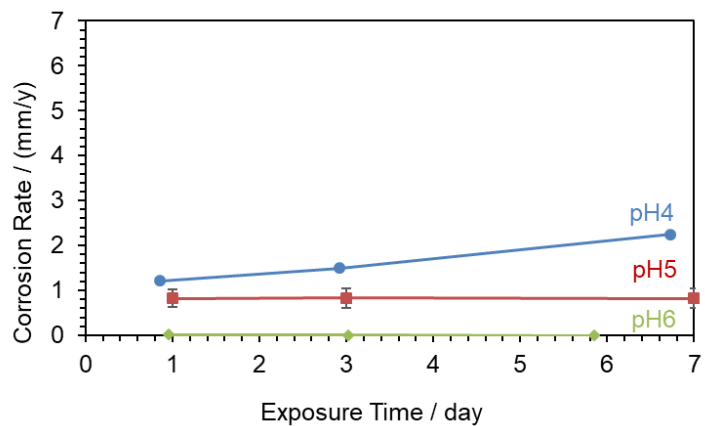
LPR and weight loss corrosion rates under various pH in the bulk solution

(X 65 carbon steel, 30°C, pH 4/5/6, $p\text{CO}_2 = 0.97$ bar, $p\text{H}_2\text{S} = 0.04$ mbar, 1 wt.% NaCl,

300 rpm, 7 days, $[\text{O}_2]_{\text{aq}} \approx 20$ ppb_(w))



(a) LPR corrosion rate



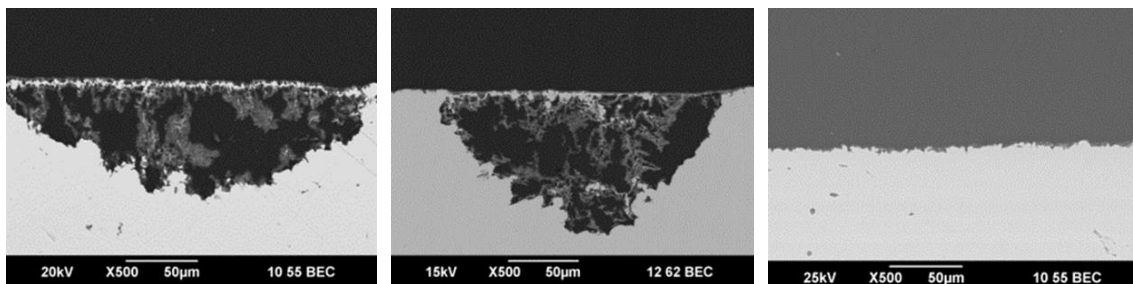
(b) Weight loss corrosion rate

Cross-section images, shown in Figure 33, indicate a high degree of pitting corrosion at pH 4 and 5, with similar pit depth in both cases. At pH 6, no pits are visible in the cross-section image, and this observation can be generalized over the entire specimen surface, as shown by profilometry analysis.

Figure 33

SEM cross-section images at different pH after 7 days exposure

(pH = 4/5/6, X65 carbon steel, 30 °C, $p\text{CO}_2 = 0.97$ bar, $p\text{H}_2\text{S} = 0.04$ mbar, 1 wt.% NaCl, 300 rpm stir bar, $[\text{O}_2]_{\text{aq}} \approx 20$ ppb_(w))



(a) pH 4

(b) pH 5

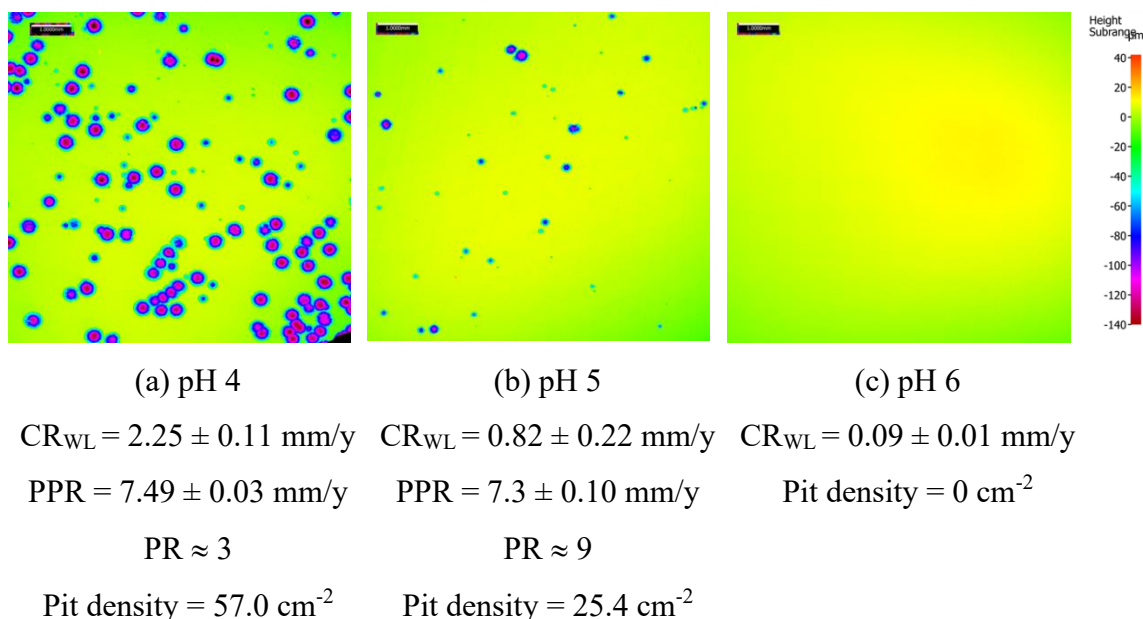
(c) pH 6

Figure 34 shows surface profilometry results done on specimens after removal of the corrosion product layer. Severe pitting is observed on the pH 4 specimen, accompanied by a very high general corrosion rate. Pitting density decreased significantly at pH 5, while the pit propagation rate remained almost the same. At pH 6, no pitting was detected and a very low general corrosion rate was measured.

Figure 34

Surface profilometry analysis at different pH after 7 days exposure after corrosion product layer was removed

(Captions show the general corrosion rate as measured by weight loss (CR_{WL}), the Pitting Penetration Rate (PPR) and the Pitting Ratio, pH = 4/5/6, X65 carbon steel, 30 °C, $pCO_2 = 0.97$ bar, $pH_2S = 0.04$ mbar, 1 wt.% NaCl, 300 rpm stir bar, $[O_2]_{aq} \approx 20$ ppb_(w))



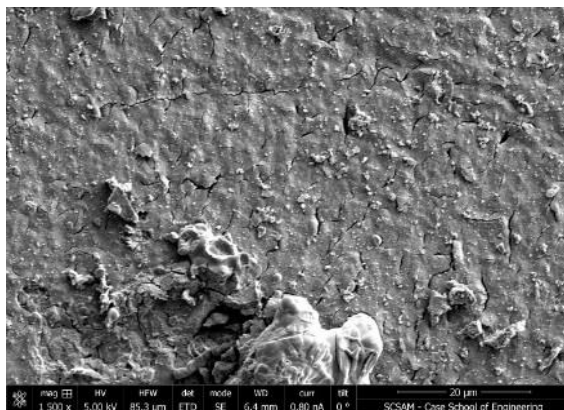
The corrosion product layer formed under the pH 6 condition, as shown in Figure 35 and Figure 36, is similar to that obtained at pH 5 (**Figure 21**). This is somehow surprising as pitting occurred at pH 5 and not at pH 6; also, the general corrosion rate at pH 5 was higher than at pH 6 (0.8 mm/year at pH 5 compared to 0.2 mm/year at pH 6). Consequently, some differences in terms of corrosion product layer coverage, attachment or compactness are expected. It is possible that the random selection of the location of the

TEM analysis did not reflect these differences while they may appear on other locations. More striking differences exist between the compact layer obtained in H₂S-only environment (Figure 28) and the seemingly more porous layer generated in systems containing both H₂S and CO₂, at pH5 or 6 (**Figure 21** b and c). In the presence of CO₂, the dissociation of H₂CO₃ leads to a lower surface pH, which could be the reason for the lack of compactness and increased porosity of the corrosion products.

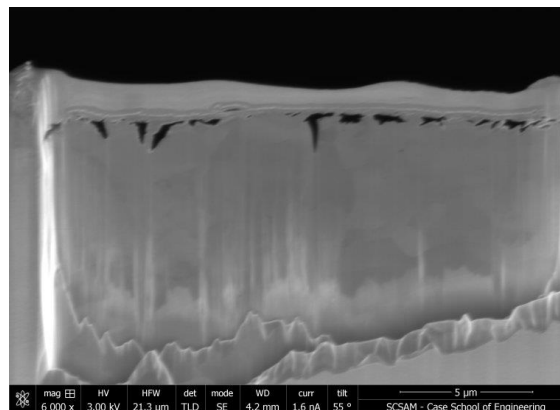
The explanation behind the absence of pitting at pH 6 remains fairly elusive but could be linked to the surface pH, which is logically higher compared to pH 5. A higher surface pH represents a less aggressive environment and may also favor the formation of iron oxides or oxyhydroxides.

Figure 35

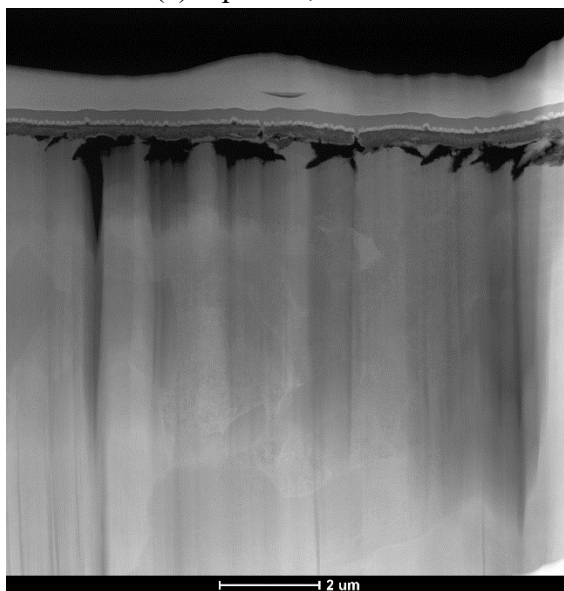
TEM images of the cross section cut out by FIB from the specimen of pH 6 experiments (30°C, pH6, 0.97 bar CO₂, 0.04 mbar H₂S, X65, 1wt.% NaCl, 300 rpm, 7 days, [O₂]_{aq} ≈ 20 ppb_(w))



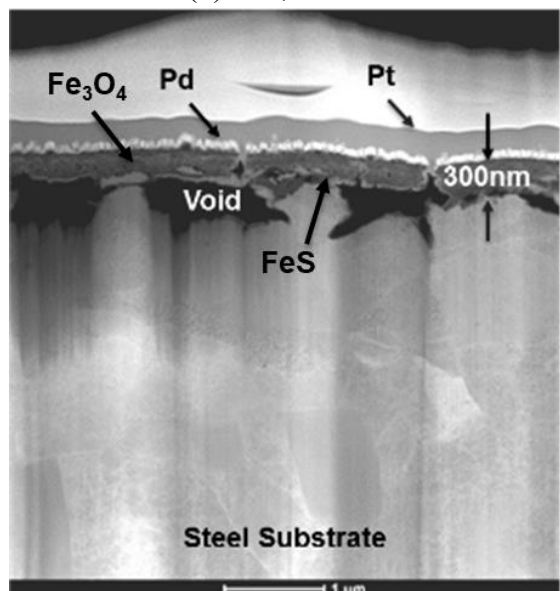
(a) top view, ×1500



(b) FIB, ×6000



(c) TEM, ×8500

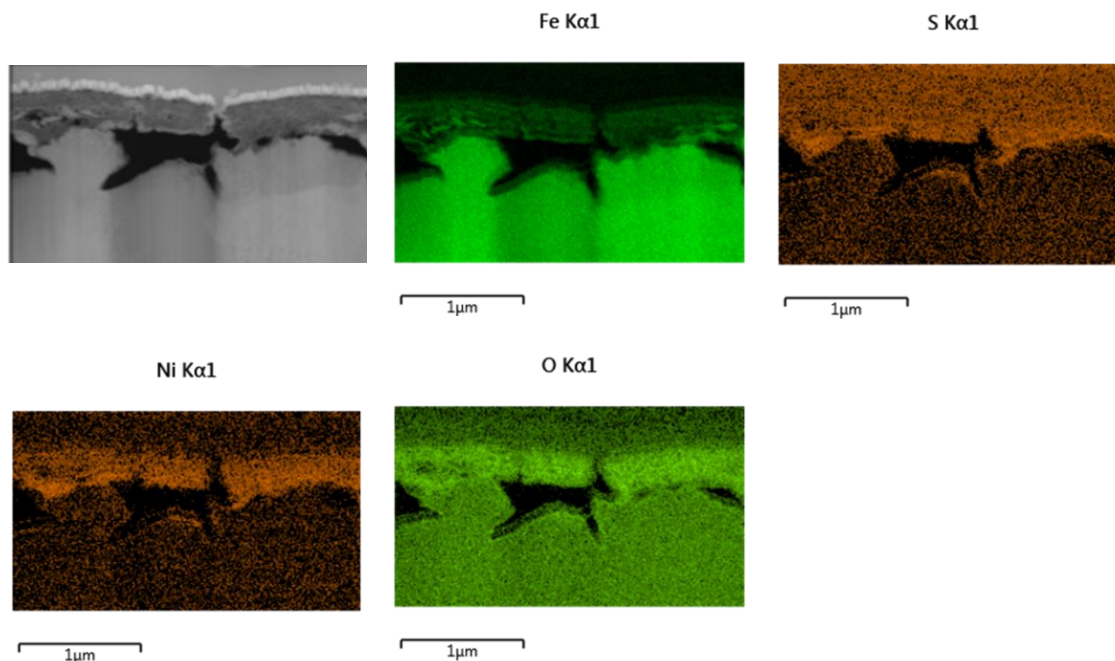


(d) TEM, ×17000

Figure 36

TEM-EDS mapping results of the specimen of pH 6 experiment

(30 °C, 0.04 mbar H₂S and 0.97 bar CO₂, pH 5, 1 wt.% NaCl, 300 rpm, 7 days, [O₂]_{aq} ≈ 20ppb_(w))



TEM-EDS line scan result of the specimen corresponding to the pH 6 experiment is shown in **Figure 37**. This distribution of elements along the indicative line shows that the layer is comprised of Fe, O, S and Ni. This could infer the presence of iron oxides and sulfides in the layer (0.2 to 0.4 μm), although it is unclear at this point if the oxides were formed during the test or during post-processing and exposed to air. The coexistence of oxides and sulfides has been observed already for high temperature sour conditions [59], [150]: magnetite was formed due to reaction between steel and water, then the outer part of the layer was converted into iron sulfide. However, this work was done at low

temperatures, direct reaction between steel and water vapor is less likely to occur. Further studies and discussion about the existence of oxides will be one of the topics in the following Chapter 5.

Figure 37

TEM-EDS line scan results of the specimen pH 6 experiment

(30°C, X65 steel, 0.04 mbar H₂S and 0.97 bar CO₂, 1 wt.% NaCl, 300rpm, 7 days, [O₂]_{aq} ≈ 20 ppb_(w))

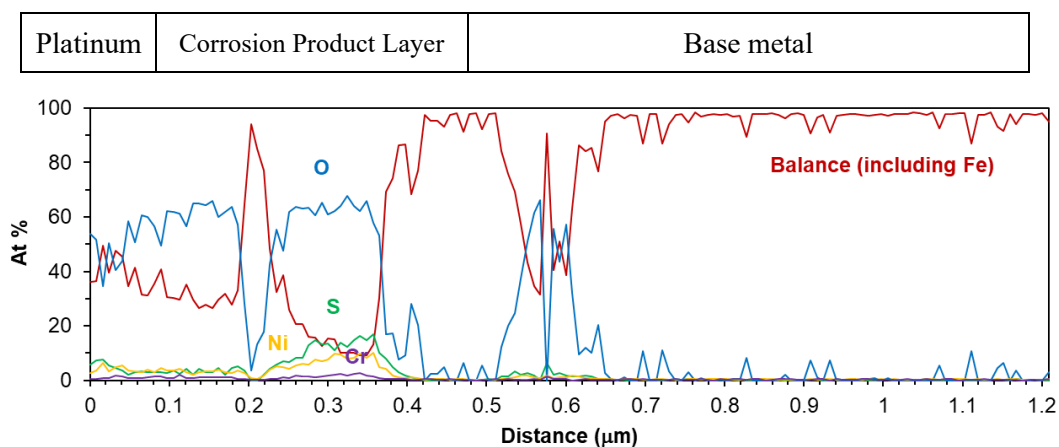
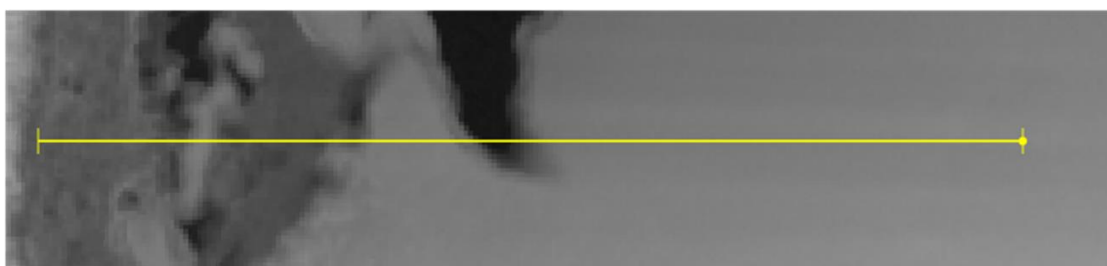


Figure 38 shows the electron diffraction pattern (image on the right side) at the circled area near the inner layer in the image on the left side. The ring pattern is unfortunately not very clear but can be used to identify the polycrystalline sulfide

compounds. The diameter of a ring is measured (Figure 39) and converted to the d-spacing in real space between lattice planes. When comparing this pattern with the database of crystal diffractions, a possible match can be established with pyrrhotite ($\text{Fe}_{0.91}\text{S}$, Table 10), although mackinawite (FeS) was expected. The discrepancy can be explained by the fact that the first few molecular layers where nanocrystal mackinawite is supposed to form cannot be derived by the diffraction equation, which requires long-range order of the crystal structure repeat units [19].

Figure 38

TEM-SAED results near the inner layer of the specimen of pH 6 experiment

(30°C, X65 steel, 0.04 mbar H_2S and 0.97 bar CO_2 , 1 wt.% NaCl, 300rpm, 7 days, $[\text{O}_2]_{\text{aq}} \approx 20 \text{ ppb}_{(\text{w})}$)

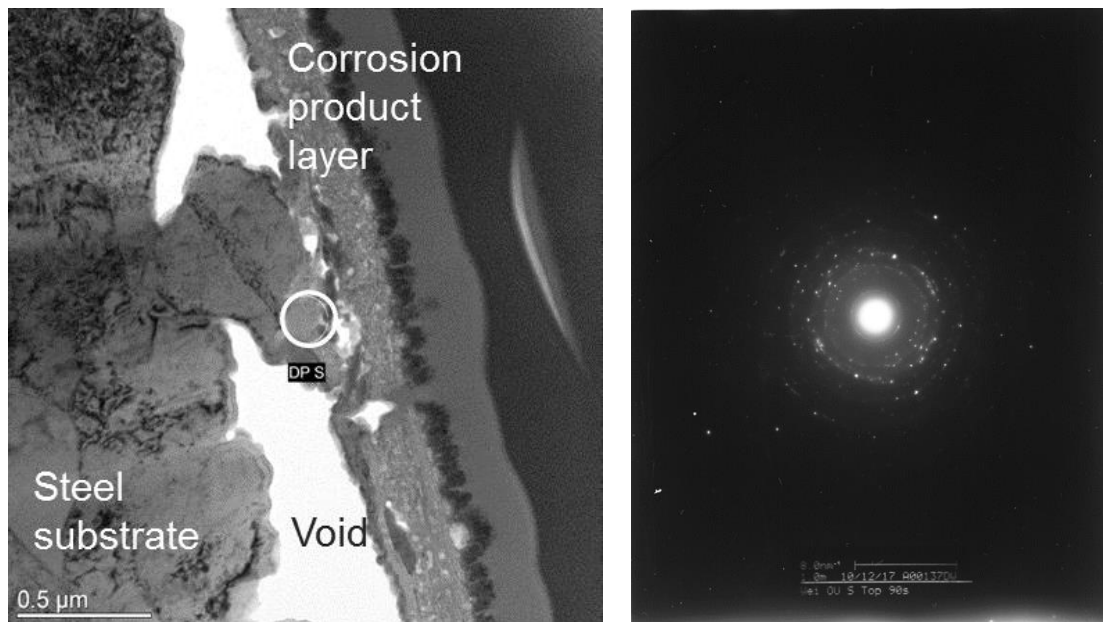
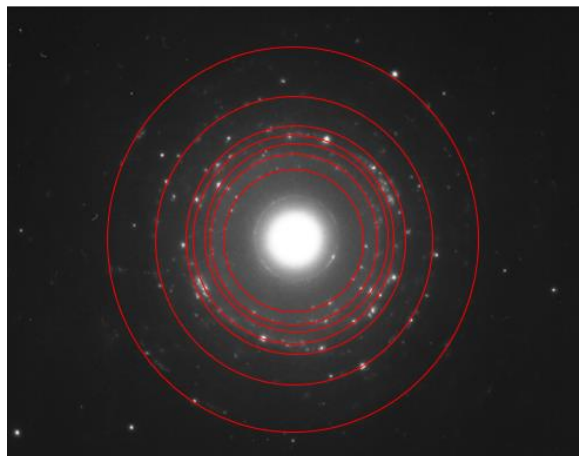


Figure 39

Pattern analysis of the specimen of pH 6 experiment

(30°C, X65 steel, 0.04 mbar H₂S and 0.97 bar CO₂, 1 wt.% NaCl, 300 rpm, 7 days, [O₂]_{aq}

≈ 20 ppb_(w))

**Table 10**

Sulfide analysis - possible match with Fe_{0.91}S

Ring number	Ring Diameter (nm ⁻¹)	Ring Radius (nm ⁻¹)	d Spacing (nm)
1	6.78	3.39	0.29
2	8.08	4.04	0.25
3	8.73	4.37	0.23
4	9.91	4.96	0.20
5	10.8	5.4	0.19
6	13.63	6.82	0.15
7	17.8	8.9	0.11

Figure 40 shows the precession electron diffraction (PED) acquired in the rectangular area. Each pixel on the map represents a square of $4 \text{ nm} \times 4 \text{ nm}$. The orientation map suggests that the crystal lattice parameter of the oxide compound was around 10 nm. Several phases of iron sulfides (FeS, Fe₇S₈, etc., as listed in the upper right corner in **Figure 40**) were selected for the data analysis. The colored map, in the lower right corner, suggests that mackinawite (FeS) is the most dominant iron sulfide present.

Figure 40

Orientation/phase map by PED near the inner layer of the specimen of pH 6 sample (30°C, X65 steel, 0.04 mbar H₂S and 0.97 bar CO₂, 1 wt.% NaCl, 300 rpm, 7 days, [O₂]_{aq} ≈ 20 ppb_(w))

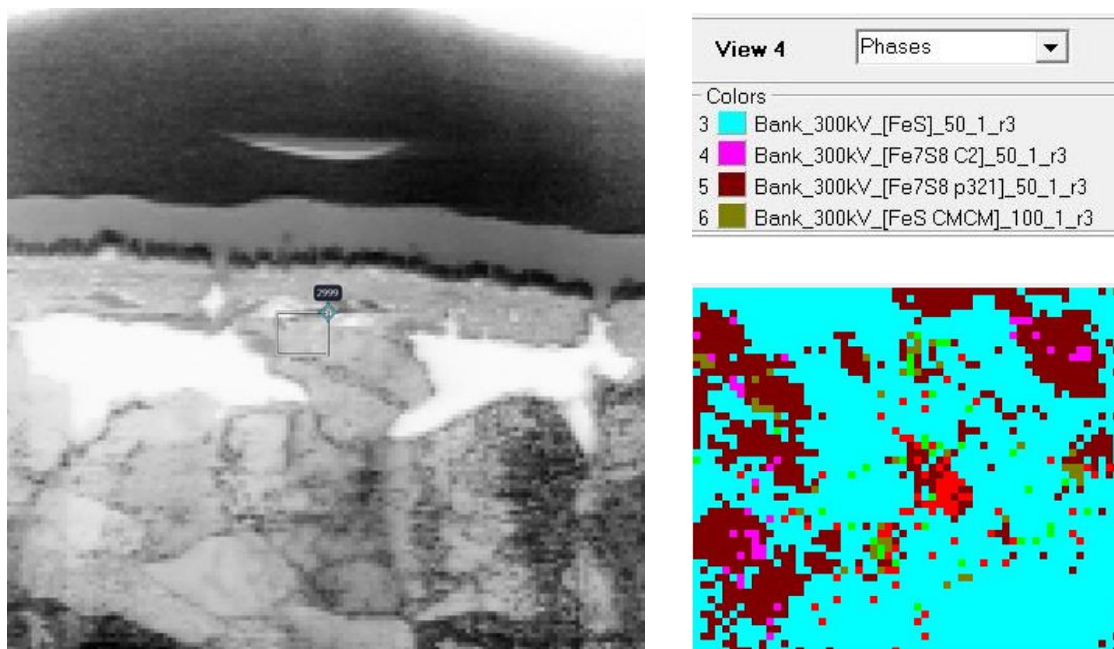


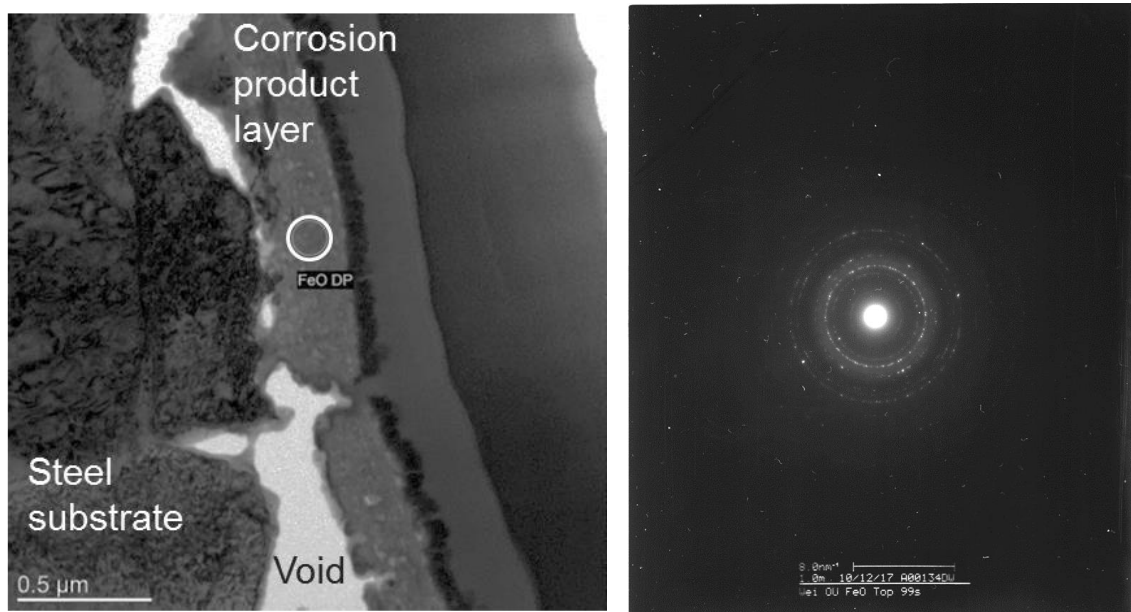
Figure 41 shows the TEM-SAED results near the outer layer of the specimen corresponding to the pH 6 experiment. The diameter of a ring is measured and converted to the d-spacing in real space between lattice planes. Five rings were measured. They all match with magnetite very well. Therefore, the oxide formed near the outer layer can be identified as magnetite, Fe_3O_4 .

Figure 41

TEM-SAED results near the outer layer of the specimen of pH 6 experiment

(30 °C, X65 steel, $p\text{H}_2\text{S} = 0.04$ mbar, $p\text{CO}_2 = 0.97$ bar, 1 wt.% NaCl, 300 rpm, 7 days,

$[\text{O}_2]_{\text{aq}} \approx 20$ ppb_(w))

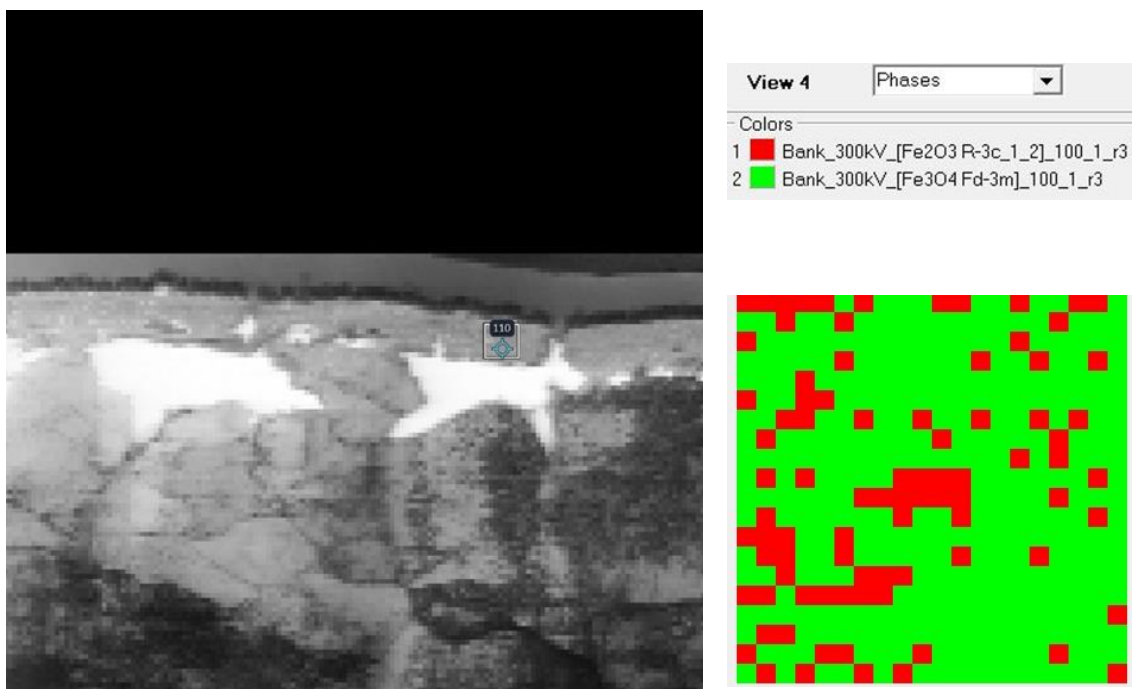


In Figure 42, a PED map (the image on the right side) was acquired in the rectangular area of the image on the left side. Each pixel in the map represents 10 nm. Both magnetite (Fe_3O_4) and hematite (Fe_2O_3) were used for data analysis, as listed in the

upper right corner. The orientation map suggests the crystal size of the oxide is around 20 nm. The overlapped map in the lower right corner suggested that PED reliably identified Fe_3O_4 . This agrees well with the previous SAED result.

Figure 42

Orientation/Phase Map by PED near the outer layer of the specimen of pH 6 experiment (30 °C, X65 steel, 0.04 mbar H_2S and 0.97 bar CO_2 , 1 wt.% NaCl, 300 rpm, 7 days, $[\text{O}_2]_{\text{aq}} \approx 20 \text{ ppb}_{(\text{w})}$)



In summary, pitting in marginally sour environments was observed at pH 4 and 5. Also, the tendency of occurrence of localized corrosion could be lowered by increasing the pH in the system. Phase identification by SAED and PED indicate that nanocrystalline mackinawite was the phase most likely present as the inner layer; the

outer layer being composed of magnetite, as a possible product of mackinawite oxidation. However, when and how the oxidation of the outer layer happened remains unknown. Further investigation is required. The findings revealed that the presence of a buffering weak acid (H_2CO_3) seems to be related to a weakening of the protectiveness of the layer, at least at pH 5 and lower.

4.3.4 Effect of Temperature on Pitting

The effect of temperature on pitting was investigated at $\text{pH}_2\text{S} = 0.04$ mbar (40 ppm) by performing experiments at 30°C , 60°C , and 80°C . Since the experiments were conducted in a glass cell at atmospheric pressure ($P_T=1$ bar), the changes in vapor pressure lead to different values of pCO_2 with temperature, from 0.97 bar at 30°C , to 0.82 bar at 60°C and 0.53 bar at 80°C . According to the water chemistry calculation for the bulk conditions, the solution was under-saturated with respect to FeS and FeCO_3 in experiments at 30°C , saturated only with respect to FeS at 60°C , and saturated with respect to both FeS and FeCO_3 at 80°C , as shown in Figure 43. Based on the arguments developed above, one should expect localized corrosion to happen at 30°C , probably not at 60°C , and definitively no pitting was expected at 80°C , due to high supersaturation with respect to both FeS and FeCO_3 .

Figure 43

Saturation degree of both $FeS_{mackinawite}$ (blue line and above) and $FeCO_3$ (orange line and above) at various temperatures in bulk solution

(X65 carbon steel, 30/60/80 °C, target pH5, $pCO_2 = 0.97/0.82/0.53$ bar, $pH_2S = 0.04/0.03/0.02$ mbar, 1 wt. % NaCl, 300 rpm stir bar, 7 days, $[O_2]_{aq} \approx 20$ ppb_(w))

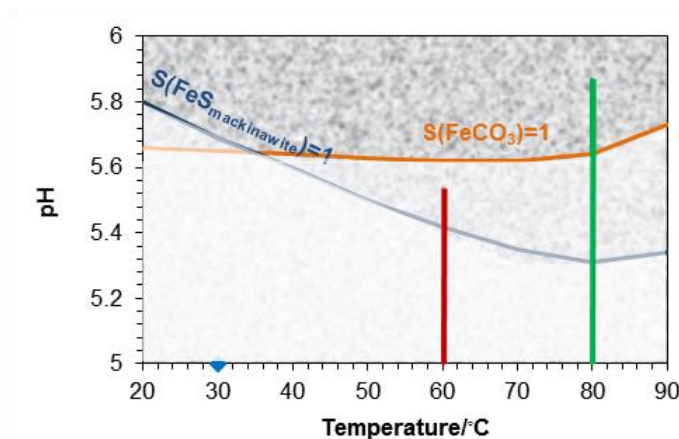


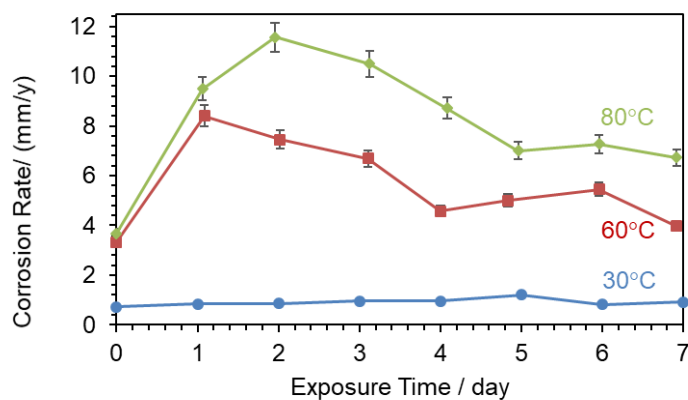
Figure 44 shows that the general corrosion rates increased dramatically as the temperature increased, which was also fully expected. As a rule of thumb, an increase of temperature by 10°C leads to a doubling of the reaction rate. The weight loss corrosion rate results were lower than the utilized electrochemical method (LPR), especially at higher temperature, but the general trend was similar. The reason for the discrepancy between LPR and WL results typically is related to the determination of the B value used for the conversion of polarization resistance and current density. This B value is chosen based on previous experiments [3] and is kept constant for all the experiments for the sake of consistency. Although it is expected to change with operating conditions, the dependence of temperature on the B value is still difficult to determine experimentally.

Overall, the corrosion rate values obtained with WL are to be trusted while the LPR data help defining their trend with time. Generally, the corrosion rates decreased with time at 60 °C and 80 °C, with the only exception at the time when the experiments started. At 30 °C, the corrosion rates did not decrease with time due to the propagation of pitting.

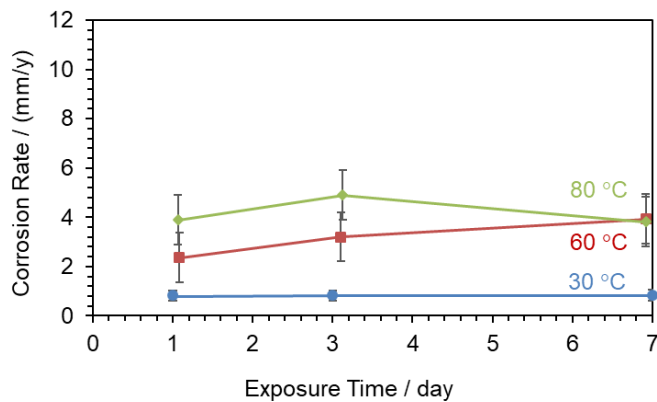
Figure 44

LPR and weight loss corrosion rates at various temperatures

(X65 carbon steel, 30/60/80 °C, target pH 5, $pCO_2 = 0.97/0.82/0.53$ bar, $pH_2S = 0.04/0.03/0.02$ mbar, 1 wt. % NaCl, 300 rpm stir bar, 7 days, $[O_2]_{aq} \approx 20$ ppb_(w))



(a) LPR corrosion rate

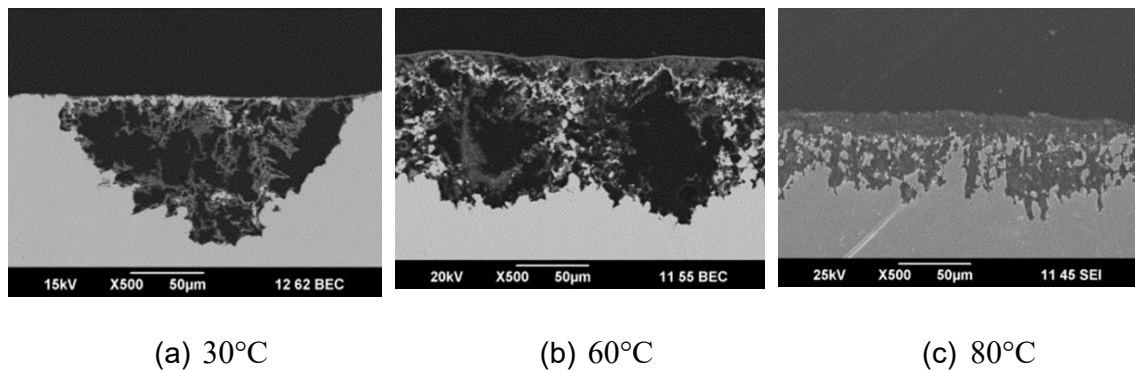


(b) Weight loss corrosion rate

Figure 45 shows SEM cross-section images of specimens at different temperatures, which confirm the hypothesis based on saturation. At 30°C, pitting is clearly detected, while at 60°C, the surface morphology seems to indicate that pits initiated and then grew larger and agglomerated to form a uniformly rough surface. This is a typical description of uniform corrosion. At 80°C, the morphology of the corrosion attack appeared different with a very rough surface but no distinct pitting.

Figure 45

SEM cross-section images of specimens at different temperatures after 7 days exposure (X65 carbon steel, 30/60/80 °C, 0.97/0.82/.53 bar CO₂, pH5, 1 wt.% NaCl, 300 rpm stir bar, [O₂]_{aq} ≈ 20 ppb_(w))

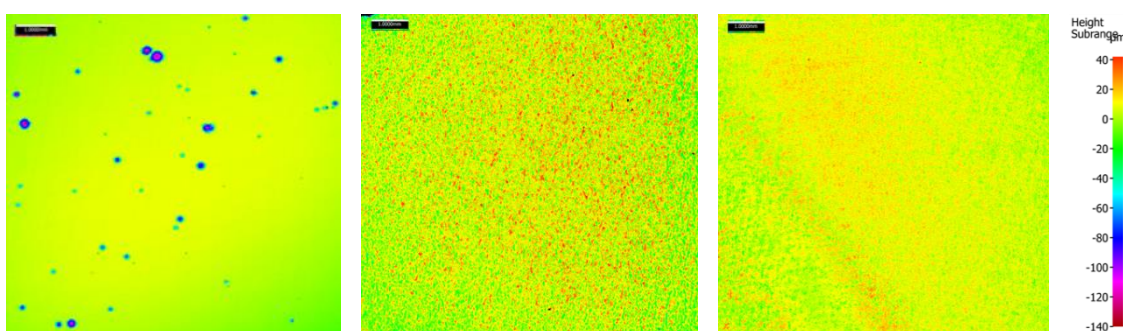


Surface profilometry shown in Figure 46 clearly indicates that pitting was observed at 30°C with a very high pit penetration rate, while at 60°C and 80°C the corrosion attack was extensive but uniform.

Figure 46

Surface profilometry scanning images of different temperatures after 7 days exposure after corrosion product layer removed

(pH = 5, X65 carbon steel, 30/60/80 °C, pCO₂ = 0.97/0.82/.53 bar, pH₂S = 0.04 mbar, 1 wt.% NaCl, 300 rpm stir bar, [O₂]_{aq} ≈ 20 ppb_(w)). The scales of the surface height of the three images were deliberately kept the same.)



(a) 30°C

CR_{WL} = 0.82 ± 0.22 mm/y

PPR = 7.3 ± 0.10 mm/y

PR ≈ 9

Pit density = 25.4 cm⁻²

(b) 60°C

CR_{WL} = 3.92 ± 0.01 mm/yPit density = 0 cm⁻²

(c) 80°C

CR_{WL} = 3.82 ± 0.01 mm/yPit density = 0 cm⁻²

Pitting corrosion was only observed at 30°C, while severe but uniform corrosion was experienced at higher temperatures. It is postulated that above 60°C, the pitting density is so high that pits agglomerate rapidly leading to a uniformly corroded surface. In these conditions, the corrosion product layer is not protective. High temperature simultaneously accelerated both uniform corrosion and the pit initiation related reactions at the same time. At lower temperatures, localized corrosion is more likely to occur because the initiation sites are much fewer than at elevated temperatures. According to

the rule of thumb of localized corrosion: “large cathode area, small anode area”, the less the pit initiates, the more dangerous it could be.

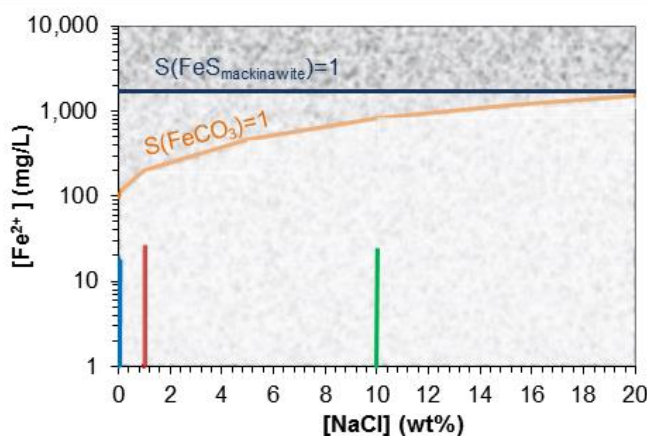
4.3.5 Effect of Salt Concentration on Pitting

The effect of sodium chloride concentration on pitting was investigated at pH 5, $p_{\text{H}_2\text{S}} = 0.04$ mbar (40 ppm) and $p_{\text{CO}_2} = 0.97$ bar by performing experiments without any NaCl and with adding 1 and 10 wt.% NaCl. The saturation degrees of FeS and FeCO₃ are illustrated in Figure 47, which shows that both FeS and FeCO₃ are far from being saturated, over the whole range of bulk NaCl concentrations tested. Here, the saturation degree of FeS does not change with NaCl concentration because neither the dissociation equilibrium constant equation [151] nor the solubility constant equation [39] of FeS includes dependence on the ionic strength. It is understood to be incorrect but no other expression of the equilibrium constants is available. This is not the case with FeCO₃ where both the solubility constant as well as the dissociation constants are a function of ionic strength (NaCl concentration) [14].

Figure 47

Saturation degree of both $FeS_{mackinawite}$ (blue line and above) and $FeCO_3$ (orange line and above) of various salt concentrations in bulk solution

(X65 carbon steel, 30 °C, pH 5, $pCO_2 = 0.97$ bar, $pH_2S = 0.04$ mbar, 0/1/10 wt.% NaCl, 300 rpm stir bar, 7 days, $[O_2]_{aq} \approx 20$ ppb_(w))



It should be noted that besides deionized water, about 20 ml of 0.1 M Na_2CO_3 was added into the solution of the 0 wt.% NaCl (blank) experiment for pH control purposes. Therefore, it was not strictly salt-free. As shown in **Table 11**, the ionic strength of the 0 wt.% NaCl solution with 20 ml of 0.1 M Na_2CO_3 is of the order of 10^{-6} compared with 10^{-2} for the 1 wt.% NaCl solution. Therefore, the comparison between the two solutions is meaningful.

Table 11*Ionic strength of solutions of various NaCl weight percentage*

Weight percent	Concentration	Ionic strength	Salt
0.01%	1.71×10^{-3}	2.92×10^{-6}	NaCl
0.1%	0.0171	2.92×10^{-4}	NaCl
1%	0.171	0.0292	NaCl
10%	1.71	2.92	NaCl
0.01%	0.001	4×10^{-6}	Na ₂ CO ₃

Figure 48 shows that the highest general corrosion rate was obtained at 1 wt. % of NaCl; while the lowest was at 10 wt. % of NaCl. With the increase in NaCl concentration to 10%, the general corrosion rate decreased significantly, as was expected (from a previous experimental study by Fang et al. [152]). Increases in NaCl concentration, or by extension in any salt concentration, decreases the solubility of CO₂ and H₂S in water; a phenomenon called the “salting out” effect, as mentioned in Chapter 2. The presence of high salt content also renders the solution highly non-ideal, affecting the activity of ionic and dissolved species; and therefore, the physical properties of the solution. Elaborating on these phenomena is out with the scope of this study, the main purpose of this experimental series being to test if high NaCl contents affect the pitting tendency in marginally sour environments. As mentioned earlier, the presence of Cl⁻ is known to affect the protectiveness of passive films. In addition, increasing the ionic

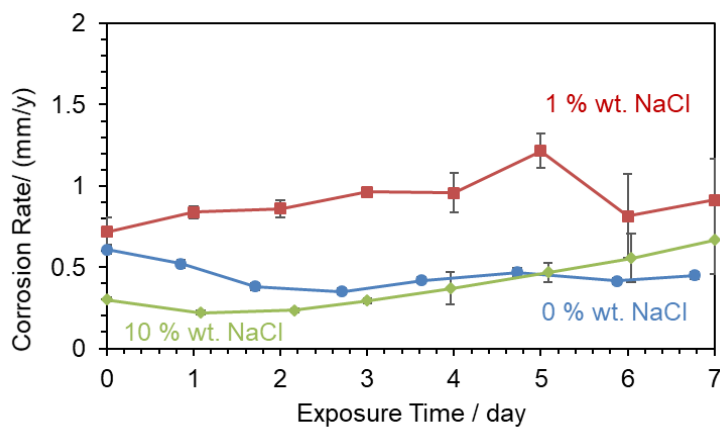
strength of the solution, and therefore its conductivity, could also enhance any galvanic corrosion if present.

Figure 48

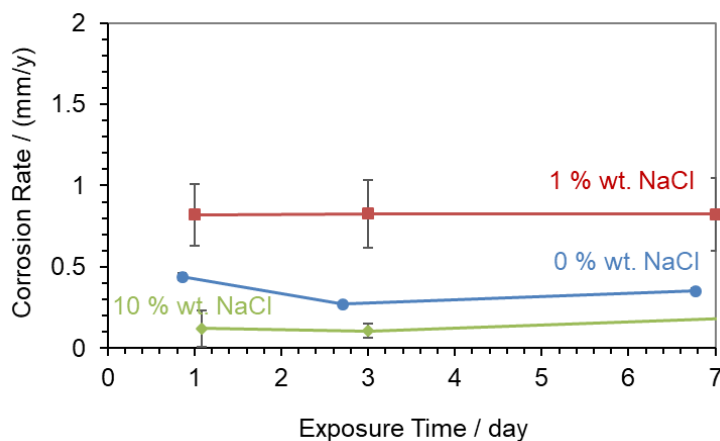
LPR and weight loss corrosion rates of various salt concentrations

(X65 carbon steel, 30 °C, pH 5, $p\text{CO}_2 = 0.97$ bar, $p\text{H}_2\text{S} = 0.04$ mbar, 0/1/10 wt.% NaCl,

300 rpm stir bar, 7 days, $[\text{O}_2]_{\text{aq}} \approx 20$ ppb_(w))



(a) LPR corrosion rate



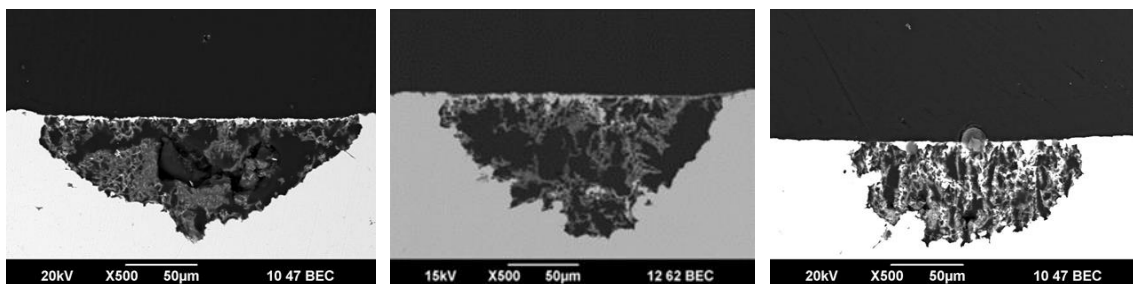
(b) Weight loss corrosion rate

SEM cross-section images of specimens at different NaCl concentrations are shown in Figure 49. There does not seem to be a major difference in the pit morphology or depth with different NaCl concentrations, which is consistent with the reasoning presented above and the saturation calculations shown in Figure 47.

Figure 49

SEM cross-section images of specimens at different salt concentrations after 7 days exposure

(X65 carbon steel, 30 °C, pH 5, 0.97 bar CO₂, pH₂S = 0.04 mbar, 0/1/10 wt.% NaCl, 300 rpm, 7 days, [O₂]_{aq} ≈ 20 ppb_(w))



(a) 0 wt.% NaCl

(b) 1 wt.% NaCl

(c) 10 wt.% NaCl

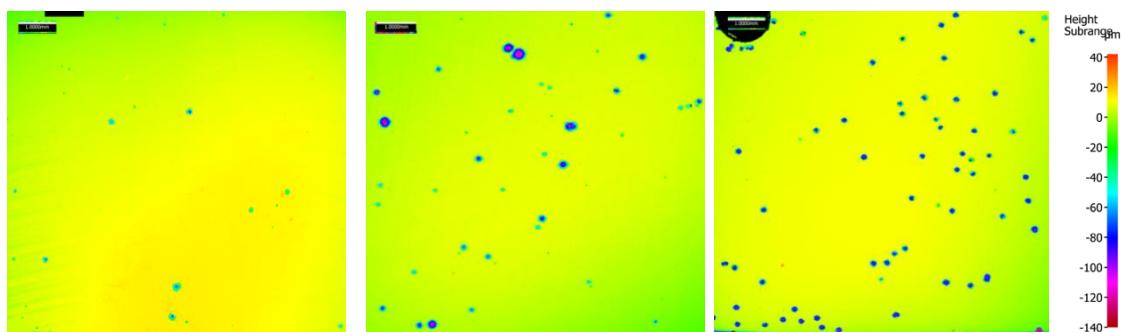
Surface profilometry scanning images of specimens exposed to different NaCl concentrations are shown in Figure 50. As the concentration of NaCl increased, the pit density increased even if there was no significant change in pit penetration rates. The pitting density could be related to the conductivity of the solution. Higher salt concentrations made the galvanic coupling effect between the steel and iron sulfide layer stronger [108, 124]. In summary, the presence of NaCl or Cl⁻ does not seem to directly

affect layer protectiveness breakdown and the occurrence of pitting corrosion. It does have an effect on the extent of pitting, which can be linked to the enhancement of the galvanic coupling in the presence of highly conductive electrolyte. NaCl or Cl⁻ concentration is consequently not found to be a controlling parameter in the protective layer breakdown mechanism.

Figure 50

Surface profilometry scanning images of specimens at different salt concentrations after 7 days exposure after corrosion product layer removed

(X65 carbon steel, 30 °C, pH5, pCO₂ = 0.97 bar, pH₂S = 0.04 mbar, 0/1/10 wt.% NaCl, 300 rpm stir bar, 7 days, [O₂]_{aq} ≈ 20 ppb_(w))



(a) 0 wt.% NaCl

(b) 1 wt.% NaCl

(c) 10 wt.% NaCl

CR_{WL} = 0.35 ± 0.01 mm/y CR_{WL} = 0.82 ± 0.22 mm/y CR_{WL} = 0.18 ± 0.01 mm/y

PPR = 4.69 ± 0.22 mm/y PPR = 7.3 ± 0.10 mm/y PPR = 4.86 ± 0.20 mm/y

PR ≈ 13

PR ≈ 9

PR ≈ 27

Pit density = 11.2 cm⁻²

Pit density = 25.4 cm⁻²

Pit density = 34.7 cm⁻²

4.3.6 Effect of Microstructure on Pitting

The purpose of this section is to identify the effect of material microstructure and composition on pitting occurrence and characteristics. A series of experimental results were performed with pure iron and X65 steel at 30 °C, $p_{\text{H}_2\text{S}} = 0.04$ mbar (40 ppm), $p_{\text{CO}_2} = 0.97$ bar, pH 5 and 1 wt.% NaCl (baseline conditions). The experiments were done with pure iron as a control since its microstructure does not contain iron carbide (Fe_3C). X65 and pure iron specimens were tested in independent experiments. The bulk solution saturation degrees of FeS and FeCO_3 were always below unity, as presented in **Figure 51**. The saturation degree for the pure iron and X65 experiments are exactly the same in this chart since the water chemistry is not affected by the substrate microstructure.

Figure 51

Saturation degree in the bulk solution of systems featuring different working electrode materials

(X65 carbon steel, 30 °C, pH 5, $p_{\text{CO}_2} = 0.97$ bar, $p_{\text{H}_2\text{S}} = 0.04$ mbar, 0/1/10 wt.% NaCl, 300 rpm stir bar, 7 days, $[\text{O}_2]_{\text{aq}} \approx 20$ ppb_(w))

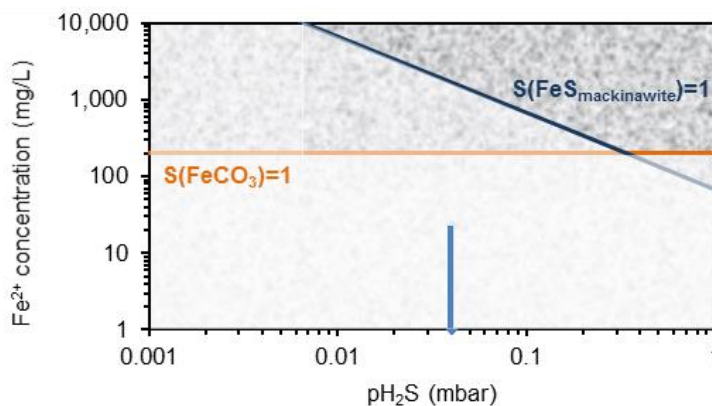


Figure 52 shows the general corrosion rates of pure iron and X65 in the tested conditions. Weight loss corrosion rates show the corrosion rate of X65 was higher than pure iron, because: 1) galvanic coupling between ferric and carbide microstructure could contribute slightly to the general corrosion rate; 2) localized corrosion happened on X65, not on pure iron.

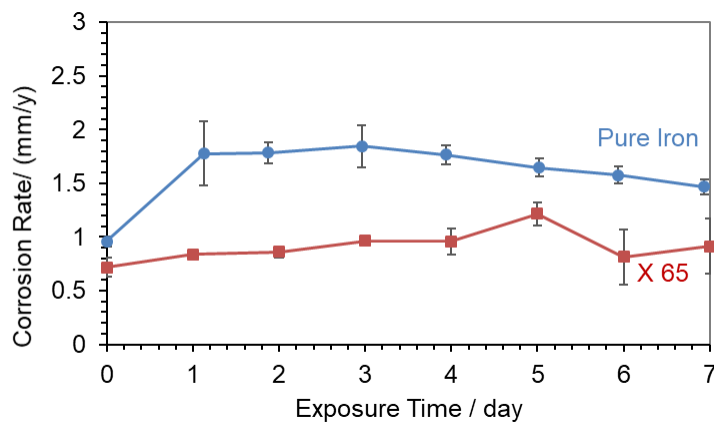
The cross-section images of X65 and pure iron specimens acquired by SEM backscattering and EDS mapping (highlighting sulfur) are displayed in Figure 53. Neither pitting nor a corrosion product layer could be observed on the surface of the pure iron specimen. As for the X65 steel, a thin corrosion product layer could be observed by SEM on the surface of the specimen. As mentioned earlier, this thin layer is hypothesized to be made of an inner FeS layer and an outer Fe₃O₄ layer. According to EDS analysis, the corrosion product layer contained: iron, sulfur and carbon as major elements, lesser amounts of oxygen, and trace amounts of alloying elements; which is similar to the TEM-EDS results in Figure 22.

Figure 52

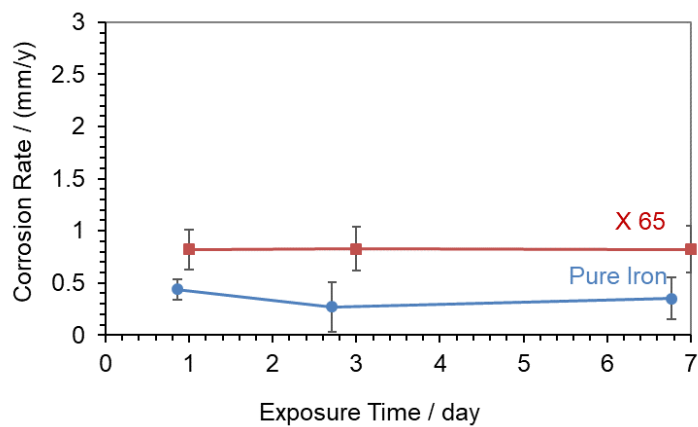
LPR and weight loss corrosion rates of different working electrode materials

(X65 carbon steel, 30 °C, pH 5, $p\text{CO}_2 = 0.97$ bar, $p\text{H}_2\text{S} = 0.04$ mbar, 0/1/10 wt.% NaCl,

300 rpm stir bar, 7 days, $[\text{O}_2]_{\text{aq}} \approx 20$ ppb_(w))



(a) LPR corrosion rate

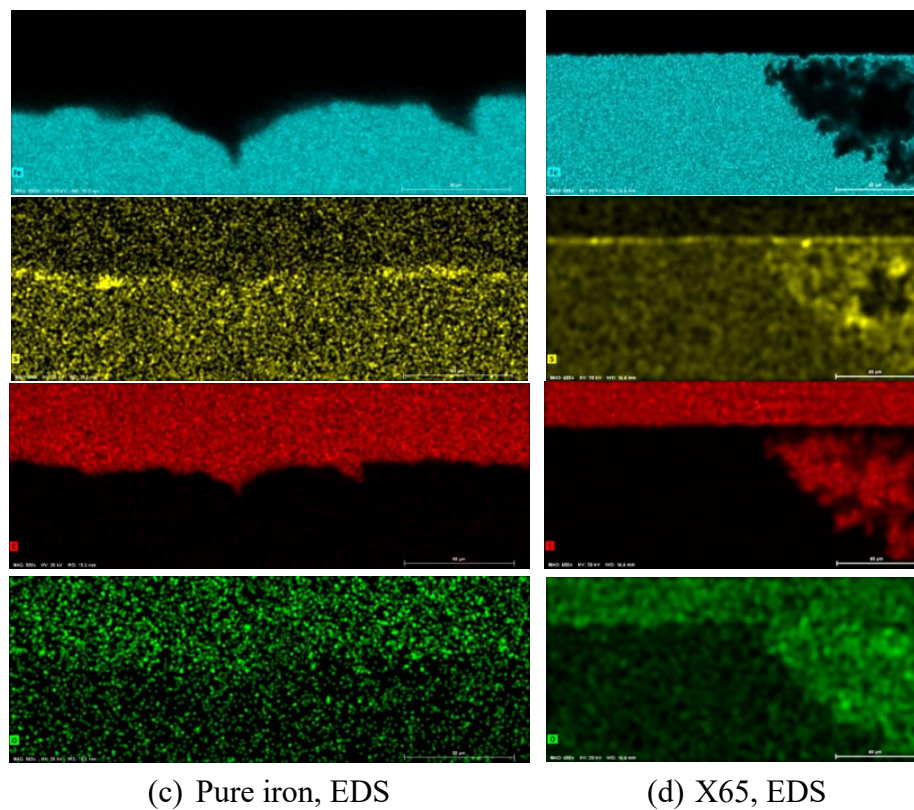
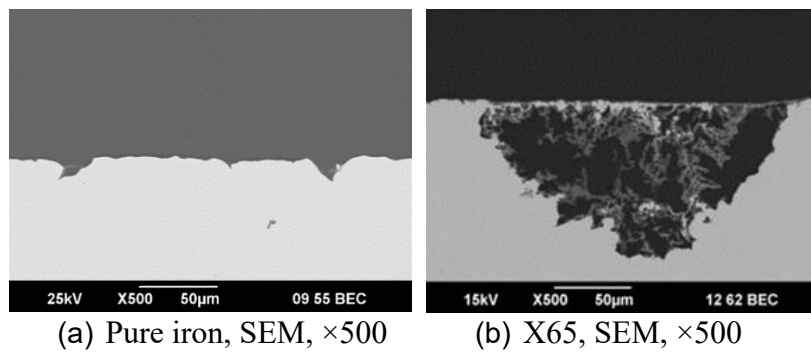


(b) Weight loss corrosion rate

Figure 53

The cross-section images by SEM backscattering and EDS mapping for the iron (blue), sulfur (yellow), carbon (red) and oxygen (green) element

(Pure iron/X65 carbon steel, 30 °C, pH5, $p\text{CO}_2 = 0.97$ bar, $p\text{H}_2\text{S} = 0.04$ mbar, 1 wt.% NaCl, 300 rpm stir bar, 7 days, $[\text{O}_2]_{\text{aq}} \approx 20$ ppb_(w))

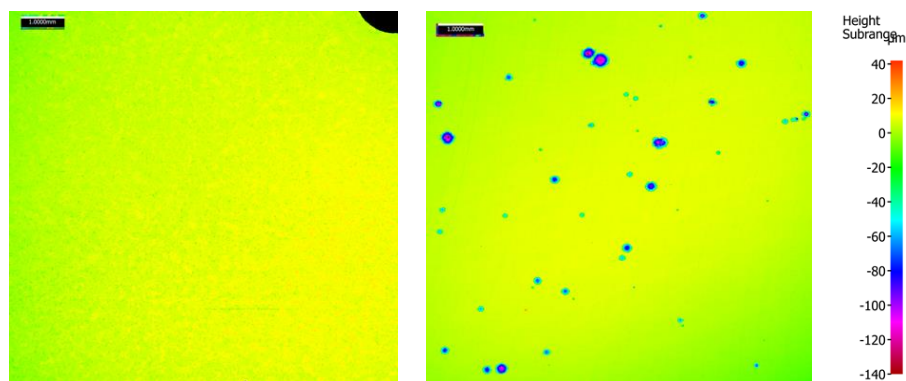


Surface profilometry images of X65 and pure iron specimens are shown in Figure 54. No pits were found on the entire surface of the pure iron specimen, although the experimental conditions were the same as for X65 steel, where severe pitting occurred. This is consistent with the existence of a thin FeS layer as seen in Figure 53, and the arguments presented above stating that for pitting to occur a damaged layer needs to be present on the metal surface.

Figure 54

Surface profilometry scanning images of specimens of X65 and pure iron specimens after 7 days exposure after corrosion product layer removed

(Pure iron/X65 carbon steel, 30 °C, pH 5, $pCO_2 = 0.97$ bar, $pH_2S = 0.04$ mbar, 1 wt.% NaCl, 300 rpm, $[O_2]_{aq} \approx 20$ ppb_(w))



(a) Pure iron

$CR_{WL} = 0.72 \pm 0.01$ mm/y

Pit density = 0 cm⁻²

(b) X65

$CR_{WL} = 0.82 \pm 0.22$ mm/y

PPR = 7.3 ± 0.10 mm/y

PR \approx 9

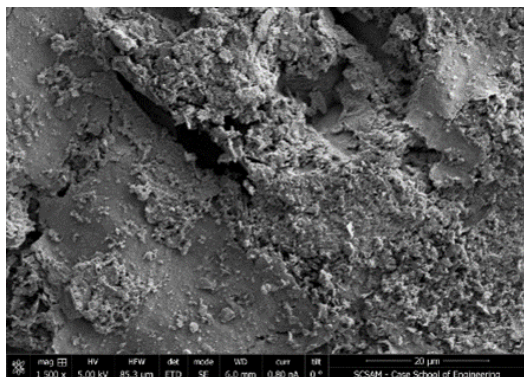
Pit density = 25.4 cm⁻²

For the pure iron case, no layer could be detected with SEM (Figure 53). However, a higher magnification analysis using TEM revealed the presence of a thin film. As shown in Figure 55, the layer found on the pure iron surface is broken and detached. A gap up to 1 μm can be seen between the substrate metal and the layer on more than 50% of the analyzed surface.

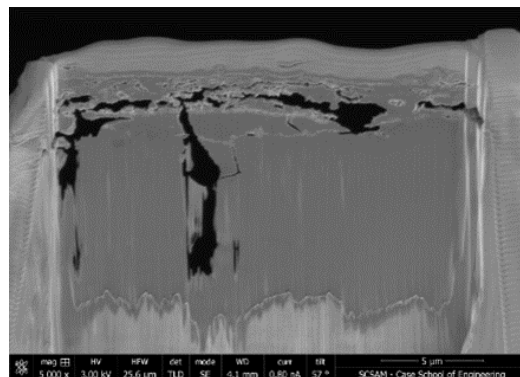
Figure 55

TEM images of the corroded pure iron specimen cross section cut out by FIB

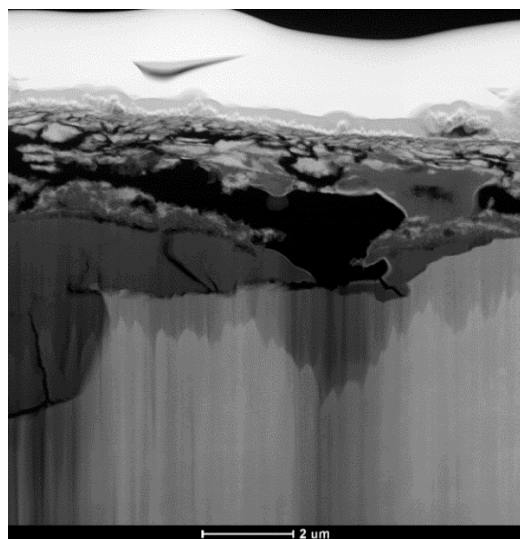
(30 °C, Pure iron, CO₂ = 0.97 bar, pH₂S = 0.04 mbar, pH 5.01 ± 0.01, 1 wt.% NaCl, 300 rpm, 7 days, [O₂]_{aq} = 20 ppb_(w))



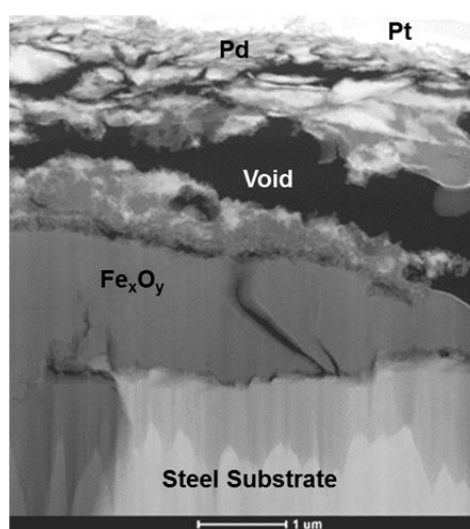
(a) Pure iron, top view, ×1500



(b) Pure iron, FIB, ×5000



(c) Pure iron, TEM, ×8500



(d) Pure iron, TEM, ×17000

TEM-EDS mapping results of the pure iron sample are shown in Figure 56. The presence of Fe, S and O could be clearly identified. However, the S element signal displays the same intensity on the substrate, the layer or the palladium layer. This could

be an indication that the S element content in the layer is extremely low. Besides that, the interface appears broken and many voids can be seen. These voids could have been created during the FIB cutting process and may not have been present during the experiments. It is quite likely that the layer was intact during the test since the general corrosion rate for pure iron, in this case, was lower than for X65, and since no pitting was observed on pure iron. Anyhow, the results indicate that the breakdown of this protective layer is related, to some extent, to the carbon content, alloying, and the microstructure of the steel.

Figure 56

TEM-EDS mapping results of pure iron sample

(30 °C, $p_{H_2S} = 0.04\text{mbar}$, $p_{CO_2} = 0.97\text{ bar}$, $pH\ 5$, 1 wt.% NaCl, 300 rpm, 7 days, $[O_2]_{aq} \approx 20\text{ ppb}_{(w)}$)

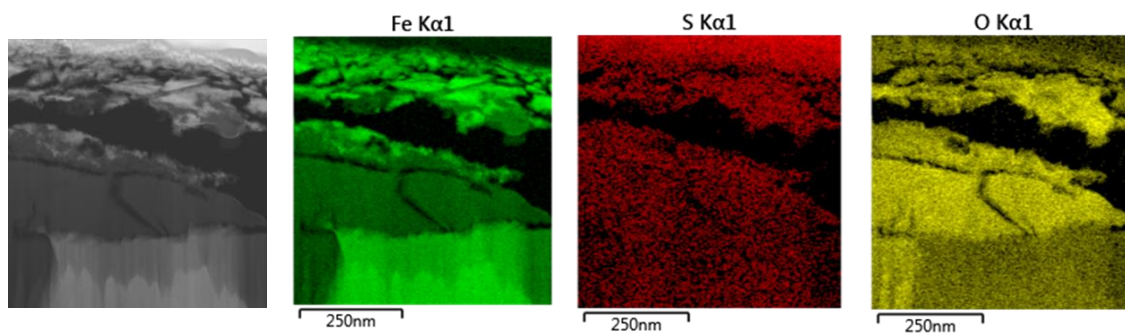


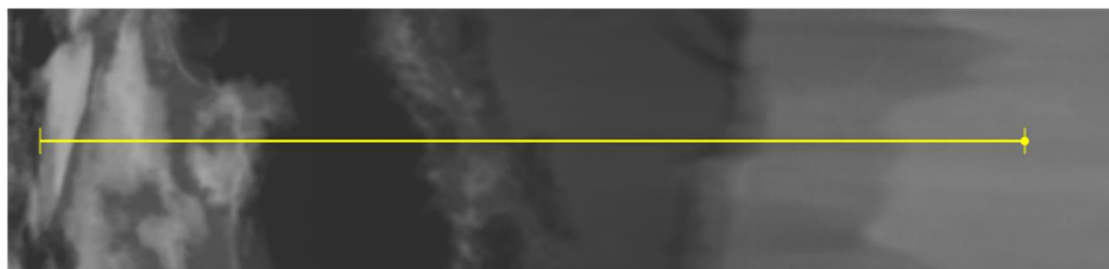
Figure 57 shows the line scan result of the pure iron specimen under TEM. Sulfur is detected, yet the signal for oxygen is stronger.

Figure 57

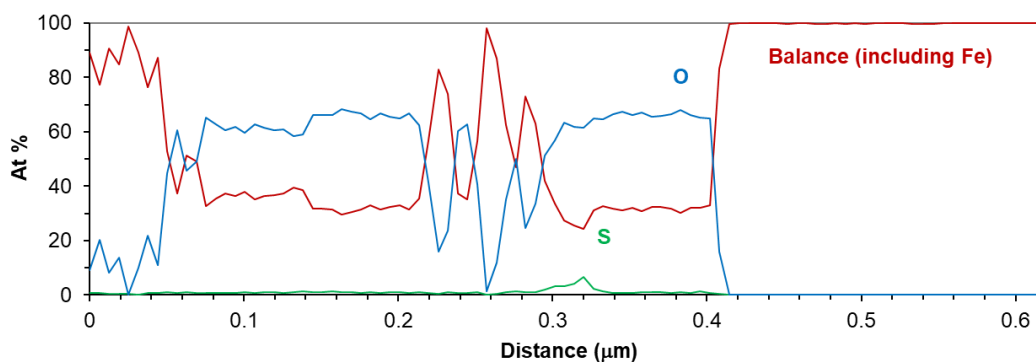
TEM-EDS line scan results of pure iron sample

(30 °C, $p_{H_2S} = 0.04\text{mbar}$ and $p_{CO_2} = 0.97\text{ bar}$, pH 5, 1 wt.% NaCl, 300 rpm, 7 days,

$[O_2]_{aq} \approx 20\text{ ppb}_{(w)}$)



Platinum	Corrosion Product Layer	Base metal
----------	-------------------------	------------



4.3.7 Effect of Time on Pitting

A longer-term experiment (14 days long) was run at the baseline condition, in order to investigate if the pitting would sustain with time. The SEM images of the corrosion product layers are shown in Figure 58. The surface profilometry images after the corrosion product layer was removed by Clarke solution are shown in Figure 59. These images clearly indicate that pits continue to grow over time, although the pits would tend to become shallow. The pits seemed to be partially filled with corrosion

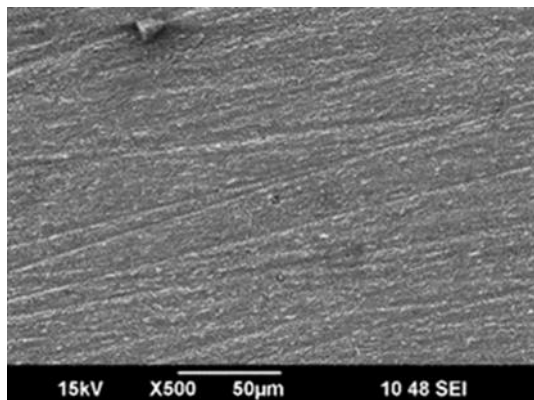
products. The corrosion product layer covered the pit at the early stage, then the layer would collapse and expose the pit. A single test is not enough to draw firm conclusions on the pitting density or pitting rate trends with time. However, the results show that the pitting rate after 7 and 14 days of exposure is about the same, indicating that the pitting corrosion was still very much active even after 14 days of exposure.

Figure 58

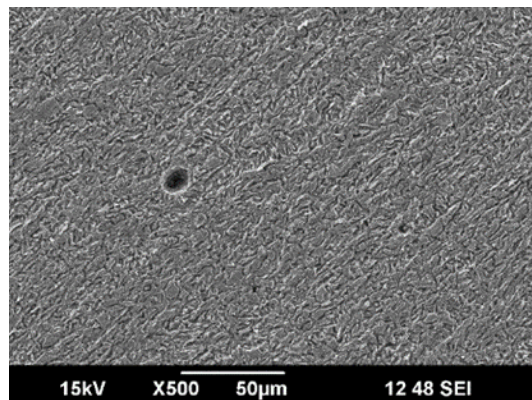
SEM images at different exposure time

(X65 carbon steel, 30 °C, pH 5.01 ± 0.01, pCO₂ = 0.96 bar, pH₂S = 0.04 mbar, 1 wt.%

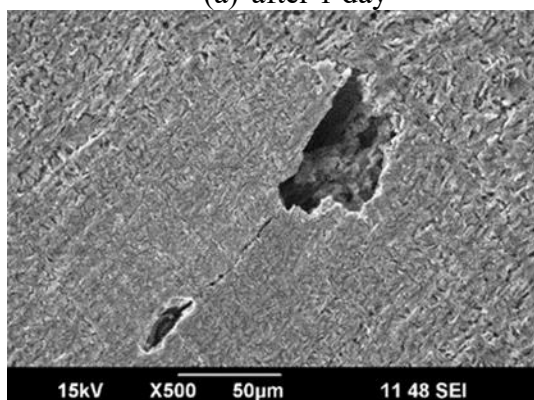
NaCl, 300 rpm, 7 days, [O₂]_{aq} ≈ 20 ppb_(w))



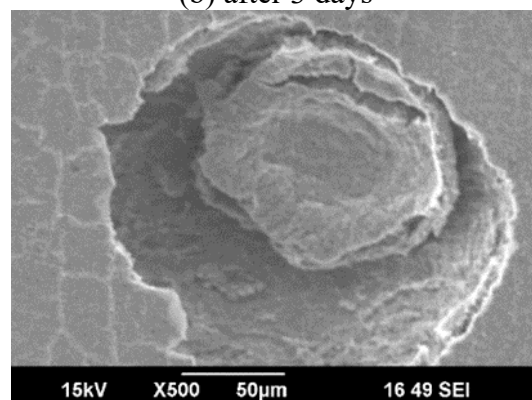
(a) after 1 day



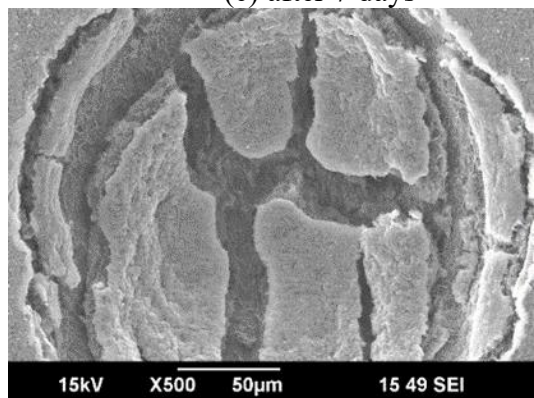
(b) after 3 days



(c) after 7 days



(d) after 10 days

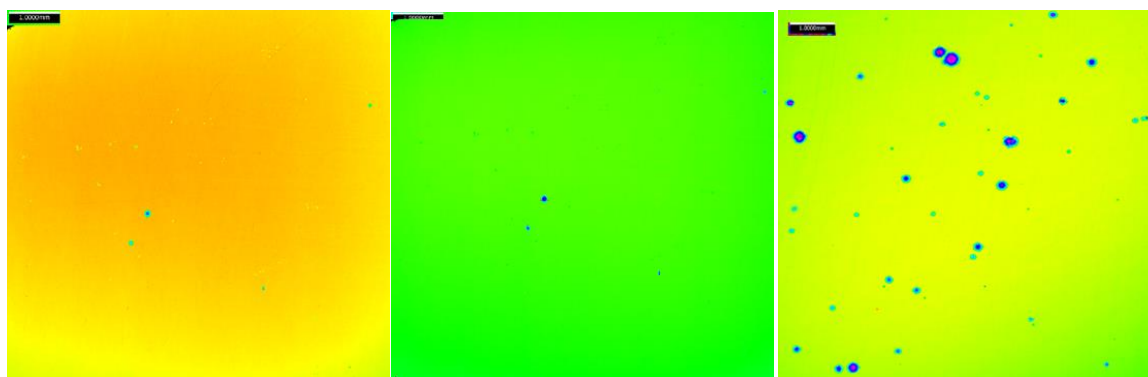


(e) after 14 days

Figure 59

Surface profilometry of steel surface after the layer was removed by Clarke solution at different exposure time

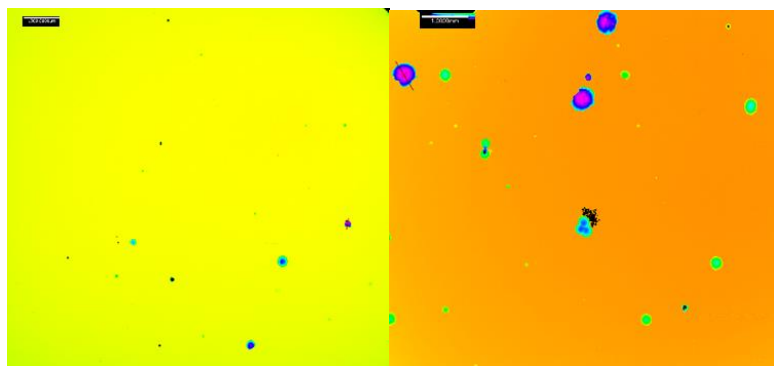
(X65 carbon steel, 30 °C, pH 5.01 ± 0.01 , $pCO_2 = 0.96$ bar, $pH_2S = 0.04$ mbar, 1 wt.% NaCl, 300 rpm, 7 days, $[O_2]_{aq} \approx 20$ ppb_(w))



(a) After 1 day,
PPR = 22.6 mm/y
Pit density = 18.6 cm^{-2}

(b) After 3 days,
PPR = 7.2 mm/y
Pit density = 2.48 cm^{-2}

(b) After 7 days,
PPR = 7.3 mm/y
Pit density = 25.4 cm^{-2}



(c) After 10 days,
PPR = 9.5 mm/y
Pit density = 8.06 cm^{-2}

(d) After 14 days,
PPR = 6.6 mm/y
Pit density = 13.0 cm^{-2}

4.4 Conclusions

The experimental results clarified the effect of particular parameters on the occurrence of pitting in marginally sour environments. The most severe localized corrosion was found at 30 °C, 0.04 mbar H₂S and 0.97 bar CO₂, pH 5, 1 wt.% NaCl, 300 rpm, 7 days, [O₂]_{aq} = 20 ppb_(w), which is referred to as the baseline condition hereafter.

Pitting was observed at the following conditions:

- a) H₂S partial pressures of 0.02 to 0.09 mbar (but not at 0 mbar and 0.15 mbar);
- b) CO₂ partial pressure of 0.53 to 0.97 bar (but not at 0 bar i.e. in pure H₂S solution);
- c) pH 4 and 5 (but not at pH6);
- d) 30°C only (but not 60 or 80°C);
- e) NaCl concentrations from 0 to 10%;
- f) On specimens containing a Fe₃C phase (but not on pure iron).

The partial pressure of H₂S and CO₂, pH, temperature, and ionic strength all can affect the saturation degree of the FeS in solution. Pitting only initiated when H₂S was present in this system and propagated only when CO₂ was present. These were proven by the fact that: 1) no pitting was found in CO₂ only experiments; 2) localized corrosion initiated but never propagated in the H₂S only experiments.

Chloride concentration was not found to be related to pit initiation as pitting was found in experiments at 0 wt.% of NaCl. However, the pitting density seemed to increase with increase in NaCl content, inferring a process controlled at least in part by galvanic coupling.

As summarized in **Table 12**, FIB-TEM, SAED, and PED analysis showed that a very thin layer of FeS, thought to be mackinawite, formed within the porous iron carbide network at the steel surface to retard general corrosion of the steel surface. Damage and breakdown of this thin FeS layer is hypothesized to lead to pit initiation. This finding, together with the observation that no pitting happened without CO₂, indicated that the pit propagated when the breakdown spots of the protective FeS layer were exposed to the H⁺ buffering effect conferred by H₂CO₃. Further pit propagation then followed due to galvanic coupling between the underlying steel and the conductive mackinawite corrosion product layer.

Table 12

A Summary of FIB-TEM analysis of the product layer of the selected conditions related to the occurrence of localized corrosion. Iron oxides was found together with sulfides in the layer. (30 °C, $pH_2S = 0.04$ mbar, $[NaCl] = 1$ wt. %, 7 days)

pH	5.0	5.0	6.0	5.0
pCO_2 /bar	0.97	0	0.97	0.97
WE material	X65 (carbide)	X65 (carbide)	X65 (carbide)	Pure Iron (no carbide)
Uniform or localized corrosion	Severe pitting	No pit	No pit	No pit
Layer thickness	100~200 nm	1 μ m	200-300 nm	> 1 μ m
Morphology:	Porous layers	Two-layer structure	Porous layers	Thick oxide layer
Phase identification	Amorphous FeS and Fe_xO_y	Inner Fe_xO_y rich layer, 500nm; Outer Fe_xS_y rich layer, 800nm	Inner part of the layer: $Fe_{0.91}S$; outer part of the layer: Fe_3O_4	Thick oxides layer

However, despite all the above enlightening findings, there were several questions yet to be answered. The origin and effect of oxides or oxyhydroxides discovered by TEM-SAED in this system need further investigation. Answers to these unexplained

observations could help to reveal the detailed pit initiation mechanism in marginally sour environments.

Chapter 5: Pit Initiation Based on the Oxidation of the Chemisorbed Iron Sulfide Layers

5.1 Introduction and Research Goals

“Marginally sour” or “slightly sour” environment [53, 93] features low temperature and a trace amount of H_2S . It has been reported that even a trace amount of H_2S in a CO_2 dominant environment (sweet) will decrease general corrosion rate by forming thin iron sulfide layers, but can increase the possibility of localized attack [93, 94]. Previous studies [93, 94, 130, 131, 153, 154] have shown occurrences of localized corrosion, but have not fully revealed the mechanism of this type of pitting attack. The ratio of H_2S and CO_2 partial pressures [155] has been used to define this transition between sweet and marginally sour environments. However, this description has its limitations [63] as the occurrence of localized corrosion is related to the water chemistry and the state of the steel surface, not just the composition of the gas phase. Alternatively, the surface saturation degree of FeS and $FeCO_3$ at the steel substrate surface should be considered [53, 93].

Localized corrosion is usually thought to initiate due to a localized failure of a protective layer formed on the steel surface. In general, the pit initiation mechanism remains fairly elusive, especially as it relates to how exactly the layer breaks down to induce pitting. For example, in O_2 containing systems, the effect of Cl^- is observed as an important detrimental factor in the breakdown of passive layers. According to Strehblow [73], there are three major interpretations of passive layer breakdown, all involving the effect of chloride ions: the penetration mechanism (diffusion of anion and cation

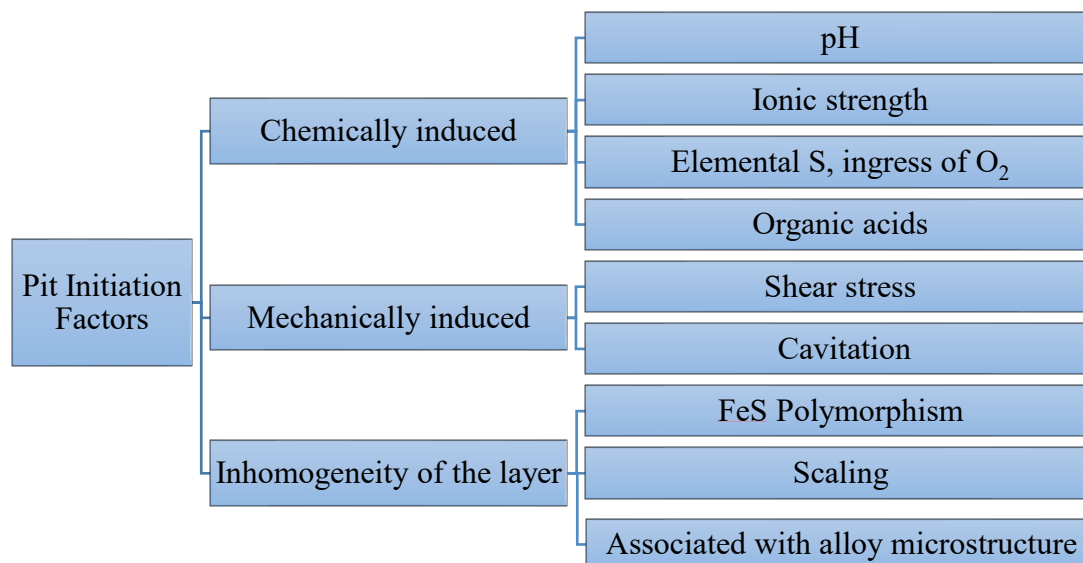
vacancies through the passive layer), the film breaking mechanism (microcracks produced by potential fluctuation), and the adsorption mechanism (the passive layer was dissolved by the complexation effect of aggressive ions such as SO_4^{2-}). However, the characteristics of most sour corrosion product layers differ greatly compared to passive films and different breakdown mechanisms must be considered.

In CO_2 dominated environments, the corrosion product layer is often comprised of a mixture of FeCO_3 , Fe_3C , and possibly iron oxides. FeCO_3 cannot be qualified as a passive layer as it is typically very thick (few microns). The formation of the layers in CO_2 corrosion could bring the open circuit potential higher ($\Delta E < 100$ mV) [140], but not as high as is typically the case in truly passive behavior. In addition, it has been hypothesized that the decrease in corrosion, accompanied by the formation of FeCO_3 , is due mostly to the formation of a thin (few nm) iron oxide layer between the steel substrate and the FeCO_3 crystals [140]. This so called “pseudo-passive” layer, provides protection on uniform corrosion. Localized corrosion may initiate if the oxide layer coverage is not uniform. However, the relationship between potential and occurrence of pitting, typical of stainless steel for example, is not observed in CO_2 corrosion [140]. Therefore, there is no “critical potential” in CO_2 localized corrosion driving the initiation of localized corrosion. Mechanical damage of the layer could lead to pitting and has been attributed to the effect of fluid flow shear stress [121, 156] and erosion [157]. However, it was found that except for cavitation, the shear force of the fluid flow is never high enough to damage an FeCO_3 layer [121]. Sun attributed the observation of damage to an FeS layer to internal stresses and the initiation to the microcracks within the corrosion

product layer [4]. However, the reported case cannot be applied in a wider scope because microcracks and defects are common in these precipitated layers, but pitting is not always there. An incompletely generated layer, a partially dissolved layer, or a broken layer (by intrinsic stress or external mechanical forces) could be explanations for pit initiation. The characteristics of an incompletely generated layer or a partially dissolved layer is governed by local water chemistry. In CO₂ environments, the “grey zone” theory describes how such damages in the layer can develop and how localized corrosion can be initiated [6, 49]. The factors that can lead to localized corrosion of mild steel in H₂S/CO₂ environments are summarized in **Figure 60**.

Figure 60

Factors that can lead to localized corrosion of mild steel in H₂S/CO₂ environments



Chapter 4 described the parametric study performed to identify the key parameters controlling the occurrence of pitting in marginally sour environments [53]. The baseline condition, for which severe pitting occurred, was selected at 30°C, pH 6.00 ± 0.01, 0.97 bar CO₂, 0.04 mbar H₂S, 300 rpm stir bar, O_{2(aq)} ≈ 20 ppb_(w), 7 days. A very thin layer of FeS thought to be mackinawite, formed within the porous iron carbide network of mild steel to retard general corrosion. Although the bulk aqueous environment was not saturated with respect to FeS, it was postulated that this layer formed by precipitation that occurred because of a higher saturation of iron sulfide within the porous iron carbide structure. This was due to water chemistry being inherently different close to an actively corroding surface. The surface characterization of the specimen surface after the experiment revealed that the corrosion product layer was a porous 100~300 nm layer of iron sulfides and iron oxides (FIB-TEM, **Figure 35**). SAED showed the phases in question to be mackinawite (FeS) and magnetite (Fe₃O₄). However, the existence of the oxide was not expected since O₂ content was thought to be very low (O_{2(aq)} ≈ 20 ppb_(w)).

Limited research has been reported on the effect of oxygen on CO₂ corrosion [158, 159]. In the presence of CO₂ (pCO₂ > 0.5 bar) but without H₂S, ingress of oxygen below 100 ppb_(w) in the aqueous phase is commonly reported to have a negligible effect on general or localized corrosion. Noticeable effects are only observed with a dissolved O₂ content above 1 ppm_(w) [158, 159]. More broadly, the formation of oxides in the absence of O₂ (or with only traces of O₂ present) has been observed by FIB-TEM underneath a FeCO₃ layer in a CO₂ environment. The formation of this oxide layer was accompanied by an increase in potential [140] and very high surface pH (pH 8) [48]. The

pH near the steel surface was much higher than that in the bulk solution because the FeCO_3 corrosion product layers served as the mass transfer barrier. This oxide was proposed to be formed due to high pH value near the steel surface, not due to the dissolved O_2 . This discontinuous character of the iron oxide layer was related to the initiation of localized corrosion in CO_2 environments.

In high-temperature H_2S environments, magnetite has been reported to be always found underneath iron sulfide [60]. It was proposed that this magnetite was formed by a precipitation reaction between water and steel at high temperature (20), because the saturation degree of the Fe_3O_4 was much higher than for mackinawite at high temperature ($\sim 120^\circ\text{C}$). The outer side of the Fe_3O_4 layer was also reported to be converted partially into iron sulfide [109]. As partial pressure of H_2S increased, the outer layer was characterized as mackinawite, troilite, pyrrhotite, and pyrite [60]. The authors found that, at 25°C , no magnetite was detected and mackinawite was the only product of corrosion [60]. However, there was one piece of information missing: the oxygen ingress content was not monitored during the experiments. This said, the experiments were performed in a closed autoclave, so O_2 ingress could be expected to be minimal [60].

In the simultaneous presence of O_2 (ppm level) and H_2S , several oxidized sulfur-containing compounds can form [30, 31] that strongly influence uniform and localized corrosion. A number of research works deliberately blending a relatively large amount of oxygen (more than 500 ppm) into H_2S environments were performed to study the effect of oxygen on corrosion [30] and stress cracking [31]. Oxygen has been linked to the occurrence of localized corrosion and pH decreases in the aqueous solution in the high

H₂S pressure environments [30]. In relation to the oil and gas production industry, Crolet [29] warned that oxygen is detrimental in sour corrosion environments because of acidification effects.

For low temperature low H₂S concentration experiments, if any oxide was found together with sulfide, usually it was considered as an aftereffect from specimen handling and analysis. Since CO₂ and H₂S gases continuously flow into the test cell, the concentration of dissolved oxygen in the aqueous solution is thought to be kept at a minimum. Mackinawite was found to be vulnerable to oxidation in the air, especially in the presence of water [19], heat [74], and light [160]. Therefore, the oxides found are often considered as the product of mackinawite oxidation during material analysis. In the glass cell experimental setup, the O₂ concentration in the liquid phase was measured at a level between 20 to 40 ppb_(w). The presence of low levels of oxygen in the system was mainly due to the test apparatus (small leakage around o-rings) and procedure (specimen insertion and retrieval), which led to limited ingress of air. As mentioned above, in the presence of CO₂ (pCO₂ > 0.5 bar) but without H₂S, noticeable effects of O₂ contamination are only visible with dissolved O₂ content above 1 ppm_(w) [158, 159].

However, considering the high reactivity between H₂S and O₂, the presence of 20 to 40 ppb_(w) of O₂ in the aqueous phase may have a non - negligible effect, especially in marginally sour environments. In this section, a series of experiments was designed to investigate how O₂ content (≤ 40 ppb_(w)) can affect the corrosion process, how oxides can form on the steel surface, and what roles these oxides may play in localized corrosion initiation.

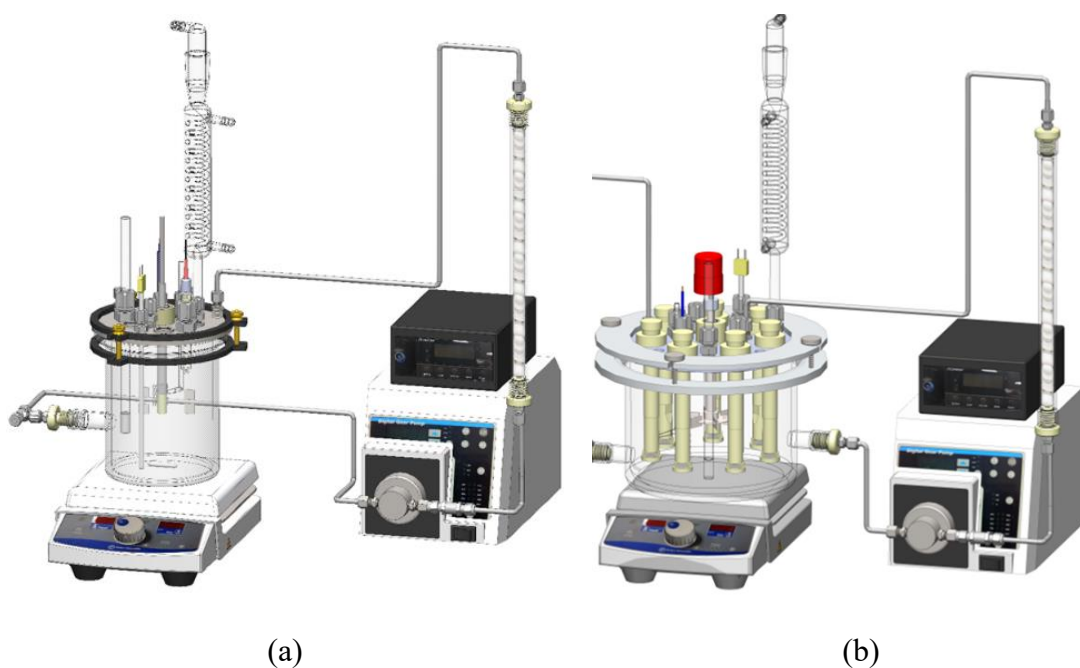
5.2 Experimental Procedure

Two kinds of testing apparatuses were used in this study – they are shown in Figure 61. Figure 61(a) shows the original reactor “type (a)” with rubber stoppers in the lid for hanging steel specimens using nylon line; this setup exhibited poor oxygen ingress control, with aqueous oxygen concentrations of around 20 ppb_(w). Figure 61(b) presents the updated reactor “type (b)” featuring ports on the lid, which enabled insertion and retrieval of specimens without risking O₂ contamination. This new design ensured that the concentration of O₂ in the aqueous phase could be maintained below 3 ppb_(w). Two different mixing elements were used: hanging specimens with stir bar agitated solution for the original reactor (type a), and fixed specimen holders with central rotating impeller for the updated glass cell setup (type b). While the impeller glass cell system provided better control over the chemistry and mass transfer characteristics, the two experimental setups yielded comparable results in term of corrosion. Both types of the cells were connected to a H-type ion exchange column to bring down the pH value in the solution to the set value during the experiments [144]. However, this system was only capable of correcting increases in pH (not decreases). The (a) type cell was used in the experiments with [O₂]_(aq) ≈ 20 ppb_(w) or above, type (b) cell was used in the experiments with [O₂]_(aq) < 3 ppb_(w). Half square inch specimens made of API 5L X65 mild steel were used for corrosion testing in all the experiments. The chemical composition of the API 5L X65 steel is listed in Table 9.

Figure 61

Stable solution chemistry system for small scale lab test: (a) with hanging specimens and stir bar in a glass cell; (b) with fixed specimen holders and rotating impeller in a glass cell

(Images courtesy of Cody Shafer, ICMT)

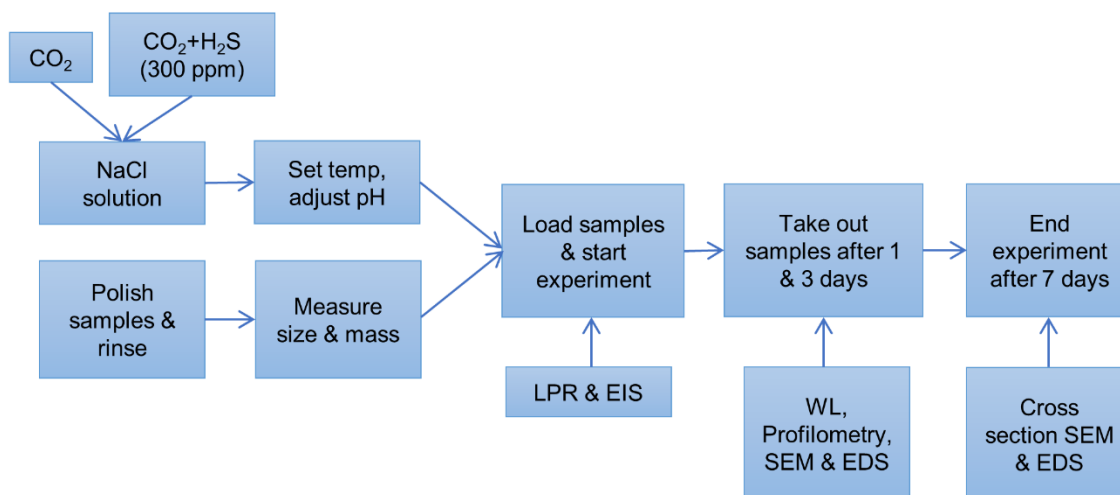


The experimental methodology is shown in Figure 62. The procedure for both types of reactors is similar. First, the 1wt.% NaCl electrolyte (pH was set to 5.01 ± 0.01) was sparged with CO₂ for over two hours, then with a mixture of H₂S and CO₂ for 30 minutes. This brought down the dissolved O₂ concentration in the system to the desired value. Four steel specimens were loaded to begin the corrosion experiment. Single specimens were retrieved after one day, three days and seven days of exposure for surface analysis by, on a select basis, scanning electron microscopy (SEM), energy

dispersive X-ray spectroscopy (EDS), surface profilometry (for pitting measurement), Raman microscopy, and focused ion beam-transmission electron microscopy (FIB-TEM).

Figure 62

Flow chart of experimental procedure



In order to investigate whether a trace amount of oxygen ingress would play a role in pitting in marginally sour environments, three experiments were conducted with dissolved oxygen concentration below 3 ppb_(w), at 20 ppb_(w), and above 20 ppb_(w). As listed in **Table 13**, the other environmental conditions were identical: 30°C, pH 5.01 ± 0.01, 0.97 bar CO₂, 0.04 mbar H₂S, 300 rpm stir bar, 7 days. The other conditions were chosen based on the previous parametric study [53] where the most severe pitting happened.

Table 13

Test matrix of the effect of various oxygen ingress concentrations

Temperature	30°C		
pH	5.0		
Material	API 5L X65		
P _{total}	1 bar		
P _{CO2}	0.96 bar		
P _{H2S}	0.04 mbar		
[O ₂] _(aq)	Between 40 and 20 ppb _(w)	≈ 20 ppb _(w)	< 3 ppb _(w)
Glass Cell Setup	Stir bar Type (a)	Impeller Type (b)	Impeller Type (b)

5.3 Investigation of the Origin of O₂ Ingress and the Formation of Oxides

In order for any iron oxides to form in the sour corrosion test, three scenarios were hypothesized:

- 1) The freshly polished steel surface could have been oxidized at the pre-processing stage, after the isopropanol and deionized water rinse but before loading into the glass cell.
- 2) The corrosion product layer, which formed during the experiment on the steel specimen, could have been oxidized after it was retrieved from the electrolyte and dried in the air before analysis.
- 3) Iron oxide could have formed in the liquid phase during the corrosion experiments.

A series of short experiments were designed to test each hypothesis. The corresponding method and results are listed together, considering each hypothesis, in Table 14.

Table 14

Possible explanations for the presence of oxides

Hypothesis	Testing Methodology	Observation/Comments
#1. The specimen was oxidized before loading in the glass cell.	Collect Raman spectra of the freshly polished and rinsed specimens.	No peaks observed, implying no attachment of any oxides to the steel surface. This hypothesis was refuted.
#2. The corrosion product layer was oxidized after specimen retrieval from the glass cell and drying.	XRD, XPS, FIB-TEM and Raman to analyze the possible oxidation of the layer.	Mackinawite is oxidized easily in the air. The oxidizing speed depends on the thickness of the layer. Specimen preservation is needed in material analysis.
#3. Iron oxides form during the corrosion experiments due to oxygen ingress into the system.	Oxygen level monitored at the outlet scrubber of the system; Use of <i>in situ</i> Raman flow cell and flow loop.	Mackinawite corrosion product layer can be oxidized by $[O_2]_{aq}$ during the corrosion experiment.

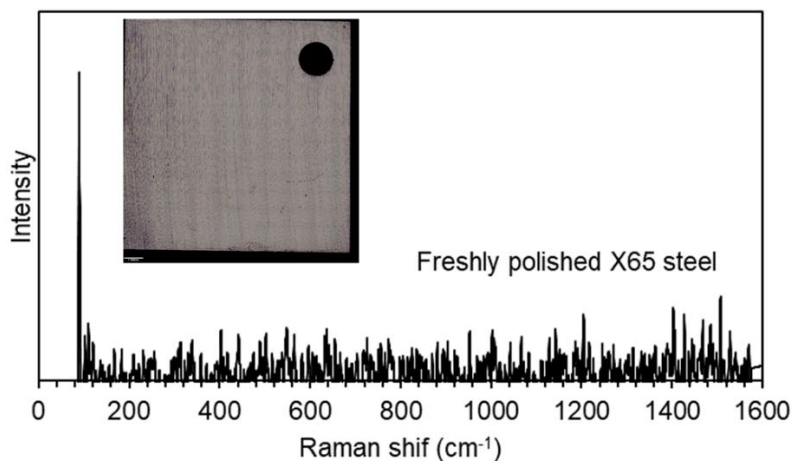
It must be noted that iron oxidized could also be generated without the presence of oxygen; rather, it is a redirect reaction between iron and water. Based on the thermodynamics, iron could react with water directly at high temperatures or high pH

[161]. As discussed in the introduction part, magnetite was found in high temperature and H_2S concentration environments, due to the higher saturation degree of Fe_3O_4 than any iron sulfides, as proposed by Gao et al [60]. However, when it comes to the baseline condition at 30 °C and pH 5 in this work, this possibility of direct reaction is small. That is why this possibility was not proposed in Table 14.

To challenge the first hypothesis in **Table 14**, a Raman spectrum was collected from the freshly polished and isopropanol / deionized water rinsed X65 steel specimen (Figure 63). The spectrum shows no oxides were present on the steel surface. This meant that no significant oxidation occurred before the steel specimen was loaded into the glass cell. Therefore, the first hypothesis was refuted.

Figure 63

No oxidation observed on freshly polished X65 specimen



To test the second hypothesis as shown in Table 14, a X65 specimen was immersed in a 1 wt.% NaCl electrolyte saturated with a gas phase of 0.97 bar CO₂ and 0.04 mbar H₂S at 30°C, pH 5, and agitated with a 300 rpm stir bar for 7 days. After the experiment, the specimen was retrieved from the glass cell, rinsed with deoxygenated deionized water, dried with a cold air blower, placed in a vacuum desiccator for about 5 minutes, and sealed in a nitrogen purged, gas-filled, and sealed plastic bag. The bag was not opened until it was ready for analysis on the Raman microscope platform. The first scan result is line (a) in Figure 64. Only two characteristic peaks for mackinawite [162] were detected, and the spectrum indicated no prominent sign of oxidation. After the first scan, another focus spot was selected, the second scan result after approximately 20 minutes exposure to air is line (b) in Figure 64. Besides mackinawite, characteristic peaks for magnetite were also detected. The only explanation for this change is that mackinawite was oxidized in the air [74]. Then, a different spot was selected and a third Raman scan was conducted after approximately 60 minutes exposure to air, which is shown by line (c) in Figure 64. Apart from mackinawite and magnetite, the third scan also picked up hematite, which is a further oxidation product of mackinawite. This analysis shows that mackinawite is very sensitive to oxidation in air in plain daylight [160] and especially under the high intensity laser of a Raman microscope.

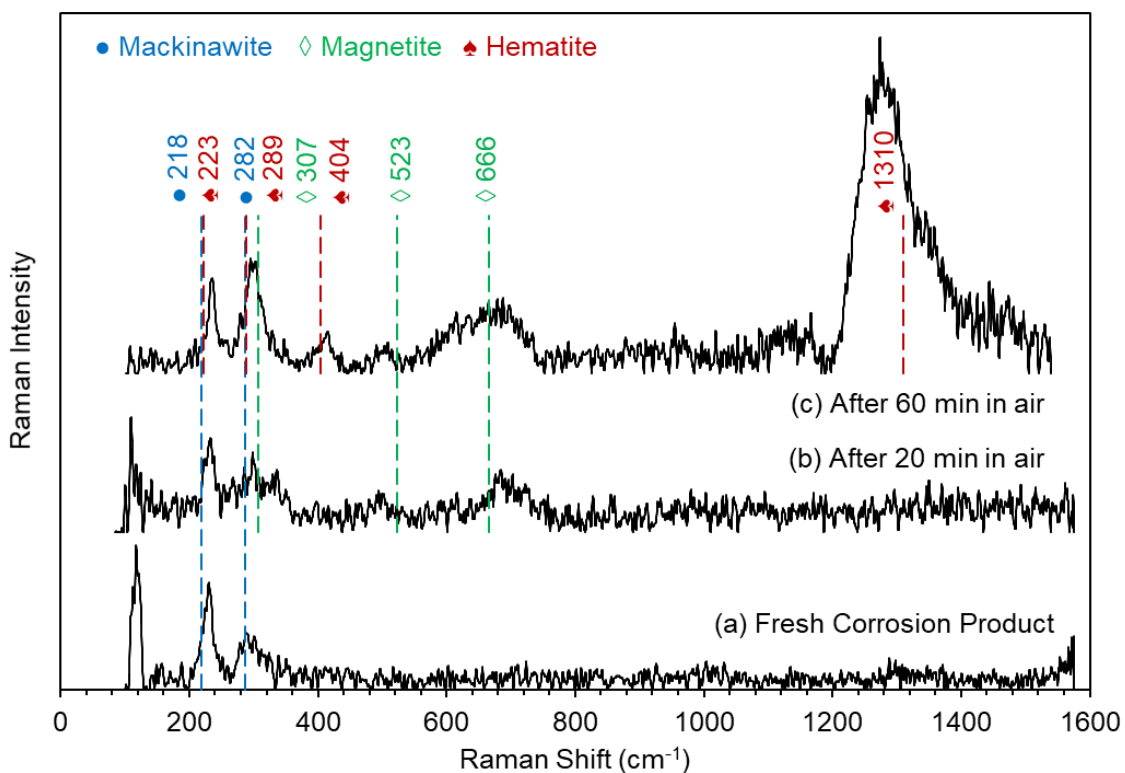
The extent of oxidation depended on the initial thickness of the FeS layer. In similar experiments, it has been noted that when the analyzed mackinawite layer was thinner than 100 nm, it had entirely turned yellow in color immediately after being retrieved from the glass cell. In the present case, the layer was thicker than 300 nm, so it

is suspected that not all the layer was yet oxidized, as shown in the Raman spectrum collected as line (a) in Figure 64. This observation confirmed that the second hypothesis in Table 14 is plausible: the magnetite identified by SAED with FIB-TEM in Figure 21 (d) and **Figure 35** (d) could be an oxidation product of mackinawite after exposure to air, in post-processing analysis.

Figure 64

Oxidation of mackinawite with time measured with a Raman microscope (laser excitation line 532 nm, power 25W)

The specimens were corroded at 30 °C, pH 5.01 ± 0.01, 0.97 bar CO₂, 0.04 mbar H₂S, 300 rpm stir bar, 7 days, [O₂]_(aq) ≈ 20 ~ 40 ppb_(w)).



In order to address the third hypothesis listed in Table 14, O₂ content in the aqueous phase was monitored continuously with an oxygen meter for the entire duration of the test (as opposed to the beginning and end of the test only, as is commonly done), as shown in Figure 65. The minimum O₂ content obtained for the best sealing case is listed in Figure 66. It was achieved using the updated type b 2-liter glass cell with the sampling ports as shown in Figure 61(b). The following observations could be made: (1) The initial two hours sparging with CO₂ or N₂, before injection of H₂S, decreased the dissolved O₂ content from 8 ppm_(w) to 3 ppb_(w); (2) during the seven days of testing, dissolved O₂ content could reach as low as 3 ppb_(w) even though CO₂/H₂S sparging was maintained; (3) loading/removing specimens (day 1, 3 and 7) through pulling specimens out from the sampling ports on the glass cell lid would lead to a temporary spike in dissolved O₂ up to 1 ppm_(w), slowly decreasing back to less than 3 ppb_(w) over a period of 20 minutes.

Table 15 shows some of the typical oxygen concentration in a glass cell reactor when a continuous gas flow of CO₂/N₂ with H₂S is sparged at ambient pressure at 30 °C. As shown in Figure 66, the minimum oxygen content achievable in the type b glass cell setup was [O₂]_{aq} = 3 ppb_(w). Using the type (a) glass cell setup, the minimum level was [O₂]_{aq} = 20 ppb_(w) of dissolved oxygen, especially in long term experiments (e.g., 7 days). [O₂]_{aq} = 8000 ppb_(w) is the dissolved oxygen level in the atmosphere with 20% of O₂ in the air. Considering the baseline conditions, the corresponding partial pressure of O₂ and H₂S are as follows: pO₂ = 7.92×10⁻⁵ bar (by oxygen meter) and pH₂S = 4×10⁻⁵ bar (by gas detector tube). Although the dissolved H₂S concentration is 3.75×10⁻⁶ mol/L, which is 100 times more than the dissolved oxygen (9.38×10⁻⁸ mol/L), oxygen was continuously replenished in the cell due to leakage.

Table 15

Oxygen concentration in the experimental setup

[O ₂] _{aq} /ppb _w *	[O ₂] _{aq} /(mol/L)	pO ₂ /bar	O ₂ gas content in the gas phase (ppm _v)
3	9.38×10 ⁻⁸	7.92×10 ⁻⁵	78
20	6.25×10 ⁻⁷	5.28×10 ⁻⁴	521
40	1.25×10 ⁻⁶	1.06×10 ⁻³	1042
8000	2.50×10 ⁻⁴	2.11×10 ⁻¹	208508

* 1 ppb_w = 1 ng/g

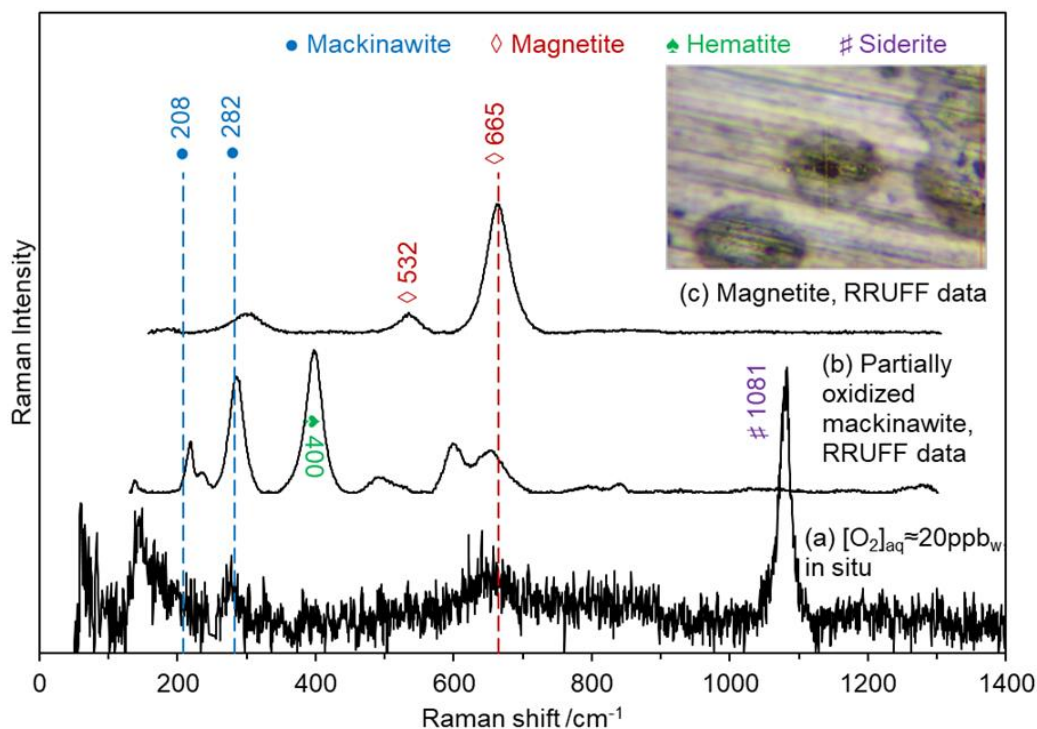
Only *in situ* observation of the oxidation of the FeS layer could prove that the presence of about 20 ~ 40 ppm_(w) of dissolved oxygen in solution was enough to alter the corrosion product layer during an experiment. For that purpose, a specially designed cell was developed for *in situ* Raman spectroscopy analysis. Details of the *in situ* Raman cell design are shown in chapter 7 and only the results are discussed here. **Figure 67** shows the experimentally acquired Raman spectrum of the corrosion product obtained *in situ* [spectrum (a)], the standard curve of oxidized mackinawite (FeS) [spectrum (b)], and the standard curve of magnetite (Fe₃O₄) [spectrum (c)]. The results confirmed that, under baseline condition with 20 ~ 40 ppb_(w) of dissolved oxygen, the corrosion product layer was made of mackinawite that was partially oxidized into magnetite. A peak corresponding to the carbonate group was also identified and likely corresponds to the presence of siderite (FeCO₃). This finding confirmed that the oxidation of mackinawite product layer into iron oxide, due to the presence of 20 ~ 40 ppb_(w) of dissolved oxygen, can occur in sour corrosion experiments.

Consequently, the presence of oxides in the corrosion product layer composition can be explain by *in situ* as well as *ex situ* (post processing) oxidation of mackinawite corrosion product layer.

Figure 67

In situ Raman spectroscopy analysis: direct proof of oxidation of mackinawite into magnetite in the aqueous solution on a corroding surface

(Baseline condition with $[O_2]_{aq} = 3\sim 20\text{ ppb}_{(w)}$, after 4 days)



While these preliminary results provided insight on the possible source of O_2 contamination, a more thorough and systematic study, performed in well-controlled environments, was warranted to differentiate the effects of trace amounts of O_2 present during the experiments, from the inevitable exposure to air in specimens post-processing.

5.4 Effect of Various Oxygen Concentrations

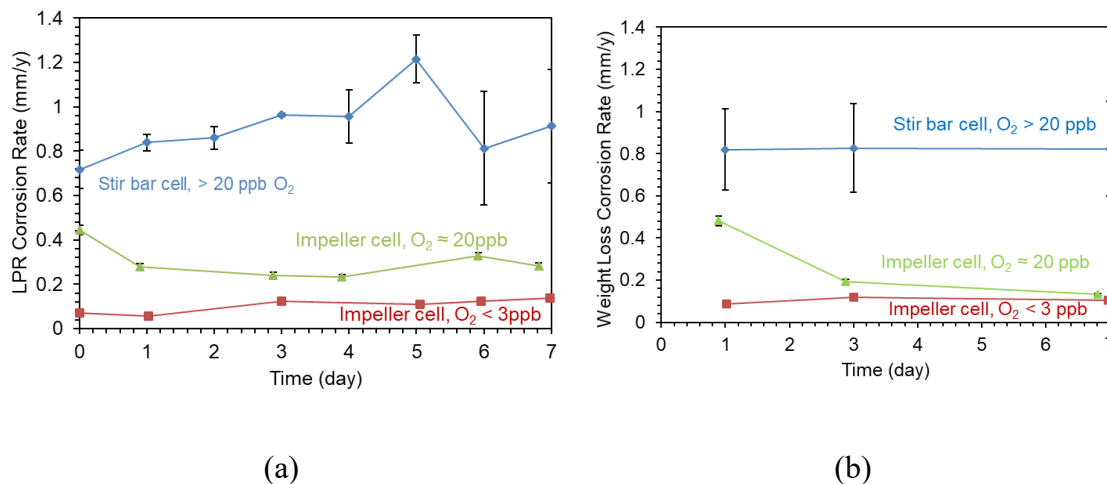
The preliminary results, presented above, seem to indicate that even traces of O₂ present during a test can influence both general and localized corrosion in marginally sour environments. To clarify this scenario, a series of experiments (Table 13) were designed and conducted in the improved setup (Figure 61b), enabling better control of O₂ concentration in the aqueous phase. The results present the core of the discussion about this work.

Linear polarization resistant (LPR) and weight loss corrosion rates obtained from these three experiments are compared in Figure 68. The general corrosion rate decreased as the oxygen concentration decreased. The basic mechanism of H₂S corrosion, without oxygen, dictates that H₂S should adsorb on the steel surface to form a chemisorbed FeS layer – S_{ads}(Fe) [24]. More mackinawite could precipitate but only if the surface saturation value, S(FeS), exceeds unity [5]. In the presence of less than 3 ppb_(w) dissolved O₂, it is thought that the low corrosion rate (0.1 mm/y) was due to the protectiveness of the FeS chemisorbed layer since the FeS surface saturation never exceeded unity. However, for the experiment where around *ca.* 20 ppb_(w) of oxygen was maintained, the general corrosion rate was higher than the <3 ppb_w case (0.3 mm/y). The corrosion rate reached 0.9 mm/y when the oxygen ingress level is 20~40 ppb_w. This experimental observation suggested that the chemisorbed FeS layer, assuming it is unaffected by the presence of dissolved oxygen, provides most of the protection against corrosion. For comparison, similar conditions but without H₂S would yield a corrosion rate of 2~3 mm/y.

Figure 68

Linear polarization resistance (a) and weight loss (b) corrosion rate

(The specimens were corroded at 30 °C, $pH = 5.01 \pm 0.01$, $pCO_2 = 0.97$ bar, $pH_2S = 0.04$ mbar, 300 rpm stir bar, 7 days.)



With less than 3 ppb_(w) of dissolved O₂, TEM analysis in Figure 69 and Figure 70 shows that there was no visible layer at the surface after the 7 day corrosion test. Figure 70 shows the Pt (orange) and Pd (green) plated layers on top of the steel surface (red). Figure 70 also shows that there was no oxygen (blue) or sulfur (purple) near the surface. The presence of sulfur was detected but at the wrong location – above the Pd plated layer, which is obviously a mischaracterization and should be disregarded. The most plausible explanation for the low corrosion rate obtained in O₂ < 3 ppb_(w) condition is the presence of an extremely thin chemisorbed FeS layer protecting the surface.

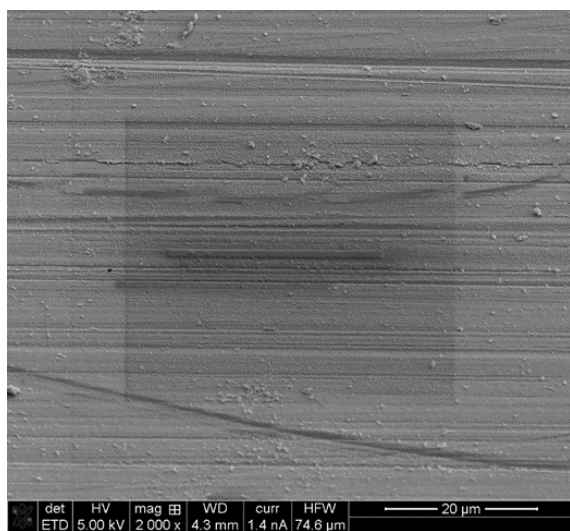
In the presence of dissolved O₂ from 20 ppb_(w) to 40 ppb_(w), this chemisorbed layer could have been damaged, leading to higher corrosion rates. In turn, the release of

Fe^{2+} increased the FeS surface saturation leading to the precipitation of a much thicker (100~300 nm) layer of FeS that could then be partially oxidized, as shown in **Figure 21** (d). The corrosion mechanism and layer formation process in the presence of oxygen seem significantly more complex. The initial chemisorbed FeS layer may have been damaged by reaction with O_2 , leading to exposure of the underlying metal and severe pitting corrosion. Once the chemisorbed FeS layer was damaged, the rate of metal loss was driven by the presence of corrosive CO_2 . As a consequence, the increased corrosion rate led to an increase in pH and in FeS saturation level, then eventually to further precipitation of mackinawite that was unprotective.

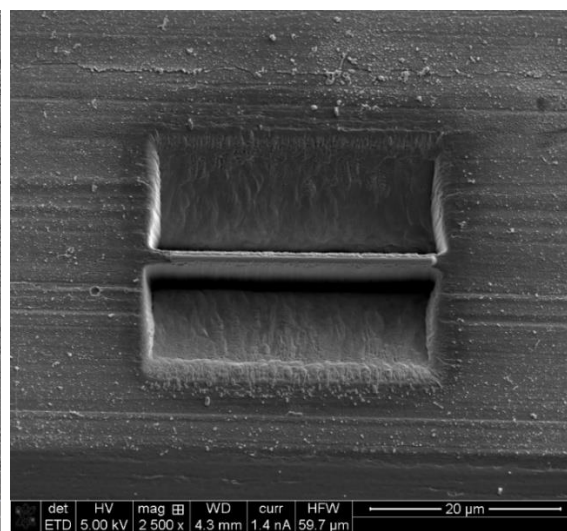
Figure 69

FIB-TEM analysis of the corroded specimen with dissolved oxygen concentration less than 3 ppb_(w)

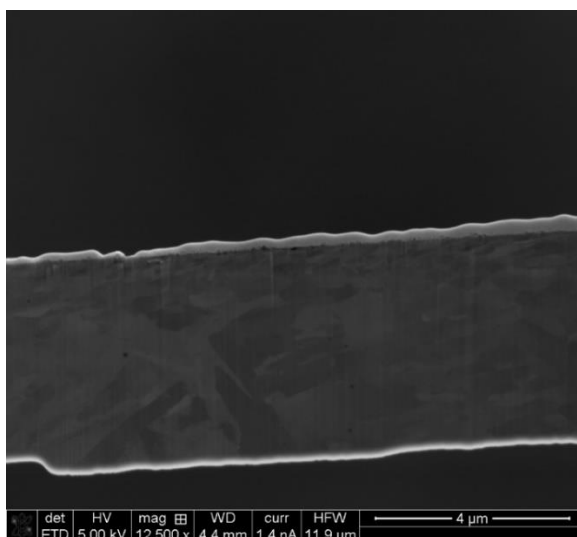
(The specimens were corroded at 30 °C, pH5, 0.97 bar CO₂, 0.04 mbar H₂S, 300 rpm stir bar, 7 days, [O₂]_(aq) < 3 ppb_(w).)



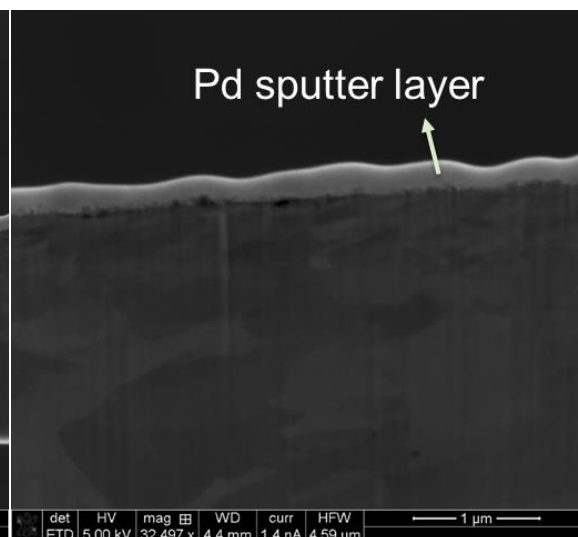
(a) Surface morphology of the corroded specimen



(b) FIB cutting



(c) TEM cross section image

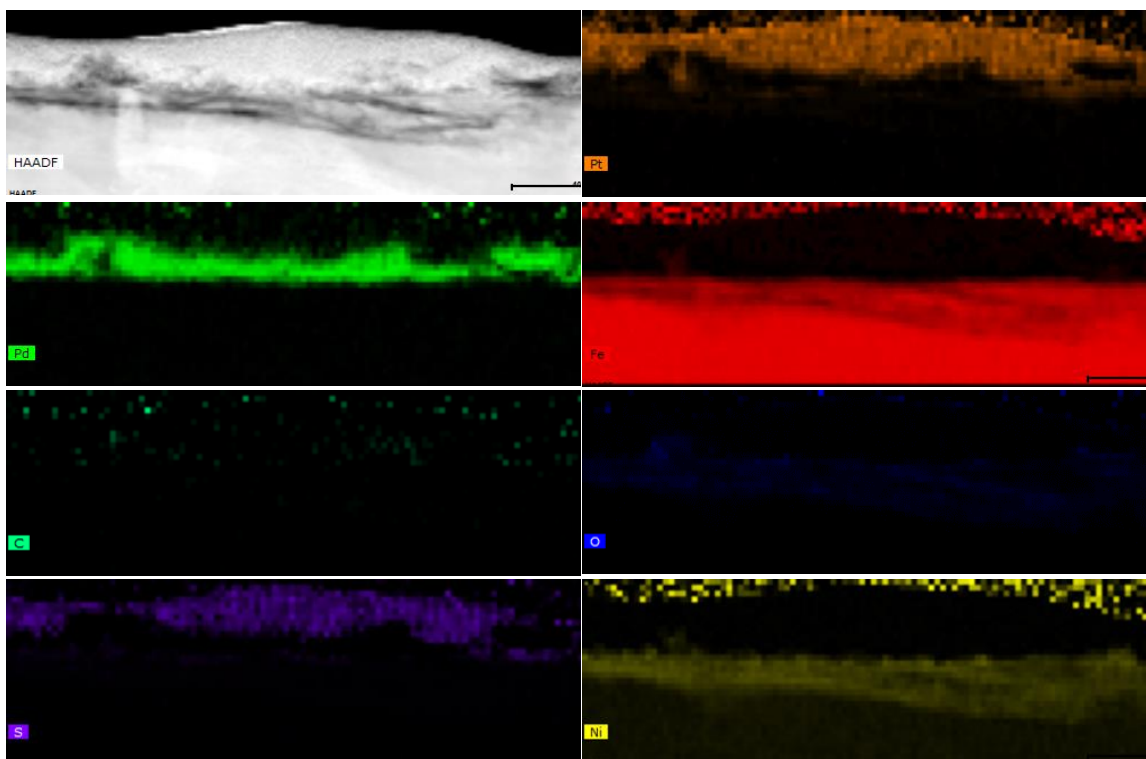


(d) TEM image with high magnification

Figure 70

TEM-EDS analysis of the corroded specimen with dissolved oxygen concentration less than 3 ppb(w)

(The specimens were corroded at 30 °C, pH5, 0.97 bar CO₂, 0.04 mbar H₂S, 300 rpm stir bar, 7 days, [O₂]_(aq) < 3 ppb_(w).)



In the conditions where $[O_2]_{aq} < 3 \text{ ppb}_{(w)}$, it is important to mention that no visible corrosion layer could be detected (Figure 69). Efforts were made to confirm that a thin chemisorbed FeS layer could form on the steel surface. These efforts centered around the use of Pourbaix diagrams since experimental detection of chemisorbed layer using standard microscopy tools is difficult even with highly specialized equipment. The Pourbaix diagram (E-pH), shown in Figure 71, was drawn considering both

chemisorption and precipitation reactions based on literature data [24]. The large light blue area represents the domain of stability of chemisorbed $S_{ads}(Fe)$. The small rectangle overlain on the diagram represents the actual experimental conditions of the baseline test (steel specimen OCP of 400~440 mV vs. SHE and pH = 5.00~5.10). The location of this baseline condition is outside the stability domain of mackinawite (grey-colored zone in the diagram). However, the baseline conditions do fall within the domain of stability of chemisorbed $S_{ads}(Fe)$. It is hypothesized that the presence of this chemisorbed $S_{ads}(Fe)$ film is enough to decrease the corrosion rate to 0.1 mm/y with 0.00004 bar H_2S in 1 bar CO_2 . The thermodynamic calculation results seem to agree with the experimental observations. The main reactions applicable to the system are displayed below [24]:

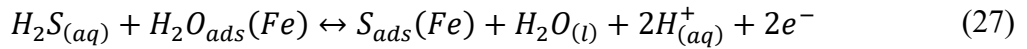
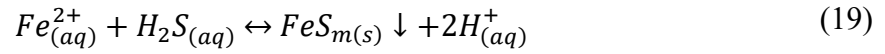


Figure 71

Fe-S-H₂O Pourbaix diagram at 298.15 K considering chemisorbed layers, excluding the pyrite phase

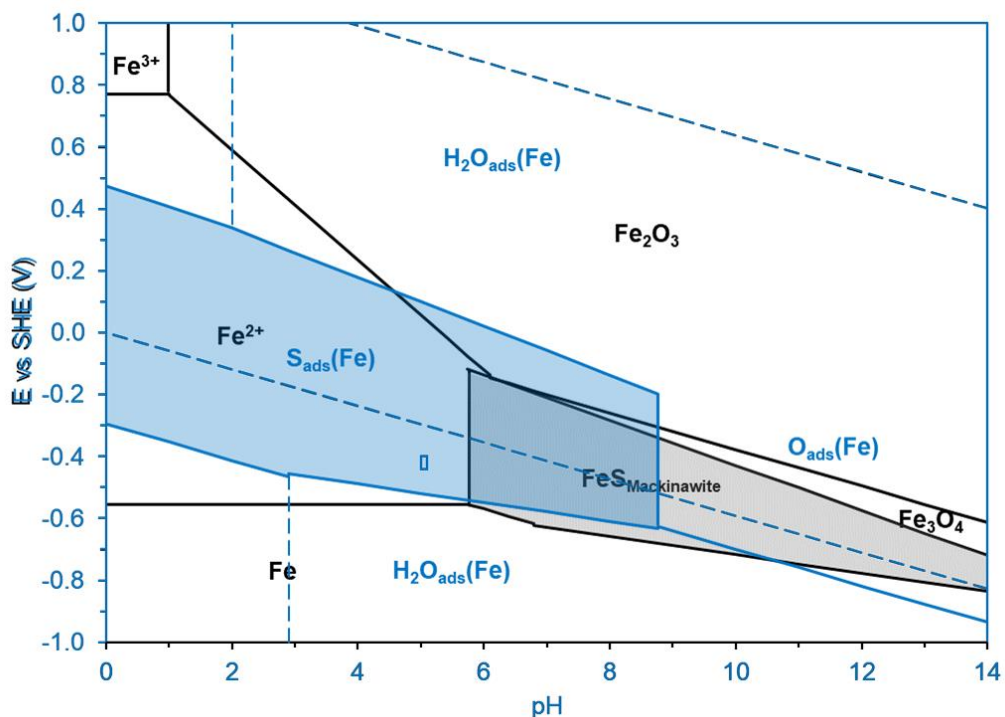


Figure 72 shows the surface profilometry of the corroded specimens after the corrosion product layers were removed by Clarke solution [163]. Figure 72 (a) shows high pitting density and high pit penetration rates with $[O_2]_{(aq)} > 20 \text{ ppb}_{(w)}$. Figure 72 (b) ($[O_2]_{(aq)} \approx 20 \text{ ppb}_{(w)}$) shows lower pitting density (although the absolute density value is still high considering that the total area is as small as 1.6 cm^2) and similar pit penetration rate compared with Figure 72 (a) ($[O_2]_{(aq)} > 20 \text{ ppb}_{(w)}$). Figure 72 (c) ($[O_2]_{(aq)} < 3 \text{ ppb}_{(w)}$) shows no pitting at all.

In summary, localized corrosion became a severe risk when oxygen concentration was higher than or equal to 20 ppb_(w) [O₂]_(aq) in marginally sour environments. In other words, only the “oxygen - free” ([O₂]_(aq) < 3 ppb_(w)) condition was able to eliminate the risk of pitting in marginally sour environments. It should be noted that the corrosion product layer became thinner as the oxygen concentration decreased. In the oxygen-free condition ([O₂]_(aq) < 3 ppb_(w)), it seems that there was no corrosion product layer formed at all. However, it has been documented that H₂S, unlike H₂CO₃, can be chemisorbed very easily onto the steel surface in aqueous solution [24]. The presence of this nanometer thick chemisorbed layer explains why the general corrosion rate was low, even if no layer could be visually detected on the steel surface (Figure 69 and Figure 70) when the oxygen content was less than 3 ppb_(w). It is somewhat counterintuitive, albeit well documented, that such a thin mackinawite layer (much less than 100 nm or only several layers of molecules) could decrease the general corrosion rate from 2 ~ 3 mm/y (in H₂S free environment) to about 0.1 mm/y. In addition, this layer seems to be very sensitive to even a trace amount of oxygen (more than 3 ppb_(w)). It can thereby be postulated that oxygen partially oxidized the metastable S_{ads}(Fe) layer, leading to inhomogeneities in the layer, and ultimately causing the occurrence of pitting. The exposed bare steel locations were then exposed to the corrosive aqueous CO₂ environment at pH 5. A typical corrosion rate in this condition but without H₂S should be 2 ~ 3 mm/y, which is similar to the pitting corrosion measured on the steel specimens.

Figure 72

Surface profilometry image after layer removal. (the specimens were corroded at 30°C, pH 5.01 ± 0.01, 0.97 bar CO₂, 0.04 mbar H₂S, 300 rpm stir bar, 7 days)

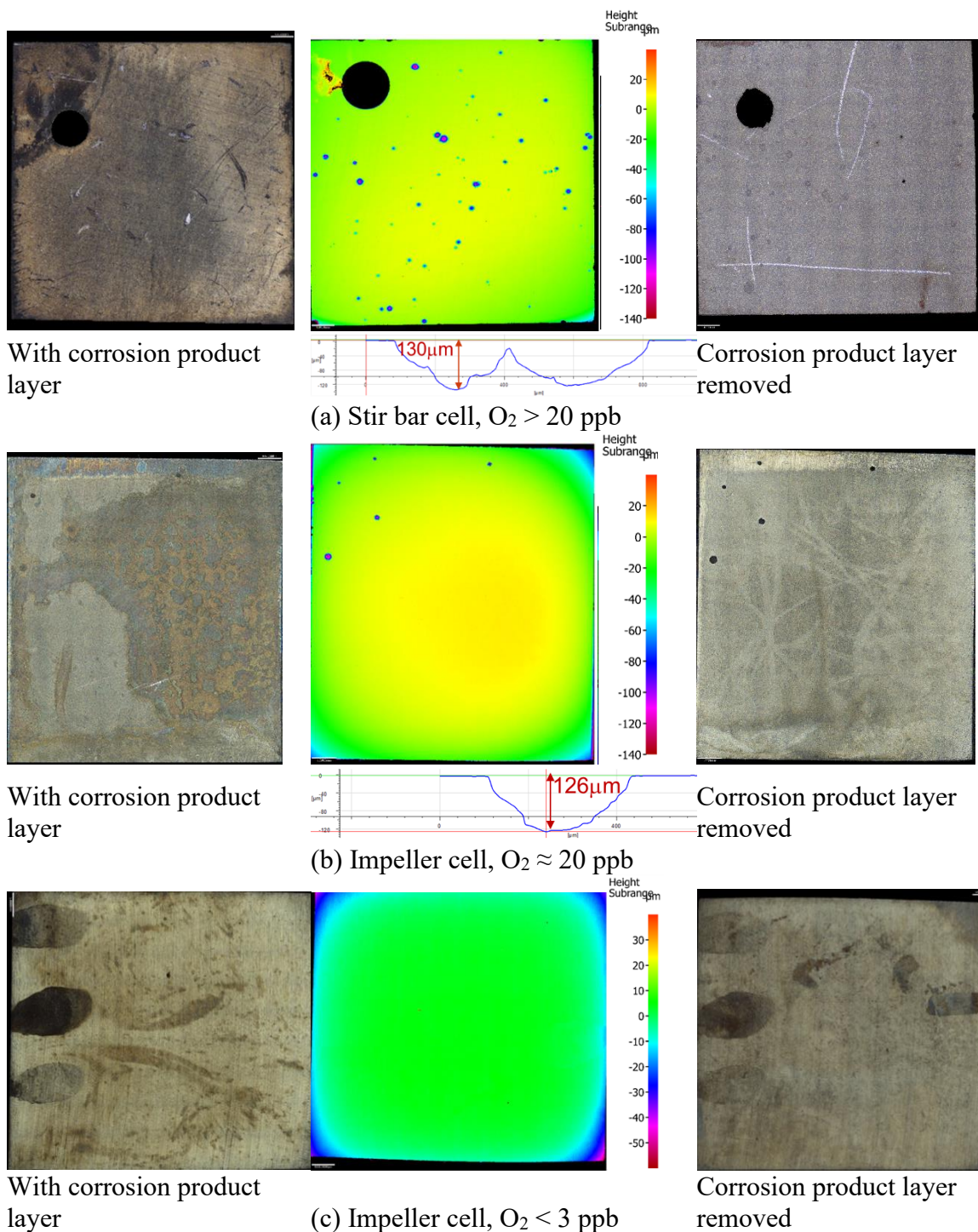
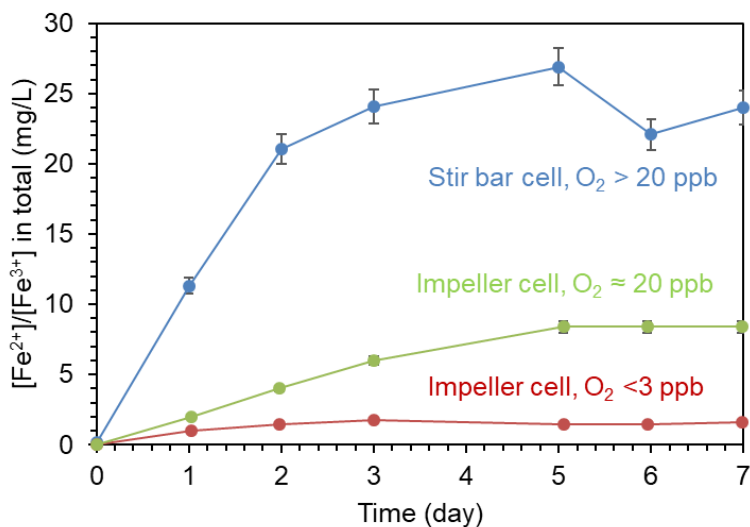


Figure 73 shows the ferrous ion concentration measurements at different oxygen concentrations. The general trend is that the dissolved iron concentration increased with the increased general corrosion rate, which was caused by the increase of oxygen concentration. It is important to mention that the spectrophotometry technique used to measure the iron ion concentration cannot discriminate between Fe^{2+} and Fe^{3+} and that the measurement result should be interpreted as the total dissolved iron ($[\text{Fe}^{3+}] + [\text{Fe}^{2+}]$) in the solution.

Figure 73

The change of total amount of $[\text{Fe}^{2+}]/[\text{Fe}^{3+}]$ with time

(The specimens were corroded at 30 °C, $\text{pH} = 5.01 \pm 0.01$, $\text{pCO}_2 = 0.97$ bar, $\text{pH}_2\text{S} = 0.04$ mbar, 300 rpm stir bar, 7 days.)



Increases or decreases in pH are expected in corrosion experiments due to the release of Fe^{2+} or the precipitation of metal carbonates or sulfides. As mentioned earlier,

any change in pH was adjusted using the H-type exchange resin and this section discusses the tendency of the system to either increase or decrease the pH. Figure 74 shows that pH had a tendency to decrease with time when $[O_2]_{(aq)} < 3 \text{ ppb}_{(w)}$, although this tendency is reversed when $[O_2]_{(aq)} \approx 20 \text{ ppb}_{(w)}$. As mentioned previously in the experimental setup section, the H-type ion exchange resin column could only decrease (not increase) the pH of the solution. Therefore, deoxygenated Na_2CO_3 solution was injected into the system through a syringe to bring the pH back to near 5.0 when necessary, so that corrosion rates at different O_2 concentration but the same other experimental conditions remained comparable.

Multiple reactions govern the pH in this system: 1) electrochemical reaction involving Fe and H_2S to produce Fe^{2+} and HS^- which tend to increase pH; 2) precipitation of FeS releases H^+ ; 3) direct reduction of O_2 at the cathode consumes H^+ ; 4) oxidation of H_2S by O_2 into sulfite [31], thiosulfate [29], or even sulfate [31] producing H^+ ions in this process (through a process that might involve metal cations as a catalyst [27, 28]).

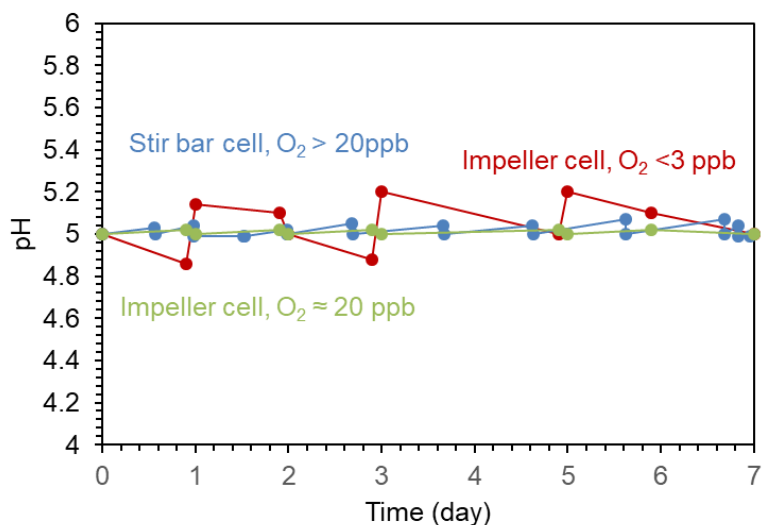
Apparently, there is no simple linear relation between pH and O_2 content. It is important to mention that the extent of H_2S oxidation occurring in these sets of experiments is still a speculation at this stage. It is the subject of investigation presented in Chapter 6.

Figure 74

pH changes with time

(The specimens were corroded at 30 °C, 0.97 bar CO₂, 0.04 mbar H₂S, 300 rpm stir bar,

7 days.)



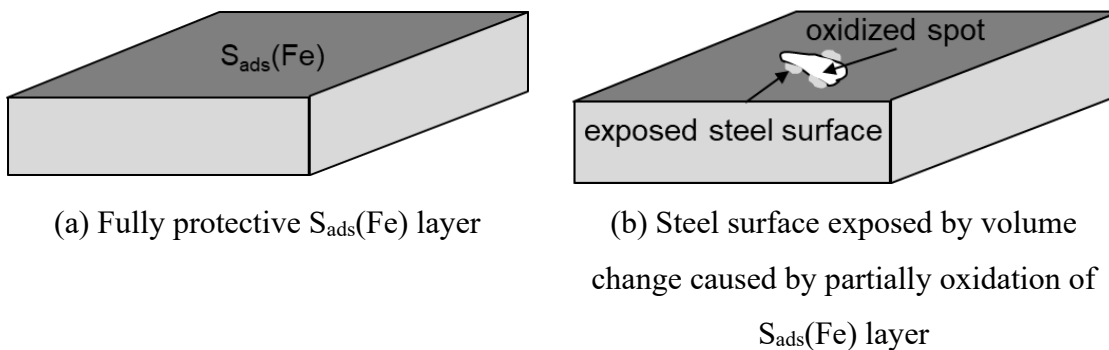
5.5 Proposed Mechanism of Pit Initiation in Marginally Sour Environments

According to thermodynamic calculations in the Fe-S-H₂O system (see Figure 71 [24]), a chemisorbed S_{ads}(Fe) film is very stable over a large area on the Pourbaix diagram, particularly in low pH conditions where precipitated iron sulfides are usually unstable. This S_{ads}(Fe) chemisorption film protects the steel surface from corrosive species such as H₂CO₃ or H⁺. However, this layer seems to be vulnerable to O₂ ingress and can be partially oxidized into iron oxides if enough dissolved O₂ is present, as shown by the *in situ* Raman spectrum in Figure 67. Experimental observations showed that pit initiation occurred due to the presence of oxygen, which means that the phase change from iron sulfide to iron oxide is related to pit initiation. However, this does not

automatically translate into part of steel surface being directly exposed to the corrosive environment. After all, Fe_3O_4 and Fe_2O_3 are very difficult to be dissolved in aqueous solution [164], just as FeS and NiS . This said, based on the fact that the single crystal volume of mackinawite, greigite, and magnetite are different, the total volume changes induced by the phase change from mackinawite to magnetite could be sufficient to expose part of the steel surface, leaving behind localized spots free of the protective layer that can then actively corrode. This pit initiation mechanism is schematically represented in **Figure 75**.

Figure 75

Proposed mechanism of pit initiation in marginally sour environments



5.6 Summary

Trace amount of oxygen can cause pitting of mild steel in a marginally sour environment. This was verified by experiments at different oxygen concentrations (< 3 ppb_(w), $3 \sim 20$ ppb_(w), $20 \sim 40$ ppb_(w)) at baseline conditions of $30\text{ }^\circ\text{C}$, $\text{pH} = 5.00 \pm 0.01$, $\text{pCO}_2 = 0.97$ bar, $\text{pH}_2\text{S} = 0.04$ mbar, 300 rpm stir bar, 7 days.

Specifically, for each experimental condition, the following observations can be made:

- No pitting occurred when the dissolved O_2 concentration was kept below 3 ppb_(w) during the entire duration of the test and no corrosion product could be identified with TEM. The general corrosion rate remained as low as 0.1 mm/y.
- Pitting was found when the dissolved O_2 concentration was greater than or equal to 20 ppb_(w). A 200 nm thick corrosion product layer (mixture of iron sulfide and iron oxide) was identified with TEM. The general corrosion rate was about 0.8 mm/y.
- It is hypothesized that the dissolved O_2 partially oxidized the protective chemisorbed FeS layer, leaving small unprotected areas exposed to corrosive solution. This scenario can explain the initiation of localized corrosion.

This conclusion only applies to specific conditions in marginally sour environments (i.e., low pH_2S and low pH). Previous research results [53] show that when the H_2S partial pressure was higher than 0.15 mbar or when the pH was higher than 6.00 ± 0.01 , no pitting occurred. This mode of localized corrosion could be mitigated either by eliminating dissolved oxygen or by increasing the pH of the aqueous environment.

Chapter 6: Pit Propagation Based on Acidification by Catalytic Oxidation of Dissolved Hydrogen Sulfide

6.1 Introduction

A common characteristic of marginally sour environments is that they feature low partial pressure H_2S that often translates into a saturation degree of FeS lower than unity. In other words, unless the surface pH and/or Fe^{2+} concentration are high, no corrosion product is expected to precipitate in these conditions according to thermodynamic calculations. However, pitting was found in marginally sour environments repeatedly [53, 93, 94, 95], which should imply the presence of a partially protective layer or film on the substrate surface. A systematic parametric study indeed found that the occurrence of this type of pitting failure was related to the lack of protectiveness of a mackinawite corrosion product layer, which could have formed through a chemisorption process (in chapter 4) [165]. It also found that the pH of the aqueous solution played a key role (in chapter 4 and chapter 5) [165, 166]. Analysis of the main constituents of the corrosion product layer identified the presence of sulfides but also of oxides, which was rather unexpected. Additional experiments were designed to trace the origin of these oxides and revealed that a minuscule degree of oxygen ingress during the completion of the tests was the reason why pitting occurred in marginally sour environments (in chapter 5) [166]. When the $O_{2(aq)}$ concentration was kept below 3 $ppb_{(w)}$, the chemisorbed FeS layer [$S_{ads}(Fe)$] was able to protect the steel surface from acidic corrosion caused by the presence of H^+ and $H_2CO_{3(aq)}$. However, this chemisorbed FeS layer could be oxidized by trace amounts of dissolved oxygen ($> 3 ppb_{(w)}$). Therefore, this partially oxidized layer was

heterogeneous in terms of protectiveness. It was hypothesized that the volume change caused by phase change led to exposure of the unprotected steel surface to the corrosive aqueous environment (H^+ and $H_2CO_{3(aq)}$). This mechanism was proposed for explaining pit initiation in marginally sour environments.

However, two additional questions remained unanswered:

1) How do pits propagate in marginally sour environments?

2) Why does the pH decrease during the corrosion process when $[O_2]_{aq} < 3$ ppb_(w)?

Both thermodynamic calculations and experimental verifications are described in the section below in order to address these two problems, which seem inevitably linked.

Traditional models of pit propagation often feature “a cathode of large area and an anode of small area”. This means that while most of the area of the steel surface is protected, and acts as a cathode, small localized areas of the steel surface act anodically and experience environments conducive to sustained high corrosion rates. More specifically, in order to maintain a high corrosion rate inside the pit, the potential at the bottom of the pit must be lower than the surrounding area, or/and the water chemistry inside the pit must prevent the formation of a corrosion product layer. Usually, the latter scenario can be narrowed down to situations where the pH inside the pit is lower than in the bulk solution, or where some other aggressive ions (Cl^- in the case of stainless steel, for example) are present. Another factor to consider in localized corrosion is the conductivity of the corrosion product layer. If the layer has a larger electrical conductivity, the galvanic coupling effect between the actively corroding small area and

the large protected area can be enhanced. Therefore, most of the pit propagation models couple mass transfer, electrochemical reactions, chemical reactions, potential and current density distributions inside of the pit, seeking de-passivation, pit acidification, and galvanic coupling to support a higher corrosion rate in the pit.

In aerated environments, hydrolysis of Fe^{3+} could produce H^+ and thereby leads to pit acidification [133]. This lower pH would make the environment inside the pit more corrosive. The presence of “aggressive ions” such as Cl^- or SO_4^{2-} could also prevent re-passivation [73].

In CO_2 corrosion environments, the “grey zone” theory has been used to explain both pit initiation and pit propagation [140]: When the saturation degree of FeCO_3 inside the pit is less than unity, no FeCO_3 layer can precipitate, thereby promoting pit propagation. Han, *et al.*, [98] measured the galvanic coupling effect and surface pH value inside a pit and calculated the current density and potential distribution [115]. However, inside the pit, the pH naturally tends to increase due to the release of Fe^{2+} and consumption of H^+ , increasing the saturation degree and making the environment paradoxically less corrosive and favorable for corrosion product precipitation. Only periodic changes in the environment or specific fluid flow conditions (top-of-the-line corrosion (TLC) [167] or high local turbulence level) can explain how saturation degree could remain less than unity [115].

In $\text{H}_2\text{S}/\text{CO}_2$ corrosion environments, the galvanic coupling effect occurring between the steel surface and pyrite [108] or pyrrhotite [124] were studied extensively. The existence of galvanic coupling in the presence of mackinawite remains to be

identified due to its instability. However, the facts that conductivity of mackinawite (metallic) is larger than pyrite (semiconducting) [168] and that the corrosion rate inside the pit was much higher than the mackinawite layer-free corrosion rate [53, 165] seem to suggest galvanic coupling does work when mackinawite is the protective layer. Analysis of the bulk solution chemistry related to pitting in sour environments showed H₂S can be oxidized into elemental sulfur, SO₃²⁻, and SO₄²⁻ [30], but no effort was done to generate a potential current distribution between the pit and the surrounding area.

Since the occurrence of pitting in marginally sour environments can be directly linked to the presence of trace amounts of O_{2(aq)}, it is essential to investigate the effects of oxygen in detail (see chapter 5) [166]. Overall, the effect of the presence of dissolved oxygen on a sour corrosion system can be divided into three aspects: 1) Oxygen can be directly reduced on the steel surface, adding an additional cathode reaction; 2) Oxygen can react with H₂S in the aqueous solution producing multiple possible sulfur compounds as possible oxidation products; 3) Oxygen can induce the transformation of the corrosion product layer from ferrous sulfides (mackinawite) to ferric oxides (hematite).

The addition of the oxygen reduction reaction increases the general corrosion rate, but the added rate would be proportional to the dissolved O₂ concentration, which is very small in this case, and may not be sufficient to explain the occurrence of pitting [166]. This will be discussed in more detail in this chapter.

Oxidation kinetics between H₂S and O₂ has been studied extensively and typically leads to the formation of sulfite (SO₃²⁻), sulfate (SO₄²⁻), thiosulfate (S₂O₃²⁻), polysulfides (S_x²⁻), and elemental sulfur (S₈) [30, 31, 169]. When it happens in the gas phase, most

often the application is in the synthesis of elemental sulfur or sulfuric acid. The most common industrial process for this is the well described Claus process. V_2O_5 was chosen as the catalyst in the sulfuric acid synthesis industry because it is the only transitional metal that can remain as an oxide rather than sulfide at very high temperature (above 250°C). The gas phase H_2S oxidation reaction is reported not to occur below 120°C [26]. Oxidation of H_2S has also been reported to occur in the aqueous phase at lower (near room) temperatures, in the presence of dissolved oxygen. Two very common industrial applications use this reaction: oxygen scavengers [28] or water treatment [170]. Most published works naturally focus on the selection of highly efficient catalysts and on kinetic studies. Thermodynamic aspects have not experienced the same level of research focus and are as of yet not fully understood. The catalytic efficiency of transition metal oxides other than V_2O_5 , such as Fe, Ni, Co, and Cu containing oxides (or salts of these metals), have been determined at low temperature in aqueous solution [19]. However, in this case, the type of sulfur compounds produced depends on conditions such as temperature and reactant concentrations through the laws of thermodynamics and not the type of catalyst, which is a kinetic parameter. For instance, A. K. Dalai and coworkers reported that they could not experimentally identify elemental sulfur as a desired commercial byproduct of these oxidation reactions [170]. This is in part because there were no thermodynamic predictions in their research work. Therefore, thermodynamics of low temperature, low concentration H_2S oxidation will be revisited in this chapter. Water sample analysis and pH monitoring performed during the corrosion experiments are used to experimentally verify the thermodynamic predictions in this chapter.

The crystallization process of mackinawite, its transformation and oxidation are common topics of interest for geochemists [19]. Mackinawite can be formed homogeneously in freshwater environments. It can also precipitate heterogeneously, in the form of nanocrystals, and can easily be mistakenly reported as amorphous FeS by XRD [19] or electron diffraction. While the oxidation of mackinawite has been reported to occur in the absence of O₂ above 70 °C through direct reaction with water [19], most studies agree that oxygen is necessary, especially at low temperature [76]. The most common products of mackinawite oxidation are greigite [19] and pyrite [39]. Greigite has been reported to form only at low pH, the reason being that the mackinawite crystal structure must first partially dissolve before transforming to form the greigite lattice [19]. Other products of mackinawite transformation could be goethite, magnetite, and hematite, depending on the presence of an aqueous phase and on temperature [74]. Thermodynamic calculation of oxidation of mackinawite will be discussed in this work together with the oxidation of dissolved H₂S, because both are related to the sulfur chemistry in sour corrosion.

6.2 Contribution of the O₂ Reduction to the Overall Cathodic Reaction

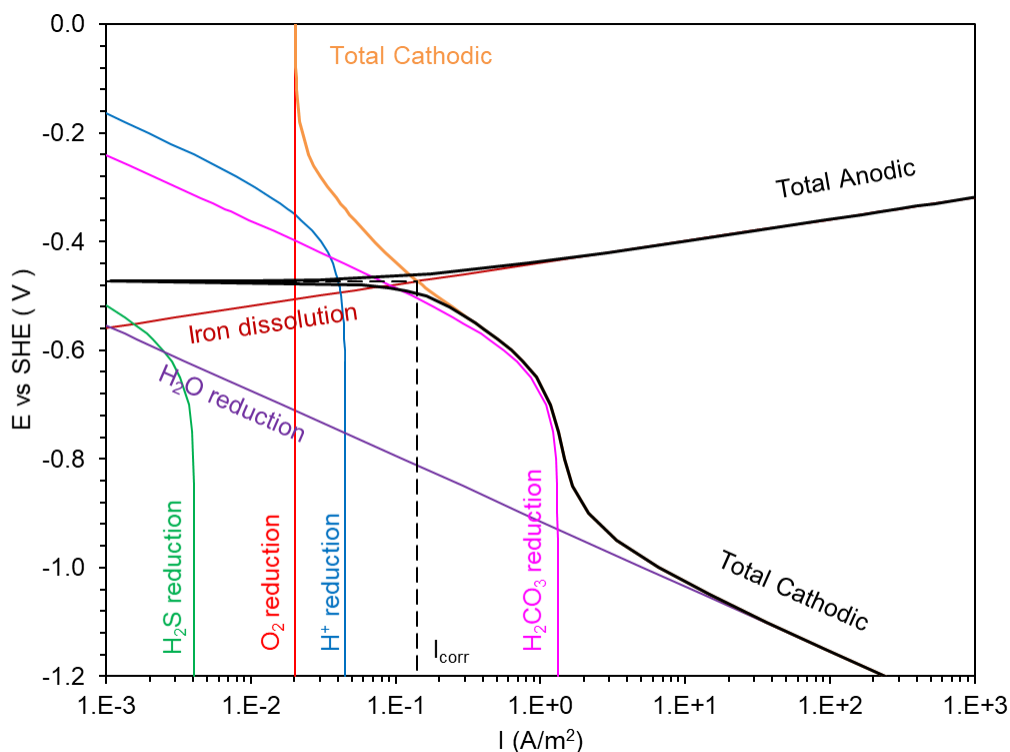
As stated in the introduction, the most straight-forward effect brought by oxygen to an electrochemical system is its cathodic reduction. The presence of O₂ increases the general corrosion rate as its reduction can be added to the total cathodic reaction. However, given the small amount of O₂ ingress, this contribution is indeed minimal. As shown in Figure 76, calculated by a corrosion model, the contribution of the O₂ reduction

reaction to the total cathodic current density is negligible, even considering 1000 ppb_(w) of dissolved O₂.

Figure 76

Evans diagram in marginally sour environment with O₂

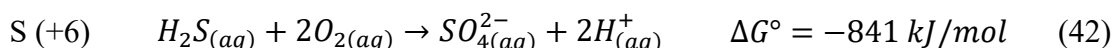
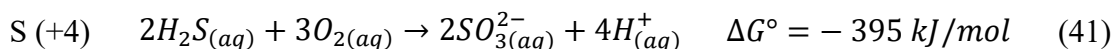
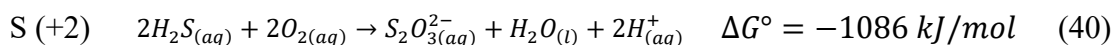
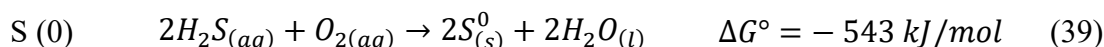
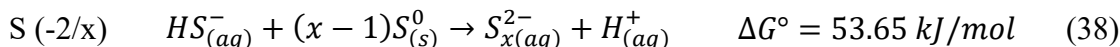
(30 °C, pH5, 0.97 bar CO₂, 0.04 mbar H₂S, [O₂]_(aq) = 1 ppm_(w)). Only the limiting current of the O₂ reduction is shown here.)



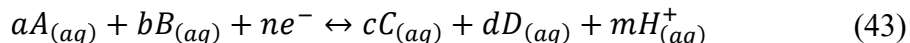
6.3 Thermodynamics of the oxidation of dissolved H₂S at low temperatures

Multiple possible oxidation products of H₂S have been reported, and are listed in reactions (40) - (42); the calculated standard Gibbs free energies for these reactions are also listed. Most of the reactions release H⁺ as a byproduct, except for reaction (39). This

means that the solution will tend to acidify only if the oxidation product of H₂S is not elemental sulfur. Pourbaix diagram and phase equilibrium diagrams are developed in order to determine which product is the most stable species at a given set of conditions (*i. e.*, temperature, concentrations).

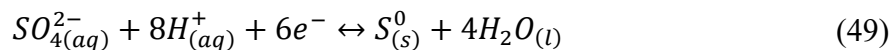
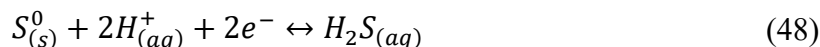
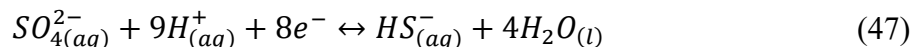
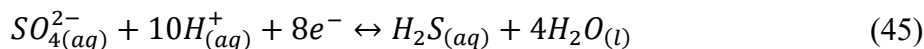


Stability diagrams, such as Pourbaix diagrams, are frequently used to demonstrate the most stable species in an electrochemical system. Usually, the *x*-axis shows the most influential factor in water chemistry speciation – pH, while the *y*-axis shows the equilibrium potential with respect to the standard hydrogen electrode (SHE) as calculated by the Nernst equation. The open circuit potential (OCP) measured during the electrochemical experiments is the resting potential measured between working electrode and the environment (with respect to the reference electrode). The OCP is the potential at which the electrochemical system has reached a steady state, which is typically used as the potential of the electrochemical system in the Pourbaix diagram [171, 172]. The Pourbaix diagram can be used to identify zones corresponding to the most thermodynamically stable species under a given pH and OCP. A Pourbaix diagram can be drawn based on electrochemical reactions written in a generalized form as in reaction (43) and equation (44).



$$E = E^o - \frac{RT}{nF} \left(\ln \frac{[C]^c [D]^d}{[A]^a [B]^b} - 2.303mpH \right) \quad (44)$$

As shown in Figure 77, a Pourbaix diagram of 0.01 bar H₂S in aqueous solution at 298.15 K was made to predict the oxidation product of H₂S at the electrode surface. The thermodynamic data used is derived from the literature [173]. Here, the transformation reactions used are listed in equation (45)- (50). These reactions shown here only involve with the thermodynamically most stable species (e.g., only SO₄²⁻, no S₂O₃²⁻). It should be noted that there is no oxygen in these reactions – here, the oxygen effect is reflected by the potential of the electrode, which is supposed to be pushed to the positive side due to the oxygen reduction reaction (reaction (51)). It shows that at pH 5, the steel surface must be polarized to above 0V vs. SHE in order for H₂S to be oxidized. The measured OCP in the corrosion test was usually not as high as 0V vs. SHE. Assuming that the OCP can be used to represent the electrochemical potential of the system, the oxidation of dissolved H₂S should not happen. However, the diagram clearly identifies conditions when oxidation of H₂S into elemental sulfur and sulfates is thermodynamically possible.



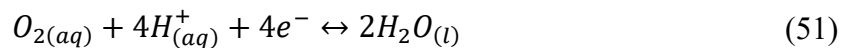
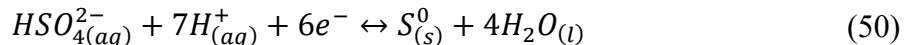
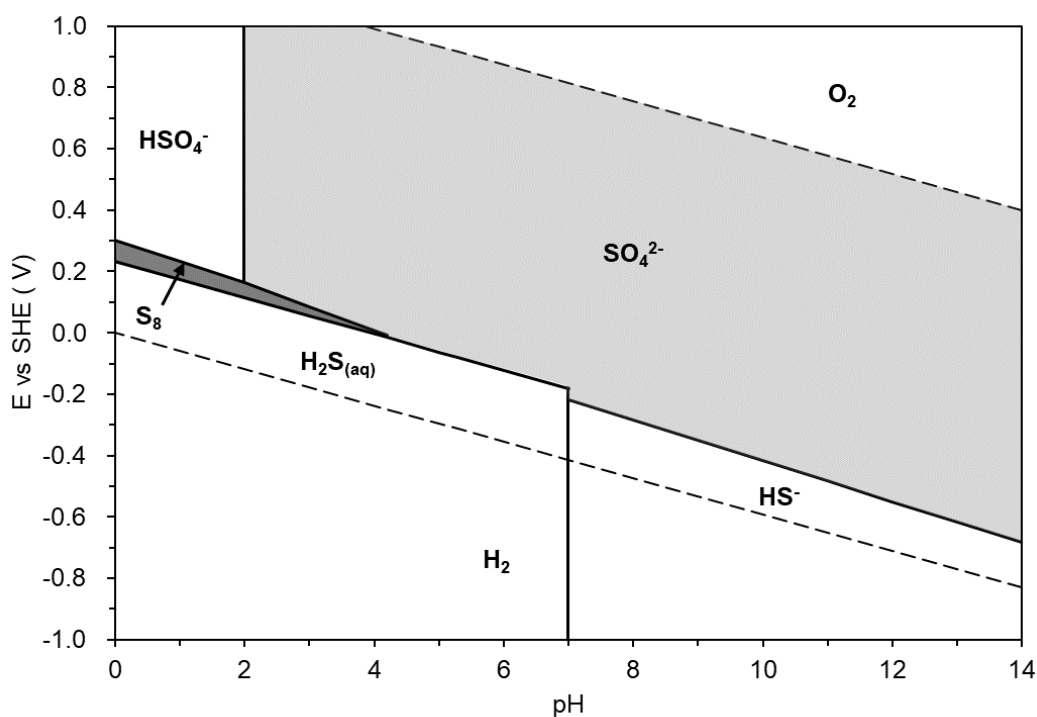


Figure 77

Pourbaix diagram of the H₂S - H₂O system [298.15K, 1 atm, p_{H₂S} = 0.01 bar (1 v.%)]

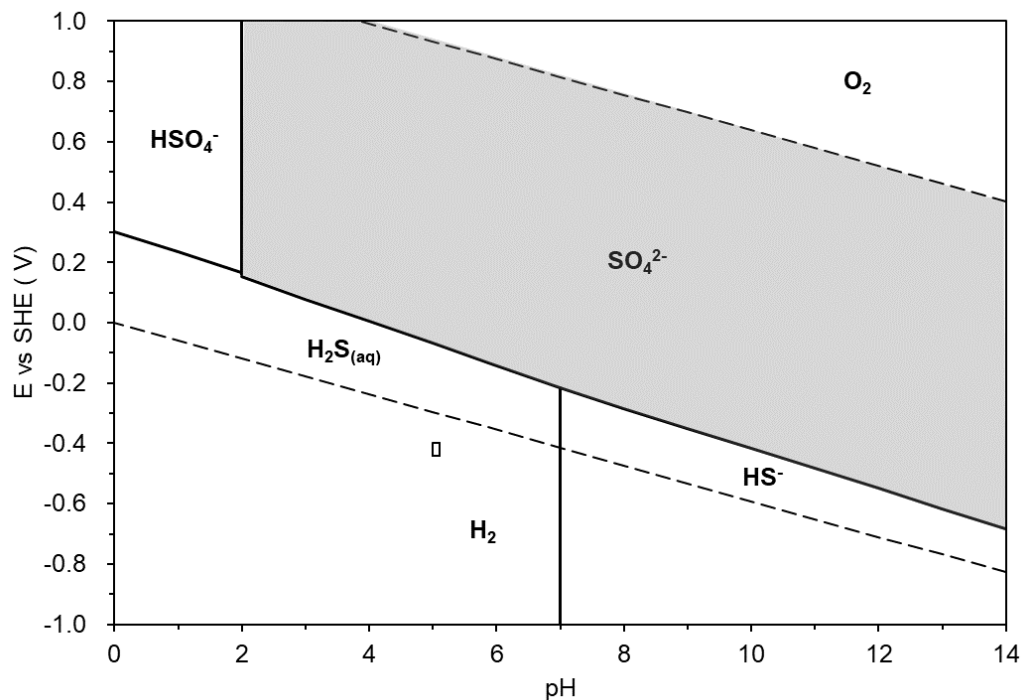


A second Pourbaix diagram was developed considering a lower H₂S content (0.04 mbar, Figure 78) that corresponds to the baseline condition in the previous parametric studies (indicated with a small rectangle in the diagram). These conditions led to pitting corrosion. This diagram shows that the oxidation of dissolved H₂S was also not thermodynamically favored in these conditions. In addition, elemental sulfur is not predicted to be stable under any conditions, as opposed to what is shown with a higher

H₂S content (0.01 bar, Figure 77). In other words, H₂S can only be oxidized into SO₄²⁻ directly when the H₂S content is sufficiently low. Again, if the measured OCP during the corrosion experiments is representative of the electrochemical potential of the system, there should be no oxidation of dissolved H₂S. However, as it will be shown later on, experimental observations seem to indicate otherwise, since a decrease in pH, which can be associated with H₂S oxidation, as well as direct measurement of SO₄²⁻ in the water samples, were observed during the test.

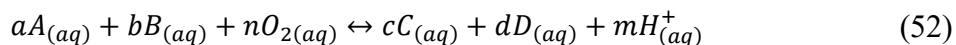
Figure 78

*Pourbaix diagram of H₂S -H₂O system [298.15K, 1 atm, p_{H₂S} = 0.04 mbar (40 ppm_v)].
(The small rectangle (E = -440 ~ -400 mV, pH_(bulk) = 5.00 ~ 5.10) in the diagram is the baseline condition in terms of localized corrosion in marginally sour environments.)*



Both Figure 77 and Figure 78 show that the electrode must be polarized into a more positive potential to enable oxidation of dissolved H_2S in anoxic environments. However, the presence of some O_2 is not reflected in the measured electrode potential indicated in Fig.3 (the latter reflecting the mixed potential of the corroding Fe surface rather than the bulk aqueous conditions). What is more relevant here than the corroding surface, is how much oxygen is needed to enable the oxidation of dissolved H_2S . Therefore, the oxidation driving force in the diagram should be changed from potential (concentration of electrons) to concentration of dissolved oxygen in this system. The phase equilibrium diagram in Figure 79 was drawn to identify the threshold of dissolved oxygen concentration enabling H_2S oxidation. The thermodynamic data again comes from the literature [173]. The main idea is to correlate oxygen concentration with pH based on the Gibbs free energy. Therefore, this phase equilibrium diagram is a prediction tool similar to the Pourbaix diagram but now reflecting aqueous solution conditions. Several of the redox reactions considered are listed in reactions (38) - (42); the rest are similar oxidation reactions with HS^- and S^{2-} rather than $\text{H}_2\text{S}_{(\text{aq})}$. The equilibrium constants associated with these reactions are calculated according to their associated standard Gibbs free energies. The reaction quotient can be written as shown in equation (53), considering a generalized form of the redox reaction, shown in reaction (52). Therefore, the equilibrium concentration of one reactant or product can be calculated from the equilibrium constant and concentrations of the remaining reactants and products (equation (54)). Reactions that do not produce H^+ are reflected as horizontal lines in the

diagram. Similarly, for reactions that do not involve O_2 are reflected as vertical lines in the diagram.



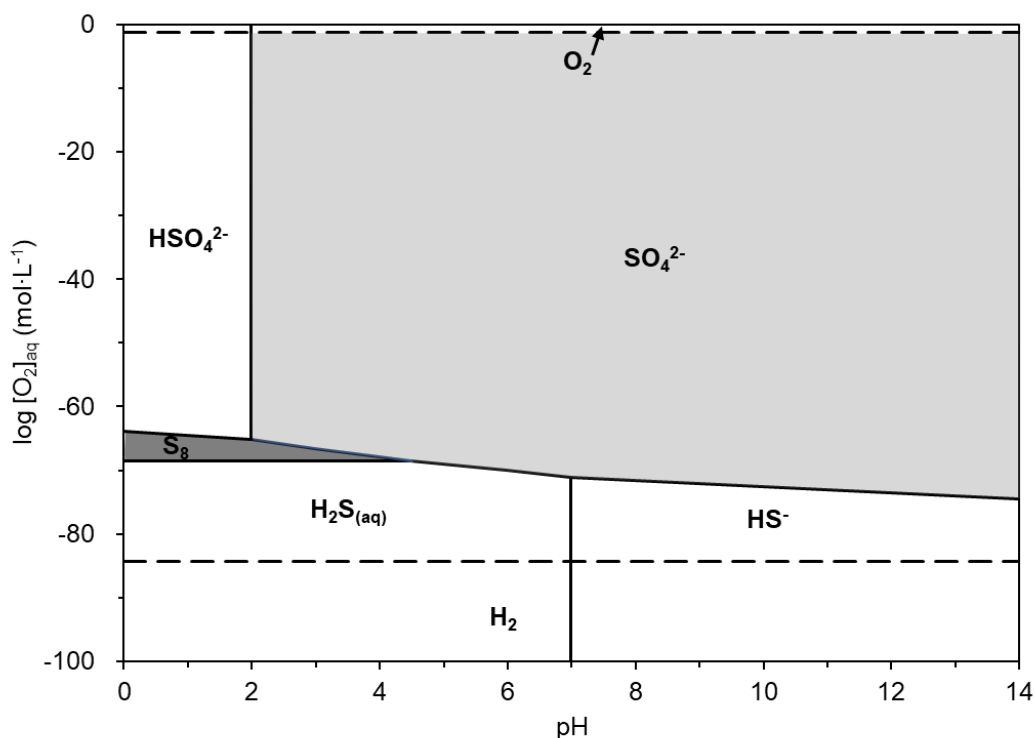
$$K_c = \frac{[C]^c [D]^d [H^+]^m}{[A]^a [B]^b [O_{2(aq)}]^n} \quad (53)$$

$$\log[O_{2(aq)}] = \frac{1}{n}(-mpH + c \log[C] + d \log[D] - a \log[A] - b \log[B] - \log K_c) \quad (54)$$

Using the method described above, a phase equilibrium diagram plotting $\log[O_{2(aq)}]$ vs. pH (**Figure 79**) was drawn for the H_2S - O_2 - H_2O system at 298.15 K, 1 atm with 1 v. % H_2S . The predictions in this work were compared with commercial software (Geochemist's WorkBench) and its database [174, 175]. As a result, it showed good agreement. The diagram shows that when $pH < 4.5$, dissolved H_2S is predicted to be readily oxidized into elemental sulfur, then further oxidized into sulfate with higher O_2 content. This reaction is thermodynamically predicted to occur even with $O_{2(aq)}$ concentrations far below the $ppt_{(w)}$ level. By comparison, the lowest residual dissolved oxygen concentration measured during all the experimental series was of the order of $ppb_{(w)}$ (**Table 15**), which should be more than enough to enable this conversion. This means that oxidation of dissolved H_2S is thermodynamically possible under the experimental conditions associated with sour corrosion studies. The extent and speed of this reaction are indeed not predicted by these equilibrium diagrams. The observations derived from the $\log[O_{2(aq)}]$ vs. pH diagram are consistent with those from the E-pH diagram (Figure 77), in the sense that both diagrams identify conditions when H_2S can indeed be oxidized into elemental sulfur or sulfates.

Figure 79

Phase equilibrium diagram of the $H_2S-O_2-H_2O$ system [298.15K, 1 atm, $p_{H_2S} = 0.01$ bar (1 v.%)]



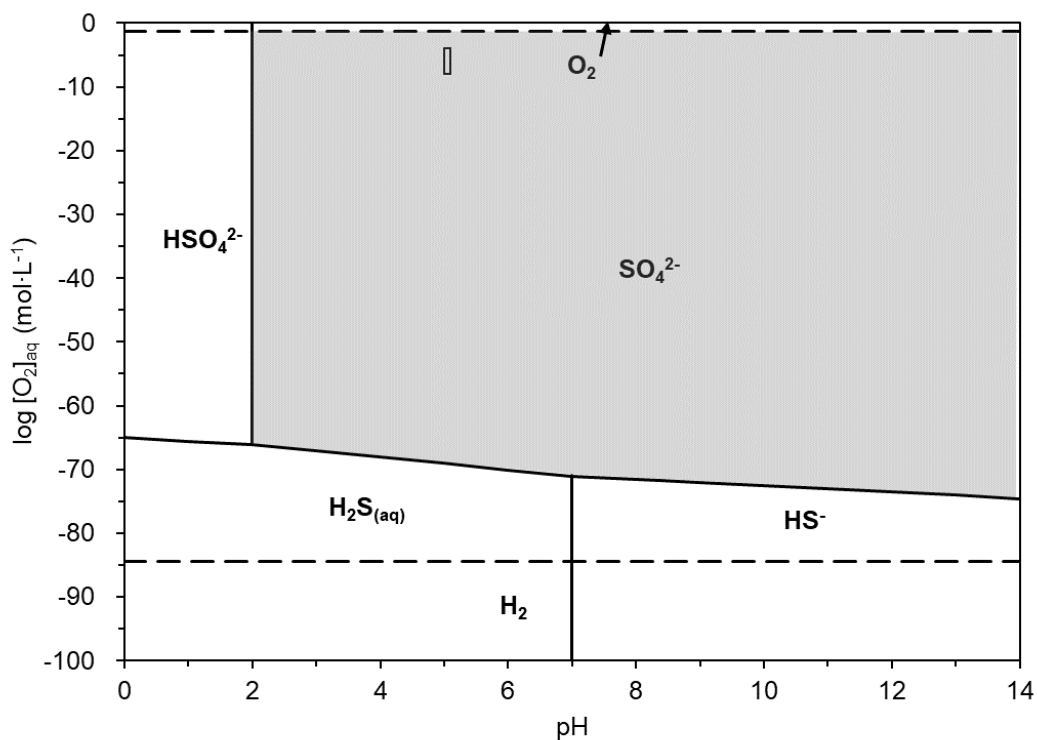
To better simulate the experimental conditions corresponding to the marginally sour environments of this study, another $\log [O_2]_{aq}$ vs. pH phase equilibrium diagram (Figure 80) was drawn for the $H_2S-O_2-H_2O$ system at 298.15 K, 1 atm with 40 ppm_v H_2S . The conditions corresponding to the baseline experiments are depicted as a small rectangle in the diagram. Some differences exist when compared with the equilibrium diagram developed for a higher concentration of H_2S (Figure 79). In the case of 40 ppm H_2S , dissolved H_2S can be oxidized into sulfate directly, and the zone of elemental sulfur stability does not exist. An important finding is that the dissolved H_2S can indeed be oxidized considering the baseline condition. This seems to be inconsistent with the E-pH

diagram generated for the same condition (Figure 78). The explanation is related to the fact that the reactions between dissolved oxygen and dissolved H_2S did not occur at the surface of the working electrode. Therefore, the OCP may not be an accurate reflection of the electrochemical potential of the system, especially considering reactions occurring in the bulk solution. In other words, this finding suggests that while Pourbaix diagrams can effectively predict the thermodynamics of electrochemical and chemical reactions occurring on the substrate surface, other phase equilibrium diagrams may also be useful to characterize homogeneous reactions happening in the bulk solution and identify thermodynamically stable bulk species.

Figure 80

Phase equilibrium diagram of $H_2S-O_2-H_2O$ system [298.15K, 1 atm, $p_{H_2S} = 0.04$ mbar (40 ppm_v)]

(The small rectangle ($[O_2]_{aq} = 10^{-8} \sim 10^{-4}$ mol/L, $pH = 5.00 \sim 5.10$) in the diagram is the baseline condition in terms of localized corrosion in marginally sour environments.)

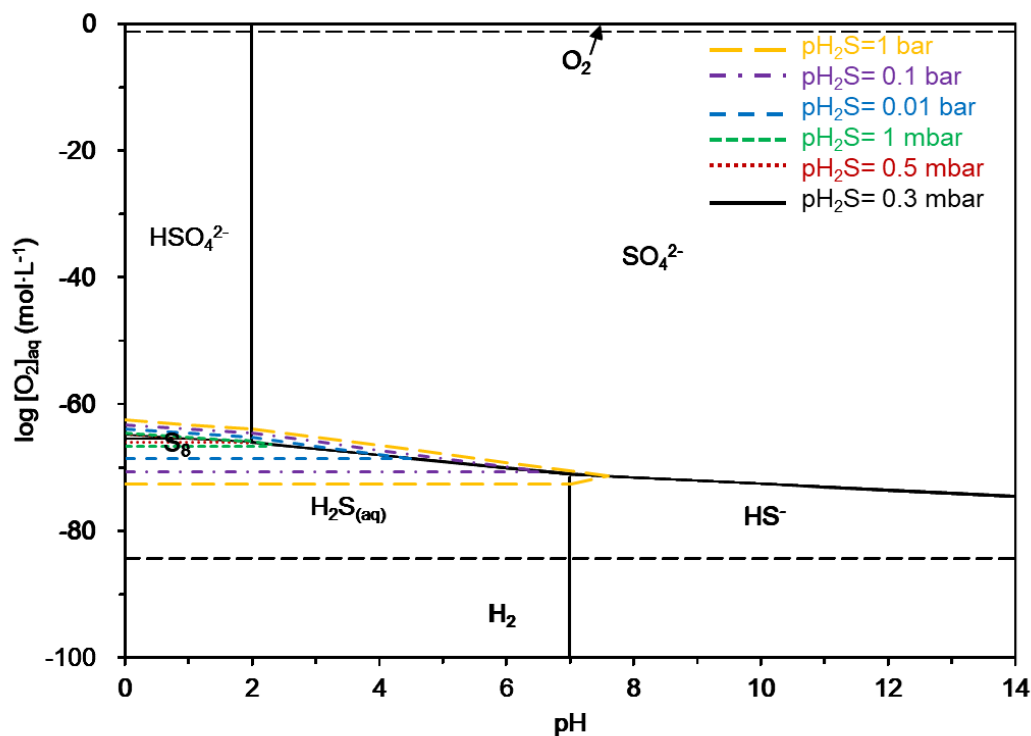


NACE standard TM 0177 [176] states that “oxygen contamination is evident by a cloudy (opaque) appearance of the test solution”, which corresponds to the formation of elemental sulfur. Since in marginally sour conditions, elemental sulfur is not expected as a by-product of H_2S oxidation, the solution should remain transparent and clear even though sulfate species may be formed in the solution. Since whether an H_2S containing solution would turn to opaque when exposed to air depends on such conditions as

temperature, pH, and H₂S concentration (or partial pressure in the corresponding gas phase), a third phase equilibrium diagram (Figure 81) was developed to characterize this phenomenon based on various H₂S partial pressures (pH₂S=1 bar, 0.1 bar, 0.01 bar, 1 mbar, 0.5 mbar, 0.3 mbar) at 25°C. According to this diagram, elemental sulfur formation, for example, is expected when pH₂S > 0.01 bar at pH 5 and when pH₂S > 300 ppm at pH 1.

Figure 81

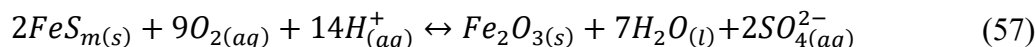
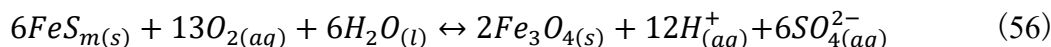
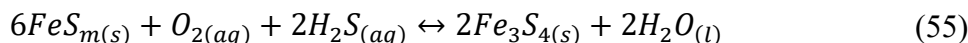
Using phase equilibrium diagram of H₂S-O₂-H₂O system to predict formation of elemental sulfur (298.15K, 1 atm)

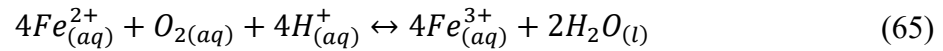
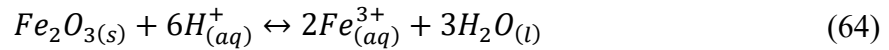
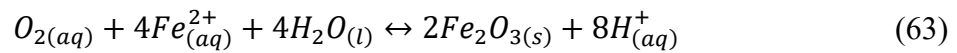
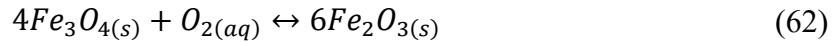
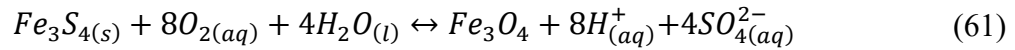
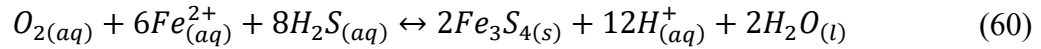
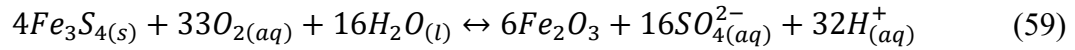


Other less stable oxidation products of dissolved H₂S, such as SO₃²⁻ and S₂O₃²⁻, can be included in the phase equilibrium diagram if the presence of the most stable species (SO₄²⁻ for example) is suppressed [173]. Although they are not as stable thermodynamically speaking, they could still be detected experimentally by analyzing the composition of the aqueous phase if their formations are kinetically favored [30, 31]. In summary, the oxidation of H₂S should generate SO₄²⁻ although traces of SO₃²⁻ and S₂O₃²⁻ could also be detected - elemental sulfur would only precipitate if the H₂S content is significantly higher. In marginally sour environments, considering the low content of H₂S, SO₄²⁻ is probably the most prominent detectable product, although equilibrium diagrams are not indicators of reaction kinetics.

6.4 Thermodynamics of the oxidation of mackinawite corrosion product layer

The prediction exercise as described above was repeated considering the mackinawite - O₂ - H₂O system to investigate the overall effect of oxygen on the corrosion product layers in the marginally sour environments, using reactions (55) - (65). These reactions revealed that the most stable sulfur containing product during the transition from iron sulfides to iron oxides is SO₄²⁻, not elemental sulfur. Therefore, it makes sense that no elemental sulfur was observed in the acquired *in situ* Raman spectrum for the partially oxidized mackinawite (**Figure 67**, [166]).





In the absence of oxygen, the chemisorption of H₂S and precipitation of the thin mackinawite layer on the steel surface can be illustrated by a Pourbaix diagram, as shown in Figure 71. In this chapter, the effect of the presence of dissolved oxygen is presented as a log[O_{2(aq)}] vs. pH phase equilibrium diagram, as shown in Figure 82 that considers 0.01 bar H₂S. This diagram indicates that mackinawite can be oxidized into greigite, magnetite or hematite depending on the pH.

Figure 82

Phase equilibrium diagram of the mackinawite- O_2 - H_2O system [298.15 K, 1 atm, $p_{H_2S} = 0.01$ bar (1 v.%)]

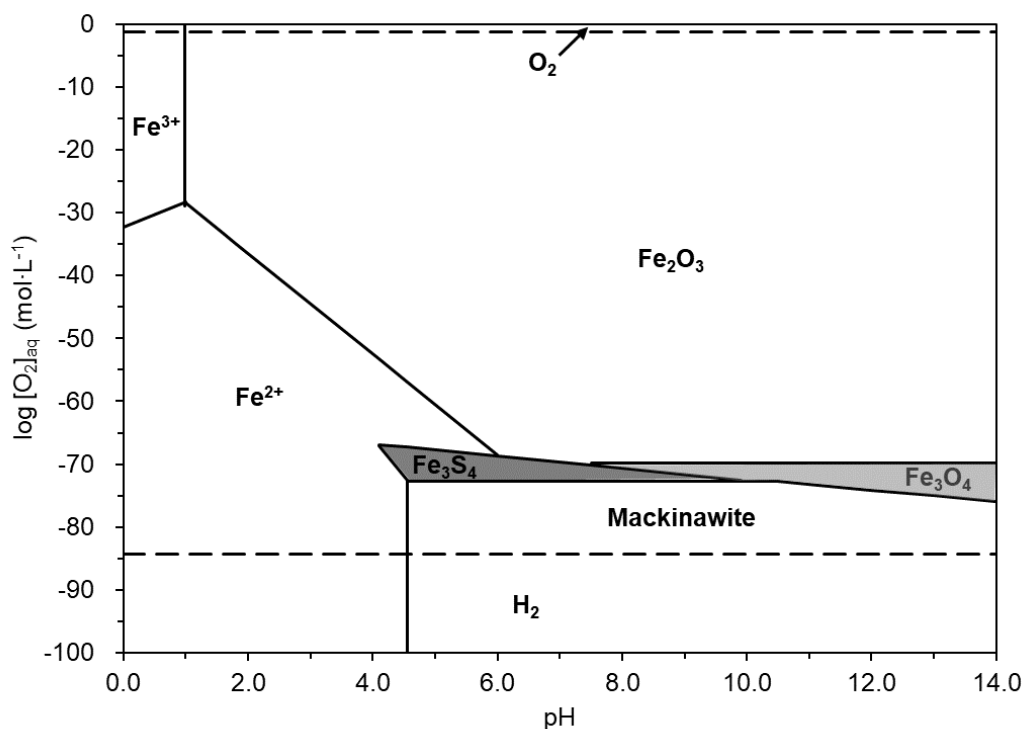


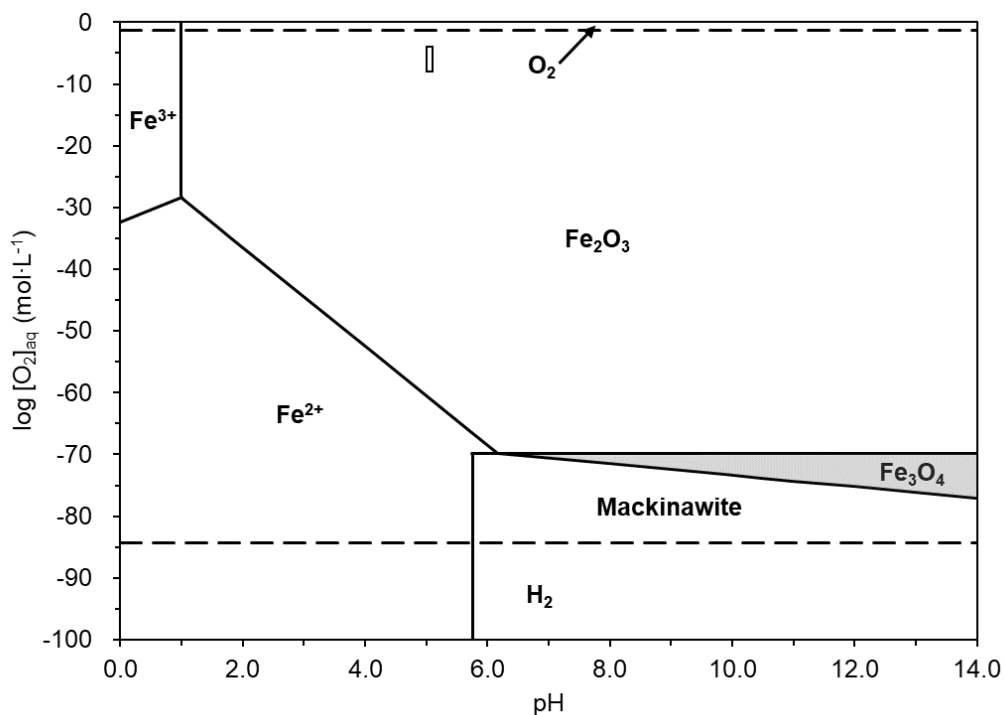
Figure 83, which depicts a marginally sour environment with 40 ppm_(v) of H_2S , shows that mackinawite can only be oxidized to magnetite and hematite when $pH > 6$. The specific conditions of the baseline test (bulk pH 5 and 20 ppb_(w) of dissolved oxygen) are indicated in Figure 83 by the small rectangle. It clearly shows that hematite is the most stable species in these conditions. The chemisorbed or precipitated FeS layer formed during the experiments would gradually dissolve, releasing Fe^{2+} , which ends up being oxidized into hematite. These reactions would also generate sulfates as byproducts. These statements, of course, do not take into account the kinetics of the reactions. Based

on the previous experimental observations at various oxygen concentrations, hematite was seldomly detected via *in situ* analysis. Instead, when $[O_2]_{aq}$ is between 20 ~ 40 ppb_(w), only magnetite (not hematite) was detected on the corroding steel surface using *in situ* Raman spectroscopy (Figure 67, [166]). However, *ex situ* Raman microscopy did reveal the presence of hematite after exposure of the precipitated layer to air plus laser induced heating (Figure 64, [166]).

Figure 83

Phase equilibrium diagram of Mackinawite-O₂-H₂O system [298.15K, 1 atm, pH₂S = 0.04 mbar (40 ppm_v)]

(The small rectangle ($[O_2]_{aq} = 10^{-8} \sim 10^{-4}$ mol/L, pH = 5.00 ~ 5.10) in the diagram is the baseline condition in terms of localized corrosion in marginally sour environments.)

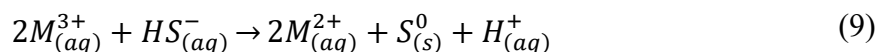
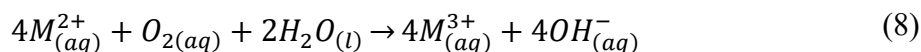


In summary, the thermodynamic predictions and the experimental observations suggest that the chemisorbed or precipitated FeS layer can be oxidized in the presence of dissolved oxygen into iron oxides (magnetite being more kinetically favored over hematite in the presence of traces of oxygen). This scenario is postulated to describe how the observed pitting initiated on X65 steel during experiments conducted in marginally sour environments [166].

6.5 Kinetics of the Oxidation of Dissolved H₂S at Low Temperatures

6.5.1 Background and Previous Results

Kinetically, oxidation of gaseous H₂S cannot readily happen without a catalyst [28]. However, H₂S oxidation can occur in aqueous solution near room temperature [30, 31, 170], the proposed mechanism involving a catalytic cycle and transition metals [19]. Transition metal ions such as Fe²⁺, Mn²⁺, Ni²⁺, and Co²⁺ could serve as a catalyst as shown in reactions (8) and (9); where M therein is representative of any of the aforementioned transition metals [27]. The catalyst has no selectivity in terms of eventual products (S⁰ or SO₄²⁻) [170].

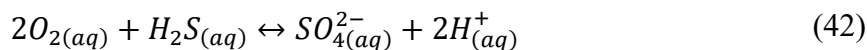
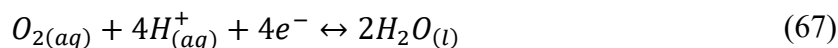
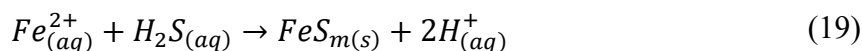
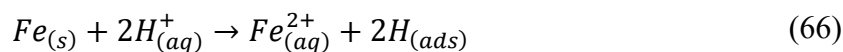


As shown in the **Table 9**, the API 5L X65 steel used in this study contains mainly Fe (97.32 wt. %), a significant amount of Mn (1.51 wt.%), and traces of Ni (0.29 wt.%) and Cu (0.17 wt.%). As proven in other kinetics related research [170], at pH 6.8, with 0.005 mg/L of Ni²⁺, 200 ppm H₂S_(aq) could bring the O_{2(aq)} down from 7 mg/L to 3 mg/L within 240 seconds. The same research also found that at pH 6.5, with 5 mg/L of Fe²⁺,

200 mg/L $\text{H}_2\text{S}_{(\text{aq})}$ could bring the $\text{O}_{2(\text{aq})}$ down from 6 mg/L to 2 mg/L within 1000 seconds [170]. Considering the baseline condition in marginally sour corrosion [X65 in 40 ppm_(v) (=0.13 mg/L) H_2S at 30°C, pH 5.01 ± 0.01], the measured $[\text{Fe}^{2+}]$ was usually around 20 mg/L after 7 days of exposure. Therefore, $[\text{Ni}^{2+}]$ dissolving proportionally should be up to 0.06 mg/L. The measured Fe^{2+} and Ni^{2+} concentrations in the marginally sour environments are within the same order of magnitude as has been reported in the literature and should be enough to catalyze the oxidation of $\text{H}_2\text{S}_{(\text{aq})}$ by $\text{O}_{2(\text{aq})}$.

As shown in Figure 74, pH increases gradually when $[\text{O}_2]_{(\text{aq})} > 20$ ppb_(w); pH decreases gradually when $[\text{O}_2]_{(\text{aq})} < 3$ ppb_(w); pH fluctuates around 5.01 when 3 ppb_{(w)} < [\text{O}_2]_{(\text{aq})} < 20 ppb_(w). This indicates that there are multiple reactions affecting pH at the same time in the system. Some of these reactions are well known: electrochemical dissolution of metal consumes H^+ *via* the reduction reaction (equation (66)); precipitation of FeS produces H^+ (equation (19)); reduction of O_2 consumes H^+ (equation (67)); oxidation of H_2S produces H^+ (equation (42)). For every 1 mol of O_2 that is reduced, 4 mol of H^+ is consumed. Therefore, when the oxygen content is higher, its effect on increasing the pH would be relatively more pronounced. However, the concentration of $\text{O}_{2(\text{aq})}$ in solution is so low that the contribution of the reduction of $\text{O}_{2(\text{aq})}$ on pH change may not be significant. The iron dissolution reactions and the precipitation of FeS could have counteracting effects. However, since not all of the dissolved Fe is expected to precipitate as FeS, the overall effect should lead to an increase in pH. As for the oxidation of H_2S , its contribution to pH change is difficult to evaluate, especially since the kinetics are dependent on the catalyst. It is unclear which of the two reactions, dissolved oxygen}

reduction and H₂S oxidation, will have the stronger effect on pH, although it can be speculated that the likelihood of a dissolved oxygen molecule being reduced at the metal surface is higher than two molecules of dissolved oxygen and H₂S reacting at a catalyst site. Anyhow, when the corrosion rate was high, the pH increased because of the effect of the corrosion reaction that dominates the other two reactions, although the dissolved oxygen content was paradoxically higher. When the corrosion rate was lower, which corresponded to a lower dissolved oxygen content, the pH decreased due to the oxidation of H₂S_(aq) – in this case the reduction of O_{2(aq)} was negligible.



As discussed in detail in section 2.1.6, separation of sulfide, sulfite, sulfate, thiosulfate, and polysulfide through HPLC remains an analytical challenge [32, 33]. Fortunately, according to the thermodynamic predictions in the last section, sulfate is the most stable and most common oxidation product of H₂S. Therefore, a simple and effective analytical method for water samples in marginally sour environments was used in order to verify the predictions by the phase equilibrium diagram here. The [SO₄²⁻] was measured by the SulfaVer 4 method[®] (employing BaCl₂) using UV/Vis spectroscopy to verify if catalytic oxidation was happening in this system. At the same time, the pH was left uncontrolled during the entire seven-day experiment to observe how much the pH would drop.

6.5.2 Experimental Procedure

As depicted in Figure 61(b), a two-liter glass cell reactor with a specially designed stainless lid featuring five polyether ether ketone (PEEK) sampling ports (one for an epoxy sealed X65 working electrode, four for half-square inch X65 steel corrosion coupons) was used in the experiments. pH was monitored but not controlled in these experiments. The testing condition was at 30 °C, 1 bar total pressure. The beginning pH = 5.01 ± 0.01 . The stir bar rotation speed was 300 rpm. A 1 wt. % NaCl solution was prepared. CO₂ gas was used to sparge the sealed system for at least two hours to bring the dissolved oxygen concentration to less than 10 ppb_(w), then a mixture of 100 ppm_(v) H₂S in CO₂ was sparged into the sealed system. Gas flows were adjusted to control the ratio between the pure CO₂ and H₂S/CO₂ mixed gas flow to achieve the 40 ppm_(v) concentration of H₂S, which was verified by a special H₂S testing reagent. The H₂S and CO₂ gases used contains a measured [O₂]_(aq) less than 0.6 ppb_(w). The [O₂]_(aq) in the glass cell during experiments was controlled by cleaning and tightening of all the contact surfaces. Therefore, each experiments achieve a [O₂]_(aq) as measured by the oxygen meter. The electrolyte was sparged with the H₂S/CO₂ mixture for 5 hours prior to specimen loading. A water sample was taken after the five hours of sparging. Then the X65 specimens were loaded into the system after this measurement. The corrosion experiment was started with the pH monitored and recorded during the entire experimental process. Water samples were again retrieved after 5 and 7 days of the corrosion experiment and analyzed with the HACH® 600 UV/Vis to detect if there was any SO₄²⁻. The two-liter aqueous solution was extracted with toluene at 50°C after the

corrosion experiment to determine if any elemental sulfur was present. The extracted concentrated toluene solution was placed into a glass petri dish for Raman microscopy analysis.

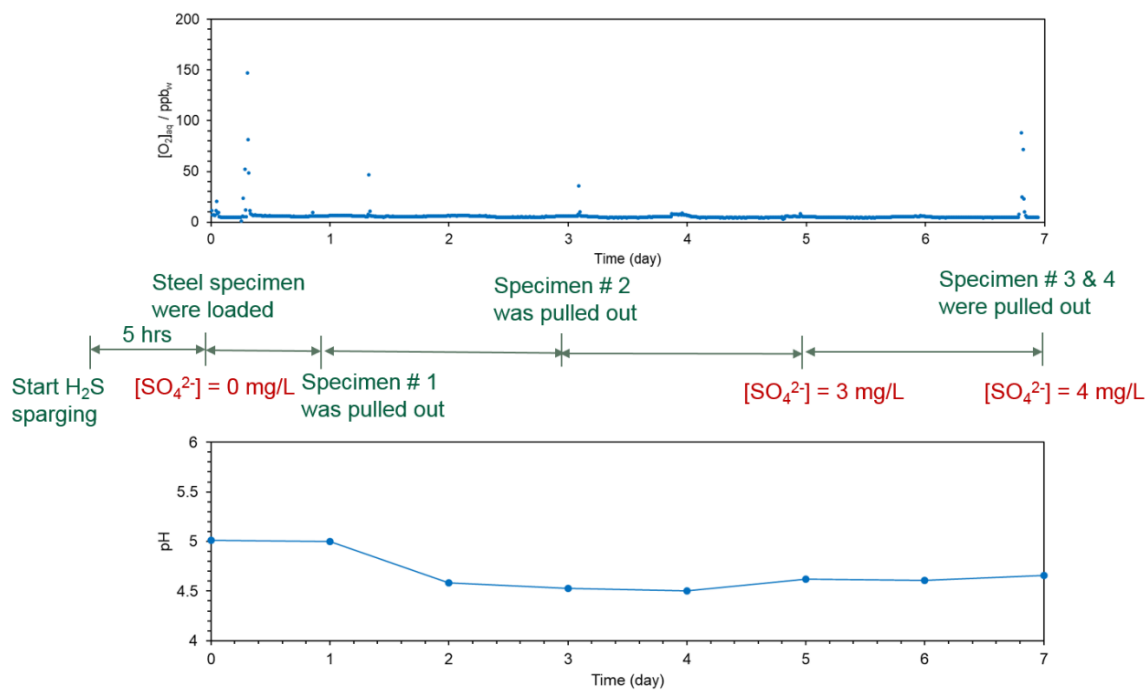
6.5.3 Results and Discussion

The experimental results are shown in Figure 84. Overall, the average $[\text{O}_2]_{\text{aq}}$ was measured to be *ca.* 7 ppb_(w). As shown in the timeline of the experimental procedures, a water sample was taken after five hours of sparging before the steel specimens were loaded. At that point, the measured $[\text{SO}_4^{2-}]$ was zero. When the specimens were loaded, a sharp increase of $[\text{O}_2]_{\text{aq}}$ was measured, but the $[\text{O}_2]_{\text{aq}}$ content decreased quickly and reached a stable level of around 7 ppb_(w) in the liquid phase. After five days, the measured $[\text{SO}_4^{2-}]$ was 3 mg/L; after seven days, it was 4 mg/L. This reading is indeed small but has to be compared with the concentration of O_2 in this system. Actually, the $[\text{SO}_4^{2-}]$ measurements in the related research [30, 31] also only found small concentrations. The trend of pH changes was in agreement with the production of SO_4^{2-} : it began to drop after the steel specimens were inserted in the solution. An estimation of the generated concentration of $[\text{SO}_4^{2-}]$ corresponding to a pH drop from 5.0 to 4.6 in 24 hours via oxidation reaction (42) yielded values around 5 mg/L $[\text{SO}_4^{2-}]$ and consumption of 0.6 ppb_(w)/min of O_2 . A more precise calculation should include the effect of the O_2 diffusion and reduction, as well as the consumption of H_2S through the corrosion reactions and FeS precipitation. In summary, the simultaneous increase in H^+ and SO_4^{2-} concentrations seems to prove that the catalytic oxidation of H_2S occurred at the low dissolved oxygen concentration present. Coincidentally, this effect is only visible when the

oxygen content is low enough to ensure that the FeS layer remains undamaged (*i.e.*, the corrosion rate remains low). It should also occur at higher oxygen content, but its effect on bulk pH would be masked by the products of the corrosion reactions. It is postulated that this reaction can also play a role in the pitting process, contributing to the local acidification of the pit.

Figure 84

Water chemistry analysis by UV/Vis & pH monitoring (30 °C, initial pH=5.01, $pCO_2 = 0.97$ bar, $pH_2S = 40$ mbar, $[O_2]_{aq} = 7$ ppb_(w)).



Another point worth discussing is the accuracy of this measurement. The measurement range of the SulfaVer 4 method[®] (BaCl₂) by UV/Vis is 2~70 mg/L. Therefore, readings of 3 and 4 mg/L may quantitatively not be very convincing since they

are very near the detection limit. However, the accuracy of the measurement is not as important as the knowledge that the reaction (H₂S oxidation) does occur. The measurement method is based on the reaction between Ba²⁺ and SO₄²⁻ to form a homogeneous white solid suspension of BaSO₄ (68). Naked eye observation of the solution during the measurement clearly showed that the reaction was indeed happening giving confidence in the overall findings.

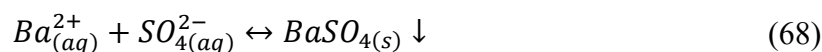
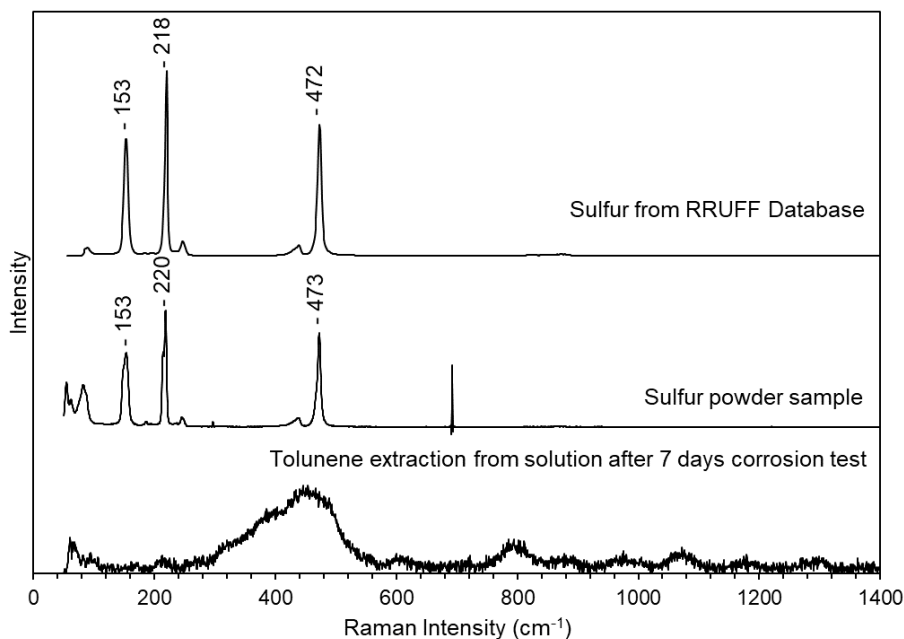


Figure 85 shows Raman results from toluene extraction of the two-liter solution after a 7-day corrosion experiment in comparison to the standard RRUFF database [177] (top) and a sulfur powder measured with the same equipment (middle). The results (the bottom curve) did not capture the fingerprint peaks of elemental sulfur compared with the sulfur powder sample or the RRUFF database value. This could be due to the fact that: 1) no elemental sulfur was generated in this system; 2) the amount of elemental sulfur was too small to be detected by the Raman microscope; or 3) the sulfur stayed within the corrosion product layer without leaching out into the bulk solution.

Figure 85

Toluene extraction after 7-day experiment for Raman analysis detection of elemental sulfur



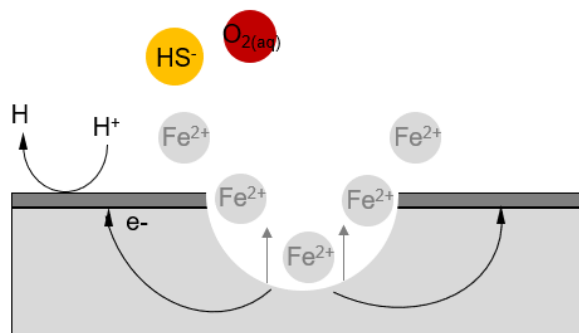
6.6 Pit Propagation Mechanism: Solution Acidification near Steel Surface by Catalytic Oxidation of H₂S_(aq)

The previous sections helped identify possible reactions that could explain the *in-situ* formation of oxides and the acidification of the solution in marginally sour corrosion with traces of oxygen ingress. A qualitative pit propagation mechanism is proposed here considering: 1) galvanic coupling between the small actively corroding anode (exposed to a solution containing H₂CO₃) and the larger protected surface covered by FeS acting as the cathode; 2) the pit acidification caused by catalytic oxidation of H₂S_(aq) by O_{2(aq)}. Based on the pH monitoring observation in this work, the pit acidification, in this case, is

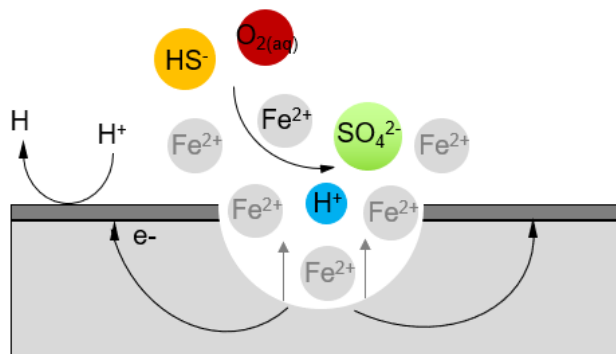
very mild (from 5.0 to 4.5). It is not comparable to the large pH shifts expected for the passive system, well-known pit acidification theory. Therefore, the implication of this mild pit acidification in marginally sour environments is mostly related to a decrease in FeS saturation value inside the pit, which prevents the regeneration of a protective FeS layer despite a high $[\text{Fe}^{2+}]$ in the pit. The pit acidification is not thought to drive the increase in corrosion rate, at least at the same level as the galvanic coupling does. This process is represented in **Figure 86**. In this scenario, due to the conductivity of mackinawite and the geometry of the small anode area inside the pit, the current density inside the pit is much larger than at the outside cathode area. At the same time, $\text{H}_2\text{S}_{(\text{aq})}$ is oxidized by dissolved O_2 , even at low temperatures. The reaction is catalyzed by Fe^{2+} , which is most abundant inside the pit. This reaction releases H^+ and SO_4^{2-} as products. Therefore, inside the pit a pH result that is lower than in the bulk solution. These factors taken together constitute a credible pit propagation mechanism in marginally sour environments.

Figure 86

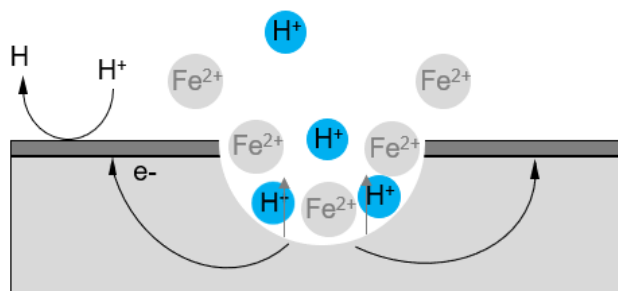
Proposed pit propagation mechanism



(a) $[\text{Fe}^{2+}]$ is higher inside the pit



(b) Catalytic oxidation of $\text{H}_2\text{S}_{(\text{aq})}$ by $\text{O}_{2(\text{aq})}$, most significant where $[\text{Fe}^{2+}]$ is elevated



(c) $[\text{H}^+]$ is higher inside the pit

6.7 Summary

The modelled potentiodynamic sweep showed that the contribution of the O_2 reduction to the overall cathodic reaction was not prominent enough to provoke a significant increase of corrosion rate observed with increased but limited ingress of oxygen. Thermodynamic calculation predicted that an extremely low concentration of oxygen (i.e. at the ppb_(w) level) would be enough to oxidize dissolved H_2S at low temperatures, be it in the presence of catalysts such as Fe^{2+} or Ni^{2+} . The thermodynamic calculation also predicted that the mackinawite corrosion product layer could be oxidized into magnetite and finally hematite in the presence of traces of oxygen in the aqueous solution. Measurements proved that H^+ and SO_4^{2-} , products of H_2S oxidation, were formed during the corrosion experiments with traces of oxygen.

The initial hypothesis introduced in chapter 3 was: in a marginally sour environment, localized corrosion is initiated and sustained when a partially protective corrosion product layer is formed. To decide whether such a layer would form, the saturation degrees of FeS and $FeCO_3$ were the core of the discussion. However, both the thermodynamic calculations and the experimental observations presented in this work revealed that the pitting mechanism of mild steel in marginally sour environments was not related to a partially formed layer, but rather to a layer that was partially damaged by reaction with dissolved oxygen. However, it is still unclear whether these damages can be attributed to oxidation of the chemisorbed layer [$S_{ads}(Fe)$] or to the competitive chemisorption between oxygen [forming $O_{ads}(Fe)$] and H_2S [forming $S_{ads}(Fe)$], or if the H_2S chemisorption layer [$S_{ads}(Fe)$] was converted into oxides remains unclear.

Consistent with the experimental observations, pit acidification and galvanic coupling were proposed as the cause of pit propagation in this study.

Chapter 7: Application of *in situ* Raman Microscopy on the Study of Corrosion Product Formation in Marginally Sour Environments

7.1 Introduction

Understanding the structure and properties of surface layers is of key importance in the study of localized corrosion. Understanding mechanisms associated with the localized corrosion of steel in oxygen containing aqueous solutions has been the topic of a vast body of literature over the past century [97, 178, 179, 180]. As stated by H. Strehblow: “One of the most important developments over the past 20 years in the study of passivity has been the application of surface analytical techniques” [73]. Mechanisms of localized corrosion of steel in carbon dioxide containing aqueous solutions have also received a lot of attention [181]. However, research on localized corrosion of mild steel in hydrogen sulfide containing solutions is relatively sparse due to the complexity of the required experimental methods due to the toxicity of H₂S. Therefore, a lot of work remains to be done on understanding the role of corrosion product layers formed in sour environments relating to localized corrosion.

In O₂ containing aqueous solution, the layer growth begins after the adsorption of O₂ on the steel surface. Usually, the thickness of the oxide layer is less than 100nm. If these oxides films have semiconducting properties, as for the oxides of Fe, Cr, Ni, and Cu, they will grow only up to a few nanometers in thickness [66]. For example, the thickness of the passive film on stainless steel is usually up to only 5 nm [7]. The study of this type of nano-scale films carries a lot of analytical challenges as very specialized techniques must be used. X-ray photoelectron spectroscopy (XPS) [68], secondary ion

mass spectrometer (SIMS), extended X-ray absorption fine structure (EXAFS), Auger electron spectroscopy (AES) [67] and scanning tunneling microscope (STM) [69] are typically needed to identify passive layers and study their structures. Oxide layers are also often examined in cross-section analysis using transmission electron microscopy (TEM) enabling direct visualization of the layer.

It has been noted that the as-characterized passive layer structure could be different following *ex situ* and *in situ* materials analysis processes. This is because post-processing of the specimen (drying process, exposure to air) can lead to structural changes to the layers. For example, Bockris and co-workers [69] reported, using a transfer device for Auger analysis, that the passive film on iron is composed of $\text{Fe}(\text{OH})_2$, forming a polymeric layered structure. O'Grady [71] used *in situ* Mössbauer spectroscopy to examine both *in situ* and “dried” (*i.e.*, *ex situ*) passive films. The *in situ* films consisted of chains of iron atoms connected by dioxy and dihydroxy bonds, further linked by water. However, the film changed to more closely resemble $\gamma\text{-Fe}_2\text{O}_3$ upon removal from the passivating medium and upon drying and aging.

In CO_2 environments, a FeCO_3 precipitation layer can typically reach several tens of microns in thickness, plus incorporate residual Fe_3C inside. These layers are easily visible in cross section analysis under SEM. However, their degree of protectiveness has been linked to the presence and characteristics of a thin layer of oxide formed on the metal surface, rather than being ascribed to the presence of a thicker FeCO_3 layer. FIB-TEM analysis was required to make this observation [140].

In sour environments ($\text{H}_2\text{S}/\text{CO}_2$), study of the structure and properties of corrosion product layers is much more complicated because of the potential for numerous FeS polymorphs to co-exist as well as because of the complications associated with sulfur chemistry. A large body of knowledge does exist, derived from geochemistry research, particularly that related to the formation of mackinawite (FeS)/troilite (FeS)/pyrrhotite (Fe_{1-x}S) as well as the S_2^{2-} containing mineral pyrite (FeS_2). Pyrite typically forms at high H_2S pressure and high temperature [109]. Its conductivity has been used to explain the occurrence of localized corrosion and galvanic coupling between pyrite and steel [108]. Pyrite is the thermodynamically most stable product of several formation and transformation reactions involving mackinawite, greigite, troilite, and pyrrhotite [109]. On the other hand, mackinawite is often found to be the initial (kinetically favored) iron sulfide corrosion product forming on the substrate surface under most conditions [39]. Localized corrosion was also found at low H_2S partial pressure and low temperature. Therefore, studies considering mackinawite, instead of pyrite, are crucial in understanding localized corrosion mechanisms in low temperature and low H_2S partial pressure environments. However, this is quite challenging because of the following aspects:

- 1) Mackinawite is unstable and easily oxidized during post-processing.
- 2) Freshly formed mackinawite is usually amorphous or nanocrystalline [19], which can lead to misidentification using typical diffraction-based techniques.

- 3) Mackinawite formed as corrosion product layer can be very thin at low temperature and low H₂S partial pressure, which can add to the difficulty of the analysis, especially when the substrate is actively corroding underneath.
- 4) The precursor or first few layers of mackinawite, which is formed by chemisorption (Sads(Fe), [100]) is very difficult to detect using common analysis techniques.
- 5) The co-existence of other corrosion products or residual phases, such as iron oxides, iron carbide, and iron carbonate all increase the complexity of the analysis.

Therefore, it is necessary to find a suitable, preferably *in situ*, analytical tool to facilitate the study of localized corrosion.

Oxidation of mackinawite in the air at room temperature can readily occur, although it is logically not as fast as at higher temperature. Studies have reported only partial oxidation of mackinawite into another phase [39]. Therefore, if the layers of interest are thick enough (for example, if they are formed at comparatively higher H₂S partial pressure), scanning electron microscopy/energy dispersive X-Ray spectroscopy (SEM/EDS) and X-ray powder diffraction (XRD) can give satisfactory results and provide the correct phase identification information. XPS only provides information about the top several layers of atoms, consequently, this can provide information about surface oxidation of mackinawite. Cross-sectional analysis using the focused ion beam technique combined with transmission electron microscopy (FIB-TEM) could offer information about the entire layer and, if further combined with selected area electron

diffraction (SAED) and process electron diffraction (PED), enables phase identification, provided that the layer thickness is greater than 100 nm [165, 166]. However, if the outer layer of mackinawite has been oxidized, no *ex situ* analysis could determine if the oxidation occurred due to the experimental environment or due to post processing.

Therefore, *in situ* Raman spectroscopy is an appealing technique since:

- 1) Raman spectroscopy is relatively simple to use and does not require vacuum.
- 2) The applied incident laser light can transmit through several types of transparent media, such as air, water, glass, and plexiglass or any other transparent plastics (e.g., acrylic, polyethylene, polypropylene, polycarbonate), without significant losses.
- 3) Both crystalline and amorphous materials can be detected by Raman shift responses.
- 4) Species in aqueous solution can also be detected by confocal Raman spectroscopy if the concentration is higher than the detectable threshold [182, 183].

These characteristics make *in situ* Raman spectroscopy a very promising analytical tool for the study of corrosion product layers formed at low H₂S pressures and low temperature. This is especially adaptable to marginally sour environments that have fewer safety-related complications but result in extremely thin, albeit complicated, corrosion product layers that are difficult to be identified. A properly designed system enables the Raman laser signal to go through the aqueous solution and the transparent reactor window to arrive at the surface of interest, interact with the surface layer structure, and then scatter back to the detector. Although the freshly precipitated mackinawite was

usually nanocrystalline or “amorphous”, the characteristic Raman peaks can be detected [74, 75].

However, the corrosion product layers formed in the marginally sour environments may contain several phases; their responses to the Raman signal must be considered and differentiated if an effective spectrum with characteristic peaks is desired. Carbonyl groups usually have one very strong peak at Raman shift round 1300 cm^{-1} , therefore FeCO_3 can be detected by this characteristic peak [184]. Iron oxides have multiple close peaks, but these peaks are not overlapping with each other. Therefore, they can be differentiated from one another. Fe_3C displays a plateau with double peaks at around 1100 cm^{-1} [185, 186]. Both iron sulfides (e.g., mackinawite, pyrite) and elemental sulfur are weak Raman scatterers; this makes their certain identification a challenge. This present work described the design and development of an *in situ* Raman cell and addressed these issues mentioned above about the proposed identification of phases formed during the corrosion process. The work also logically focuses on corrosion product layers formed in marginally sour environments.

7.2 Experimental Setup and Procedures

7.2.1 Experimental Equipment

A Bruker confocal Raman microscope SENTERRA II was used in the experimental work. A $\times 10$ objective with 7 mm focal length, a $\times 50$ objective with 1 mm focal length, and a $\times 50$ objective with 10 mm focal length were used for calibration with mineralogical specimens, *ex situ* analysis and *in situ* spectral acquisition, respectively. A He–Ne laser of 514 nm wavelength with 25 mW output power and 732 nm wavelength

with 100 mW output power at backscattering mode was applied for each analysis. The confocal pinhole diameter was of $25 \times 100 \mu\text{m}$. Raman spectra were first collected in the spectral region of $80 \sim 4000 \text{ cm}^{-1}$ with a resolution of 4 cm^{-1} , then at $80 \sim 1600 \text{ cm}^{-1}$ with a spectra resolution of 1.5 cm^{-1} at a different spot on each sample. Spectral acquisitions required five accumulations for a good signal-to-noise ratio.

The *in situ* Raman flow cell was designed as shown by the 2D sketch in Figure 87, which displays a cross section of the reactor. The specimen was fixed in the center of the reactor, with the fluid flowing through the reactor. The 3D sketch drawn by Solidworks is shown in Figure 88. The specimen was inserted into a gas-tight 3D printed plastic enclosure with a sapphire window. The idea was based on the fact that glass is transparent under the Raman signal (laser).

Figure 87

2D design sketch of the 3D printed in situ Raman flow cell (IRFC) reactor

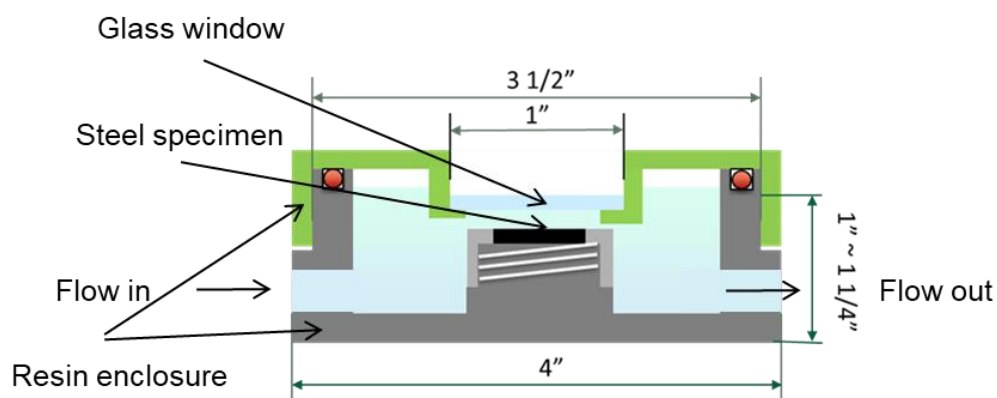
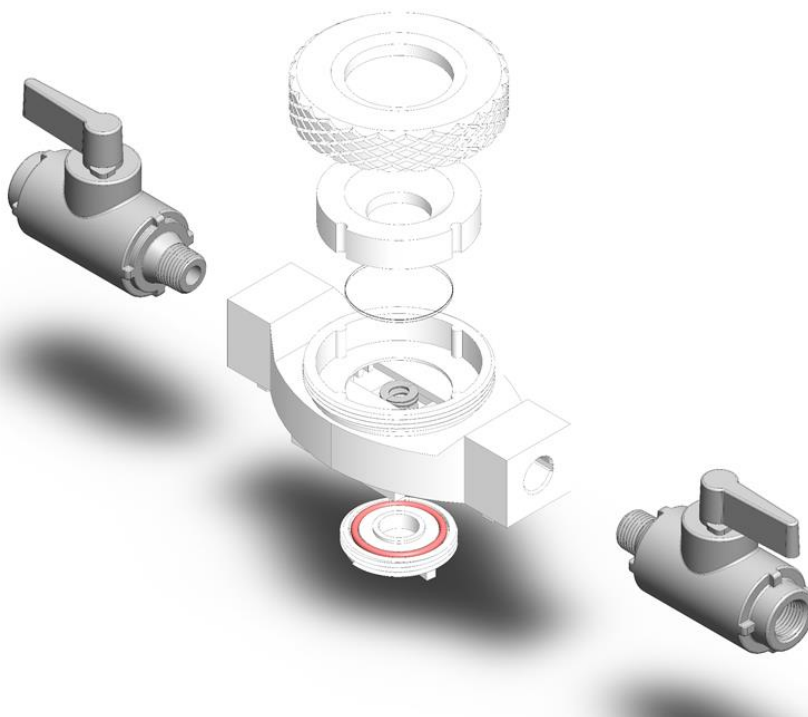


Figure 88

In situ Raman flow cell (IRFC) reactor 3D sketch

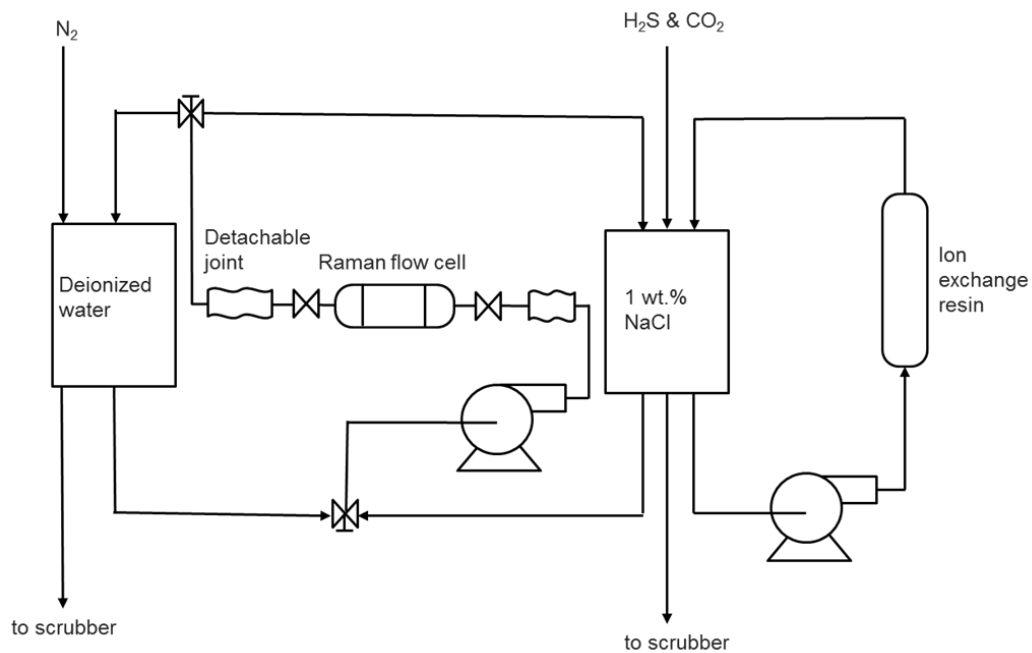
(Image courtesy of Cody Shafer, ICMT)



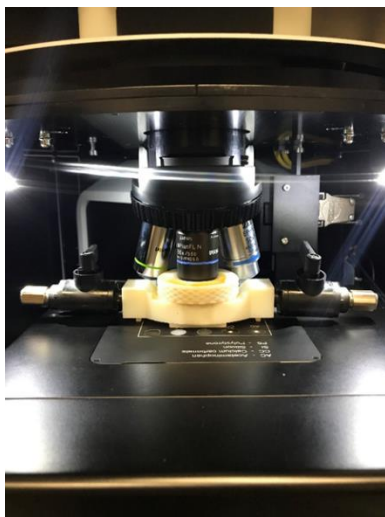
The *in situ* Raman flow loop was designed based on the sketch shown in Figure 89. The *in situ* Raman flow cell (IRFC) reactor was connected with two reservoirs of aqueous solutions with detachable connectors and three-way valves. The flow loop could be switched between 1) the 30 °C, pH 5.01 ± 0.01 , 0.97 bar CO₂ and 0.04 mbar H₂S saturated 1wt.% NaCl solution; and 2) the nitrogen saturated deionized water at 30 °C. Pictures in Figure 91 show the finished *in situ* Raman flow loop and cell.

Figure 89

P&ID of the designed in situ Raman flow loop

**Figure 90**

Pictures of the in situ Raman flow cell & flow loop



7.2.2 Experimental Procedure

The entire flow loop was rinsed thoroughly with deionized water before each experiment. Then, two liters of 1 wt. % NaCl, prepared with deionized water, was added into the flow loop. The temperature was set at 30°C. CO₂ gas with chemical grade purity was sparged into the aqueous solution for at least 2 hours. The pH was first adjusted to near 5 by addition of Na₂CO₃, then the automatic titration system with an ion exchange resin column was turned on to adjust the pH to precisely 5.01 ± 0.01 and where it was maintained at this value. Then a H₂S/CO₂ gas mixture with the ratio of 100 ppm H₂S in 1 bar CO₂ was sparged into this solution together with the pure CO₂ gas. A rotameter was used to adjust the volume ratio between the H₂S/CO₂ mixture and the pure CO₂ gas to get the required concentration of H₂S. Five X65 steel specimens (four for weight loss, one as the working electrode) were loaded into the 2-liter glass cell after the conditions were stable. Another X65 steel specimen was loaded into the *in situ* Raman flow cell. The *in situ* Raman flow cell was connected to the flow loop. The corrosion experiment was then started. During the 7-day exposure, the *in situ* Raman flow cell could be detached from the flow loop whenever needed. The dissolved oxygen concentration of the solution was monitored by a Hach[®] Orbisphere oxygen sensor at the outlet of the gas sparging system during the 7 days of each experiment.

7.3 Results and Discussion

7.3.1 Seal test of the IRFC

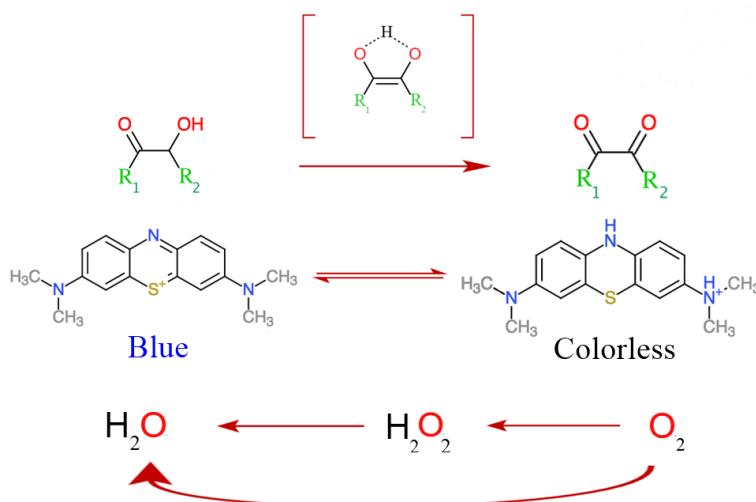
Methylene blue as an oxygen indicator was used together with glucose to test whether oxygen ingress could occur inside the Raman cell after it was disconnected from

the flow loop. The redox reaction, which induces the color change, is shown in Figure 91 [187].

Figure 91

Using methylene blue as oxygen indicator to test cell tightness

(Thyphoon7979 https://commons.wikimedia.org/wiki/File:Complete_reactions_of_blue_bottle_experiment.png, <https://creativecommons.org/licenses/by-sa/4.0/legalcode>)

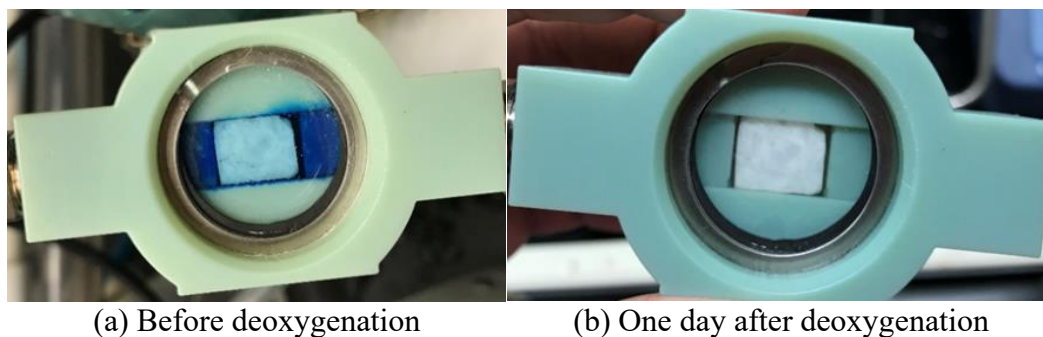


As shown in Figure 92, the methylene solution is originally blue in color. After being heated to above 40°C , it is reduced into a colorless anoxic solution. The solution would only turn blue if exposed to oxygen. During operation, the solution remained colorless for at least one day. The threshold of color change for methylene blue is measured to be 1.3 ppm by an Orbisphere oxygen meter at the gas outlet incorporated in the experimental setup. It is understood that this method is rather crude since it cannot

detect dissolved oxygen content below 1.3 ppm. However, it constituted an initial pass/fail method to validate the cell design.

Figure 92

Sealing capacity of the IRFC



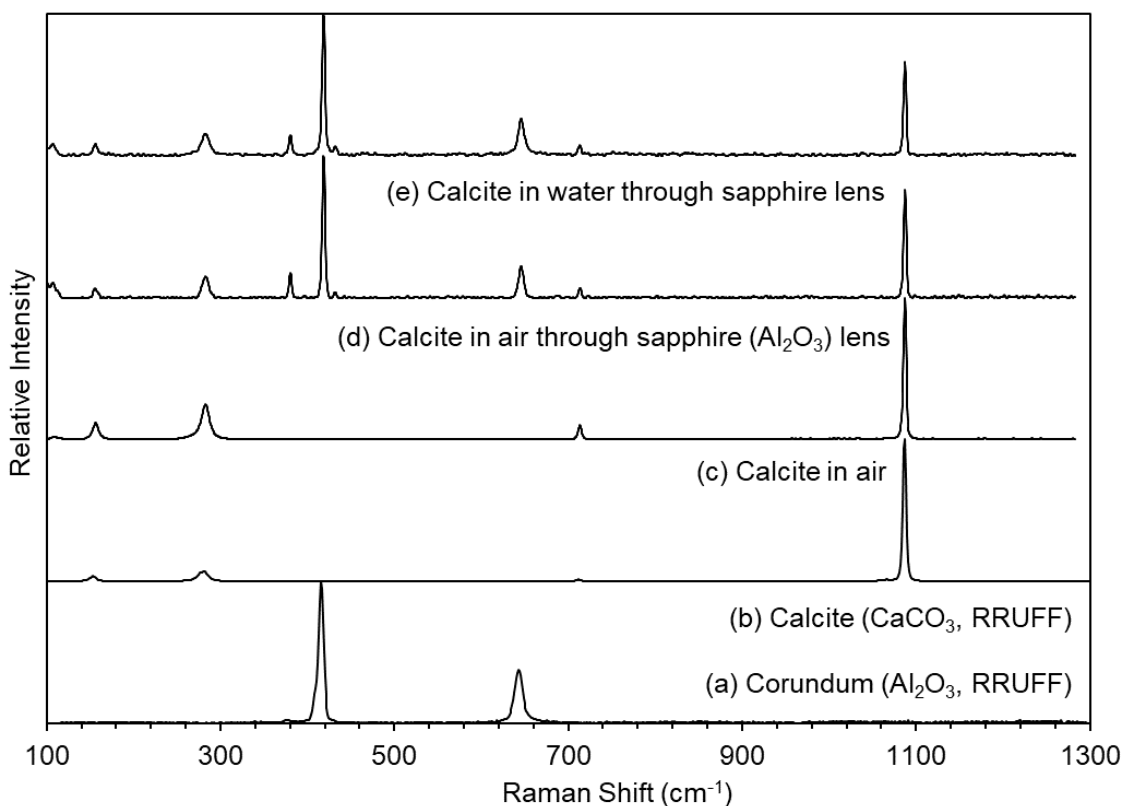
7.3.2 Calibration with Minerals of Known Structures

Bulk mineral specimens of known crystalline identity were introduced into the Raman cell to verify that they could be successfully identified during normal operating conditions. The cell was first tested with calcite because calcite has a hugely prominent intense peak of a carbonyl group (C=O in carbonate), which is expected to be easily detectable through a sapphire lens, given the sapphire itself will contribute to the background signal on the Raman spectrum. The calibration result by $\times 10$ objective is shown in Figure 93. From bottom to top: the first (a) and second (b) spectra are reference data of calcite and corundum (sapphire window), respectively, from the RRUFFTM database (American Mineralogist Crystal Structure Database); the third spectrum (c) is commercially available calcite mineral in air, directly exposed to the laser; the fourth spectrum (d) is calcite inside the IRFC; the fifth spectrum (e) is with deionized water

injected into the IRFC with the calcite. The fourth spectrum (d) shows that both the lens and the sample signal were picked up in the spectrum when the $\times 10$ objective was used. With the two characteristic peaks of corundum near 400 cm^{-1} and 600 cm^{-1} labeled and subtracted, the Raman spectrum appears just as it would without the lens. The fifth spectrum (e) shows that water does not add extra peaks below a Raman shift of 1300 cm^{-1} , where the inorganic bond movement relating to corrosion products and scales is located. Since the focusing length of the $\times 10$ objective is *ca.* 7 mm in this case, the optical system failed to focus on the different horizontal heights. Therefore, the structural information from the lens, the sample, and the media in between were combined in one spectrum. If an objective of higher magnification and longer working focal length is applied, and the confocal function at different heights is enabled, the sample information could be separated from the media and the lens.

Figure 93

Calibration of IRFC with calcite mineral standard sample ($\times 10$ objective)

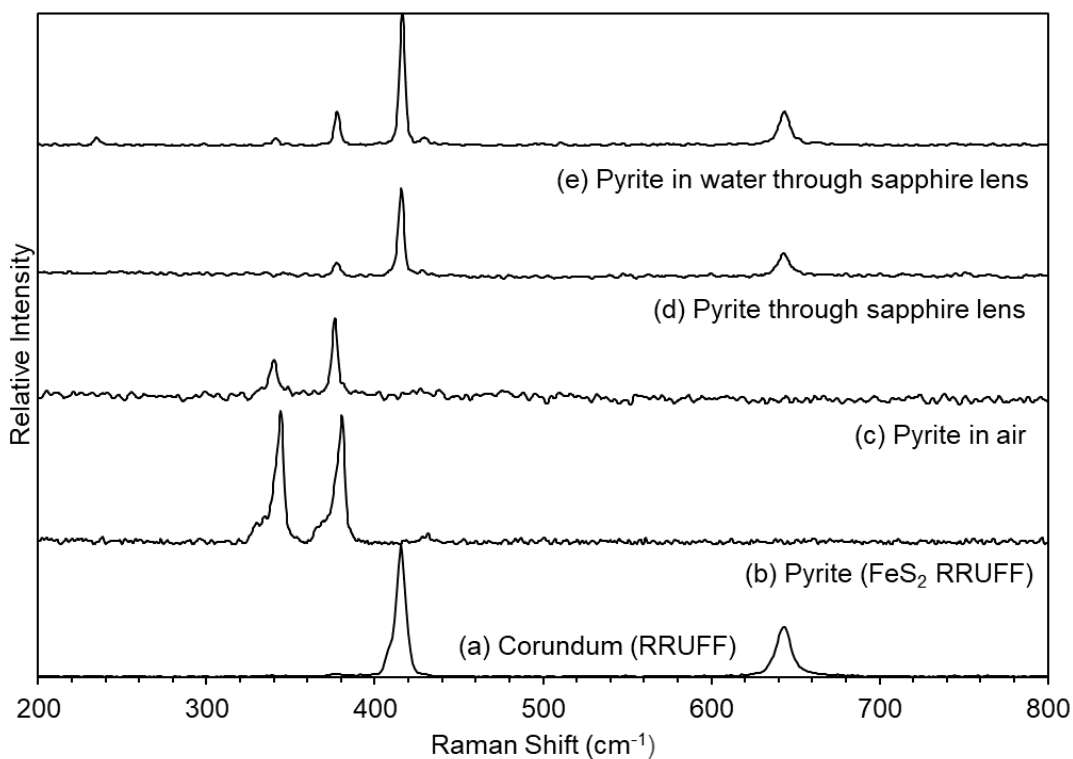


After calibration with calcite, which takes advantage of strong intensity of the signal, pyrite was tested to check for smaller signal intensity (compared to corundum) and whether Raman fluorescence would be a concern of the IRFC. The calibration result is shown in Figure 94. From bottom to the top, the first (a) and second (b) spectra are references from the RRUFFTM database of pyrite and corundum, respectively; the third spectrum (c) was acquired from a commercially available pyrite mineral in air, directly exposed to the laser; the fourth (d) spectrum was pyrite inside the IRFC; the fifth (e) spectrum was acquired after deionized water was injected into the IRFC with the pyrite.

Although the peak intensity of pyrite was small compared with that of corundum, as shown in the fourth spectrum, a very good focus facilitated by water made it detectable, as shown in the fifth spectrum. Pyrite is not as easily oxidized in air near room temperature as has been stated elsewhere [188], nor was it oxidized immediately after being in contact with water in air.

Figure 94

Calibration of IRFC with pyrite



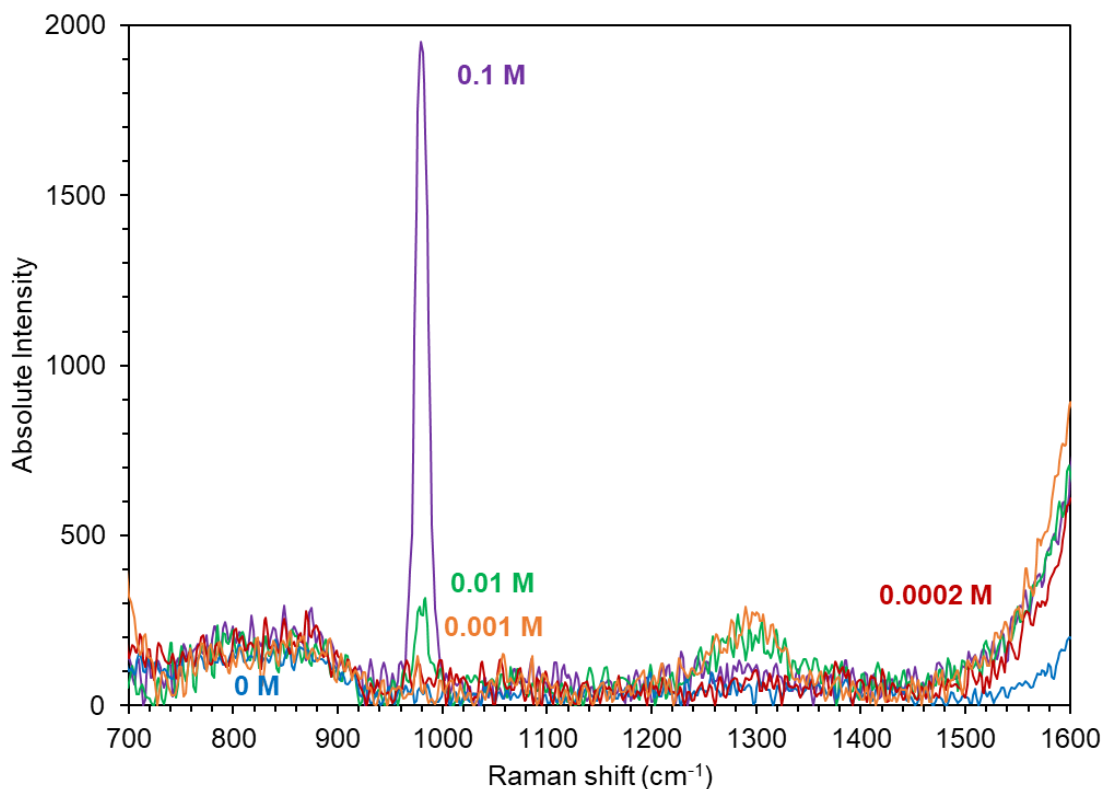
7.3.3 Detection of Sulfate Species with *in situ* Raman

As shown above, the Raman cell showed promising results with identifying deposited solid phases on metal specimens. It can also be used to detect specific

chemicals present at small concentration in a solvent. This is of prime interest for the research reported in this dissertation since it could potentially be used to detect products of H₂S oxidation (*i.e.* sulfate species). Consequently, a series of a calibration tests were performed to explore the resolution limit for SO₄²⁻ detection. As shown in Figure 95, different concentrations of Na₂SO₄ could influence the intensity of its characteristic peak near 980 cm⁻¹ [189]. However, the detection limit for Na₂SO₄ is 0.01 mol/L, which may be too high to be truly useful. For instance, water chemistry calculation shows that at baseline condition (30°C, 1 wt. % NaCl, pH 5.01 ± 0.01, 0.97 bar CO₂ and 0.04 mbar H₂S), the HCO₃⁻ concentration is 0.002 mol/L, and the dissolved H₂S concentration is 3.7 × 10⁻⁶ mol/L. Therefore, it is unlikely that sulfate solute will be detected in *in situ* Raman spectra in the sour corrosion experiments. Although there is 0.17 mol/L NaCl in the solution, neither Na⁺ nor Cl⁻ can be detected by Raman spectroscopy as they are simple, rather than polyatomic, ions [189]. NaCl could affect the position of H₂O's characteristic peak near 3500 cm⁻¹, but this information is not helpful in corrosion studies.

Figure 95

Raman spectra of standard Na_2SO_4 solution of various concentrations showing the characteristic peak of Na_2SO_4 detectable above 0.01 mol/L



7.3.4 Possible Oxidation Products of Mackinawite

Raman spectroscopy uses an inelastic scattering of monochromatic light to detect vibrational, rotational, and other low-frequency modes. One of the unique merits of this method is that Raman spectroscopy can be applied through water and through glass, which makes analysis of the material through a specialized holder possible. It is understood that mackinawite is vulnerable to oxidation in air, especially considering laser heating effects, as well as traces of dissolved oxygen in the H_2S aqueous solution.

However, as stated in Chapter 5, *ex situ* Raman spectra cannot tell whether the oxidation happened during the corrosion tests or post-processing [166]. Therefore, the optimal option is to apply *in situ* Raman in an anaerobic environment to prevent oxidation.

There are many possible oxidation products of mackinawite and it is worth investigating what phases could be expected. Reported oxidation products of mackinawite include greigite [82, 190], elemental sulfur, magnetite [75, 191], goethite (α -FeO(OH)), and lepidocrocite (γ -FeO(OH)) [74]. Greigite was deemed as an intermediate oxidation product, which converts into oxides and elemental sulfur over a period of time [191]. In addition, hematite (α -Fe₂O₃) and maghemite (γ -Fe₂O₃) have been reported as oxidation products of mackinawite [74]. It has been found [75] that mackinawite oxidation does not necessarily mean that a new phase will be detected. Fe (III) has been reported to incorporate into the tetrahedral sites of mackinawite [192] and will not be detected as a new phase if its content is lower than 20% [193].

One of the challenges facing this study is that the standard database of iron sulfides for Raman spectra is in places sparse and incomplete. Generally speaking, the nanocrystalline [75], amorphous [193, 194], or partially oxidized mackinawite [75, 195] all have distinct peaks, shifted peaks, or broadened peaks as compared to a well-crystallized mackinawite [75]. Typical Raman shift peak positions for mackinawite and its oxidation products are summarized in Table 16. According to Bourdoiseau *et al.*, [75], freshly synthesized nanocrystalline mackinawite has two peaks, one at 208 cm⁻¹, which corresponds to its lattice mode [196]; and another at 281~298 cm⁻¹, which is the symmetric stretching mode of FeS [75]. Further, the degree of crystallinity will change

the latter, not the former. The 208 cm^{-1} peak shifts to $214\sim 218\text{ cm}^{-1}$ in amorphous mackinawite, and even shifts to 254 cm^{-1} in the case where the specimen is first pre-corroded aerobically before sulfide is added. However, a careful comparison between some of the *in situ* Raman spectra [74, 75] with other *ex situ* Raman spectra [193, 194, 197] reveals that hematite is commonly mistakenly labeled as mackinawite. Simply put, any “mackinawite” spectrum that includes peaks other than 208 cm^{-1} (1st peak in Table 16) and 282 cm^{-1} (2nd peak in Table 16), like 395 cm^{-1} (3rd peak in Table 16) or 1310 cm^{-1} (4th peak in Table 16), does not identify mackinawite but is representative of its oxidation.

Table 16

Reported Raman peak positions for mackinawite and other relevant iron sulfur-containing phases

Compound	Composition	1 st peak	2 nd peak	3 rd peak	4 th peak
Nanocrystal Mackinawite [75]	FeS	208	282		
Amorphous Mackinawite [193]	FeS	214	282		
Amorphous Mackinawite [194]	FeS	218	281	395	
Oxygen Pre-corroded Mackinawite [198]	FeS	254	302	362	
Mackinawite (This work)	FeS	218	284	395	
Pyrrhotite [199]	Fe _(1-x) S	326	376		
Greigite [200]	Fe ₃ S ₄	248	345		
Goethite [201]	α -FeO(OH)		300	390	
Lepidocrocite [75, 202]	γ -FeO(OH)	250	380	525	
Magnetite [203]	Fe ₃ O ₄	297	523	666	
Hematite [204, 205]	Fe ₂ O ₃	223	289	404	1310
Maghemite [206]	Fe ₂ O ₃	377	510	670	715
Cementite (Cohenite) [207]	Fe ₃ C	1360	1580		
Elemental sulfur [208]	S ₈	154	220	473	
Siderite [209]	FeCO ₃	188	290	732	1087

7.3.4.1 Ex situ Raman Spectra of Thick Mackinawite/Pyrrhotite Layer

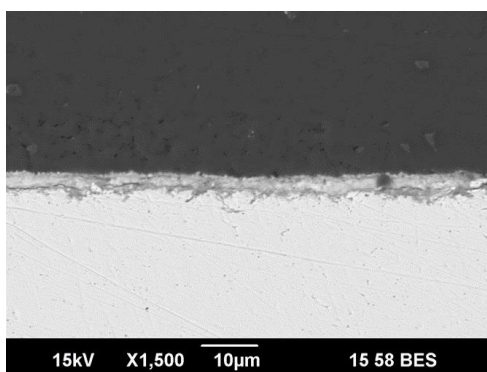
Formed at High H₂S Partial Pressure. *Ex situ* Raman spectroscopy was used to analyze both thick and thin layers in order to verify if the corrosion product layers have been oxidized after being retrieved from the reactor and dried. Later, it will be compared with the *in situ* Raman spectra.

First, a thick FeS layer formed on C1018 steel and prepared at 80 °C under 2 bar H₂S, pH 4.0, 1 wt.% NaCl for 2 weeks, was analyzed by *ex situ* Raman spectroscopy. Figure 96 shows the thickness of the layer is about 3 μm (a), with scattered pyrrhotite crystals on top of mackinawite (b) [210].

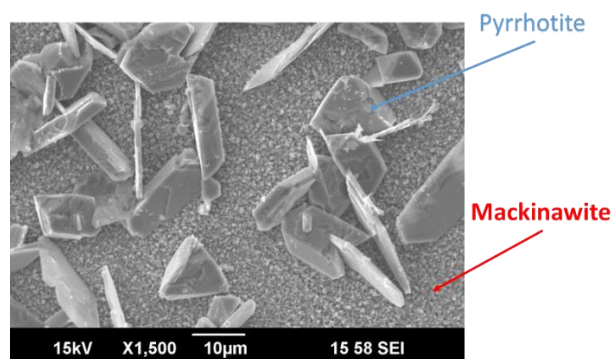
Figure 96

SEM analysis of the thick mackinawite layers

(Reprinted with permission from [210]. Copyright 2019 OhioLINK.)



(a) SEM of cross section of the layers.



(b) SEM shows pyrrhotite on top of mackinawite

Figure 97 shows the XRD analysis of the layer confirming both mackinawite and pyrrhotite were present [210]. This analysis was performed immediately after the specimen was retrieved from the reactor, so no sign of oxidation was found.

Figure 97

XRD analysis of the layer showing both mackinawite and pyrrhotite

(Reprinted with permission from [210]. Copyright 2019 OhioLINK.)

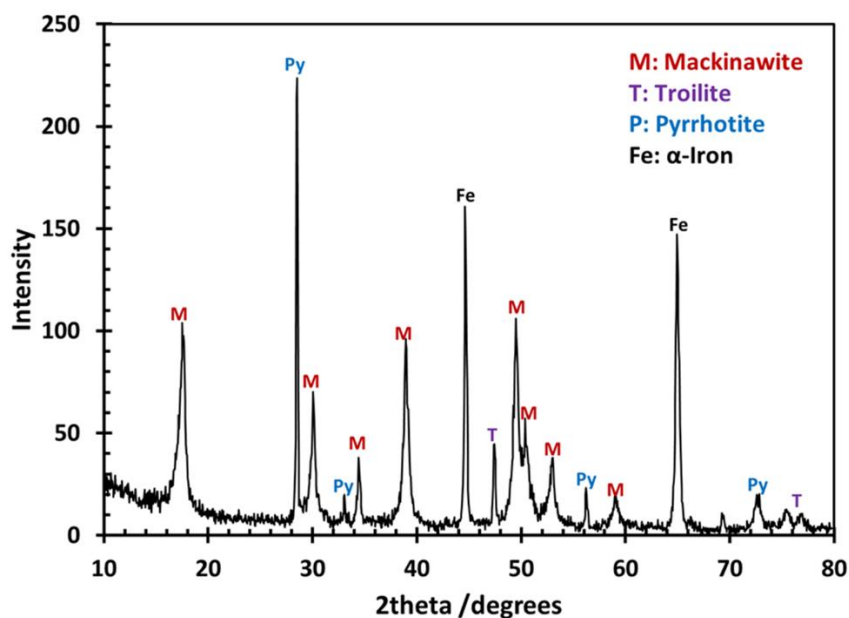
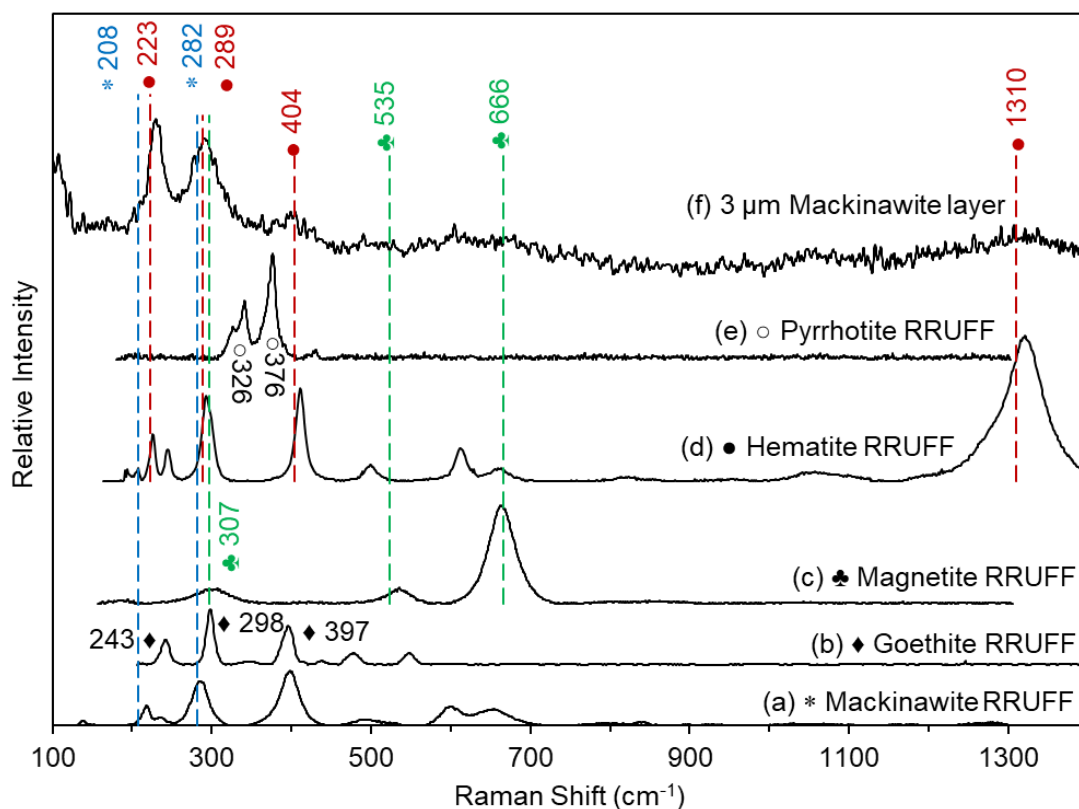


Figure 98 compares two Raman spectra of the corroded C1018 steel specimen with a 3 μm thick mackinawite/pyrrhotite layer, with related RRUFFTM database spectra. This specimen was the same one that was characterized by XRD, but was exposed to air for a significant time before Raman analysis was performed. Both mackinawite and hematite were identified in the Raman spectra, although mackinawite seemed to be dominant. Here the mackinawite qualitatively corresponds to the bulk of the layer

composition. However, the pyrrhotite crystals could not be detected by Raman analysis, possibly because they were too scattered on the surface and because the location of the analysis missed them; Raman microscopy (laser spot size $0.5 \sim 10 \mu\text{m}$) yields spectra from an area orders of magnitude smaller than XRD (spot size $> 20 \mu\text{m}$).

Figure 98

Ex situ Raman spectra of the 3 μm thick mackinawite / pyrrhotite corrosion product layer and comparison with RRUFF data

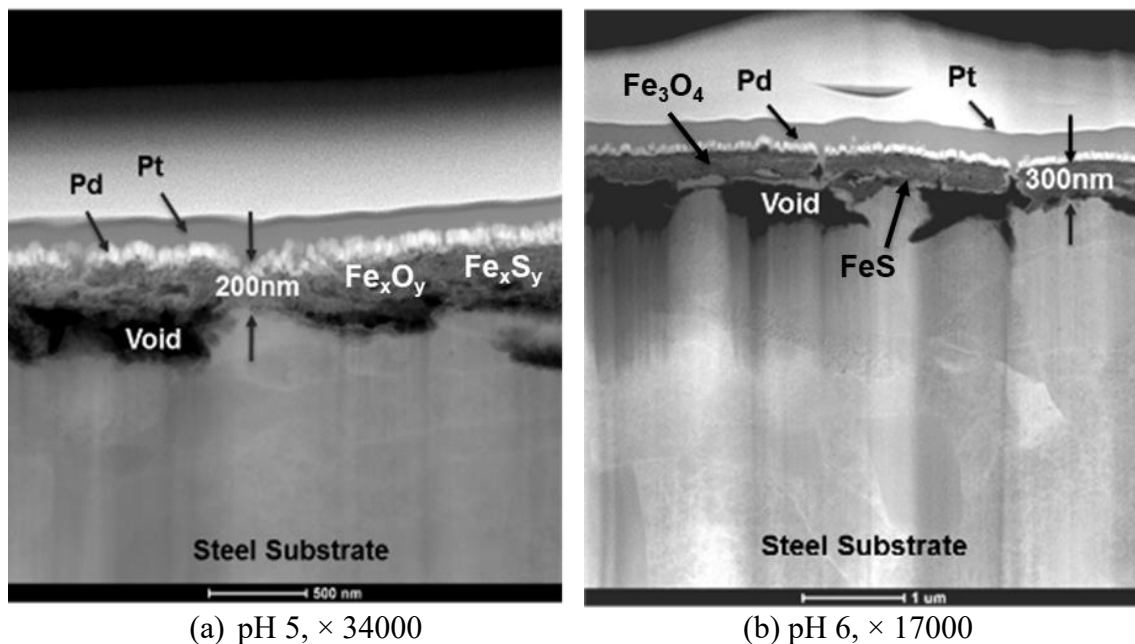


7.3.4.2 Ex situ Raman Spectra of Thin Mackinawite Layers Formed at Low H_2S Partial Pressure. The analysis was repeated *ex situ* on a much thinner layer. Two

experimental conditions were chosen: 1) 30°C, pH 5.01 ± 0.01 , 0.97 bar CO₂, 0.04 mbar H₂S, 300 rpm stir bar, 7 days, [O₂]_(aq) $\approx 20 \sim 40$ ppb_(w); 2) 30°C, pH 6.01 ± 0.01 , 0.97 bar CO₂, 0.04 mbar H₂S, 300 rpm stir bar, 7 days, [O₂]_(aq) $\approx 20 \sim 40$ ppb_(w). The corrosion product layers formed under these two conditions were typically porous, existing as a *ca.* 200 nanometer thick mixture of iron sulfide and iron oxide. As shown in Figure 38 and Figure 39, neither XRD nor SAED could provide precise diffraction patterns of these nanolayers. SAED could identify the outer layer at pH 6 as magnetite, the inner layer was mistakenly matched with Fe_{0.91}S (Figure 39, Table 10). PED made the correct diffraction mapping match as mackinawite (FeS, Figure 40). Figure 99 summarizes these layers' structural information and compares them.

Figure 99

TEM images of the cross section cut out by FIB from the specimen of pH 6 experiments (30°C, 0.97 bar CO₂, 0.04 mbar H₂S, X65, 1wt.% NaCl, 300 rpm, 7 days, [O₂]_{aq} = 20 ppb_(w)) [166]



Besides TEM-EDS, XPS was also applied on the specimen generated at the pH 6 condition (X65, 30°C, 0.04mbar H₂S and 0.97 bar CO₂, pH 6.01 ± 0.01, 1wt.% NaCl, 300 rpm, 7 days). As Figure 100 and Figure 101 show, iron sulfide, oxide or hydroxide were detected, which agrees with the FIB-TEM results. The sampling depth of the XPS is very limited compared with FIB-TEM. Therefore, the sample could not be plated with any protective layer such as Au or Pd for preservation before transferring to the XPS sampling chamber. Although the samples had been sputtered to remove contamination, whether this procedure was completely effective to remove *ex situ* oxidation products is unknown. Consequently, whether the oxyhydroxide or oxide was generated *in situ* or *ex*

situ cannot be unequivocally determined with this method. Therefore, XPS is not an ideal tool in terms of layer analysis in sour corrosion studies when specimen oxidation is expected.

Figure 100

XPS results—the elemental composition of the corrosion product layers

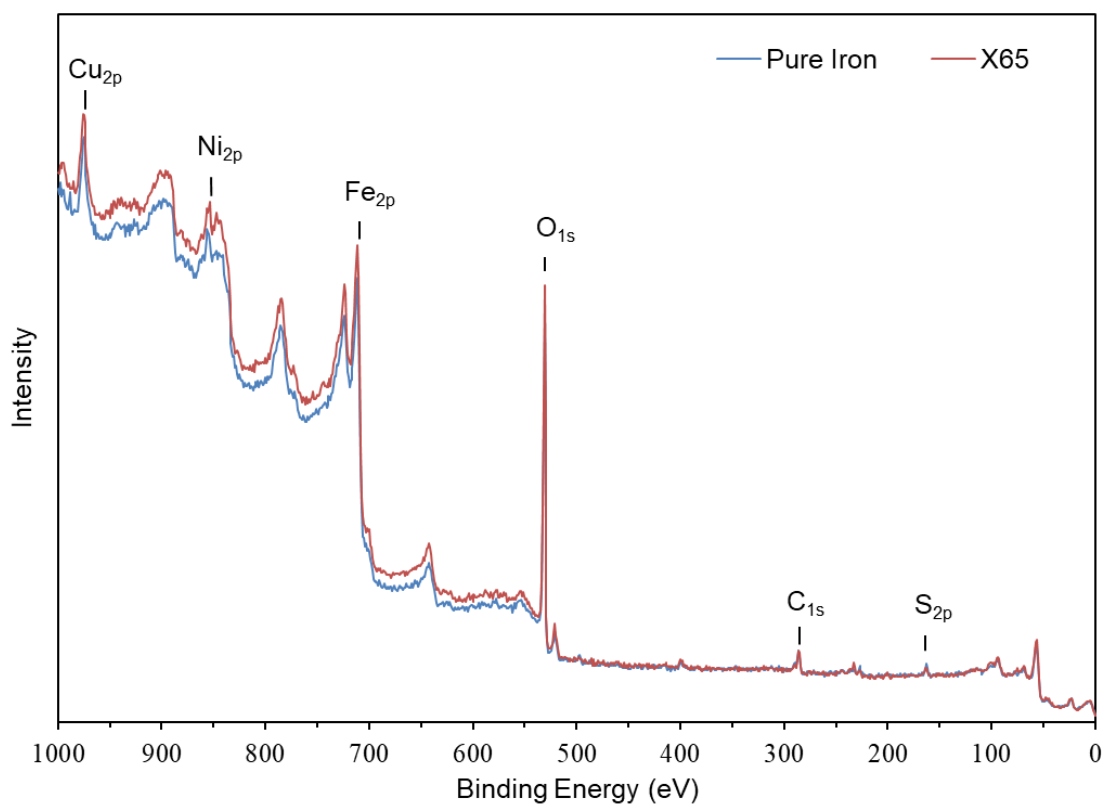
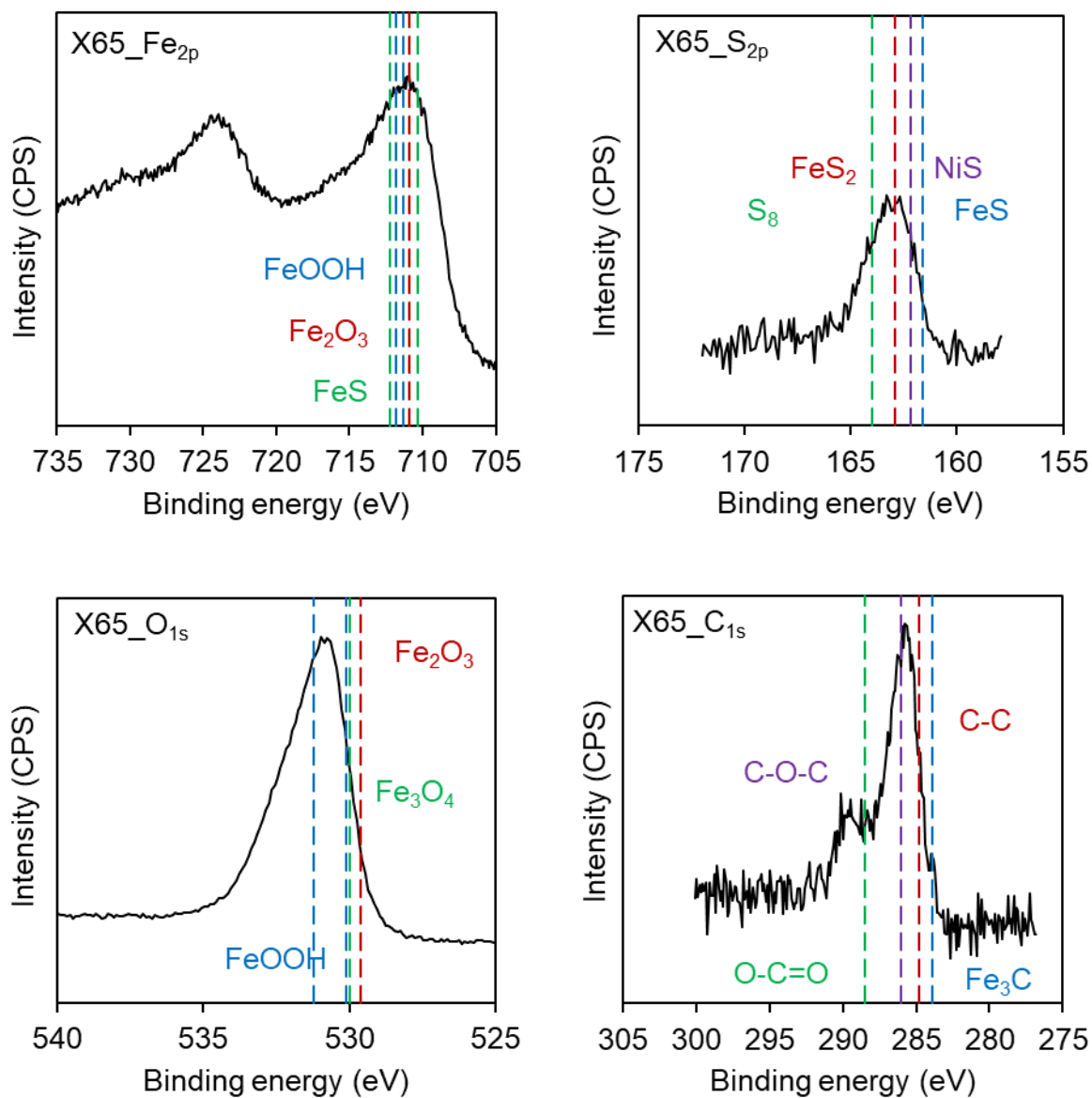


Figure 101

XPS spectra of pure iron and X65 specimens exposed to the pH 6 condition (X65, 30°C, 0.04 mbar H₂S and 0.97 bar CO₂, pH 6.01 ± 0.01, 1wt.% NaCl, 300 rpm, 7 days)

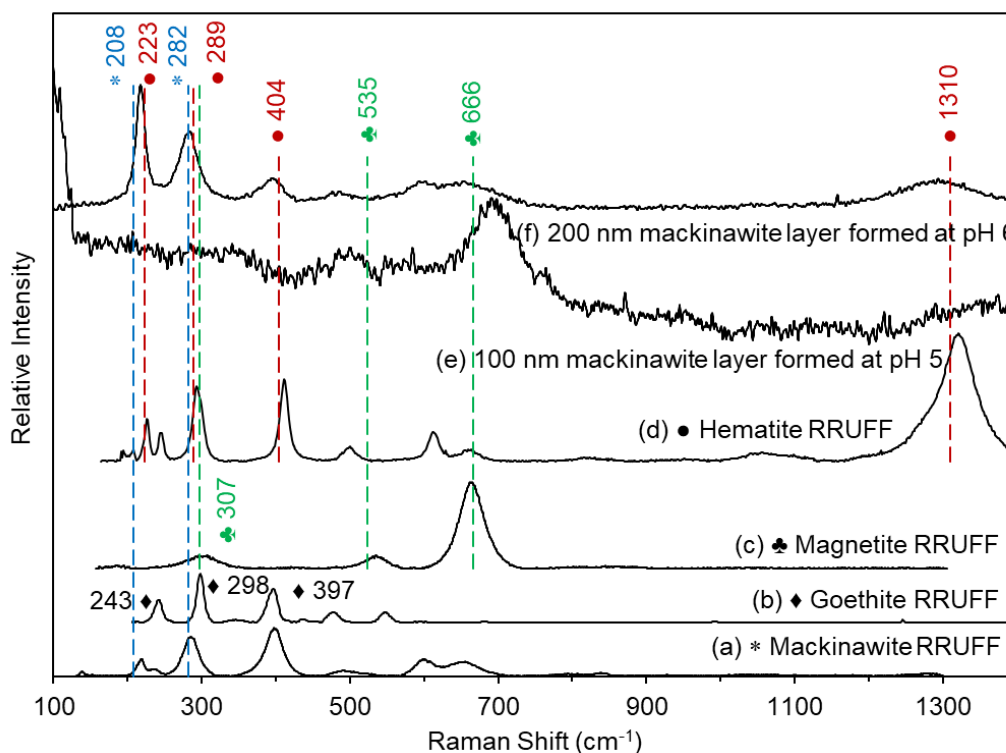


In Figure 102, the Raman spectra of both pH 5 (baseline condition) and pH 6 specimens were compared with the RRUFF database spectra of all the possible oxidation

products of iron sulfides. The curve (f) is the Raman spectra of a corroded X65 steel specimen with a 200 nm porous corrosion product layer, according to FIB-TEM analysis. A possible combination of mackinawite and hematite fits spectrum (f), because: 1) the first peak of curve (f) from the left could be explained by an overlap between 218 cm^{-1} (mackinawite) and 223 cm^{-1} (hematite, Fe_2O_3); 2) the second peak of curve (f) could be an overlap with mackinawite at 282 cm^{-1} , hematite at 289 cm^{-1} , and goethite at 298 cm^{-1} ; 3) plateaus near the Raman peaks at 404 cm^{-1} and 1310 cm^{-1} belong to hematite only. On the other hand, only magnetite can be identified in the “baseline pH 5” spectrum (e) by the peak near 666 cm^{-1} , which indicates the mackinawite has been oxidized. The mackinawite peaks failed to be detected on spectrum (e). Again, this agrees with the previous findings based on TEM (Figure 99) that the baseline corrosion product layer was very thin and porous; the uneven surface of this layer returns weak signals. Compared to the layers formed at pH 5, the morphological features formed at pH 6 seem more ordered, which echoes the TEM-SAED findings (Figure 38 and Figure 39) once again. However, it is noteworthy that the mackinawite formed at pH 5 was oxidized into magnetite, while the similar layer formed at pH 6 was oxidized into hematite.

Figure 102

Ex situ Raman spectra of the thin mackinawite corrosion product layer and comparison with RRUFF data



7.3.4.3 Oxidation Route of Mackinawite in the Air (Converted from

Magnetite to Hematite with Time). In order to determine the oxidation route of

mackinawite, another *ex situ* Raman analysis (Figure 64) was performed on a freshly retrieved and dried specimen from a corrosion experiment at the baseline condition

(30°C, pH 5.01 ± 0.01, 0.97 bar CO₂, 0.04 mbar H₂S, 300 rpm stir bar, 7 days, [O₂]_(aq) ≈ 20 ~ 40 ppb_(w)). This first scan (a) of this specimen shows that the mackinawite in the

layer had not yet been oxidized; the second scan performed 20 minutes later on a

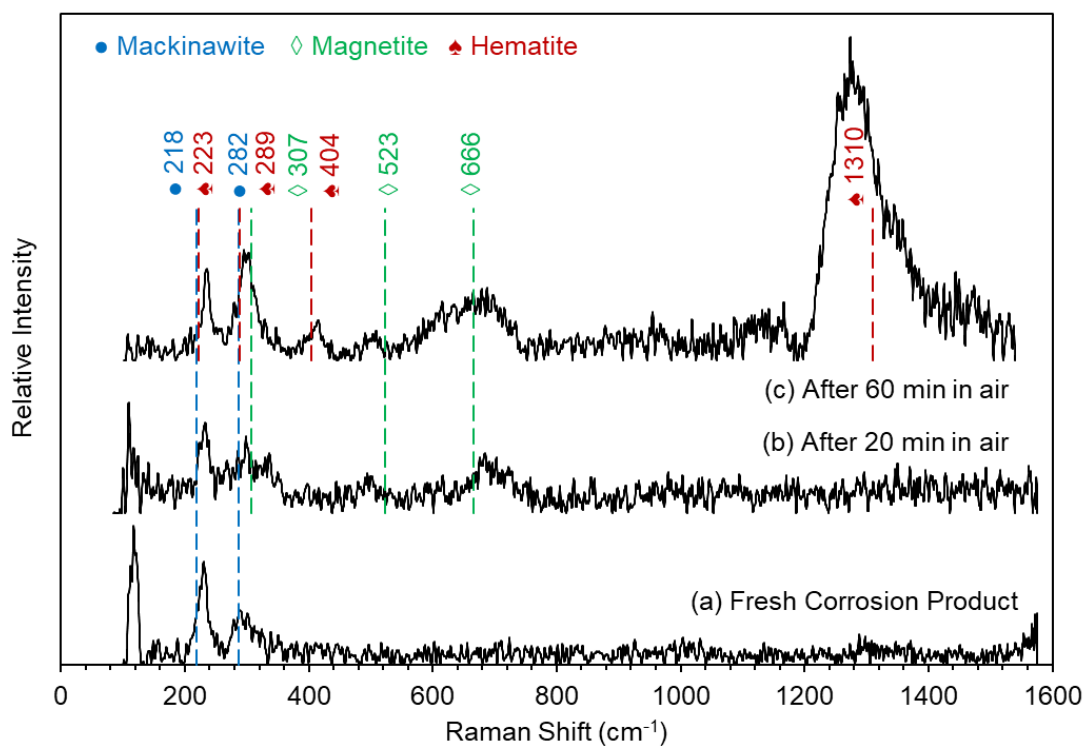
different spot shows that the mackinawite had been partially oxidized into magnetite;

while the third scan performed 40 minutes later on another spot suggests that the mackinawite was finally converted into hematite. Therefore, the oxidation route of mackinawite in the air appears to be as follows:
 mackinawite \rightarrow magnetite \rightarrow hematite.

Figure 64

Oxidation of mackinawite with time measured with a Raman microscope (laser excitation line 532 nm, power 25W

(The specimens were corroded at 30 °C, pH 5.01 \pm 0.01, 0.97 bar CO₂, 0.04 mbar H₂S, 300 rpm stir bar, 7 days, [O₂]_(aq) \approx 20 ~ 40 ppb_(w)) [166]



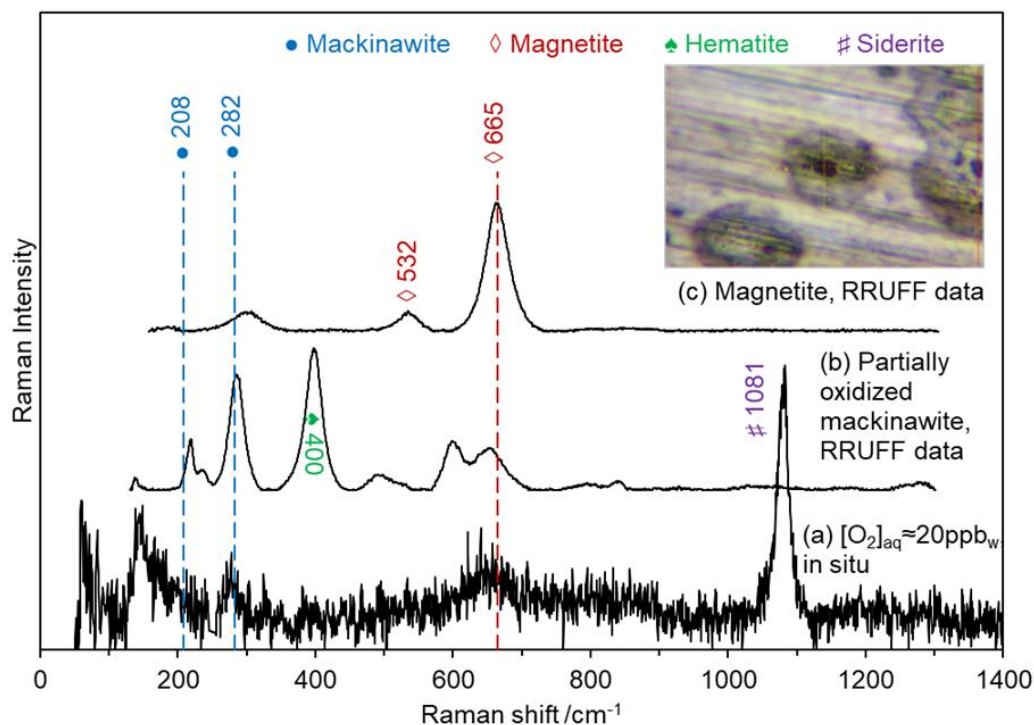
7.3.5 *In situ* Test Result on Precipitated Mackinawite Layer

Since mackinawite is extremely sensitive to oxidation in post-processing (drying process and storage), as shown by previous studies on thick, thin and freshly retrieved corrosion product layers (Figure 98, Figure 102, and Figure 64), *in situ* Raman is probably the only way to show the original status of the mackinawite corrosion product layers in sour corrosion. Therefore, a 7 day corrosion experiment was performed at the baseline conditions (30°C, pH 5.01 ± 0.01 , 0.97 bar CO₂, 0.04 mbar H₂S, 300 rpm stir bar, 7 days, [O₂]_(aq) $\approx 3 \sim 20$ ppb_(w)), where localized corrosion was observed repeatedly. *In situ* Raman analysis was done every day to investigate the formation and transformation (*i.e.*, oxidation) of corrosion product layers. As shown in Figure 67, after four days of exposure, the *in situ* Raman spectrum of the corrosion product layer shows that mackinawite has been partially oxidized into magnetite due to the presence of 7 ppb_(w) of dissolved O₂. This finding reveals that O₂ could still affect H₂S corrosion, if there are traces of dissolved O₂ (>3 ppb_(w)). When continuously sparged with gases such as H₂S, CO₂, and/or N₂, O₂ could still effectively impact this corrosion system. At this stage, it is hypothesized that the initiation of pitting is due to the partial oxidation of the FeS layer. To verify this hypothesis, no pitting should be detected at O₂ content below 3 ppb_(w).

Figure 67

In situ Raman spectroscopy analysis: direct proof of oxidation of mackinawite into magnetite in the aqueous solution on a corroding surface

(Baseline condition with $[O_2]_{aq} = 3\sim 20$ ppb_(w), after 4 days) [166]



7.3.6 *In situ* Test Result on Chemisorbed $S_{ads}(Fe)$ Layer

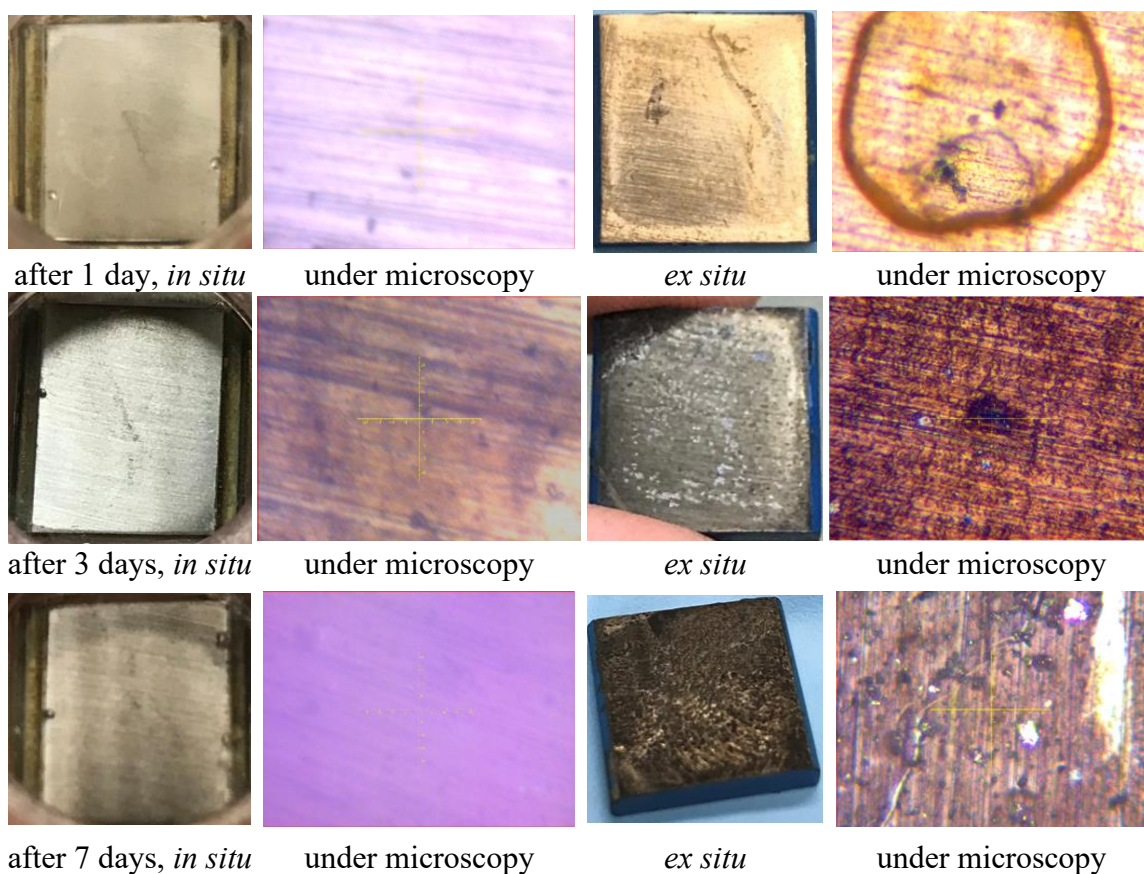
Corrosion experiments at baseline condition with $[O_2]_{aq} < 3$ ppb_(w) were performed to verify the finding that oxygen induced pitting corrosion in marginally sour environments. As a reminder, neither a corrosion product layer nor pitting was found during the 7-day experiments, as shown in the FIB-TEM (Figure 70) and IFM results (Figure 72). However, one phenomenon worth noting is that this “layer-free” steel surface featured a relatively very low corrosion rate at 0.1 mm/y (Figure 68) compared

with other conditions where a thick layer could be observed. Therefore, it was speculated that a chemisorbed $S_{\text{ads}}(\text{Fe})$ layer [24] had formed and was responsible for this lower corrosion rate and pitting-free result. It is a challenge for Raman observation given the assumption that the $S_{\text{ads}}(\text{Fe})$ is akin to a monomolecular layer. It is important to note that maintaining a dissolved O_2 content below 3 ppb_(w) is a challenge due to the complex flow loop design, which involves multiple connectors. Therefore, the best effort to control ingress of oxygen could only achieve about a $[\text{O}_2]_{\text{aq}} = 5 \sim 7$ ppb_(w) average during the 7 days experiment at the baseline conditions. The surface condition of the corroding X65 steel specimens under the naked eye and microscope after 1, 3 and 7 days are shown in Figure 103. It shows that basically, the steel surface remained shiny in the first three days, while signs of formation of a precipitated layer were apparent after seven days of exposure. This is because $[\text{O}_2]_{\text{aq}}$ reached 7 ppb_(w) at that point, compromising the chemisorbed layer and leading to a surface saturation of FeS larger than unity.

Figure 103

Surface condition of the corroding X65 steel specimens under naked eye and microscopy after 1, 3- and 7-days exposure

(The baseline condition at 30 °C, pH 5.01 ± 0.01, 0.97 bar CO₂, 0.04 mbar H₂S, 300 rpm stir bar, 7 days, [O₂]_(aq) = 5 ~ 7 ppb_(w))

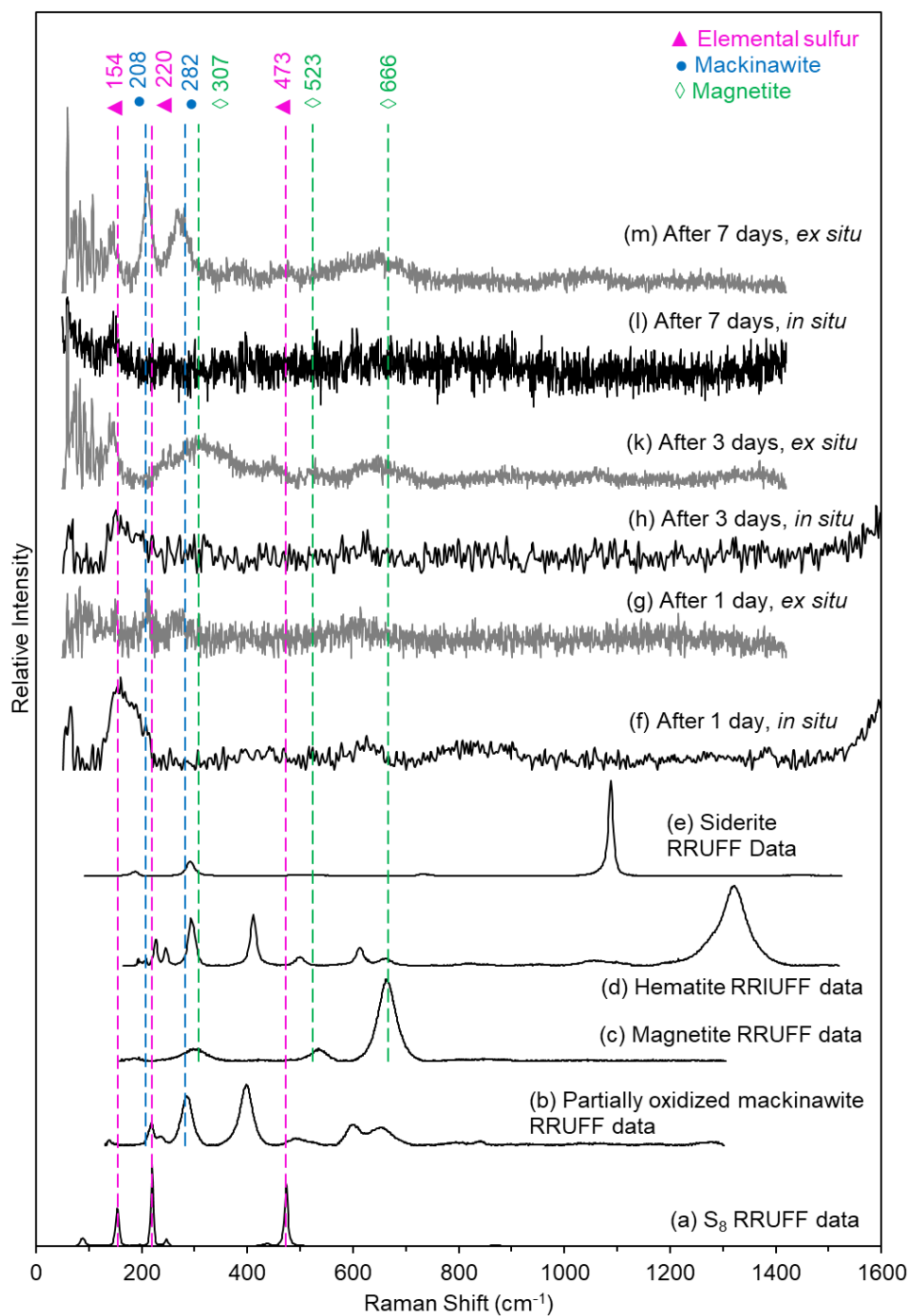


As shown in Figure 104, *in situ* and *ex situ* Raman spectra of the corroding surface at the baseline condition with [O₂]_{aq} = 5 ~ 7 ppb_(w) after 1, 3, and 7 days of exposure were compared with each other. The main result is that no clear product of mackinawite oxidation could be identified in the *in situ* analysis, yet the presence of mackinawite could also not be confirmed. The Raman peaks on the *in situ* Raman spectra

were not prominent compared with the noisy background, probably due to the attenuation of the laser signals with the longer focal length or the aqueous solution as the transmission medium. In contrast, the *ex situ* Raman spectra (line g, k and m) identified mackinawite but also magnetite. The *in situ* Raman spectra show a relatively strong peak around 150~200 cm^{-1} , which could be the possible match of bending or torsion vibration modes of the S-S bond in elemental sulfur (S_8). The literature [211] shows that the vibrations in the spectra of S_8 molecule appear as regions of stretching (ν , 400–475 cm^{-1}), bending (δ , 152–267 cm^{-1}) and torsion (τ , 86 and 150–191 cm^{-1}). However, the stretching mode related peak of S-S bond around 473 cm^{-1} was missing, although it is usually a strong peak at 25 °C in S_8 crystals. A reported Raman application on chemisorption of H_2S on copper impregnated activated carbon showed that the chemisorbed product was CuS [212]. Therefore, the $\text{S}_{\text{ads}}(\text{Fe})$ Raman spectrum should feature the same peaks as mackinawite at around 208 ~ 218 cm^{-1} (lattice vibration) and 281 ~ 298 cm^{-1} (symmetric stretching). However, once again, the peaks around 282 cm^{-1} are missing. Either the single broadened peak around 150 ~ 200 cm^{-1} in the *in situ* Raman spectra potentially related to the bending or to the torsion of the Fe-S bond without showing much stretching activity. At least the *ex situ* Raman spectrum shows that this layer featured the two characteristic peaks of mackinawite after being retrieved from the aqueous solution. More work, such as surface enhancement, is needed to obtain more detailed structural information about the $\text{S}_{\text{ads}}(\text{Fe})$.

Figure 104

In situ and ex situ Raman spectra of the corroding surface after 1, 3, 7 days of exposure (30°C, initial pH=5.01, pCO₂=0.97 bar, pH₂S=40 mbar, [O₂]_{aq} = 5~7 ppb_(w))



7.4 Summary

Due to the high reactivity between dissolved oxygen and H₂S/iron sulfides, standard analytical tools that required *ex situ* analysis are often not ideal for the analysis of generated surface layers during sour corrosion. In contrast, *in situ* Raman constitutes a promising tool in terms of phase identification of the corrosion product layers formed in H₂S corrosion. This method was implemented, and the preliminary findings are outlined below:

- An *in situ* Raman flow cell was designed, fabricated in-house using 3D printing and implemented in an existing glass cell setup enabling the study of corrosion product layer formation and transformation during experiments. O₂ ingress could be controlled to an acceptable level and a good seal of the cell could be maintained after being disconnected from the flow system to facilitate anaerobic Raman analysis;
- Aqueous sulfate species concentration lower than 0.01 mol/L cannot be detected by Raman spectroscopy using the experimental setup developed in this work;
- *Ex situ* Raman spectra showed that mackinawite layers were sensitive to oxidation in air, especially under the localized heating effect of the Raman laser;
- *In situ* Raman spectra showed that mackinawite layers were sensitive to partial oxidation in the aqueous solution by traces of dissolved oxygen ($[\text{O}_2]_{\text{aq}} > 3$ ppb_(w));

- *In situ* Raman spectra could identify very thin layers (less than 300 nm thickness), be it amorphous or nanocrystalline mackinawite, through the glass lens and aqueous solution;

In situ Raman spectra failed to identify the chemisorbed mackinawite layer – S_{ads}(Fe), while *ex situ* Raman spectra achieved it successfully.

Chapter 8: Conclusions and Future Work

8.1 Conclusions

An innovative and thorough investigation of localized corrosion of mild steel in marginally sour environments was completed. As a result, the root cause of this type of pitting, the presence of traces of oxygen, was successfully identified; a mechanism of pit initiation and propagation was proposed and verified experimentally. Thermodynamic modeling and kinetics considerations were used to explain the effect of traces of oxygen on the H₂S corrosion systems, affecting both the formation/transformation mechanism of the corrosion product layers and the chemistry of the aqueous solution. The main findings are:

- A comprehensive parametric study helped define the range of operating parameters conducive to repeatable occurrence of pitting on X65 steel in marginally sour environments containing H₂S and CO₂:
 - At H₂S partial pressure between 0.02 to 0.09 mbar;
 - At pH 4 and 5 (but not at pH6);
 - At 30°C only (but not 60 or 80°C);
 - At O₂ content above 3 ppb_(w).
- Surface analysis by FIB-TEM with SAED and PED showed that the corrosion product layer formed on X65 steel in marginally sour environments in the presence of traces of O₂ typically consisted of porous layers of 100~300 nm thickness, mainly constituted from mackinawite and magnetite.

- Experimental results obtained with different oxygen concentrations revealed that oxygen induced pitting can occur in the H₂S corrosion system.
 - In “anoxic” environments ($O_{2(aq)} < 3 \text{ ppb}_{(w)}$), H₂S is thought to first chemisorb on the steel surface to form S_{ads}(Fe). This layer is deemed to act as precursor to mackinawite, subsequently formed by precipitation from supersaturation of the local aqueous phase. Experimental results showed that the chemisorbed layer seemed to lead to a significant reduction of the corrosion rate, compared to equivalent layer-free steel environments at the same temperature, CO₂ partial pressure, and pH but without H₂S.
 - When traces of oxygen ($[O_2]_{aq} > 3 \text{ ppb}_{(w)}$) were present in marginally sour environments, the S_{ads}(Fe) protective layer is hypothesized to have been partially compromised by oxidation, exposing the base metal underneath the chemisorbed layer to the corrosive environment and leading to pit initiation.
- Results from *in situ* Raman analysis indicate that the mackinawite layer was oxidized into magnetite in the aqueous solution at the baseline condition (X65 in 0.04 mbar H₂S and 1 bar CO₂ at 30°C, pH 5.01 ± 0.01) in the presence of traces of oxygen.
- Thermodynamic modeling (using phase equilibrium diagrams) confirmed that mackinawite could be oxidized into magnetite at pH > 6, and ultimately, into hematite.

- Thermodynamic modeling also predicted that dissolved H_2S could be oxidized into H_2SO_4 in the presence of O_2 at low temperatures. Kinetic studies (measurements of sulfate species and proton buildup over time in the aqueous phase) confirmed that this reaction did happen in the tested environments, with dissolved Fe^{2+} and possibly Ni^{2+} , acting as catalysts.
- Catalytic oxidation of H_2S was proposed to be more prominent inside the pit, where the Fe^{2+} concentration was higher. Consistent with the experimental results, pit acidification and galvanic coupling are suggested to be the main drivers of the pit propagation.
- More generally, this work shows clearly that experimentation in marginally sour environments requires very tight control of the dissolved O_2 content. Many studies had shown previously that low H_2S content could lead to localized corrosion, but they all failed to identify oxygen contamination as the culprit. This led to erroneous conclusions that the present work is, in part, correcting.

8.2 Future Work

- Sulfur chemistry is very complex as many different redox and other chemical reactions can occur. While such reactions may not play a significant role in the modeling of uniform corrosion (especially when the oxygen content is low), they can become very influential in localized corrosion studies. A more comprehensive water chemistry model including the oxygen effect will likely prove useful to fully understand how sour corrosion is affected.

- The chemisorption process of H_2S on the iron/steel surface and the FeS formation should be further studied in strictly anoxic conditions. It is important for any future work to monitor and report oxygen concentration for any kind of sour corrosion study. The effect of oxygen should be included in the modeling of sour pitting corrosion. FeS saturation and layer formation kinetics should be studied in rigorously oxygen-free environments.
- In situ Raman is a promising tool in terms of phase identification in sulfur chemistry research. It is also a versatile technique that could be applied to other systems (CO_2 corrosion, corrosion inhibition). More work should be done to utilize its potential in corrosion research.
- One observation that remains unresolved so far is that no pitting occurred on pure iron in marginally sour environments. From the perspective of microstructure of iron and steel, it might relate to the selective adsorption of oxygen or H_2S on carbide and/or ferrite phases, or the formation of pentlandite $[(Ni,Fe)_9S_8]$ on X65. However, more details should be proposed and verified to evaluate this line of reasoning. For example: Is the Sads(Fe) layer different due to the presence of carbide? Or is the difference only shown with the presence of oxygen?
- It seems worthwhile to consider the consequences of the presence of trace amounts of oxygen as evidenced in this work for industrial systems such as marginally sour oil and gas production, where oxygen ingress may occur.

References

- [1] Y. Zhu, "Analysis and assessment of the Qingdao crude oil vapor explosion accident: Lessons learnt", *J. Loss Prevent. Proc.*, 33 (2015): 289-303.
- [2] A. Kreimer, M. Arnold, C. Barham, P. Freeman, R. Gilbert, F. Krimgold, R. Lester, J. D. Pollner, and T. Vogt, "Managing disaster risk in Mexico: market incentives for mitigation investment", *World Bank Publications*, ISBN 9780821344910, (1999): 44.
- [3] C. De Waard and D. E. Milliams, "Carbonic acid corrosion of steel," *Corros. J.*, 31 (1975): 175.
- [4] W. Sun, "Kinetics of iron carbonate and iron sulfide scale formation in CO₂/H₂S corrosion", *Ph.D. dissertation*, Dept. Chem. & Biomol. Chem. Eng., Ohio Univ., Athens, OH, (2006): 41-69.
- [5] Y. Zheng, "Electrochemical mechanism and model of H₂S corrosion of carbon steel," *Ph.D. dissertation*, Dept. Chem. & Biomol. Chem. Eng., Ohio Univ., Athens, OH (2014): 35-36.
- [6] Y. Sun, "Localized CO₂ corrosion in horizontal wet gas flow", *Ph.D. dissertation*, Dept. Chem. & Biomol. Chem. Eng., Ohio Univ., Athens, OH (2003): 31-32.
- [7] B. MacDougall and M. Graham, "Growth and stability of passive films", in *Corrosion Mechanisms in Theory and Practice*, P. Marcus editor, Marcel Dekker, Inc. (2002).
- [8] R. Crovetto, "Evaluation of solubility data for the system CO₂-H₂O", *J. Phys. Chem. Ref. Data*, 20, 575, 1991. In L. H. Gevantman, *Solubility of selected gases in water*,

Handbook of chemistry and physics, 2004 - 2005. Chemical Rubber Publ. Co., Cleveland. 84th ed., 8-87, 1318.

[9] R. Battino, Ed., "IUPAC Solubility Data Series", Vol. 7, *Oxygen and ozone*, Pergamon Press, Oxford, England, 1981. In L. H. Gevantman, *Solubility of selected gases in water*, *Handbook of chemistry and physics*, 2004 - 2005. Chemical Rubber Publ. Co., Cleveland. 84th ed., 8-89, 1318.

[10] W. Knoche, "Chemical reactions of CO₂ in water". In: C. Bauer C, G. Gros, H. Bartels (eds) *Biophysics and Physiology of Carbon Dioxide*, Proceedings in Life Sciences. Springer, Berlin, Heidelberg (1980).

[11] D.A. Palmer, R. van Eldik, "The chemistry of metal carbonato and carbon dioxide complexes", *Chem. Rev.* 83 (1983): 651.

[12] J. E. Oddo, M.B. Tomson, "Simplified calculation of CaCO₃ saturation at high temperatures and pressures in brine solutions", SPE of AIME (Richardson, TX: Society of Petroleum Engineers, 1982): 1,583.

[13] "Comprehensive chemical kinetics", vol. 6 (Amsterdam, The Netherlands: Elsevier Publishing Co., 1972): 283-284.

[14] M. Nordsveen, S. Nestic, R. Nyborg, and A. Stangeland, "A mechanistic model for carbon dioxide corrosion of mild steel in the presence of protective iron carbonate Films—Part 1: Theory and Verification", *Corrosion*, vol., 59 (2003): 443-456.

[15] S. Nestic, "Key issues related to modelling of internal corrosion of oil and gas pipelines – A review", *Corr. Sci.*, 49 (2007): 4308-4338.

-
- [16] P. G. T. Fogg and C. L. Young, Eds., "IUPAC Solubility data series", vol. 32, "Hydrogen Sulfide, Deuterium Sulfides, and Hydrogen Selenide", Pergamon Press, Oxford, England, 1988. In L. H. Gevantman, *Solubility of selected gases in water, Handbook of chemistry and physics*, 2004 - 2005. Chemical Rubber Publ. Co., Cleveland. 84th ed., 8-90: 1318.
- [17] F. J. Millero, "The thermodynamics and kinetics of the hydrogen sulfide system in natural waters", *Marine Chemistry*, 18 (1986): 121—147.
- [18] D. Koschel, J.-Y. Coxam, and V. Majer, "Enthalpy and solubility data of H₂S in aqueous salt solutions at conditions of interest for geological sequestration", *Ind. Eng. Chem. Res.*, 52 (2013):14483–14491.
- [19] D. Rickard and G. W. Luther III, "Chemistry of iron sulfides", *Chem. Rev.*, 107 (2007): 514-562.
- [20] P. Flowers, K. Theopold, and R. Langley, "7.6 Molecular structure and polarity", in "Chapter 7. Chemical Bonding and Molecular Geometry", in *Chemistry*, an OpenStax resource. <https://opentextbc.ca/chemistry/chapter/7-6-molecular-structure-and-polarity/>
- [21] T. L. Brown, H. E. Lemay Jr., B. E. Bursten, C. J. Murphy, P. M. Woodward, and M. W. Stoltzfus, "Chemistry: the central science", 13/e, Pearson Higher Education.
- [22] J. Rayel. "Explain why molecules of water and hydrogen sulfide have the same shape" eNotes, 29 July 2013, <https://www.enotes.com/homework-help/explain-why-molecules-water-hydrogen-sulfide-have-445347>. Accessed 18 June 2019.

-
- [23] Y. Zheng, "Electrochemical mechanism and model of H₂S corrosion of carbon steel," *Ph.D. dissertation*, Dept. Chem. & Biomol. Chem. Eng., Ohio Univ., Athens, OH, (2014): 134-225.
- [24] P. Marcus and E. Protopopoff, "Potential-pH diagrams for adsorbed species, application to sulfur adsorbed on iron in water at 25 °C and 300 °C", *J. Electrochem. Soc.*, 137 (9): 2709-2712 (1990).
- [25] T. Richard, "Calculating the oxygen diffusion coefficient in water", Cornell Waste Management Institute, Cornell University, Ithaca, NY, 1996.
<http://compost.css.cornell.edu/oxygen/oxygen.diff.water.html>
- [26] O.N. Kovalenko, N.N. Kundo and P.N. Kalinkin, "Kinetics and mechanism of low-temperature oxidation of H₂S with oxygen in the gas phase", *React. Kinet. Catal. Lett.*, 72 (1): 139-145 (2001).
- [27] S. Ma, A. Noble, D. Butcher, R. E. Trouwborst, G. W. Luther III, "Removal of H₂S via an iron catalytic cycle and iron sulfide precipitation in the water column of dead end tributaries", *Estuarine, Coastal and Shelf Science*, 70 (2006): 461-472.
- [28] E. S. Snavely and F. E. Blount, "Rates of reaction of dissolved oxygen with scavengers in sweet and sour brines", *NACE Corrosion Conf.*, Houston, Texas, Paper No. 45 (1969).
- [29] J. L. Crolet, M. Pourbaix, A. Pourbaix, "The role of trace amounts of oxygen on the corrosivity of H₂S media", *NACE Corrosion Conf.*, paper no. 22 (Houston, TX: NACE, 1991).

-
- [30] Y. Song, A. Palencsár, G. Svenningsen, and J. Kvarekvål, T. Hemmingsen, “Effect of O₂ and temperature on sour corrosion”, *NACE Corrosion Conf.*, Paper no. 4299, (San Antonio, TX. NACE, 2014).
- [31] M. D. Deffo Ayagou, C. Mendibide, C. Duret-Thual, J. Kittel, K. Belkhadiri, T. T. Mai Tran, E. Sutter, B. Tribollet, and N. Ferrando, “Corrosion and Hydrogen Permeation in H₂S Environments with O₂ Contamination, 1: Tests on Pure Iron at High H₂S Concentration”, *Corros. J.*, 74 (11): 1192 – 1202 (2018).
- [32] J. Rethmeier, A. Rabenstein, M. Langer, U. Fischer, “Detection of traces of oxidized and reduced sulfur compounds in small samples by combination of different high-performance liquid chromatography methods,” *Journal of Chromatography A*, 760 (1997): 295-302.
- [33] Y. Miura, Y. Matsushita, P. R. Haddad, “Stabilization of sulfide and sulfite and ion-pair chromatography of mixtures of sulfide, sulfite, sulfate and thiosulfate”, *Journal of Chromatography A*, 1085 (2005): 47–53.
- [34] R. Lin, S. Bhardwaj, K. Srinivasan, and C. Pohl, “Improved analysis of sulfur-containing anions from polysulfide matrix by suppressed ion chromatography”, Dionex Corporation, Sunnyvale, CA, USA.
- [35] B. S. Krumgalz, “Mineral Solubility in Water at Various Temperatures”, Israel Oceanographic and Limnological Research Ltd., Haifa, 1994. In D. R. Lide, ed. (2003-2004). *CRC Handbook of Chemistry and Physics* (84th ed.). Boca Raton, FL: CRC Press: 8-110.

-
- [36] D. R. Lide, ed, *CRC Handbook of Chemistry and Physics* (85th ed.). CRC Press. 2004 :4–45.
- [37] “Solubility data series”, International Union of Pure and Applied Chemistry, volume 26, Pergamon Press, Oxford, 1979-1994. In D. R. Lide, (1998), *Handbook of Chemistry and Physics* (87 ed.), Boca Raton, Florida: CRC Press: 8–110.
- [38] Справочник по растворимости. - Т.1, Кн.1. - М.-Л.: ИАН СССР (1961): 34.
<http://chemister.ru/Database/properties-en.php?dbid=1&id=5293>
- [39] L. G. Benning, R. T. Wilkin, H.L. Barnes, “Reaction pathways in the Fe–S system below 100° C”, *Chemical Geology*, 167 (2000): 25–51.
- [40] Lay, Manchiu D. S.; Sauerhoff, Mitchell W.; Saunders, Donald R.; “Carbon Disulfide”, in *Ullmann's Encyclopedia of Industrial Chemistry*, Wiley-VCH, Weinheim, 2000.
- [41] M. Bamberg, “Gmelin handbuch der anorganischen chemie, schwefel”, Teil A, Lieferung 3, VCH, Weinheim, 1953. *Dissertation*, Univ. Saarbrücken, 1959.
- [42] “Health effects of toluene”, Canadian Centre for Occupational Health and Safety.
- [43] Y. Kitamaki, Y. Shimizu, K. Kato, “Sulfur standard solution for use in the determination of low sulfur concentration in liquid fuels”, *Anal. Bioanal. Chem.* 391(2008): 2089–2094.
- [44] J. O’ m. Bockris, M. A. V. Devanathan, K. Müller (1963). "On the structure of charged interfaces". *Proceedings of the Royal Society of London. Series A. Mathematical and Physical Sciences.* 274 (1356): 55–79.

-
- [45] S. Nestic, "Carbon dioxide corrosion of mild steel", in *Uhlig's Corrosion Handbook*, 3rd edition, edited by W. Revie, John Wiley and Sons Inc. (2011): 229.
- [46] S. Nestic, J. Postlethwaite and S. Olsen, "An electrochemical model for prediction of corrosion of mild steel in aqueous carbon dioxide solutions", *Corros. J.*, 52 (4): 280-294.
- [47] T. Tanupabrunsun, B. Brown, S. Nestic, "Effect of pH on CO₂ corrosion of mild steel at elevated temperatures", in NACE Corrosion Conf., Houston, TX. Paper no. 2348 (2013).
- [48] J. Han, B. N. Brown, D. Young, S. Nestic, "Mesh-capped probe design for direct pH measurements at an actively corroding metal surface", *J. Appl. Electrochem.*, 40 (2010): 683–690.
- [49] E. van Hunnkik, B. F. M. Pots, and E. L. J. A. Hendriksen, "The formation of protective FeCO₃ corrosion product layers in CO₂ corrosion," in *NACE Corrosion Conf.*, paper no. 6, Houston TX: NACE International (1996).
- [50] P. Marcus, "Sulfur-assisted corrosion mechanisms and the role of alloyed elements", In *Corrosion mechanisms in theory and practice*, 2nd ed, Marcel Dekker, Inc. New York (2002): 307.
- [51] W. Sun, "Kinetics of iron carbonate and iron sulfide scale formation in CO₂/H₂S corrosion", *Ph.D. dissertation*, Dept. Chem. & Biomol. Chem. Eng., Ohio Univ., Athens, OH (2006).
- [52] Y. Zheng, B. Brown, S. Nešić, "Electrochemical study and modeling of H₂S corrosion of mild steel", *Corros. J.*, 70 (4): 351-365 (2014).

-
- [53] W. Zhang, B. Brown, D. Young, S. Netic, M. Singer, “Factors influencing localized corrosion of mild steel in marginally sour environments”, *NACE Corrosion Conf.* Houston TX, paper no. 10984 (2018).
- [54] A. Cutright, “Investigation of mild steel corrosion rates in CO₂ environments with trace H₂S”, *CCJIP board meeting report*, Institute of Corrosion and Multiphase Technology, Ohio university, March, 2020.
- [55] D. W. Shoesmith, M. G. Bailey and B. Ikeda, “Electrochemical formation of mackinawite in alkaline sulphide solutions”, *Electrochimica Acta*, 23 (1978) 1329-1339.
- [56] M. Wolthers, S. J. Van der Gaast, D. Rickard, “The structure of disordered mackinawite”, *Am. Mineral.*, 88 (2003): 2007.
- [57] A. Lennie and D. J. Vaughan, “Spectroscopic studies of iron sulfide formation and phase relations at low temperatures”, In *Mineral Spectroscopy: A Tribute to Roger G. Burns*; Dyar, M. D., McCammon, C., Schaefer, M. W., Eds.; The Geochemical Society: Houston, TX, 5 (1996) 117-131.
- [58] H, Fang, “Investigation of localized corrosion of carbon steel in H₂S environments”, *Ph. D dissertation*, Dept. Chem. & Biomol. Chem. Eng., Ohio University, Athens, OH, 2012.
- [59] S. Gao, P. Jin, B Brown, D. Young, S. Netic, M. Singer, “Corrosion behavior of mild steel in sour environments at elevated temperatures”, *Corros. J.*, 73 (8): 915-926.
- [60] S. Gao, “Thermodynamics and kinetics of hydrogen sulfide corrosion of mild steel at elevated temperatures,” *Ph. D Dissertation*, Ohio University (2018).

-
- [60] J. Holmes, "Fate of Incorporated Metals during Mackinawite Oxidation in Sea Water," *Applied Geochemistry*, 14 (1999): 277-281.
- [61] A. K. Dunlop, H. L. Hassell, and P. R. Rhodes, "Fundamental considerations in sweet gas well corrosion," in *NACE Corrosion Conf.*, Anaheim, CA, paper no. 46, (1983).
- [62] O. Vosikovsky, M. Macecek, and D. J. Ross, "Allowable defect sizes in a sour crude oil pipeline for corrosion fatigue conditions," *Int. J. Pres. Ves. & Piping*, 13(1983): 197-226.
- [63] S. N Smith. "Discussion of the history and relevance of the CO₂/H₂S ratio," in *NACE Corrosion Conf.*, Houston, TX, Paper no. 11065 (2011).
- [64] J. Marsh, et al., "Evaluation of inhibitor performance for protection against localized corrosion", in *NACE Corrosion Conf.*, Houston, TX. Paper no. 02288 (2002).
- [65] B. N. Brown, "The influence of sulfides on localized corrosion of mild steel", *Ph. D Dissertation*, Dept. Chem. & Biomol. Chem. Eng., Ohio University (2013): 232.
- [66] F. Fehlner and M. Graham, "Thin oxide film formation on metals", in *Corrosion mechanisms in theory and practice*, P. Marcus editor, Marcel Dekker, Inc. (2002).
- [67] M. Seo, J. B. Lumsden, R. W. Staehle, "An AES analysis of oxide films on iron", *Surface Science*, 50 (2): 541-552 (1975).
- [68] S. Haupt, U. Collisi, H.D. Speckmann, H.-H. Strehblow, "XPS and ISS examinations of electrode surfaces and passive layers with a specimen transfer in a closed system", *J. Electroanal. Chem.*, 194 (1985): 179.

-
- [69] A. Machet, A. Galtayries, S. Zanna, L. Klein, V. Maurice, P. Jolivet, M. Foucault, P. Combrade, P. Scott, P. Marcus, “XPS and STM study of the growth and structure of passive films in high temperature water on a nickel-base alloy”, *Electrochimica Acta*, 49 (22–23): 3957-3964 (2004).
- [70] R. Revie, B. Baker, and J. Bockris, “The Passive film on iron: An application of Auger electron spectroscopy”, *J. Electrochem. Soc.*, 122(1975): 1460.
- [71] W. E. O'Grady, “Mössbauer Study of the Passive Oxide Film on Iron”, *J. Electrochem. Soc.*, 127 (3): 555-563 (1980).
- [72] S. Haupt, C. Calinski, U. Collisi, H. W. Hoppe, H.-D. Speckmann and H.-H. Strehblow, “XPS and ISS examinations of electrode surfaces and passive layers with a specimen transfer in a closed system”, *Surface and Interface Analysis*, 9 (1986): 357-365.
- [73] H. Strehblow, “Mechanisms of Pitting Corrosion”, in *Corrosion Mechanisms in Theory and Practice*, P. Marcus editor, Marcel Dekker, Inc. (2002).
- [74] G. Genchev, and A. Erbe, “Raman spectroscopy of mackinawite FeS in anodic iron sulfide corrosion products”, *Journal of the Electrochemical Society*, 163 (6): C333-C338 (2016).
- [75] J.-A. Bourdoiseau, M. Jeannin, R. Sabot, C. Rémazeilles, Ph. Refait, “Characterisation of mackinawite by Raman spectroscopy: Effects of crystallisation, drying and oxidation”, *Corros. Sci.*, 50 (2008): 3247–3255.
- [76] A. Anderko and P. J. Shuler, “A computational approach to predicting the formation of iron sulfide species using stability diagrams”, *Computers & Geoscience*, 23 (6): 647-658, (1997).

-
- [77] J. Ning, Y. Zheng, D. Young, B. Brown, and S. Nešić, “Thermodynamic study of hydrogen sulfide corrosion of mild steel”, *Corros. J.*, 70 (2014): 375-389.
- [78] A. R. Lennie, S. A. T. Redfern, P. F. Schofield, and D. J. Vaughan, “Synthesis and rietveld crystal structure refinement of mackinawite, tetragonal FeS”, *Mineral. Mag.*, 59 (1995): 677.
- [79] D. J. Vaughan, J. A. Tossell, “Electronic structures of sulfide minerals — Theory and experiment”, *Am. Mineral.*, 66 (1981): 1250.
- [80] D. Rickard, J. Morse, “Acid volatile sulfide (AVS)”, *Mar. Chem.*, 2005, 97, 141.
- [81] R. B. Jr. Herbert, A. R. Pratt, D.W. Blowes, S.G. Benner, “Surface oxidation of iron monosulphide: An X-ray photoelectron spectroscopic study”, *Mineralogical Magazine*, 62A (1998): 608–609.
- [82] A. R., Lennie, S.A.T., Redfern, P.E., Champness, C.P., Stoddart, P.F., Schofield, and D.J., Vaughan, “Transformation of mackinawite to greigite: an in-situ X-ray powder diffraction and transmission electron microscopy study”, *American Mineralogist*, 82 (1997): 302–309.
- [83] Y. Miura, Y. Matsushita, P. R. Haddad, “Stabilization of sulfide and sulfite and ion-pair chromatography of mixtures of sulfide, sulfite, sulfate and thiosulfate”, *Journal of Chromatography A*, 1085 (2005): 47–53.
- [84] Y. El Mendili, B. Minisini, A. Abdelouasa and J.-F. Bardeau, “Assignment of Raman-active vibrational modes of tetragonal mackinawite: Raman investigations and ab initio calculations”, *RSC Adv.*, 4 (2014): 25827–25834.

[85] G. Genchev, K. Cox, T. H. Tran, A. Sarfraz, C. Bosch, M. Spiegel, and A. Erbe, “Metallic, oxygen-containing reaction products after polarization of iron in H₂S saturated saline solutions”, *Corros. Sci.*, 98 (2015): 725–736.

[86] Stephen Smith, private communication.

[87] D. J. Vaughan and M. S. Ridout, “Mossbauer studies of some sulphide minerals,” *J. inorg. nucl. Chem.*, 1971, vol. 33, pp. 741 to 746. Pergamon Press. Printed in Great Britain.

[88] D. J. Vaughen, and J. A. Tossell, “Electronic structure of thiospinel minerals: results from MO calculations,” *American Mineralogist*, vol 66, pages 1250-1253, 1981.

[89] F. W. Herbert, “Mechanisms Governing the Growth, Reactivity and Stability of Iron Sulfides,” PhD Dissertation, Massachusetts Institute of Technology, 2015.

[90] D. A. Jones, “The technology and evaluation of corrosion,” in *Principles and Prevention of Corrosion*, 2nd ed., Upper Saddle River, NJ, Prentice Hall, 1996, ch.1, sec. 1.3: 5.

[91] D. A. Jones, “Pitting and crevice corrosion,” in *Principles and Prevention of Corrosion*, 2nd ed., Upper Saddle River, NJ, Prentice Hall, 1996, ch.7: 199.

[92] J. Marsh, J. W. Palmer, and R. C. Newman, “Evaluation of inhibitor performance for protection against localized corrosion,” in *NACE Corrosion Conf.*, Houston, TX. Paper no. 02288 (2002).

-
- [93] S. Navabzadeh Esmaeely, W. Zhang, B. Brown, M. Singer, and S. Nešić, “Localized corrosion of mild steel in marginally sour environments”, *Corros. J.*, 73 (9): 1098-1106 (2017).
- [94] W. Yan, B. Brown, S. Nesic, “Investigation of the Threshold Level of H₂S for Pitting of Mild Steel in CO₂ Aqueous Solutions,” *NACE Corrosion Conf.*, Paper no. 11472, (Phoenix, AZ, NACE, 2018).
- [95] N. Yaakob, “Top of the line corrosion in CO₂/H₂S environments,” *Ph.D. Dissertation*, Dept. Chem. & Biomol. Chem. Eng., Ohio Univ., Athens, OH (2014).
- [96] J. Kvarekvål and G. Svenningsen, “Effect of high H₂S partial pressures on localized corrosion of carbon steel,” in *NACE Corrosion Conf.*, Dallas, TX., Paper no. 5720 (2015).
- [97] H. Uhlig, “Passivity in metals and alloys”, *Corro. Sci.*, 19 (1979): 777 - 791.
- [98] J. Han, “Galvanic mechanism of localized corrosion for mild steel in carbon dioxide environments”, *Ph.D. dissertation*, Dept. Chem. & Biomol. Chem. Eng., Ohio Univ., Athens, OH (2009).
- [99] E. van Hunnkik, et al., “The formation of protective FeCO₃ corrosion product Layers in CO₂ Corrosion,” in *NACE Corrosion Conf.*, paper no. 6, Houston TX: NACE International (1996).
- [100] P. Marcus and E. Protopopoff, “Potential-pH diagrams for adsorbed species: application to sulfur adsorbed on iron in water at 25 °C and 300 °C,” *J. Electrochem. Soc.*, 137 (9): 2709–2712 (1990).

-
- [101] S. N. Smith and E. J. Wright, "Prediction of minimum H₂S levels required for slightly sour corrosion," in *NACE Corrosion Conf.*, paper no. 11, Houston TX: NACE International (1994).
- [102] W. F. Smith and J. Hashemi, "Foundations of Materials Science and Engineering", 4th ed., McGraw-Hill, 2006, ISBN 0-07-295358-6.
- [103] J. L. Mora-Mendoza and S. Turgoose, "Fe₃C influence on the corrosion rate of mild steel in aqueous CO₂ systems under turbulent flow conditions", *Corros. Sci.*, 44 (2002): 1223–1246, 2002.
- [104] D. A. Lopez, et al., "The influence of microstructure and chemical composition of carbon and low alloy steels in CO₂ corrosion: A state-of-the-art appraisal", *Mater. & Design*, 24 (2003): 561–575.
- [105] S. Al-Hassan, et al., "Effect of microstructure on corrosion of steels in aqueous solutions containing carbon dioxide", *Corros. J.*, 54 (1998): 480-491.
- [106] J. L. Crolet, et al., "Role of conductive corrosion products in the protectiveness of corrosion layers", *Corros. J.*, 54 (1998): 194-203.
- [107] S. Ieamsupapong, "Mechanisms of iron carbonate formation on mild steel in controlled water chemistry conditions", *Ph. D dissertation*, Ohio University (2016).
- [108] J. Ning, Y. Zheng, B. Brown, D. Young, and S. Netic, "The role of iron sulfide polymorphism in localized H₂S corrosion of mild steel", *Corros. J.*, 73 (2016): 155-168.
- [109] S. Gao, B. Brown, D. Young, M. Singer, "Formation of iron oxide and iron sulfide at high temperature and their effects on corrosion", *Corros. Sci.*, 135 (2018): 167-176.

-
- [110] G. Wranglen, "Review article on the influence of sulphide inclusions on the corrodibility of Fe and steel", *Corros. Sci.*, 9 (1969): 585-602.
- [111] A. W. Gjønnnes, "Effect of sulfide inclusions in austenitic stainless steel on the initiation of pitting in base metal and heat affected zone after welding", *Ph. D Dissertation*, Dept. of Mater. Sci. and Eng., Norwegian Univ. of Sci. and Techn., Trondheim, Norway (2012).
- [112] D. D. Macdonald, "The point defect model for the passive state", *J. Electrochem. Soc.*, 139 (12): 3434-3449 (1992).
- [113] H.-H. Strehblow, "Nucleation and repassivation of corrosion pits for pitting on iron and nickel", *Werkst. Korros.*, 27 (1976): 792.
- [114] H.-H. Strehblow, "Breakdown of passivity and localized corrosion: Theoretical concepts and fundamental experimental results", *Werkst. Korros.*, 35 (1984) :437.
- [115] H. Li, "A mechanistic model for CO₂ localized corrosion of carbon steel", *Ph.D. Dissertation*, Dept. Chem. & Biomol. Chem. Eng., Ohio Univ., Athens, OH (2011).
- [116] K. J. Vetter and F. Gorn, "Kinetics of layer formation and corrosion processes of passive iron in acid solutions", *Electrochim. Acta.*, 18 (1973): 321.
- [117] I. Milosev and H.-H. Strehblow, "The behavior of stainless steels in physiological solution containing complexing agent studied by X-ray photoelectron spectroscopy", *J Biomed Mater Res.*, 52 (2): 404-12 (2000).
- [118] S. Haupt and H.-H. Strehblow, "Corrosion, layer formation, and oxide reduction of passive iron in alkaline solution: a combined electrochemical and surface analytical study", *Langmuir*, 3 (1987): 873.

-
- [119] N. Sato, "A theory for breakdown of anodic oxide films on metals", *Electrochim. Acta.*, 16 (1971): 1683.
- [120] N. Sato, K. Kudo, and T. Noda, "The anodic oxide film on iron in neutral solution", *Electrochim. Acta.*, 16 (1971): 1909.
- [121] W. Li, "Mechanical effects of flow on CO₂ corrosion inhibition of carbon steel pipelines", *Ph. D. Dissertation*, Dept. Chem. & Biomol. Chem. Eng., Ohio Univ., Athens, OH (2016).
- [122] K.-L. J. Lee, "A mechanistic modeling of CO₂ corrosion of mild in the presence of H₂S", *Ph. D. Dissertation*, Dept. Chem. & Biomol. Chem. Eng., Ohio Univ., Athens, OH (2004).
- [123] D. W. Shoesmith, P. Taylor, M. G. Bailey, and D. G. Owen, "The formation of ferrous monosulfide polymorphs during the corrosion of Iron by aqueous hydrogen sulfide at 21 °C", *J. Electrochem. Soc.*, 127 (1980): 1007-1015.
- [124] S. Navabzadeh, G Bota, B Brown, S Nešić, "Influence of pyrrhotite on the corrosion of mild steel", *Corros. J.*, 74 (2017): 37-49.
- [125] H.-H. Strehblow and J. Wenners, "Investigation of the processes on iron and nickel electrodes at high corrosion current densities in solutions of high chloride content", *Electrochim. Acta.*, 22 (1977): 421.
- [126] J. Ning, "A descriptive model for localized corrosion of mild steel in an aqueous H₂S environment," in *CCJIP Advisory Board Meeting*, Institute for Corrosion and Multiphase Technology, Ohio Univ., (2014).

-
- [127] R. C. Woollam, J. R. Vera, C. Mendez, A. Huggins, and W.H. Durnie, “Localized corrosion due to galvanic coupling between FeS-covered and uncovered areas: another oilfield myth?” in *NACE Corrosion Conf.*, Houston, TX, Paper no. 2715 (2013).
- [128] S. N. Smith and M. Joosten, “Corrosion of carbon steel by H₂S in CO₂ containing oilfield environments - 10 year update”, *NACE Corrosion Conf.*, Paper No. 5484, NACE, Houston, TX, USA, (2015).
- [129] J. Larsen, “Downhole nitrate applications to control sulfate reducing bacteria activity and reservoir souring”, *NACE Corrosion Conf.*, Paper No. 02025, NACE, Houston, TX, USA (2002).
- [130] B. Brown, D. Young, and S. Nešić, “Localized Corrosion in an H₂S / CO₂ Environment”, *International Corrosion Congress/17*, NACE, Houston, TX, USA (2009).
- [131] N. Yaakob, F. Farelas, M. Singer, S. Nesic, D. Young, “Localized top of the line corrosion in marginally sour environments”, *NACE Corrosion Conf.*, Paper No. 96026, NACE, Houston, TX, USA, (2016).
- [132] B. Brown, “H₂S multiphase flow loop: CO₂ corrosion in the presence of trace amounts of hydrogen sulfide”, *Master’s Thesis*, Ohio University, 2004.
- [133] J. R. Galvele, “Transport processes and the mechanism of pitting of metals”, *J. Electrochem. Soc.*, 123 (1976): 464–474.
- [134] D. D. Macdonald, “The point defect model for the passive state”, *J. Electrochem. Soc.*, 139 (1992): 3434-3449.
- [135] A. Dugstad, “Mechanism of protective film formation during CO₂ corrosion of carbon steel”, *NACE Corrosion Conf.*, Paper No. 31, NACE, Houston, TX, USA, (1998).

-
- [136] W. Sun and S. Netic, “A mechanistic model of uniform hydrogen sulfide/carbon dioxide corrosion of mild steel”, *Corros. J.*, 65 (2009): 291–307.
- [137] Y. Zheng, J. Ning, B. Brown, and S. Nešić, “Advancement in predictive modeling of mild steel corrosion in CO₂- and H₂S-containing environments”, *Corros. J.*, 72 (2016): 679-691.
- [138] D. E. Jiang and E. A. Carter, “Adsorption, diffusion, and dissociation of H₂S on Fe (100) from first principles”, *J. Phys. Chem. B*, 108 (2004): 19140–19145.
- [139] Z. Ma, Y. Yang, B. Brown, S. Netic, and M. Singer, “Investigation of FeCO₃ and FeS precipitation kinetics by EQCM”, *NACE Corrosion Conf.*, Paper No. 11192, NACE, Houston, TX, USA (2018).
- [140] J. Han, S. Netic, Y. Yang, B. N. Brown, “Spontaneous passivation observations during scale formation on mild steel in CO₂ brines”, *Electrochimica Acta.*, 56 (2011): 5396–5404.
- [141] “API specification 5L: specification for line pipe”, Forty-Third Edition, March 2004. Effective Date: October 2004 Errata December, 2004.
- [142] Test Report, Method: Fe-10-M, Type Standard: N-NIST-1763a, by Laboratory testing inc. May 14, 2014.
- [143] A. A. Al-Asadi, “Iron carbide development and its effect on inhibitor performance”, *Master’s Thesis*, Ohio University (2014).
- [144] X. Zhong, B. Brown, W. Li, S. Netic, M. Singer, “How to maintain a stable solution chemistry when simulating CO₂ corrosion in a small volume laboratory system”, *NACE Corrosion Conf.*, Paper No.7780, NACE, Houston, TX, USA (2016).

-
- [145] “Standard guide for examination and evaluation of pitting corrosion”, ASTM G46, 2013.
- [146] B. Brown, “The likelihood of localized corrosion in an H₂S/CO₂ environment”, *NACE Corrosion Conf.*, Paper No. 5855, NACE, Houston, TX, USA (2015).
- [147] H. Fang, B. Brown and S. Nešić, “Effects of sodium chloride concentration on mild steel corrosion in slightly sour environments”, *Corros. J.*, 67 (2011): 015001-1-015001-12.
- [148] Prepared in the context of cooperation between the International Programme on Chemical Safety and the European Commission © IPCS 2004-2012,
http://www.ilo.org/dyn/icsc/showcard.display?p_card_id=0928
- [149] “The peculiarity of nickel and Cobalt Sulphides”, science intelligence in the *American Journal of Science*, Edward S. Dana, 4th series, New Haven, 1914.
Original article in German: A. Thiel and H. Gessner, “Über Nickelsulfid und Kobaltsulfid. I. Die scheinbare Anomalie im Verhalten des Nickelsulfids gegen Säure”, *Journal of Inorganic and General Chemistry* (Zeitschrift für anorganische Chemie), 86 (1), 1–57, May 1914.
- [150] P. Jin, G. Bota, W. Robbins, and S. Nesic, “Analysis of oxide scales formed in the naphthenic acid corrosion of carbon steel”, *Energy Fuels*, 30 (8): 6853–6862 (2016).
- [151] Y. K. Kharaka, W. D. Gunter, P. K. Aggarwal, E. H. Perkins, and J. D. DeBraal, “Solmineq 88: A computer program for geochemical modeling of water rock interactions”, Menlo Park, CA: Alberta Research Council, 1989.

-
- [152] H. Fang, B. Brown and S. Nešić, "Sodium chloride concentration effects on general CO₂ corrosion mechanisms", *Corros. J.*, 69 (2013): 297-302.
- [153] F. Pessu, R. Barker, A. Neville, "Pitting and uniform corrosion of X65 carbon steel in sour corrosion environments: The Influence of CO₂, H₂S, and Temperature," *Corros. J.*, 73 (2017): 1168-1183.
- [154] F. Pessu, Y. Hua, R. Barker, A. Neville, "A study of the pitting and uniform corrosion characteristics of X65 carbon steel in different H₂S-CO₂-containing environments," *Corros. J.*, 74 (2018): 886-902.
- [155] Bert. F.M. Pots, Randy C. John, "Improvements on De Waard - Milliams corrosion prediction and applications to corrosion management", *NACE Corrosion Conf.*, Paper no.02235, (Denver, CO, NACE, 2002).
- [156] E. Heitz, "Chemo-mechanical effects of flow on corrosion", *NACE Corrosion Conf.*, paper no.1, Bally's Hotel, Las Vegas, Nevada (1990).
- [157] M. Parsi, K. Najmi, F. Najafifard, S. Hassani, B. S. McLaury, S. A. Shirazi, "A comprehensive review of solid particle erosion modeling for oil and gas wells and pipelines applications", *Journal of Natural Gas Science and Engineering*, 21: 850-873.
- [158] S. Wang, "Effect of oxygen on CO₂ corrosion of mild steel," *Master's Thesis*, Ohio University (2009).
- [159] N. R. Rosli, "The effect of oxygen in sweet corrosion of carbon steel for enhanced oil recovery applications," *Ph. D. Dissertation*, Ohio University (2015).
- [160] J. Holmes, "Fate of Incorporated Metals during Mackinawite Oxidation in Sea Water," *Applied Geochemistry*, 14 (1999): 277-281.

-
- [161] D. A. Jones, "Thermodynamics and Electrode Potential," in *Principles and Prevention of Corrosion*, 2nd ed., Upper Saddle River, NJ, Prentice Hall, 1996, ch.2, sec. 2.2: 59.
- [162] J.-A. Bourdoiseau, M. Jeannin, R. Sabot, C. Rémazeilles, Ph. Refait, "Characterisation of mackinawite by Raman spectroscopy: Effects of crystallisation, drying and oxidation," *Corros. Sci.*, 50 (2008): 3247–3255.
- [163] ASTM G1-03 (2017) e1, "Standard practice for preparing, cleaning, and evaluating corrosion test specimens", ASTM International, West Conshohocken, PA, 2017, www.astm.org.
- [164] U. Schwertmann, "Solubility and dissolution of iron oxides", *Plant and Soil*, 130 (1991): 1-25.
- [165] W. Zhang, B. Brown, D. Young, Gheorghe Bota, S. Nestic, M. Singer, "Pitting of mild steel in marginally sour environments -- Part I: a parametric study based on protective layers formation", to be published in the same journal.
- [166] W. Zhang, David Young, Bruce Brown, S. Nestic, M. Singer, "Pitting of mild steel in marginally sour environments -- Part II: pit initiation based on the oxidation of the chemisorbed FeS layers", to be published in the same journal.
- [167] M. Singer, "Part VI: Advancements in modeling and prediction top-of-the-line corrosion ", in *Trends in Oil and Gas Corrosion Research and Technologies*, 1st edition, edited by A. M. El-Sherik, Woodhead Publishing (2017): 698-699.
- [168] C. I. Pearce, R. A.D. Pattrick, D. J. Vaughan, "Electrical and magnetic properties of sulfides," *Reviews in Mineralogy & Geochemistry*, 61: 127-180 (2006).

-
- [169] K.Y.Chen, and J. Carrell Morris, “Kinetics of oxidation of aqueous sulfide by O₂”, *Environmental Science & Technology*, 6 (6): 529-537 (1972).
- [170] A. K. Dalai, A. Majumdar, and E. L. Tollefson, “Low temperature catalytic oxidation of hydrogen sulfide in sour produced wastewater using activated carbon catalysts”, *Environ. Sci. Technol.*, 33(1999) :2241-2246.
- [171] P. Kissinger, and W. R. Heineman, “Laboratory techniques in electroanalytical chemistry”, 2nd ed. Marcel Dekker, Inc: New York (1996).
- [172] Wang, J. “Analytical electrochemistry”, 3rd ed. John Wiley & Sons, Inc.: Hoboken, NJ (2006).
- [173] G. H. Kelsall, I. Thompson, “Redox chemistry of H₂S oxidation in the British Gas Stretford Process, Part I: Thermodynamics of sulphur-water systems at 298 K”, *Journal of Applied Electrochemistry*, 23 (1993): 279-286.
- [174] The LLNL thermo database: thermo.tdat. This is the default dataset of thermodynamic data for the GWB applications. <https://www.gwb.com/thermo.php>.
- [175] The thermodynamic dataset from the U.S. Geological Survey's PhreeqC program with free access without any permission required within the US, formatted for the GWB applications: thermo_phreeqc.tdat. <https://www.usgs.gov/software/phreeqc-version-3/>.
- [176] “Laboratory Testing of Metals for Resistance to Sulfide Stress Cracking and Stress Corrosion Cracking in H₂S Environments”. NACE Standard, TM0177-2016-SG, (2016).
- [177] RRUFF ID: R040135, University of Arizona Mineral Museum 5818, Locality: Sicily, Italy.
- [178] J. R. Galvele, “Transport processes and the mechanism of pitting of

metals,” *J. Electrochem. Soc.*, 123 (1976): 464.

[179] G. S. Frankel, “Pitting corrosion of metals: A review of the critical factors,” *Journal of the Electrochemical Society*, 145 (6): 2186-2198 (1998).

[180] R. Newman, “Pitting corrosion of metals,” *The Electrochemical Society Interface*, 19 (1): 33-38 (2010).

[181] A. Kahyarian, M. Achour, S. Nesic, “CO₂ corrosion of mild steel,” in *Trends in Oil and Gas Corrosion Research and Technologies, Production and Transmission*, Woodhead Publishing Series in Energy, 149-190 (2017).

[182] M. D. Fontana, K. B. Mabrouk, and T. H. Kauffmann, “Raman spectroscopic sensors for inorganic salts,” *Spectrosc. Prop. Inorg. Organomet. Compd.*, 44 (2013): 40–67.

[183] K. Furic, I. Ciglenceki, and B. Cosovic, “Raman spectroscopic study of sodium chloride water solutions”, *Journal of Molecular Structure*, 550–551 (2000): 225–234.

[184] M. C. Di Bonaventura, “Effect of flow on the formation of iron carbonate and influence of exposed iron carbide layer”, *Master Thesis*, Ohio University, Chemical Engineering (2017).

[185] M. Kalbac, H. Farhat, J. Kong, P. Janda, L. Kavan, and M. S. Dresselhaus, “Raman spectroscopy and in situ Raman spectroelectrochemistry of bilayer ¹²C/¹³C graphene”, *Nano Lett.*, 11(2011):1957–1963.

[186] W. T. E. van den Beld, M. Odijk, R. H. J. Vervuurt, J.-W. Weber, A. A. Bol, A. van den Berg, and J. C. T. Eijke, “In-situ Raman spectroscopy to elucidate the influence

of adsorption in graphene electrochemistry”, *Scientific Reports* | 7:45080 | DOI: 10.1038/srep45080.

[187] By Thyphoon7979 - Own work, CC BY-SA 4.0,

<https://commons.wikimedia.org/w/index.php?curid=59883279>

[188] A. Buckley, “The surface oxidation of pyrite”, *Applied Surface Science.*, 27 (1987): 437-452.

[189] K. Furic, I. Ciglencecki, and B. Cosovic, “Raman spectroscopic study of sodium chloride water solutions”, *Journal of Molecular Structure*, 550–551 (2000): 225–234.

[190] R.A. Berner, “Iron sulfides formed from aqueous solution at low temperatures and atmospheric pressures”, *J. Geol.*, 72 (1964) 293–306.

[191] S. Boursiquot, M. Mullet, M. Abdelmoula, J.-M. Génin, J.-J. Ehrhardt, “The dry oxidation of tetragonal FeS_{1-x} mackinawite”, *Phys. Chem. Miner.*, 28 (2001): 600–611.

[192] M. Mullet, S. Boursiquot, M. Abdelmoula, J.-M. Génin, J.-J. Ehrhardt, “Surface chemistry and structural properties of mackinawite prepared by reaction of sulfide with metallic iron”, *Geochim. Cosmochim. Acta.*, 66 (2002): 829–836.

[193] A. Boughriet, R. Figueiredo, J. Laureyns, P. Recourt, “Identification of newly generated iron phases in recent anoxic sediments: ⁵⁷Fe Mössbauer and micro Raman spectroscopic studies”, *J. Chem. Soc., Faraday Trans.*, 93(1997): 3209–3215.

[194] G. Genchev, K. Cox, T.H. Tran, A. Sarfraz, C. Bosch, M. Spiegel, A. Erbe, “Metallic, oxygen-containing reaction products after polarization of iron in H₂S saturated saline solutions”, *Corros. Sci.*, 98 (2015): 725–736.

-
- [195] B.W. A. Sherar, P.G. Keech, D.W. Shoesmith, “The effect of sulfide on the aerobic corrosion of carbon steel in near - neutral pH saline solutions”, *Corros. Sci.*, 66 (2013) 256–262, <http://dx.doi.org/10.1016/j.corsci.2012.09.027>
- [196] E.B. Hansson, M.S. Odziemkowski, and R.W. Gillham, “Formation of poorly crystalline iron mono sulfides: surface redox reactions on high purity iron, spectro electrochemical studies”, *Corros. Sci.*, 48 (2006): 3767–3783.
- [197] R. Downs, “the RRUFF Project: an integrated study of the chemistry, crystallography, Raman and infrared spectroscopy of minerals”, (2014) <http://www.rruff.info>. RRUFF ID: R060388.
- [198] B.W. A. Sherar, P.G. Keech, D.W. Shoesmith, “The effect of sulfide on the aerobic corrosion of carbon steel in near - neutral pH saline solutions”, *Corros. Sci.*, 66 (2013) 256–262, <http://dx.doi.org/10.1016/j.corsci.2012.09.027>.
- [199] R. Downs, “the RRUFF Project: an integrated study of the chemistry, crystallography, Raman and infrared spectroscopy of minerals”, (2014) <http://www.rruff.info>. RRUFF ID: R060440.2.
- [200] R. Downs, “the RRUFF Project: an integrated study of the chemistry, crystallography, Raman and infrared spectroscopy of minerals”, (2014) <http://www.rruff.info>. RRUFF ID: R120103.
- [201] R. Downs, “the RRUFF Project: an integrated study of the chemistry, crystallography, Raman and infrared spectroscopy of minerals”, (2014) <http://www.rruff.info>. RRUFF ID: R050142.

-
- [202] D. Neff, P. Dillmann, L. Bellot-Gurlet, G. Beranger, “Corrosion of iron archaeological artefacts in soil: characterisation of the corrosion system”, *Corros. Sci.*, 47 (2005): 515–535.
- [203] R. Downs, “the RRUFF Project: an integrated study of the chemistry, crystallography, Raman and infrared spectroscopy of minerals”, (2014)
<http://www.ruff.info>. RRUFF ID: R060191.
- [204] L. Bellot-Gurlet, D. Neff, S. Reguer, J. Monnier, M. Saheb, and P. Dillmann, “Raman studies of corrosion layers formed on archaeological irons in various media”, *J. Nano Res.*, 8 (2009): 147.
- [205] P. Colomban, S. Cherifi, and G. Despert, “Raman identification of corrosion products on automotive galvanized steel sheets”, *J. Raman Spectrosc.*, 39 (2008): 881.
- [206] M. K. Nieuwoudt, J. D. Comins, and I. Cukrowski, “The growth of the passive film on iron in 0.05 M NaOH studied in situ by Raman micro-spectroscopy and electrochemical polarisation. Part I: near-resonance enhancement of the Raman spectra of iron oxide and oxyhydroxide compounds”, *J. Raman Spectrosc.*, 42 (2011): 1335.
- [207] R. Downs, the RRUFF Project: an integrated study of the chemistry, crystallography, Raman and infrared spectroscopy of minerals, 2014
<http://www.ruff.info>. RRUFF ID: R100076.2.
- [208] R. Downs, the RRUFF Project: an integrated study of the chemistry, crystallography, Raman and infrared spectroscopy of minerals, 2014
<http://www.ruff.info>. RRUFF ID: R040135.2.

-
- [209] R. Downs, the RRUFF Project: an integrated study of the chemistry, crystallography, Raman and infrared spectroscopy of minerals, 2014
<http://www.ruff.info>. RRUFF ID: R040034.2.
- [210] E. J. Anyanwu, “The effect of flow on the development and retention of iron sulfide corrosion product layers”, *Ph.D. dissertation*, Dept. Chem. & Biomol. Chem. Eng., Ohio Univ., Athens, OH (2019).
- [211] B. A. Trofimov, L. M. Sinegovskaya and N. K. Gusarova, “Vibrations of the S–S bond in elemental sulfur and organic polysulfides: a structural guide”, *Journal of Sulfur Chemistry*, 30 (5): 518–554 (2009).
- [212] V. Piergrosso¹, C. Fasolato, F. Capitani, G. Monteleone, P. Postorino, and P. Gislou, “Application of Raman spectroscopy in chemical investigation of impregnated activated carbon spent in hydrogen sulfide removal process”, *International Journal of Environmental Science and Technology*, 16 (2019):1227–1238.



OHIO
UNIVERSITY

Thesis and Dissertation Services